



AGH

AGH UNIVERSITY OF SCIENCE AND TECHNOLOGY

Faculty of Physics and Applied Computer Science

Doctoral thesis

Krzysztof Janas

Measurement of diffractive jets production
in proton-proton collisions with
ALFA detectors in the ATLAS experiment

Supervisors:

prof. dr hab. inż. Mariusz Przybycień
dr inż. Leszek Adamczyk

Cracow, September 2023

Declaration of the author of this dissertation:

Aware of legal responsibility for making untrue statements I hereby declare that I have written this dissertation myself and all the contents of the dissertation have been obtained by legal means.

date and author signature

Declaration of the thesis Supervisor:

This dissertation is ready to be reviewed.

date and Supervisor signature

Abstract

The dissertation presents measurements of diffractive dijet production in proton-proton collisions at the centre-of-mass energy $\sqrt{s} = 13$ TeV. The measurements are based on data with an integrated luminosity of 725 nb^{-1} , which were collected with the ATLAS detector in October 2015. The LHC was running with special beam conditions: high- β^* optics ($\beta^* = 90$ m) and low average expected number of interactions ($\mu = 0.1$). Both single and central diffraction processes are analysed, in which one or both protons remain intact and can be measured by the ALFA forward detectors. This is the first measurement of dijet production in single diffraction with proton tagging in the ATLAS experiment and the first measurement of dijet production in central diffraction at the LHC.

The fiducial region of the measurements is limited by the ALFA detectors acceptance: relative energy loss of protons is in the range $0.002 < \xi < 0.160$ and the squared four-momentum transfers are $0.02 \text{ GeV}^2 < |t| < 1.00 \text{ GeV}^2$. In addition, the requirement of high efficiency of the jet trigger imposes limits on jets: the transverse momentum and pseudorapidity of the leading jet have to meet conditions $p_{\text{T}}^{\text{LJ}} > 30 \text{ GeV}$ and $|\eta^{\text{LJ}}| < 3.0$, and in the case of the secondary jet they are $p_{\text{T}}^{\text{SJ}} > 20 \text{ GeV}$ and $|\eta^{\text{SJ}}| < 4.0$.

The measured total fiducial cross section for dijet production in single diffraction is $\sigma_{\text{JJ}}^{\text{SD}} = 57.2 \pm 0.8(\text{stat})_{-8.7}^{+9.6}(\text{syst}) \text{ nb}$. The differential cross sections are measured in terms of ξ , t , p_{T}^{LJ} , $|\eta^{\text{LJ}}|$ and the fraction β^{JJ} of the Pomeron momentum carried by jets. Results are compared with model predictions based on the Pythia 8 and EPOS generators. Both models do not describe the data well. The ratio of single diffractive to total inclusive dijet production cross sections in the fiducial region is estimated to be $R_{\text{SD}} = 0.0238 \pm 0.0004(\text{stat})_{-0.0028}^{+0.0063}(\text{syst})$.

For central diffraction, the total cross section for dijet production is equal to $\sigma_{\text{JJ}}^{\text{CD}} = 329 \pm 59(\text{stat})_{-71}^{+61}(\text{syst}) \text{ pb}$. The differential cross sections are presented in terms of ξ and p_{T}^{LJ} , and are compared with models using Pythia 8, EPOS and Herwig generators. The dissertation is complemented by the search for exclusive dijet production, a special case of central diffraction, where the central state consists of only two jets without any Pomeron remnants.

Streszczenie

W rozprawie doktorskiej przedstawiono wyniki pomiarów produkcji dżetów w procesach dyfrakcyjnych w zderzeniach proton-proton przy energii $\sqrt{s} = 13$ TeV. Pomiaru są przeprowadzone na danych o scałkowanej świetlności 725 nb^{-1} , zebranych przez detektor ATLAS w październiku 2015 r. przy specjalnych warunkach: optyce $\beta^* = 90$ m i niskiej intensywności $\mu = 0.1$. Analizowana jest zarówno pojedyncza jak i centralna dyfrakcja, w których jeden lub dwa protony nie ulegają dysocjacji i mogą być mierzone przez detektor do przodu ALFA. Jest to pierwszy pomiar produkcji dżetów w procesach pojedynczej dyfrakcji z oznaczaniem protonu w eksperymencie ATLAS oraz pierwszy pomiar produkcji dżetów w procesach centralnej dyfrakcji na akceleratorze LHC.

Pomiar jest ograniczony przez akceptancję geometryczną detektora ALFA: mierzone są tylko protony o względnej stracie energii ξ w przedziale $[0.002, 0.160]$ i kwadracie przekazu czteropędu $0.02 \text{ GeV}^2 < |t| < 1.00 \text{ GeV}^2$. Dodatkowo, wydajność zastosowanego trygera jetowego L1_J12 narzuca ograniczenie na jety: pęd poprzeczny i pseudospieszość pierwszego jetu muszą spełniać warunki $p_T^{LJ} > 30 \text{ GeV}$ i $|\eta^{LJ}| < 3.0$; dla drugiego jetu są to odpowiednio $p_T^{SJ} > 20 \text{ GeV}$ i $|\eta^{SJ}| < 4.0$.

Dla pojedynczej dyfrakcji zmierzono całkowity przekrój czynny na produkcję dżetów równy $\sigma_{JJ}^{SD} = 57.2 \pm 0.8$ (stat) $^{+9.6}_{-8.7}$ (syst) nb. Dodatkowo wyznaczono różniczkowy przekrój czynny w funkcji ξ , t , p_T^{LJ} , $|\eta^{LJ}|$ oraz β^{JJ} , gdzie ostatnia zmienna odpowiada części pędu wymienianego Pomeronu unoszonej przez dżety. Wyniki zostały porównane z przewidywaniami MC: Pythia 8 i EPOS, oba te modele nie wykazują zgodności z danymi. Oszacowano także udział dyfrakcyjnej produkcji dżetów w odniesieniu do całkowitej produkcji dżetów w procesach nieelastycznych na poziomie $R_{SD} = 0.0238 \pm 0.0004$ (stat) $^{+0.0063}_{-0.0028}$ (syst).

Dla centralnej dyfrakcji otrzymano całkowity przekrój czynny równy $\sigma_{JJ}^{CD} = 329 \pm 59$ (stat) $^{+61}_{-71}$ (syst) pb. Różniczkowy przekrój czynny pokazano w funkcji ξ i p_T^{LJ} oraz porównano go z przewidywaniami MC: Pythia 8, EPOS i Herwig. Pracę wieńczą wyniki poszukiwania ekskluzywnej produkcji dżetów, które stanowią specjalny przypadek centralnej dyfrakcji gdzie stan centralny tworzą tylko dwa jety bez żadnych dodatkowych cząstek.

Acknowledgements

It would be impossible to finish this analysis without the support of many people. First of all, sincere thanks to my supervisors: Prof. Mariusz Przybycień and Dr. Leszek Adamczyk. Prof. Przybycień developed my interest in particle physics and took care of my progress. I express my deepest gratitude to Dr. Adamczyk for his enormous support since my B.Sc. studies. He has extensive knowledge and experience and has gotten my analysis back on the right track many times. I am thankful to both of my supervisors for everything.

I want to thank my colleagues with whom I worked during my PhD studies: Łukasz Fulek, Inga Łakomic and Rafał Sikora. I had the pleasure of working with them on diffractive physics and sharing experiences. I would like to thank Dr. Wolfgang Friebel who was my mentor during the DESY Summer School in Germany. Many thanks to Dr. Rafał Staszewski for supervising the ATLAS qualification task. I received a lot of support from Prof. Iwona Grabowska-Bołd and Prof. Tomasz Bołd, and I always appreciate and respect their opinion. I express my gratitude to Prof. Janusz Tobała and M.Sc. Krystyna Sobczyk for administrative support.

Last, but not least, I would like to deeply thank my loved ones: my wife Estera, my parents, siblings and friends. They make my life colourful.

Podziękowania

Ta praca nie powstałaby, gdyby nie wsparcie wielu osób. Szczególne podziękowania należą się moim promotorom, prof. dr hab. inż. Mariuszowi Przybycieniowi oraz dr inż. Leszkowi Adamczykowi. Pan Profesor rozwinął we mnie zainteresowanie fizyką cząstek i stale nadzorował mój rozwój i pracę. Pan Doktor stanowił dla mnie nieocenione wsparcie już od czasów studiów inżynierskich, jest źródłem ogromnej wiedzy i niejednokrotnie sprowadzał moją analizę na właściwe tory. Za wszystko co otrzymałem od obu promotorów serdecznie dziękuję.

Chcę też podziękować moim kolegom, z którymi współpracowałem podczas moich studiów doktoranckich, obecnie już doktorzy inżynierowie: Łukasz Fulek, Inga Łakomic i Rafał Sikora. Razem z nimi mogłem pracować nad procesami dyfrakcyjnymi i wspólnie wymieniać się doświadczeniem. Chciałbym podziękować dr Wolfgangowi Freibelowi za jego opiekę podczas szkoły letniej oraz dr Rafałowi Staszewskiemu za nadzór nad projektem kwalifikacyjnym do kolaboracji ATLAS. Jestem wdzięczny państwu dr hab. inż. Iwone Grabowskiej-Bołd i dr hab. inż. Tomaszowi Bołd za wielokrotnie dzielenie się opiniami na temat analizy. Dziękuję kierownikowi studiów doktoranckich, prof. dr. hab. inż. Januszowi Tobole oraz mgr Krystynie Sobczyk za opiekę administracyjną oraz pomoc w dopełnieniu wszystkich wymagań.

Na koniec chciałbym podziękować moim bliskim: mojej żonie Esterze, moim rodzicom, rodzeństwu i przyjaciołom. To ich obecność dodaje kolorów mojemu życiu.

Contents

Introduction	1
1 Theoretical Framework	3
1.1 The Standard Model	3
1.1.1 Elementary particles and fundamental forces	3
1.1.2 Strong interactions	5
1.1.3 Hadronisation	6
1.1.4 Jets	7
1.2 Diffractive processes	9
1.2.1 Classification of proton-proton interactions	9
1.2.2 Kinematic variables	9
1.2.3 Regge theory	15
1.2.4 Diffractive dijets production	16
1.3 Monte Carlo models	17
1.4 Objectives of the research	18
1.5 Overview of associated analysis	19
2 Experimental Setup	22
2.1 Basics of accelerator physics	22
2.2 Large Hadron Collider	23
2.3 ALTA S experiment	25
2.3.1 ATLAS coordinate system	26
2.3.2 Inner Detector	27
2.3.3 Calorimeters System	28
2.3.4 Muon Spectrometer	30
2.3.5 Minimum Bias Trigger Scintillators	30
2.3.6 Forward Detectors	31
2.3.7 Trigger and Data Acquisition systems	32
2.4 Track and vertex reconstruction	32
2.5 Topological clusters	33
2.6 Data samples	34
2.7 MC samples	35

3	The ALFA detectors	37
3.1	ALFA Roman Pots	37
3.2	Naming convention	39
3.3	Tracks reconstruction	39
3.4	Efficiency of track reconstruction	42
3.5	Proton transport and kinematic reconstruction	44
3.6	Vertical range estimation	45
3.7	Geometrical acceptance	46
4	Fast ALFA Alignment	48
4.1	Motivation	48
4.2	Alignment strategy	48
4.3	Distance measurements	50
4.3.1	ALFA Overlapping Detectors	50
4.3.2	Measurement principle	51
4.3.3	Events selection and measurement	52
4.3.4	Simulation	54
4.3.5	Results	56
4.4	Elastic selection	58
4.5	Track based alignment	61
4.5.1	Horizontal Offset	61
4.5.2	Vertical Offset	62
4.5.3	Rotation	64
4.5.4	Time dependency	65
4.6	Optimisation	69
4.6.1	Kinematic reconstruction and alignment	69
4.6.2	Vertical optimisation	70
4.7	Alignment in MC	73
4.7.1	Introduction	73
4.7.2	Track-based alignment for MC sample	74
4.8	Summary	75
5	Jets based corrections	77
5.1	Trigger efficiency	77
5.2	Jets cleaning	82
5.3	Jets reconstruction efficiency	82
5.4	Jets calibration	85
5.4.1	Motivation	85
5.4.2	Calibration strategy	85
5.4.3	Monte Carlo based calibration	88
5.4.4	Jet Energy Resolution	89
5.4.5	η -intercalibration	91
5.4.6	Absolute Energy Scale	92
5.4.7	JES and <i>in situ</i> combined uncertainty	94

6	Background contribution	97
6.1	Correlation between ξ^P and $\tilde{\xi}_{\text{CAL}}^X$	97
6.2	Accidental background	99
6.2.1	Accidentals with one proton topology	99
6.2.2	Accidentals with two protons topology	101
6.3	Inelastic background	106
6.3.1	Inelastic events with one detected proton topology	106
6.3.2	Inelastic events with two protons topology	110
7	Event selection and unfolding	114
7.1	Reconstructed vertex requirement and pileup	114
7.2	Fiducial region	115
7.3	Event selection	116
7.4	Resolution of kinematic variables and bin widths	118
7.5	Rapidity gap $\Delta\eta$ reconstruction	119
7.6	Unfolding for SD analysis	122
7.6.1	The concept of unfolding	122
7.6.2	Bin-by-bin corrections for ξ and t	123
7.6.3	Iterative Bayesian unfolding for jet variables	123
7.7	Unfolding for CD analysis	128
8	Systematic uncertainties	132
8.1	Jet trigger uncertainties	132
8.2	Jet calibration uncertainties	133
8.3	Jet efficiencies uncertainties	134
8.4	ALFA based uncertainties	134
8.5	Unfolding uncertainties	136
8.6	Other systematic uncertainties	136
8.7	Uncertainties summary	137
9	Results	141
9.1	Dijets production in single diffraction	141
9.1.1	Differential cross section	141
9.1.2	Total cross section	143
9.1.3	Contribution of the SD component	144
9.1.4	The ratio of the SD to inclusive dijet production	151
9.2	Dijets production in central diffraction	152
9.3	Exclusive dijets production search	154
	Summary	158
	Bibliography	167
	Acronyms	168
A	ALFA alignment results	171

*For from the greatness and beauty of created things
comes a corresponding perception of their Creator.*

Book of Wisdom 13:5

*Bo z wielkości i piękna stworzeń
poznaje się przez podobieństwo ich Stwórcę.*

Księga Mądrości 13,5

Introduction

From ancient times, people were amazed by the greatness and beauty of creations. They followed the harmony of observed phenomena and constructed rules to describe the relations between each object. With time, the rules transformed to the equations, which make up physics, the natural science that deals with the study of the most universal properties of matter and energy. It has many branches, and one of them is particle physics, which is focused on the smallest constituents of matter and the fundamental interactions between them. Three of four fundamental forces: electromagnetic, weak and strong are covered by the Standard Model, only gravity is not included in it. Quantum Chromodynamics provides a description of strong forces in terms of the exchange of coloured gluons. Gluons can interact with each other, which makes the QCD equations more complicated - the perturbative calculations are limited to the processes characterised by a high momentum transfer between the interacting partons. Lower transfers have to be described by phenomenological theories.

Diffraction is a good example of such a process for proton-proton collisions. It corresponds to events where one or both protons remain intact and are separated from the central state, called single or central diffraction. The process is described by Regge theory, which postulates that a colourless Pomeron is exchanged between protons. Diffractive processes are predominantly soft, but they do not allow one to determine the underlying parton dynamics and composition of the Pomeron. This can be achieved with hard diffraction processes, which are revealed by observation of jet production. This dissertation aims to measure this kind of process and provide a total and differential cross sections for single or central diffraction. It exploits the data collected at energy $\sqrt{s} = 13$ TeV by the ATLAS experiment. Forward protons are measured by the ALFA detector, which requires special beam conditions: optics $\beta^* = 90$ m and low intensity $\mu = 0.1$. The central state that includes jets is reconstructed with the ATLAS central detector.

This thesis consists of nine chapters. The first two give a short introduction to the theoretical framework and experimental setup used in this analysis. The third provides information about the ALFA detectors. Chapter 4 contains a full description of the fast ALFA alignment procedure. Chapter 5 focuses on jet-based corrections. It includes the dedicated jet calibration prepared by the author, as the standard procedure could not be applied. The background contribution is estimated in Chapter 6. Chapter 7 describes the event selections and the unfolding procedure. The systematic uncertainties are summarised in Chapter 8. The results are presented in Chapter 9, including a comparison between the data and the MC predictions.

The analysis presented in this dissertation is the original contribution of the author, except for some common parts of software shared with other diffractive analyses. Besides

of dijet analysis, the author was responsible for the ALFA alignment for diffractive runs, which was used also in other analyses. It was developed as the ATLAS qualification task. The results were presented at the LHCP2019 conference and were published in the proceedings:

- K. Janas, *The track-based alignment of the ALFA Roman Pot detectors of the ATLAS experiment*, 7th Annual Conference on Large Hadron Collider Physics, 20-25 May 2019, Puebla, Mexico, [PoS\(LHCP2019\)060](#).

As a member of the ATLAS Collaboration, the author is also the co-author of 173 publications. The author was also a member of the AGH ATLAS group. The results of this dissertation were presented and discussed in the ATLAS Soft QCD Working Group meetings and in the ARP General Meetings. In addition, the author has spent in total of about four months at CERN, including AFP detector beam tests and the LHC Run 2 data taking with the ALFA detector.

Chapter 1

Theoretical Framework

The Standard Model provides the interpretation for most of the observed interactions between particles. However, some processes are too complicated to be calculated directly. Diffractive events are good examples, where phenomenological Regge theory successfully describes the interactions. The study of diffractive dijet production, an example of hard diffraction, can reveal the connection between the phenomenological approach and perturbative quantum chromodynamics.

This chapter provides a theoretical framework that can be used to interpret the results. Throughout the thesis, the convention $c = \hbar = 1$ is used. Mass, energy, and momentum are usually expressed in MeV or GeV.

1.1 The Standard Model

1.1.1 Elementary particles and fundamental forces

Three of four fundamental forces: electromagnetic, weak and strong are described by the Standard Model (SM) of particle physics [1]. Electromagnetic forces have an effect on the electrically charged particles and are responsible for the existence of atoms and molecules. Strong interactions bind coloured quarks into nucleons, and residual forces bind nucleons into nuclei. The weak interactions handle weak decays. Only gravity is not included in SM. The forces are explained in terms of Quantum Field Theory (QFT), where two interacting objects exchange the corresponding particle.

Several classes of elementary particles can be distinguished, as shown in Fig. 1.1. The most obvious separation comes from the spin:

- fermions with half-integer spin that obey Fermi-Dirac statistics and follow the Pauli exclusion principle;
- bosons with integer spin that obey Bose-Einstein statistics.

The first group builds the whole visible matter and consists of quarks and leptons. The up u , down d , strange s , charm c , bottom b , and top t quarks have colour charge and interact strongly. Charged leptons: electron e , muon μ , and taon τ have corresponding neutral partners, almost massless neutrinos: ν_e , ν_μ , ν_τ . Quarks and charged leptons

Standard Model of Elementary Particles








	1 st generation	2 nd generation	3 rd generation				
QUARKS	UP mass: 2.2 MeV charge: +2/3 spin: 1/2 	CHARM mass: 1.3 GeV charge: +2/3 spin: 1/2 	TOP mass: 172.7 GeV charge: +2/3 spin: 1/2 	PHOTON mass: 0 charge: 0 spin: 1 	SCALAR BOSON	HIGGS BOSON mass: 125.3 GeV charge: 0 spin: 0 	
	DOWN mass: 4.7 MeV charge: -1/3 spin: 1/2 	STRANGE mass: 93.4 MeV charge: -1/3 spin: 1/2 	BOTTOM mass: 4.2 GeV charge: -1/3 spin: 1/2 	GLUON mass: 0 charge: 0 spin: 1 			
	LEPTONS	ELECTRON mass: 0.511 MeV charge: -1 spin: 1/2 	MUON mass: 105.7 MeV charge: -1 spin: 1/2 	TAU mass: 1.777 GeV charge: -1 spin: 1/2 		W BOSON mass: 80.4 GeV charge: ±1 spin: 1 	VECTOR BOSONS (GAUGE BOSONS)
		ELECTRON NEUTRINO mass: < 1.1 eV charge: 0 spin: 1/2 	MUON NEUTRINO mass: < 0.2 MeV charge: 0 spin: 1/2 	TAU NEUTRINO mass: < 18.2 MeV charge: 0 spin: 1/2 		Z BOSON mass: 91.2 GeV charge: 0 spin: 1 	

Figure 1.1: Particles of the Standard Model. Their mass, electric charge and spin are displayed in the figure. Values are from the Particle Physics Summary Tables (2022) [9].

interact electromagnetically; all fermions, including neutrinos, interact weakly. Quarks up and down, electron and electron neutrino belong to the so-called first generation, whereas other fermions belong to subsequent generations and are heavier and unstable. The number of generations was confirmed multiple times to be three, e.g., in measuring the production of the Z boson in the e^+e^- collisions in LEP [2, 3]. Another confirmation comes from cosmology, based on the primordial nucleosynthesis¹ [4]. The quarks and leptons are accompanied by their antiparticles, which have the same mass but opposite quantum numbers.

The second group of particles consists of bosons: photon γ , gluon g , bosons W^\pm , boson Z , and Higgs boson H . The first four are vector bosons with spin 1, known as the gauge bosons, which carry fundamental forces: electromagnetic - γ , weak - W^\pm and Z , strong - eight g with different colour components. The scalar boson H is the quantum excitation of the scalar Higgs field that generates the mass of the fermions and massive bosons [5, 6]. The mechanism was proposed in 1964, but evidence of the Higgs boson was provided in 2012 by two LHC detectors, ATLAS [7] and CMS [8].

¹The production of nuclei other than those of the hydrogen ^1H during the early phases of the Universe.

1.1.2 Strong interactions

Quantum Chromodynamics (QCD) provides a description of strong forces in the SM. It is a quantum field theory with symmetry group $SU(3)$, called a non-abelian gauge theory. As the name suggests (gr. $\chi\rho\omega\mu\alpha$ [chroma] means *colour*), QCD has an analogy of electric charge called colour, which is carried by quarks and gluons. However, instead of one, there are three colours, usually denoted red R , green G , and blue B , accompanied by their anti-colours: \bar{R} , \bar{G} , \bar{B} . There are eight generators in the $SU(3)$ group, as well as eight independent linear combinations of colours, that determine the presence of eight gluons in QCD [1]:

$$\begin{aligned}
 g_1 &= R\bar{G}, & g_2 &= R\bar{B}, & g_3 &= G\bar{R}, & g_4 &= G\bar{B}, & g_5 &= B\bar{R}, & g_6 &= B\bar{G}, \\
 g_7 &= \frac{1}{\sqrt{2}}(R\bar{R} - G\bar{G}), & g_8 &= \frac{1}{\sqrt{6}}(R\bar{R} + G\bar{G} - 2B\bar{B}).
 \end{aligned}
 \tag{1.1}$$

Contrary to photons, gluons carry the colour charge, and they are also subject to strong force. The self-interaction makes the QCD equations more complicated than quantum electrodynamics, as a consequence of the non-abelian properties of the theory [10].

One of the most important conclusions of QCD, known as colour confinement, states that quarks and gluons cannot exist alone. It can be explained with the simplified form of the QCD potential V_{QCD} , generated by the coloured quark at distance r [11]:

$$V_{\text{QCD}} = C \frac{\alpha_s}{r} + \lambda r, \quad \lambda > 0.
 \tag{1.2}$$

The potential can be split into two parts, Coulomb-like and linear. The former dominates at short distances, typically below 0.2 fm, and the latter is relevant at larger distances. The linear part corresponds to the gluon screening, which surrounds the coloured quark. This means that the energy of pair of quarks increases with the distance between them. The value of λ approximates 1 GeV/fm; therefore, the energy contained in the gluon field is large enough to produce a new pair of quarks at a separation of less than 1 fm.

The factor C in the Coulomb-like term is a constant that can take discrete values between $-4/3$ to $1/6$, depending on the types and quarks' colours. The strong interacting coupling constant α_s , which is dimensionless, defines the strength of the force. It depends on the energy scale Q involved in the interaction [1]:

$$\alpha_s(Q^2) = \frac{12\pi}{(33 - 2n_f) \ln(Q^2/\Lambda_{\text{QCD}}^2)}.
 \tag{1.3}$$

The quantity n_f is the number of quark flavours that can contribute to the interaction, namely those with a mass smaller than Q . The Λ_{QCD} scale parameter is approximately 0.2 GeV. A decreasing value of α_s with increasing energy is known as asymptotic freedom: at the large energy scale (or small length scale), quarks act as if they were free, insensitive to the strong force. It enables the applicability of perturbative calculations for hard processes occurring at a large energy scale. Theoretical predictions and experimental measurements of α_s as a function of the energy scale Q are presented in Fig. 1.2.

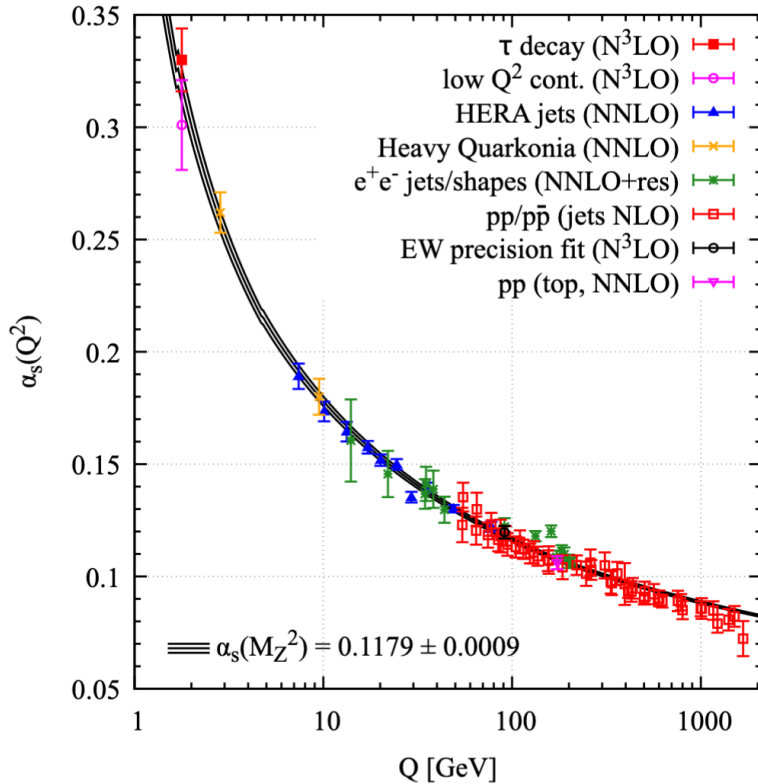


Figure 1.2: Theoretical predictions and experimental measurements of α_s as a function of the energy scale Q [9].

1.1.3 Hadronisation

As the quarks cannot be free, all of them are parts of complex particles, i.e. hadrons:

- mesons - made of the pair quark-antiquark, e.g. pions, kaons etc;
- baryons - made of the three quarks, e.g. proton uud or neutron udd .

Other combinations, e.g. pentaquarks, are very rare [12]. Aside from valence quarks that are the core of mesons and baryons, particles contain a sea of gluons and quarks, which materialise and annihilate continually.

Hadronisation corresponds to the process of transition between partons and hadrons. When two or more coloured partons are created in the collision of the two protons, only the colourless hadrons that are ultimately produced are observed experimentally. Due to colour confinement, the gluon or quark that leaves the interaction point starts to undergo parton showering and a combination of the produced partons into hadrons. The process cannot be examined perturbatively because the energy scale is relatively small. Instead, the phenomenological string model created in Lund is mostly used to calculate or simulate hadronisation.

The Lund string model assumes that the strong field between two partons forms a narrow colour tube or a string [13]. According to Eq. (1.2), the potential energy of such a string is proportional to the length (the Coulomb term is negligible for large distances).

When the initial quarks start to move away, the energy is enough to create the new pair of quark-antiquark and break the string into two - Fig. 1.3. The process is repeated recursively until the energy of the string is not high enough to create new pairs. In the end, all the quarks are bound inside the colourless mesons. The production of baryons can be simulated by, e.g. replacing a pair of quark-antiquark with a pair of diquark-antidiquark.

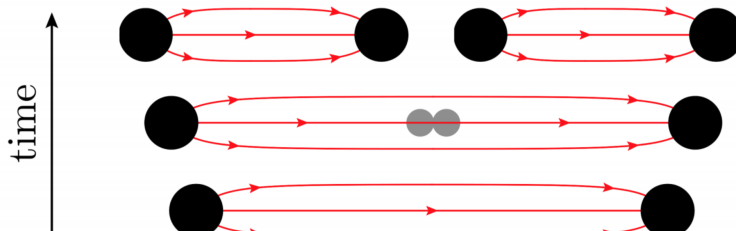


Figure 1.3: Scheme of breaking a string between a pair of partons in Lund string model. Red lines correspond to a gluon field. Grey dots represent a new pair of quark-antiquark. The figure is taken from [14].

1.1.4 Jets

The particles produced in the hadronisation share the momenta of the initial parton. Because all of them tend to move in the same direction, they form a narrow cone of particles. The ensemble of these objects is called a jet [15]. The pair of quark and antiquark have a back-to-back topology, therefore, they produce dijets, i.e. two jets with opposite directions. The example of a dijet signature can be seen in Fig. 1.4. The study of jet properties can give insight into the original parton.

There is no optimal method for defining jets. Many jet definitions have been developed and used over the last 40 years. A jet definition includes an input type, a recombination scheme and a jet algorithm [15]. Jets can be composed of different constituents, e.g. reconstructed tracks, clusters of calorimeter cells or truth plane particles. A typical recombination scheme is the four-vector scheme, which expresses the four-momentum of the jet as the sum of the constituents' four momenta. One of the most commonly used algorithms for jet clustering is the anti- k_t algorithm [17]. It satisfies basic criteria such as collinearity (collinear splitting should not change the jets) or infrared safety (soft emissions should not change the jets). It is also minimally sensitive to the effects of underlying events or pile-ups. In addition, the anti- k_t algorithm is quite simple and has good computational performance. It allows theoretical calculations to be compared with experimental measurements because it has an identical procedure on parton and hadron levels.

The anti- k_t algorithm compiles a list of distances d_{ij} and d_{iB} , where d_{ij} is the distance between each pair of objects i and j :

$$d_{ij} = \min(k_{t,i}^{-2}, k_{t,j}^{-2}) \cdot \left(\frac{\Delta R_{ij}}{R}\right)^2, \quad (1.4)$$

and d_{iB} is the distance from the object i to the beam:

$$d_{iB} = k_{t,i}^{-2}. \quad (1.5)$$

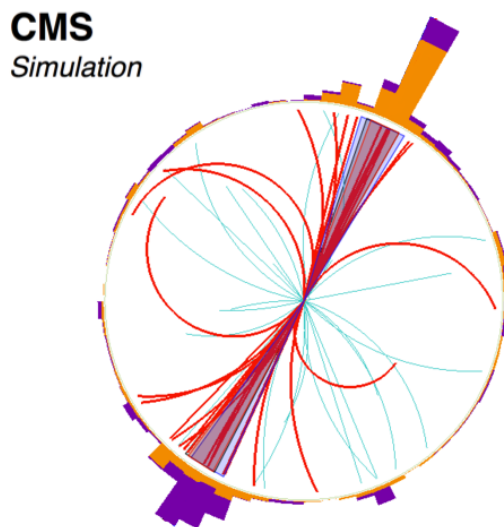


Figure 1.4: The signature of the dijet event simulated in the CMS detector. Lines correspond to the reconstructed tracks and bars show the amount of the measured energy in terms of polar angle. The figure is adapted from [16].

The variables $k_{t,i}, k_{t,j}$ denote the transverse momenta of objects i and j and ΔR_{ij} is the distance in the (η, ϕ) plane according to Eq. (2.5). If the smallest entry in the compiled list is d_{ij} , the objects i and j are combined, and the list is recalculated. Otherwise, the object with the smallest d_{iB} is considered a complete jet and is removed from the list. The parameter R is set to constant and is known as the radius parameter. It determines the size of the jets - anti- k_t produces circular cone-shaped jets, as can be seen in Fig. 1.5b. The most common value of R is 0.4, but 0.6 or 1.0 are also commonly used.

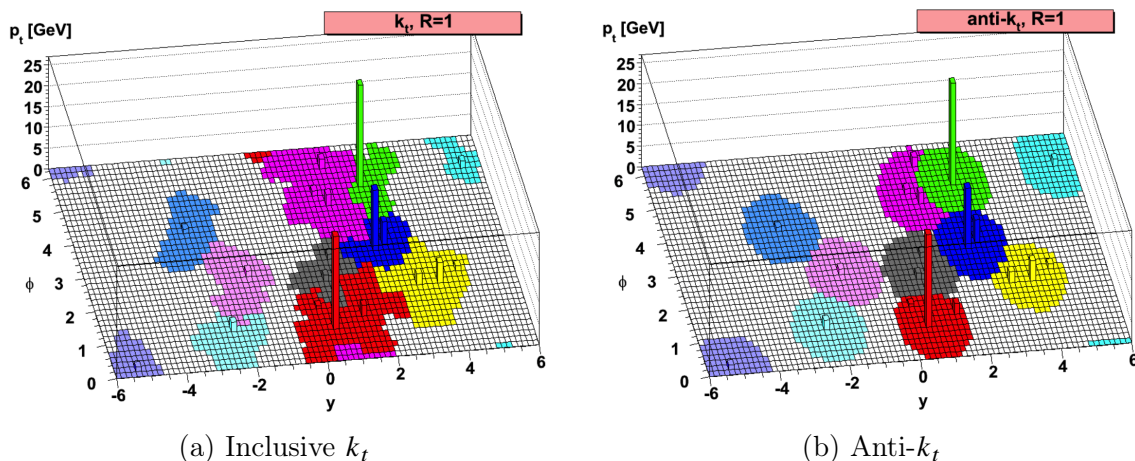


Figure 1.5: Comparison of two jet clustering algorithms: inclusive k_t and improved anti- k_t [17]. One of the advantages of the anti- k_t method is circular cone-shaped jets production.

1.2 Diffractive processes

1.2.1 Classification of proton-proton interactions

Interactions between protons can be of an elastic and inelastic nature. Elastically scattered protons have the same energy as the initials, with a small momentum transfer between them. They are scattered at small angles and can be observed in the forward region, and no new particles are produced in this kind of process. Inelastic events, on the contrary, produce a bunch of new particles and protons are typically destroyed.

An interesting subgroup of inelastic processes is diffraction². It is characterised by the exchange of Pomeron that exhibit only vacuum quantum numbers [18]. The colourless interaction produces no gluon radiation, which results in a region of the detector (in terms of rapidity - Section 1.2.2) without hadronic activity. This area is known as a Large Rapidity Gap (LRG), which can be used to distinguish the diffraction from other events. The topology of the outgoing state helps to divide diffractive processes: in single diffraction (SD), one proton dissociates into the central diffractive state X and the second proton remains intact and can be observed in the forward detector. In double diffraction (DD), both protons dissociate into states X and Y , with visible separation between them. Central diffraction (CD) describes a special kind of interaction, where both protons remain intact, but there is also a central state X , which is produced from the exchange of two Pomerons. Therefore, it is also known as the Double Pomeron Exchange (DPE). The processes schemas are shown on Fig. 1.6.

Non-diffractive events (ND) are based on the coloured exchange between partons, which gives a continuous distribution of produced particles. Large rapidity gaps may also occur in ND events because of fluctuations in particle production distributions. However, the size of the gap $\Delta\eta$ is distributed according to the Poisson statistics, related to the density of particles ρ :

$$P(\Delta\eta) = e^{-\rho\Delta\eta}, \quad (1.6)$$

and the larger gap sizes are exponentially suppressed.

Previous ATLAS measurements show that diffractive events represent about 30% of the inelastic interactions [19], with cross section ratios approximately:

$$\sigma_{SD} : \sigma_{DD} : \sigma_{CD} = 6 : 4 : 1. \quad (1.7)$$

1.2.2 Kinematic variables

Transverse momentum p_T and pseudorapidity η

The symmetry of the particle detectors makes cylindrical coordinates useful. The conversion is standard: the azimuthal angle ϕ is specified in the XY plane, and the polar angle θ is defined as the angle with the Z axis. The momentum of the particles can be decomposed into transverse and longitudinal momenta with respect to the Z axis. Taking

²Sometimes, the elastic scattering is also included in diffraction, because of similar properties and the mechanism of Pomeron exchange, contrary to non-diffractive events, see Section 1.2.3.

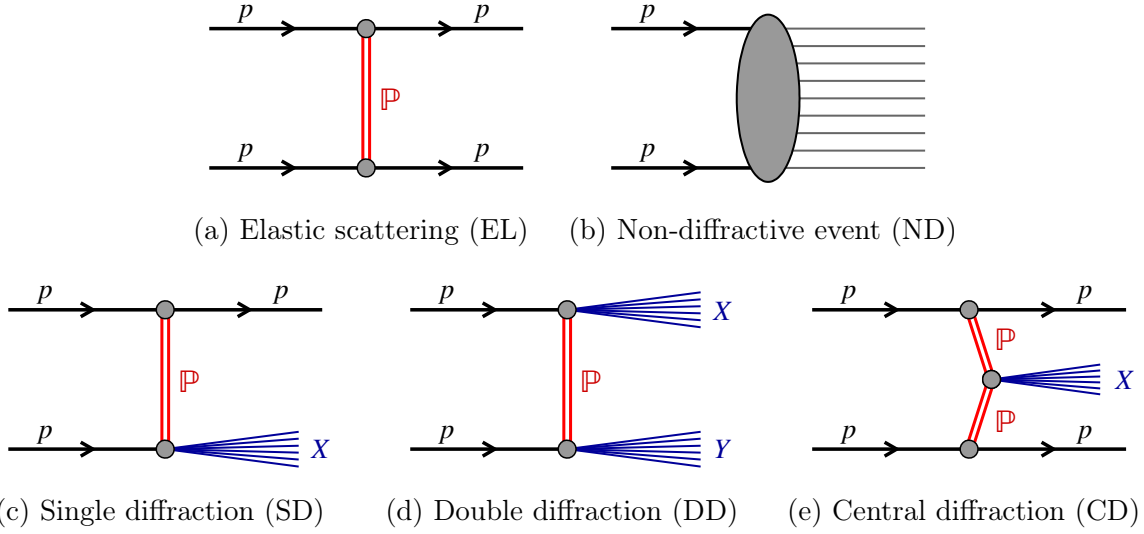


Figure 1.6: Feynman diagrams for types of proton-proton interactions. Red lines marked with \mathbb{P} symbol correspond to the exchanged Pomeron, and blue lines are diffractive states.

p as the magnitude of the momentum, the values are as follows:

$$p_T = p \sin \theta \qquad p_Z = p \cos \theta. \qquad (1.8)$$

Rapidity is commonly used to express the relativistic velocity, and corresponds to velocity v by following definition³:

$$y = \operatorname{arctanh} v. \qquad (1.9)$$

This definition has additive properties; hence, the pseudorapidity difference is invariant under Lorentz boost along the Z -axis [20]. In particle physics, the rapidity can be expressed with an equivalent equation in terms of particle energy and longitudinal momentum:

$$y = \frac{1}{2} \ln \frac{E + p_Z}{E - p_Z}. \qquad (1.10)$$

Instead of the polar angle or rapidity, the pseudorapidity η , defined as

$$\eta = -\ln \tan \frac{\theta}{2}, \qquad (1.11)$$

is more useful in analyses, because it approximates rapidity in the ultra-relativistic limit ($p^2 \gg m^2$) and is quite simple to calculate. The distributions of rapidity (or pseudorapidity) can be compared in experiments with different energies. Furthermore, particle production is almost constant as a function of η , unlike θ . The large gap in the distribution of particles η in a single event is a manifestation of a diffractive process.

³This definition follows the convention of $c = 1$.

Squared four-momentum transfer: t

In two-body scattering: $p_1 + p_2 \rightarrow p_3 + p_4$, kinematics can be expressed with three Mandelstam variables, defined by

$$\begin{aligned} s &= (p_1 + p_2)^2 = (p_3 + p_4)^2 \\ t &= (p_1 - p_3)^2 = (p_2 - p_4)^2, \\ u &= (p_1 - p_4)^2 = (p_2 - p_3)^2 \end{aligned} \quad (1.12)$$

where p_1 and p_2 correspond to the four-momenta of the incoming particles, p_3 and p_4 are the four-momenta of the outgoing particles. Mandelstam variables are Lorentz invariant. They are not independent, and it is easy to show that:

$$s + t + u = m_1^2 + m_2^2 + m_3^2 + m_4^2, \quad (1.13)$$

where m_1, m_2, m_3, m_4 denote the masses of interacting particles [1].

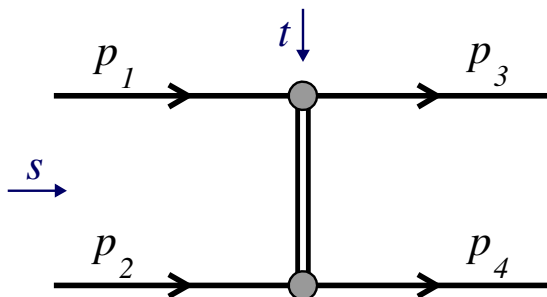


Figure 1.7: Scheme of interaction between two particles $p_1 + p_2 \rightarrow p_3 + p_4$.

By definition, the mass of the system of both colliding particles is equal to \sqrt{s} , and it is also the energy in the centre-of-mass frame. If the energy of the particles is the same, then:

$$\sqrt{s} = 2E_{beam}, \quad (1.14)$$

where E_{beam} denotes the energy of the particles in the collision beams. The t channel represents the exchange of an intermediate particle between two initial-state particles Fig. 1.7. In that case, t is called the square of the four-momentum transfer carried out by an intermediate particle.

Relative energy loss: ξ

For single diffraction processes: $p_1 + p_2 \rightarrow p_3 + X$, the invariant mass of the dissociated system M_X is equal to:

$$M_X^2 = p_X^2 = (p_1 + p_2 - p_3)^2 = (E_1 + E_2 - E_3)^2 - (\mathbf{p}_1 + \mathbf{p}_2 - \mathbf{p}_3)^2. \quad (1.15)$$

With two protons colliding in the CM frame, the $E_1 = E_2$ and $\mathbf{p}_1 = -\mathbf{p}_2$. Assuming that the outgoing proton energy is much greater than the proton mass, the momentum is approximately equal to the energy: $|\mathbf{p}_3| \approx E_3$. Then

$$M_X^2 \approx 4E_1^2 - 4E_1E_3 = 4E_1^2 \left(1 - \frac{E_3}{E_1}\right). \quad (1.16)$$

The expression in brackets is called a relative energy loss of a scattered proton:

$$\xi = 1 - \frac{E_3}{E_1}, \quad (1.17)$$

where E_1 is the beam energy and E_3 is the scattered proton energy. The analysis of SD processes is usually performed in terms of ξ . Recalling that $4E_1^2 = s$, the relative energy loss ξ is related to the invariant mass of the dissociated system M_X :

$$\xi \approx \frac{M_X^2}{s}. \quad (1.18)$$

Therefore, the value of variable ξ can also be estimated from the dissociated system mass M_X . However, due to recoil, some of the particles from the X system may fall out of the detector acceptance. This leads to information loss. The effect can be minimised by using an alternative expression. Assuming that the energy of the outgoing proton is significantly greater than the proton transverse momentum and mass, M_X^2 can be expressed with energies E^i and longitudinal momenta p_z^i of particles composing X :

$$M_X^2 \approx \sqrt{s} (E_X \pm p_{z,X}) = \sqrt{s} \sum_i (E^i \pm p_{z,X}^i), \quad (1.19)$$

where the sign is determined by the direction of the proton: positive for the proton in line with the Z -axis or negative otherwise. It can also be expressed in terms of particles' transverse momenta p_T^i and rapidities y^i :

$$M_X^2 \approx \sqrt{s} \sum_i p_T^i e^{\pm y^i}. \quad (1.20)$$

The benefit of Eq. (1.20) comes from the exponentially suppressed contribution to the mass of particles in the dissociated system travelling in very forward regions opposite to the proton (large rapidity). Therefore, the approximation is more sensitive to the particles in detector acceptance. However, for high ξ , some particles can escape the detector on the same side as the proton, and the mass will be reduced. Using the index A for positive side and C for negative side (the ATLAS experiment convention, see Section 2.3.1), ξ can be approximated by the following formulas:

$$\tilde{\xi}^{\text{XA}} = \frac{1}{\sqrt{s}} \sum_i p_T^i e^{y^i}, \quad \tilde{\xi}^{\text{XC}} = \frac{1}{\sqrt{s}} \sum_i p_T^i e^{-y^i}. \quad (1.21)$$

The sums run over the true particles or calorimeter clusters, tracks, jets, etc. depending on the context. The notation $\tilde{\xi}^{\text{X}}$ is used if a side distinction is unnecessary. The ξ reconstructed from proton energy with Eq. (1.17) will be denoted as ξ^{P} . When the side distinction is required, then the corresponding index is added: ξ^{PA} or ξ^{PC} .

The relation for central diffraction looks different. The mass of the dissociated system M_X in the reaction $p_1 + p_2 \rightarrow p_3 + p_4 + X$ is given by the following:

$$M_X^2 = p_X^2 = (p_1 + p_2 - p_3 - p_4)^2 = (E_1 + E_2 - E_3 - E_4)^2 - (\mathbf{p}_1 + \mathbf{p}_2 - \mathbf{p}_3 - \mathbf{p}_4)^2. \quad (1.22)$$

Recalling that $\mathbf{p}_1 = -\mathbf{p}_2$, the momentum part can be rewritten as:

$$(\mathbf{p}_1 + \mathbf{p}_2 - \mathbf{p}_3 - \mathbf{p}_4)^2 = (\mathbf{p}_3 + \mathbf{p}_4)^2 = |\mathbf{p}_3|^2 + |\mathbf{p}_4|^2 + 2|\mathbf{p}_3||\mathbf{p}_4| \cos \vartheta, \quad (1.23)$$

where ϑ is the angle between \mathbf{p}_3 and \mathbf{p}_4 . Approximating the momenta with energies and extracting $4E_1^2$, the mass M_X can be expressed as follows:

$$M_X^2 = 4E_1^2 \left(1 - \frac{E_3}{E_1} - \frac{E_4}{E_1} + \frac{1 - \cos \vartheta}{2} \cdot \frac{E_3}{E_1} \cdot \frac{E_4}{E_1} \right) \quad (1.24)$$

The outgoing protons are scattered in approximately the opposite directions and $\cos \vartheta \approx -1$; therefore, the invariant mass can be expressed as a product of the relative energy losses defined with Eq. (1.17):

$$M_X^2 \approx s \xi_3 \xi_4, \quad (1.25)$$

where ξ_3 and ξ_4 are the relative energy losses of the protons reconstructed on opposite sides of the interaction point (particles 3 and 4).

In central diffraction, ξ^{PP} denotes the product of the relative energy losses of the protons reconstructed on sides A and C. Then, the Eq. (1.25) transforms to:

$$M_X^2 \approx s \xi^{\text{PA}} \xi^{\text{PC}} = s \xi^{\text{PP}} \quad (1.26)$$

It can be compared to the ξ^{X} calculated directly from the mass of the central system:

$$\xi^{\text{X}} = \frac{M_X^2}{s} \approx \xi^{\text{PP}} \quad (1.27)$$

The measurement fulfils the above relation only for a well-reconstructed small M_X , with all components detected by the central detector. Otherwise, ξ^{X} is significantly lower than ξ^{PP} . Similar conclusions are correct for the second formula that binds ξ^{PA} and ξ^{PC} and the rapidity y_X of the central state X :

$$y_X = \frac{1}{2} \ln \frac{\xi^{\text{PA}}}{\xi^{\text{PC}}} \quad (1.28)$$

However, it should be noted that the relationship between $\tilde{\xi}^{\text{XA}}$ and ξ^{PA} , as well as $\tilde{\xi}^{\text{XC}}$ and ξ^{PC} , defined for SD processes, is still valid for CD analysis. This conclusion can be derived for the four-vector $p_{X'}$, which is the sum of p_X and p_4 . With this definition, the square of $p_{X'}$ is identical to Eq. (1.15), and the contribution of p_4 to the $\tilde{\xi}^{\text{X}}$ in Eq. (1.21) is exponentially suppressed. It turns out that the combination:

$$\tilde{\xi}^{\text{XA}} < \xi^{\text{PA}} \quad \wedge \quad \tilde{\xi}^{\text{XC}} < \xi^{\text{PC}} \quad (1.29)$$

allows one to separate the signal and the accidental background a little better than Eq. (1.27) and Eq. (1.28) for relatively high ξ events observed in this analysis.

Fraction of the Pomeron momentum carried by jets: β^{JJ}

The fraction of the proton momentum carried by the interacting parton in diffractive dijet production can be calculated as the ratio between the squared mass of the dijet system M_{JJ}^2 and squared mass of the diffractive system M_X^2 :

$$\beta^{JJ} = \frac{M_{JJ}^2}{M_X^2}. \quad (1.30)$$

The mass of the central state can be calculated from protons (ξ^P for SD and ξ^{PP} for CD). The mass of dijets in SD events can be approximated with Eq. (1.20), where the summation is over the leading and secondary jets, and an additional third jet, if present. Using an expression:

$$\tilde{\xi}_{JJ}^X = \frac{1}{\sqrt{s}} \sum_{jets} p_T^j e^{\pm y^j}, \quad (1.31)$$

with the sign determined by the direction of the proton, the value of β^{JJ} from Eq. (1.30) can be expressed as:

$$\beta^{JJ} \approx \frac{\tilde{\xi}_{JJ}^X}{\xi}. \quad (1.32)$$

Rapidity gap: $\Delta\eta$

The large rapidity gap characterises most of the diffractive events due to the colourless nature of the Pomeron exchange. It can be shown that for SD processes, the difference between the rapidity of the proton and the closest particle of the dissociated state is related to the fractional energy of the intact proton:

$$\Delta\eta \approx -\ln \xi. \quad (1.33)$$

A detailed derivation of the above formula can be found in [18]. Fluctuations that can break this relationship are exponentially suppressed.

Rapidity Gap Survival Probability S^2

The amount of measured diffractive event is usually less than predicted by models. The difference can be explained by introducing the concept of gap survival [21]. In some events, the diffractive production is followed by additional interaction between the central state and the outgoing protons. The large rapidity gap is then destroyed, populated by additionally produced particles, and the spectating proton can dissociate. The survival probability of a rapidity gap, denoted as S^2 is defined as the fraction of events for which the diffractive topology of the event is preserved.

With increasing \sqrt{s} , S^2 decreases, since the interactions between the remnants of the particles become stronger and tend to fill the gap. This has been confirmed by calculating the gap survival factor based on a perturbative QCD multiple interaction model [22]. The order of S^2 is estimated to be 5-10% on the TeV scale [21, 23].

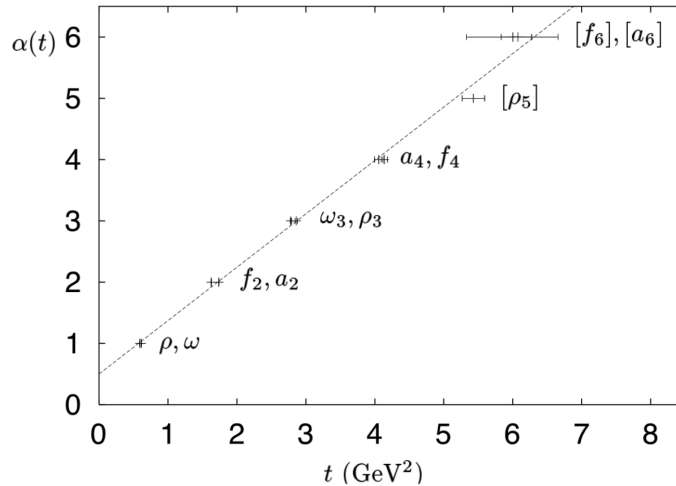


Figure 1.8: The Chew-Frautschi plot with the resonances in the function of t that lie on the line $\alpha(t) = 0.5 + 0.9t$. Plot taken from [24].

1.2.3 Regge theory

Pomeron, mentioned in the previous section, is a particle exchanged between protons and postulated with Regge theory. It is the most commonly adopted theory of diffractive interactions that cannot be described simply with QCD equations. In this theory, the particles exchanged between protons represent families of similar particles, i.e. resonances with all the same quantum numbers but the spin, and all of them provide input to the total cross section [24]. These particles are in the linear trajectories dependent on t , which can be expressed with intercept $\alpha(0)$ and slope α' :

$$\alpha(t) = \alpha(0) + \alpha' t. \quad (1.34)$$

The intercept of the trajectory is very important in the Regge theory. According to the optical theorem, the total cross section depends on the energy [25]:

$$\sigma_{tot} \propto s^{\alpha(0)-1}. \quad (1.35)$$

The trajectory with $\alpha(0) \approx 0.5$ describes quite well the data for low energies, i.e. $\sqrt{s} \lesssim 10$ GeV. The corresponding particles are presented on the Fig. 1.8. According to Eq. (1.35), a Reggeon intercept smaller than one means that σ_{tot} should be a monotonically decreasing function of s . It remains in contradiction with the experiments at higher energies, which shows an increase σ_{tot} with increasing energies, Fig. 1.9.

In 1992, Donnachie and Landshoff introduced the description of the total cross section [27]. They obtained an agreement with all the data available at that time, fitting different processes with only two main trajectories:

$$\sigma_{tot} = X s^{0.0808} + Y s^{-0.4525}, \quad (1.36)$$

where X and Y are parameters that depend on the process. The first term corresponds to the Pomeron trajectory \mathbb{P} with intercept $\alpha_{\mathbb{P}}(0) = 1.0808$, while the second represents

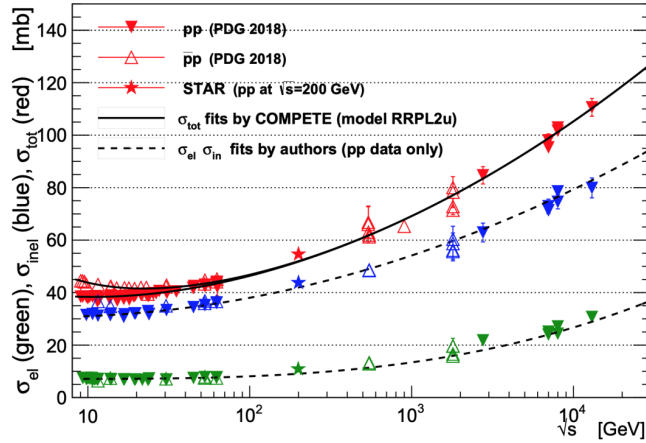


Figure 1.9: Compilation of the total σ_{tot} (red), elastic σ_{el} (green) and inelastic σ_{inel} (red) cross section measurement in the pp and $p\bar{p}$ collisions in function of \sqrt{s} [26].

the Reggeon trajectory \mathbb{R} with $\alpha_{\mathbb{R}}(0) = 0.5475$. The Pomeron is responsible for the effect of rising σ_{tot} as a function of \sqrt{s} and has been used to describe elastic and diffractive scattering. It does not have any charge - it has the quantum numbers of the vacuum. The nature of Pomeron is still not known; however, it is assumed to be a colourless multi-gluon exchange [28].

The Regge theory predicts differential cross sections in terms of ξ and t [29]:

$$\frac{d\sigma}{d\xi} \propto \left(\frac{1}{\xi}\right)^{2\alpha'_{\mathbb{P}} - \alpha_{\mathbb{P}}(0)} \quad \text{and} \quad \frac{d\sigma}{dt} \propto e^{-B|t|}, \quad (1.37)$$

where B is a constant that is proportional to the obstacle size in the scattering process.

1.2.4 Diffractive dijets production

Diffractive processes are predominantly soft, but they do not allow one to determine the underlying parton dynamics and composition of the Pomeron. This can be achieved with hard diffraction processes, which are revealed by observation of jet production. It was first proposed by Ingelman and Schlein in 1985 [30]. Within this framework, the Pomeron manifests a partonic structure and can be represented by two gluons or similar. The state can be calculated perturbatively, providing information about proton Diffractive Parton Distribution Functions (DPDFs).

The cross section for the hard process can be calculated as a convolution of the DPDF and the cross section of the parton-parton interaction:

$$d\sigma = f^D(\beta^{JJ}, Q^2, \xi, t) \otimes \sigma_{\text{hard}}(\beta^{JJ}, Q^2), \quad (1.38)$$

where β^{JJ} is a fraction of the Pomeron momentum carried by jets and Q^2 is the scale of the hard process. The DPDFs can be further decomposed into Pomeron flux component $\phi_{\mathbb{P}}(\xi, t)$, and the term $f_{\mathbb{P}}(\beta^{JJ}, Q^2)$, which describes the Pomeron partonic structure [31].

In the end, the cross section can be described by the following equation:

$$d\sigma = S^2 \phi_{\mathbb{P}}(\xi, t) f_{\mathbb{P}}(\beta^{JJ}, Q^2) \otimes \sigma_{\text{hard}}(\beta^{JJ}, Q^2), \quad (1.39)$$

where S^2 is the rapidity gap survival probability.

Fig. 1.10 shows the Feynman diagrams for diffractive dijets production. The first two correspond to the SD and inclusive CD processes, where the central state contains two jets and additional remnants of protons or Pomerons. The special case of CD dijets is presented in Fig. 1.10c, which shows the exclusive production of two jets. In this case, no additional remnants are observed; therefore, the correlations between protons and jets are fully preserved. The parameter β^{JJ} is equal to 1 by definition. These kinds of events provide the best source of information about the Pomeron structure. Unfortunately, the cross section is drastically low and it is difficult to distinguish the signal and background. Interactions between jets and spectating protons further decrease the probability of exclusivity observation.

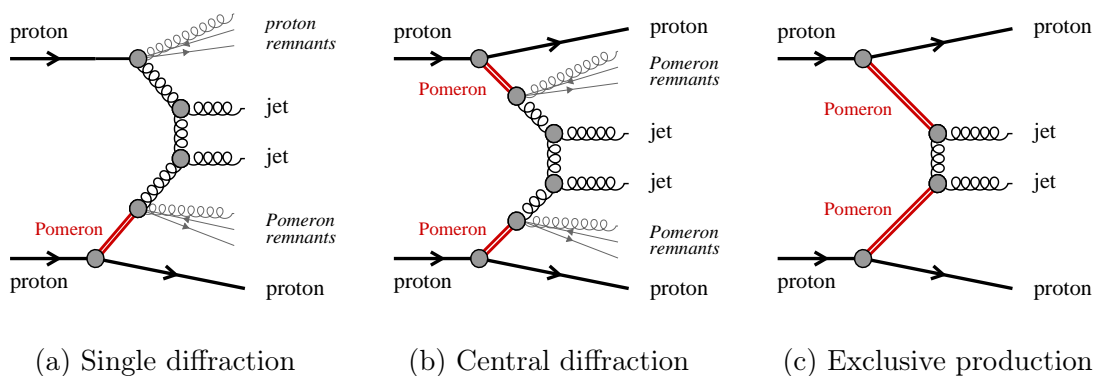


Figure 1.10: Feynman diagrams for diffractive dijet production.

1.3 Monte Carlo models

This analysis exploits simulated data generated with three types of Monte Carlo phenomenological models: PYTHIA 8, EPOS and HERWIG. They are compared with the results obtained with the experimental data. In addition, simulation can be useful for preparing corrections that involve detector effects, including unfolding (Section 7.6).

PYTHIA 8 is a standalone multipurpose event generator that serves as the main MC generator in most modern experiments. It handles collisions between hadrons or leptons and evolution from a few-body-hard process to complex multihadronic final state [32, 33]. For that, it comprises a coherent set of physics models in order to describe soft and hard processes, including but not limited to multiple parton-parton interactions, hadronisation, particle decays, beam remnants, and initial and final parton showers. By default, hadronisation is based on the Lund string model [34]. Besides non-diffractive processes, it provides support for diffractive ones (SD, CD and DD), for which it follows the Regge formalism. The generator implementation contains many parameters. In order to simplify the configuration, there are some prepared tunes, in which groups of parameters

are adjusted to deliver a sensible description of experimental data. In addition, the tune is often characterised by specific PDFs. For example, this analysis uses ATLAS tune A3 of PYTHIA 8 [35] and NNPDF23LO PDFs [36].

EPOS is an MC event generator originally used for the simulation of cosmic-ray air showers [37, 38]. It does not have parameter tunes that can be set by users; instead, a global set is used for all energies and systems. In this model, hadron-hadron interactions are described as a parton ladder from the projectile to the target, shown on Fig. 1.11. The parton ladder has two components: hard (partons) and soft (Pomerons), the latter is parameterised in the Regge pole fashion [39]. Additional particles come from two remnants of the shell, shown in Fig. 1.11. The mathematical formulation for EPOS is based on the simultaneous description of the hard and soft interactions, provided by the Gribov-Regge theory [40].

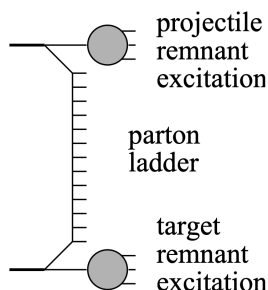


Figure 1.11: The parton ladder between hadrons, used in EPOS simulation [39].

EPOS does not have an implemented high-mass diffraction model, which is described by perturbative QCD in PYTHIA 8 [41]. Therefore, it almost does not provide the production of SD dijets explicitly. However, EPOS predicts many nondiffractive events with forward-scattered protons, which are well separated in rapidity from other final-state particles. In that event, the protons remnants turn out to be just low mass excitation ($1 < \text{GeV}$), which leads to hadronisation of them back to proton [42]. This model is very unique in EPOS compared to other string models, e.g. in PYTHIA 8. Events with this signature are separated from other ND events and are denoted as SD'.

The last, the HERWIG event generator [43, 44], is similar to PYTHIA 8. However, there are two major differences between these two generators. First, the multi-peripheral particle production model is used to evaluate the kinematics of the soft particles from the dissociation state [45]. Second, HERWIG places special emphasis on an accurate description of the multiple parton-parton interactions and final particle hadronisation, based on the cluster model [46].

1.4 Objectives of the research

Studies of diffractive dijet production, for example of the hard diffraction process, can connect the predictions of pQCD and Regge theory. It improves phenomenological theories and probes the nature of Pomeron. The distributions received in this thesis will be helpful to tune the MC models that simulate diffractive interactions. This analysis is the first

that utilises proton tagging in ATLAS diffractive dijet measurement, which significantly improves selections compared to the LRG analysis [47].

The main objective of this research is to present the differential cross sections for diffractive dijet production in pp collisions, based on the analysis of events with the ALFA proton tagging. The data are compared with the MC predictions. In addition, the total cross sections σ_{JJ}^{SD} and σ_{JJ}^{CD} for the SD and CD processes in the fiducial range are estimated. They are compared to the total cross section of inclusive dijet production σ_{JJ}^{incl} , i.e. all dijets produced in SD, CD, DD and ND events.

The SD analysis focuses on the differential cross-sections in the following terms:

- relative energy loss: $\frac{d\sigma^{SD}}{d\xi}$;
- squared four-momentum transfer: $\frac{d\sigma^{SD}}{dt}$;
- transverse momentum of leading jet $\frac{d\sigma^{SD}}{dp_T^{LJ}}$;
- pseudorapidity of leading jet $\frac{d\sigma^{SD}}{d\eta^{LJ}}$;
- fraction of the Pomeron momentum carried by jets $\frac{d\sigma^{SD}}{d\log_{10}\beta^{JJ}}$.

The last three distributions are also analysed in three regions of ξ : small, middle, and large. The middle region overlaps with the acceptance of the AFP detector Section 2.3.6. This can be helpful for a possible comparison of the AFP and ALFA analyses.

The CD analysis focuses on the measurement of the following cross-sections:

- relative energy loss: $\frac{d\sigma^{CD}}{d\log_{10}\xi^{PP}}$;
- transverse momentum of leading jet $\frac{d\sigma^{CD}}{dp_T^{LJ}}$.

1.5 Overview of associated analysis

The diffractive dijet production has been an interest of particle physics since 1985 with Ingelman and Schlein analysis [30]. After that, experiments were carried out by different collaborations, e.g. H1 Collaboration at HERA [48], which analysed the diffraction in electron-proton collisions. Fermilab Tevatron provided data from proton-antiproton collisions, which was exploited by CDS collaboration [49, 50] or D0 collaboration [51], with a collision energy of 600 GeV, 1800 GeV and 1960 GeV. This section focuses on other three papers which describe the diffractive dijet production at the LHC energies.

The diffractive dijet production analysis was performed in the ATLAS Experiment in $\sqrt{s} = 7$ TeV proton-proton collisions with an integrated luminosity of 6.75 nb^{-1} [47]. The trigger involved a combination of a minimum bias trigger and a single jet trigger. Forward protons were not exploited in this analysis. Therefore, the diffractive selection involves the large rapidity gap observed in the central detector. The fiducial cuts included two jets with $p_T > 20$ GeV, reconstructed with the anti- k_r algorithm with sizes $R = 0.4$ and $R = 0.6$. The cross section was presented with respect to the rapidity gap $\Delta\eta^F$

and fractional momentum loss of the proton ξ^{\pm} , shown in Fig. 1.12 for $R = 0.6$. The measurement shows a significant amount of ND events in the data. The reason is a small efficiency of large rapidity gap selection. This justifies the new analysis with a proton tagged by a forward detector.

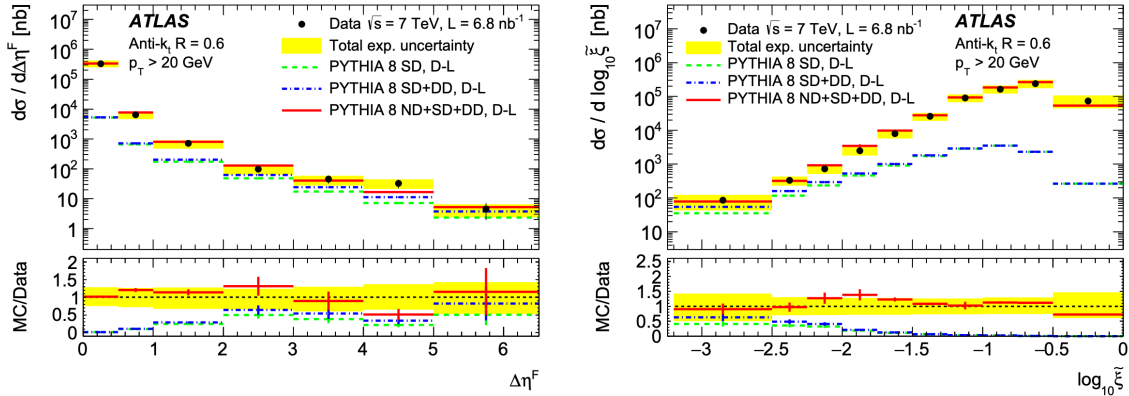


Figure 1.12: The differential cross sections in function of $\Delta\eta^F$ and ξ^{\pm} at $\sqrt{s} = 7$ GeV, compared with the particle level PYTHIA8 predictions [47]. The error bars on the data and MC models indicate their respective statistical uncertainties, while the yellow bands show the total uncertainties in the data.

The proton tagging analysis of SD dijet production was carried out using data collected simultaneously from CMS and TOTEM experiments with energies at 8 TeV [52]. In principle, current analysis is quite similar to TOTEM analysis, but it uses different detectors and energies. TOTEM provides cross sections as functions of ξ and t , in the fiducial region defined by $\xi < 0.1$, $0.03 < |t| < 1.00$ GeV² and dijets with $p_T > 40$ GeV and $|\eta| < 4.4$ - Fig. 1.13. The measured cross section was $\sigma_{jj}^{pX} = 22.6 \pm 1.0$ (stat) $^{+3.1}_{-3.4}$ (syst) ± 0.9 (lumi) nb.

The last analysis was performed by Patrycja Malinowska as her Bachelor of Engineering thesis [53]. It contains the newest PYTHIA 8 predictions with the same fiducial region as the current analysis, obtained with the RIVET framework [54]. The differential cross sections for ξ and p_T are presented on Fig. 1.14. Four types of processes were analysed, denoted as `sampleType`:

- `sampleType 1`: an inclusive sample of both diffractive and non-diffractive hard processes with additional multiparton interactions included;
- `sampleType 2`: an inclusive sample of both diffractive and non-diffractive hard processes without additional multiparton interactions included;
- `sampleType 3`: an exclusive diffractive sample with additional multiparton interactions included;
- `sampleType 4`: an exclusive diffractive sample without additional multiparton interactions included.

The results are similar to the previous version in terms of distribution shape, but it predicts a significantly larger total cross section.

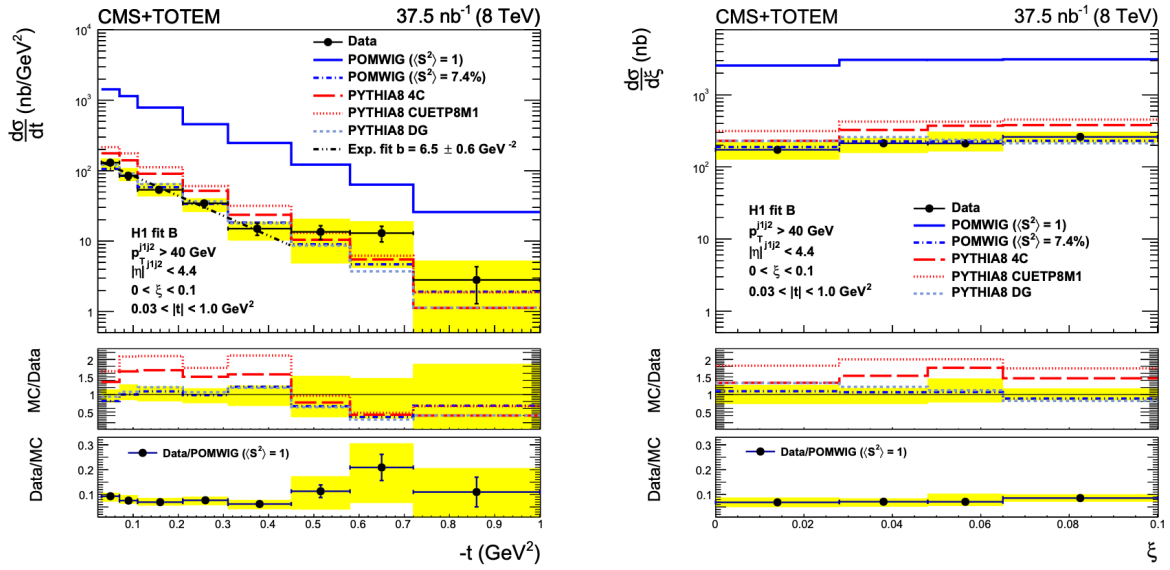


Figure 1.13: Differential cross sections as functions of t and ξ at $\sqrt{s} = 8$ GeV, compared with the MC predictions [52]. The POMWIG predictions are shown without ($S^2 = 1$) and with ($S^2 = 7.4\%$) the correction for the rapidity gap survival probability. The error bars on the data indicate statistical uncertainties, while the yellow bands show the total uncertainties.

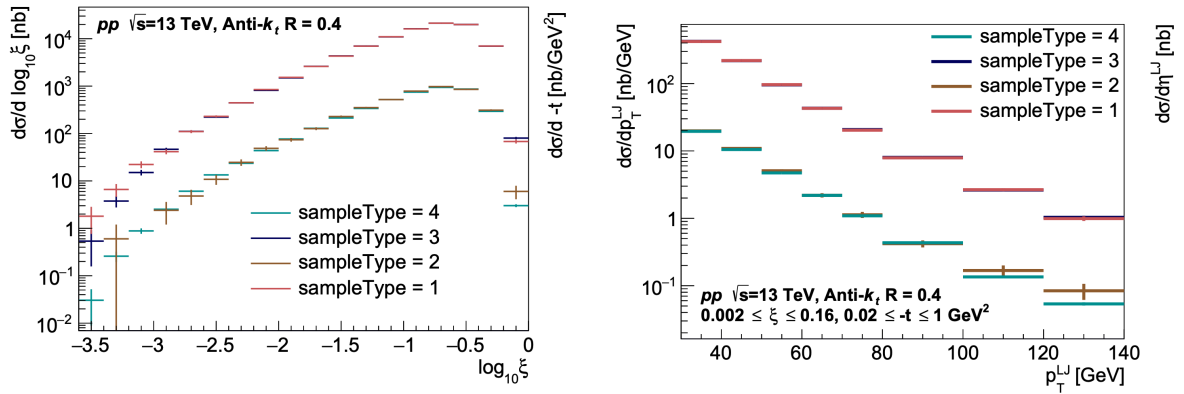


Figure 1.14: The differential cross section for SD dijet production predicted by the newest Pythia 8 generator [53], obtained with the RIVET framework [54]. The meaning of `sampleType` is described in the text.

Chapter 2

Experimental Setup

The ATLAS experiment is a general-purpose detector and is one of the four major experiments at the LHC. The central part consists of many complex subsystems, such as the Inner Detector and calorimeter system. They can record jets produced in diffractive dijets production. Furthermore, one of its forward detectors, the ALFA spectrometer, allows protons scattered at small angles to be measured in which process.

2.1 Basics of accelerator physics

In circular colliding beam accelerators, two beams of particles move in opposite directions and collide with each other at the Interaction Point (IP). The beams are not homogeneous, but the particles are grouped in bunches. The distance between two bunches is called the bunch separation and is often expressed as the time between consecutive collisions. If the two beams occupy the same axis, the bunches with small separations will meet outside the nominal IP. To avoid parasitic collisions, their trajectories must be separated by a crossing angle θ_c - Fig. 2.1.

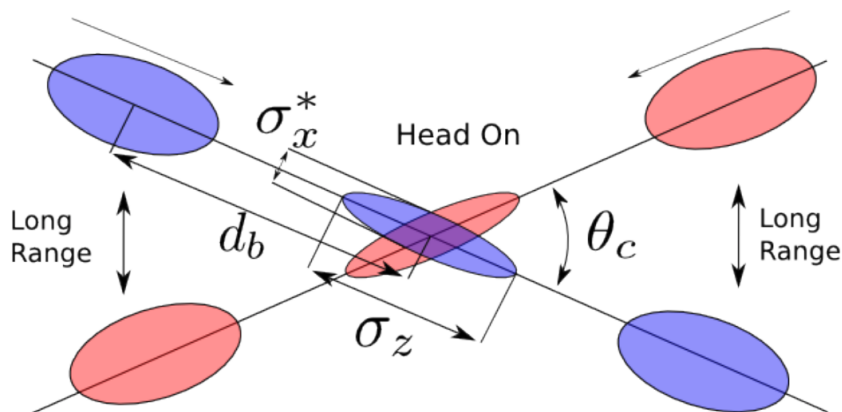


Figure 2.1: Collision of two LHC beams with crossing angle θ_c [55].

Luminosity is a measure of the number of particle interactions at the IP. The ratio of the rate of those interactions to the cross section is called instantaneous luminosity.

It does not depend on particle interaction processes, but can be expressed by the beam properties [55]:

$$\mathcal{L} = fn \frac{N_1 N_2}{4\pi\sigma_x\sigma_y} F, \quad (2.1)$$

and is proportional to the frequency of beam revolution f and the number of bunches per beam n , proportional to the number of protons in both the crossing bunches N_1 and N_2 , and inversely proportional to the transverse area of the bunch $4\pi\sigma_x\sigma_y$, where σ_x and σ_y describe the horizontal and vertical size of the bunch. The luminosity is reduced by a factor F due to the crossing angle θ_c :

$$F = \left(1 + \left(\frac{\theta_c\sigma_z}{2\sigma_x}\right)^2\right)^{-1/2}, \quad (2.2)$$

where σ_z describes the longitudinal bunch size. The luminosity integrated over time bounds the cross section σ and the number of events N for a given process [1]:

$$N = \sigma \int \mathcal{L} dt \quad (2.3)$$

The bunches are squeezed close to the collision to increase the luminosity. The betatron function in the IP denotes the distance from the IP where the beam size is doubled. It is known as β^* .

The number of particle interactions can be different for each bunch crossing due to statistical fluctuations. The average number of inelastic collisions per bunch crossing is denoted as μ :

$$\mu = \frac{\sigma_{inelastic} \int \mathcal{L} dt}{n_b} \quad (2.4)$$

where $\sigma_{inelastic}$ is the total inelastic cross section and n_b is the number of colliding bunches. Pileup is a situation where more than one pair of protons interact during a single bunch crossing. During the motion of proton bunches, some particles might also interact with the LHC instruments or with residual gas in the vacuum chambers. These processes create the beam halo - particles that stray from the bunch structure of the beam but still circulate inside the LHC beam pipe.

2.2 Large Hadron Collider

The biggest accelerator in the world, the Large Hadron Collider (LHC), is located on the border of Switzerland and France near Geneva [56]. It accelerates two beams of protons or heavy ions and collides them to study interactions at previously inaccessible energies. The highest designed centre of mass energy for proton collisions is 14 TeV, but the data analysed in this thesis were collected at $\sqrt{s} = 13$ TeV. The LHC is located in the tunnel previously occupied by the Large Electron-Positron collider, about 100 metres underground and 27 kilometres in circumference. There are 1232 dipole superconducting magnets that keep protons in a circular orbit. The beam focusing is performed by 392 quadrupole superconducting magnets.

The CERN accelerator complex Complexe des accélérateurs du CERN

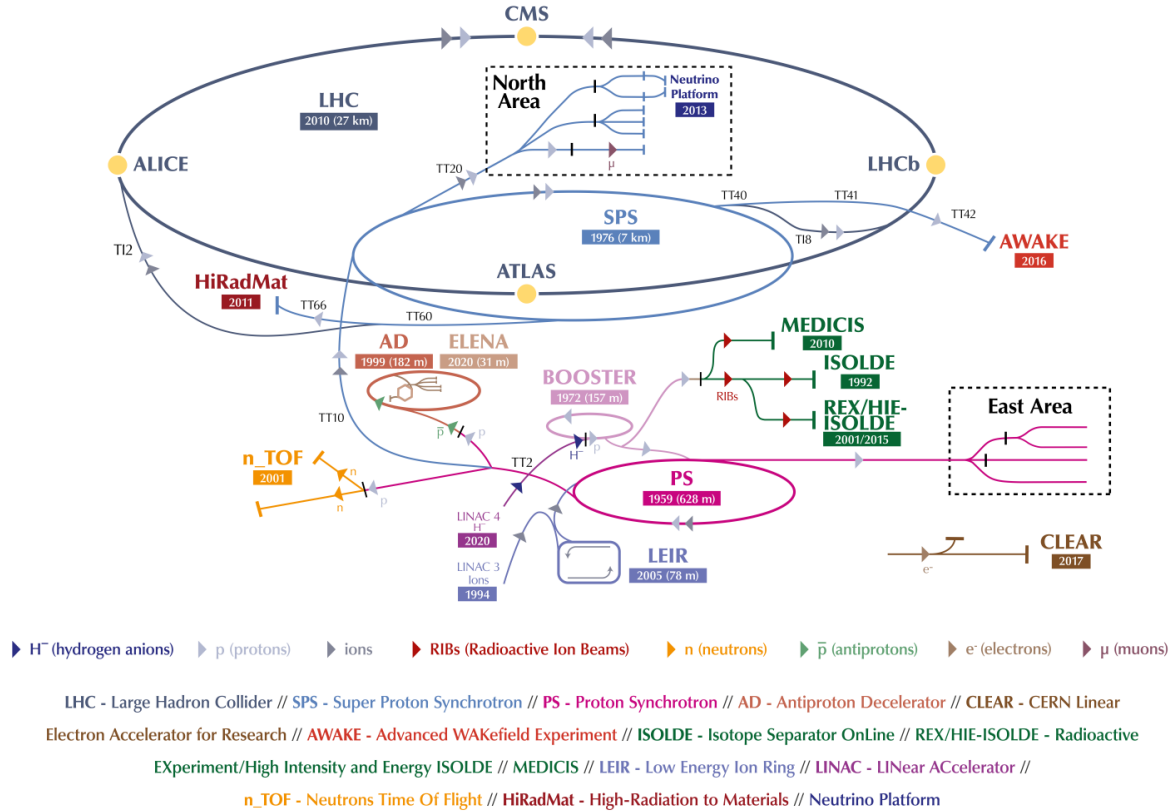


Figure 2.2: The CERN accelerators complex [57].

Particle acceleration consists of several stages. The LHC protons injection chain starts by stripping the hydrogen gas of its electrons in a machine called a duoplasmatron [56]. After that, protons are accelerated with several devices: Liniac 2, Proton Synchrotron Booster (PSB), Proton Synchrotron (PS), and Super Proton Synchrotron (SPS) - each of them accelerates protons to higher energy, they are presented on Fig. 2.2. In the final stage, protons reach their nominal energy with the LHC radio-frequency cavities. Each LHC fill has its own number. It can be divided into separate runs for each experiment, where a run is a discrete interval of data taking. Usually, a run number changes after some changes in the detector itself, such as trigger configuration or the subdetector turning on.

The LHC ring is divided into octants: in the middle of each octant is a straight sector and the ring arcs with dipole magnets between them. Four of the points are houses for beam management systems: two for cleaning, one with radio-frequency cavities, and one for beam dump. At the remaining points, the beams intersect, and collisions are studied by four main experiments. The ATLAS and CMS are general-purpose detectors, dedicated to precise measurements of Standard Model properties and search for physics beyond SM. The LHCb focuses on the CP -violation and rare B decays. The last one, the ALICE experiment, studies the properties of quark-gluon plasma in heavy-ion collisions.

2.3 ATLAS experiment

The largest particle detector ever constructed - **A Toroidal LHC ApparatuS (ATLAS)** - is a general-purpose detector located at the LHC. It has approximate cylindrical symmetry and is 44 m long and 25 m in diameter. The Interaction Point is located at the centre and is surrounded by multiple layers that form subdetectors designed to measure different characteristics of the outgoing particles. Fig. 2.3 shows an overview of the ATLAS detector.

The Inner Detector is in charge of tracking the charged particles, reconstructing their momenta and finding the vertices' positions. The Calorimeter System measures the energy of the neutral and charged particles, except for muons and neutrinos. The former are detected by the dedicated Muon Spectrometer covering the outermost layers. The subdetectors are enclosed in a magnetic field: the solenoidal magnet around the Inner Detector provides a uniform field of 2 T, whereas the barrel and two smaller air-toroidal magnets located in the end caps outside the calorimeters produce a magnetic field varying between 1 and 8 Tm [58]. Additional forward detectors outside the ATLAS cavern can measure particles at very small angles.

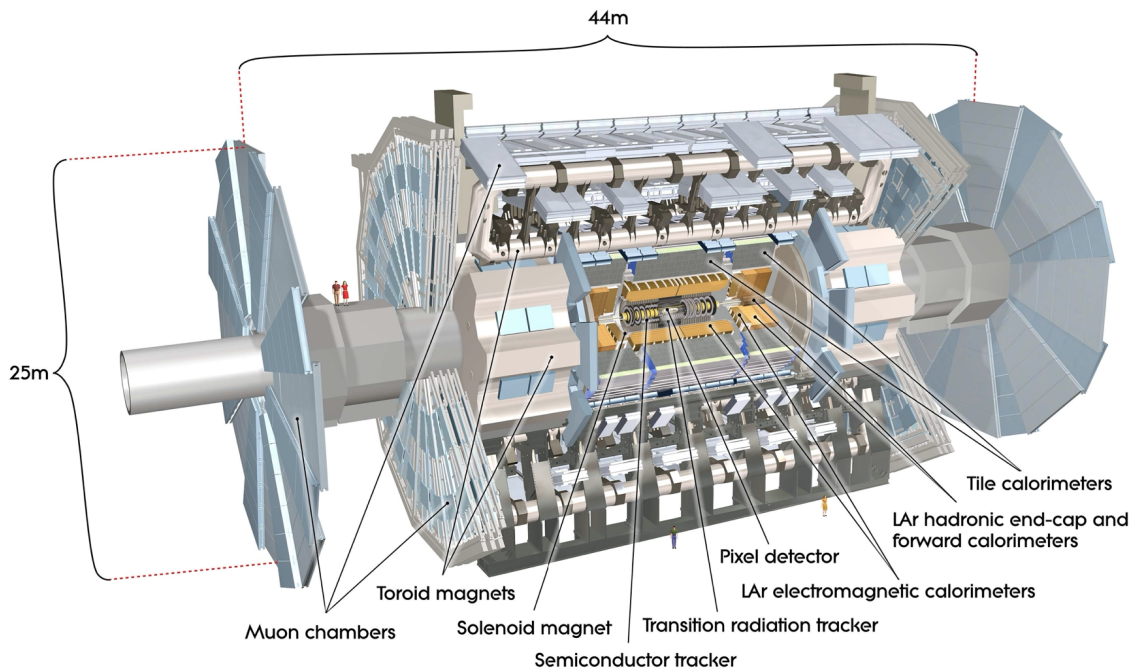


Figure 2.3: Cut-away view of the ATLAS detector [58].

The ATLAS detector participated in the discovery of the Higgs boson together with CMS [7, 8]. It also provides possibilities for precise measurement of other Standard Model particles, such as W and Z bosons or top and bottom quarks. The design of the detector aims to observe phenomena not observable earlier and to provide hints of physics beyond the Standard Model.

2.3.1 ATLAS coordinate system

The ATLAS system is designed with the nominal interaction point at the centre of the detector, which defines the origin of the ATLAS coordinate system. Three Cartesian axes are defined as a right-handed system: the X -axis points to the centre of the LHC ring, the Y -axis is directed upward, and the Z -axis is along the beamline, counterclockwise. The axes are shown in Fig. 2.4. Due to the general tilt of the LHC tunnel, the Y -axis is tilted with respect to vertical by 0.704° [59]. Two sides of the ATLAS detector are known as the A and C sides, with positive and negative z coordinates, respectively.

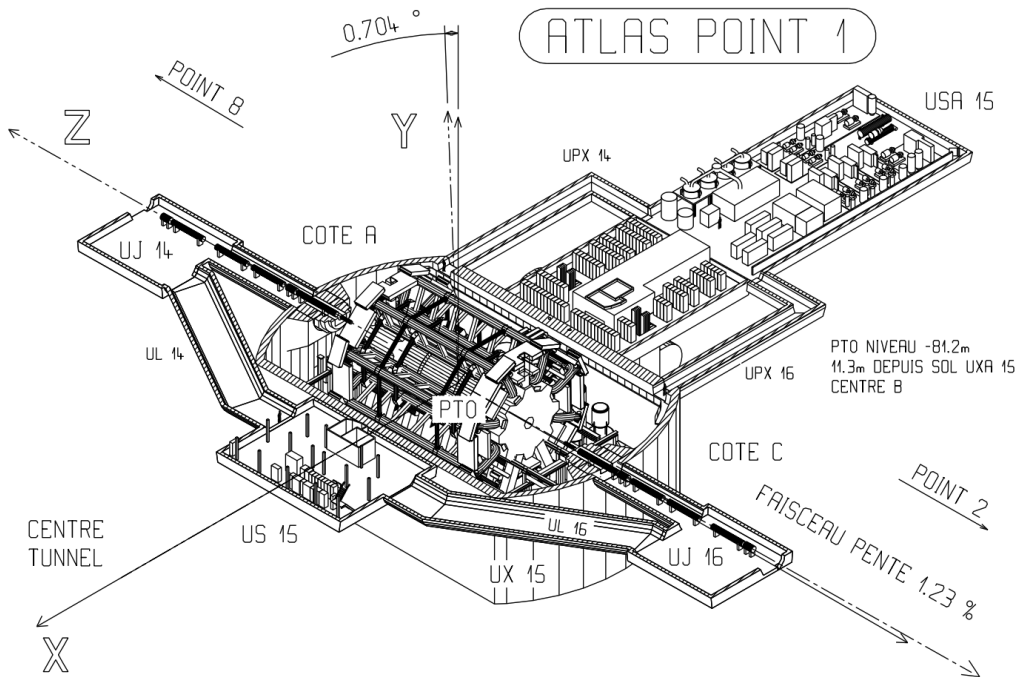


Figure 2.4: Coordinate system for the ATLAS detector [59]. The Y -axis is a bit different from the vertical due to the general tilt of the LHC tunnel.

The symmetry of the detector makes spherical coordinates useful. The conversion is standard: the azimuthal angle ϕ is specified in the XY plane, and the polar angle θ is defined as the angle with the Z -axis. Instead of the polar angle, the pseudorapidity η defined in Section 1.2.2 is exploited. Particle production is almost constant as a function of η , unlike θ . Therefore, matching between objects in the ATLAS central detector is usually performed in the pseudorapidity - azimuthal angle space (η, ϕ) . The distance between objects with coordinates (η^I, ϕ^I) and (η^{II}, ϕ^{II}) is defined as ΔR :

$$\Delta R = \sqrt{(\eta^I - \eta^{II})^2 + (\phi^I - \phi^{II})^2}. \quad (2.5)$$

2.3.2 Inner Detector

The Inner Detector (ID) consists of the innermost layers that surround the interaction point. This subdetector is 6.2 m long and 2.1 m in diameter, providing pseudorapidity coverage in the range of $|\eta| < 2.5$. The aim of ID is to accurately reconstruct charged-particle tracks and determine the vertex position. For this, the detector is comprised of three parts all immersed in a magnetic field of 2 T parallel to the beam: the Pixel Detector, the Semiconductor Tracker (SCT), and the Transition Radiation Tracker (TRT) shown in Figs. 2.5a and 2.5b, each employs different technologies and has a different resolution. The combined resolution of p_T for charged particles is approximately $\sigma_{p_T}/p_T = 0.5\% \times p_T \oplus 1\%$ [60]. To prevent a decrease in efficiency due to the energy loss of the tracks in the detector, the total detector material had to be as low as possible while maintaining sufficient rigidity.

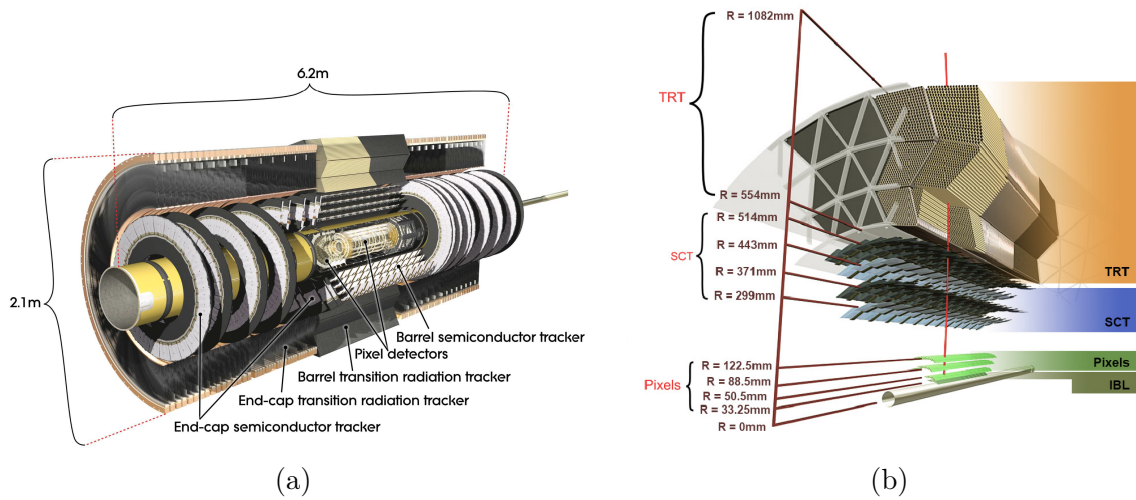


Figure 2.5: Cut-away view of the Inner Detector [58] and detailed layout of the Pixel Detector (including IBL), SCT and TRT layers [61].

Pixel Detector

The closest to the beam is the Pixel Detector. The particle density is highest here. Therefore, a high granularity is required. It consists of four layers of silicon sensors with radii between 33 and 123 mm and lengths between 664 and 800 mm. The first layer, the Insertable B-Layer (IBL), was installed in 2015 to maintain the ATLAS performance in a high luminosity environment [61]. The sensors have a pixel size of $50 \mu\text{m} \times 250 \mu\text{m}$ and $50 \mu\text{m} \times 400 \mu\text{m}$ for IBL and external layers, respectively. The ID is completed with three end caps sensors placed on both sides of the IP at a distance between 485 and 650 mm.

This subdetector contains approximately 92 million readout channels. When a charged particle traverses the silicon sensor, it loses a bit of energy due to the ionisation process, and electron-hole pairs are produced. Then, the total charge measured by the electrodes determines the hit position.

Semiconductor Tracker

The Semiconductor Tracker is the next part of the ID. The particle density is low enough here, and silicon strip sensors can be used instead of pixels, which helps reduce the readout channel number. Four barrels with a length of 1498 mm have radii between 299 and 514 mm, and 18 end caps disks (9 on each side) are located between 854 and 2720 mm from the IP. Each module is equipped with two layers of silicon strip with a strip pitch of 80 μm . The transition region between the barrel and the end caps is around $|\eta| = 1.4$. The SCT contains about 6.3 million readout channels that provide high-precision space points that are used for precise tracking measurements.

Transition Radiation Tracker

The final layer of the Inner Detector is the Transition Radiation Tracker. Unlike its neighbouring subdetectors, the TRT was not designed to provide a longitudinal coordinate of hits. TRT consists of drift tubes or straws 4 mm in diameter that have a 0.03 mm gold-plated tungsten wire in the centre. The potential difference is about 1500 V. They are filled with a gas mixture of Xe, CO₂ and O₂. The passage of a charged particle ionises the gas, and the time it takes for the charge to reach the wire is measured. The TRT is made up of two parts: the barrel where the straws are orientated parallel to the Z -axis and the end cap with the straws perpendicular to the Z -axis. There are about 50 thousand 1440 mm long straws in the former and 250 thousand 390 mm straws in the latter. In addition, the tubes are interleaved with radiator material in order to provide electron identification. The electron identification efficiency in TRT reaches 90% for energies above 1 GeV [62].

2.3.3 Calorimeters System

A calorimeter in particle physics is an apparatus that measures the energy of particles by absorbing them. ATLAS has three subsystems of calorimeters: electromagnetic (EMCAL), hadronic (HCAL), and forward (FCAL). They cover together a wide range of $|\eta| < 4.9$ which allows one to detect the missing transverse energy in the event. However, areas with significant dead material with many services (cryostat walls, cabling, etc.) limit the efficiency in transition regions: between central barrels and end caps for $|\eta| \sim 1.5$ and between EMCAL/HCAL and FCAL for $|\eta| \sim 3.1$ [63]. The granularity of the detectors provides information about the direction of the particles and helps in a particle identification procedure.

All subsystems are sampling calorimeters and use alternating layers of material where particle showers are initiated and material that measures deposited energy. It can stop most known particles, except muons and neutrinos. A cutoff view of the ATLAS Calorimeter System is presented in Fig. 2.6.

Electromagnetic Calorimeter

The Electromagnetic Calorimeter is designed to measure the energy and direction of photons, electrons, and positrons. It uses lead absorbers coated in stainless steel and liquid argon (LAr) samplings. A particle shower starts when one of the mentioned particles

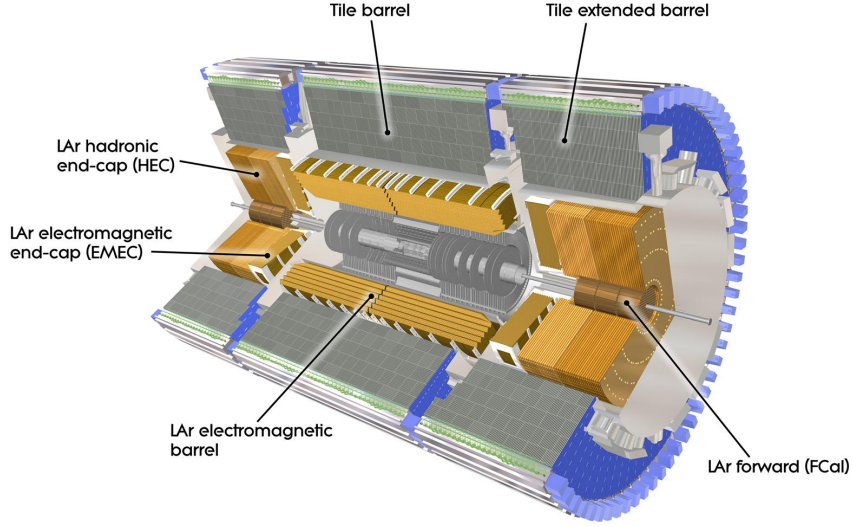


Figure 2.6: Cut-away view of the ATLAS Calorimeter System [58].

interacts with the lead nuclei. At LHC energies, Compton scattering and the photoelectric effect are insignificant; two basic processes can be recalled [1]: bremsstrahlung

$$e^{\pm} + N \rightarrow e^{\pm} + N + \gamma, \quad (2.6)$$

where an electron emits a photon after acceleration; and pair production:

$$\gamma + N \rightarrow e^{+} + e^{-} + N \quad (2.7)$$

where the atomic nucleus allows the system to conserve momentum. These two processes alternate, leading to a cascade of particles of decreasing energy. They ionise liquid argon sandwiched between the absorbers, producing an electric current. To ensure that all particles are measured, EMCAL has a honeycomb pattern with a characteristic accordion structure, as seen in Fig. 2.7.

The EMCAL is composed of one barrel ($|\eta| < 1.475$) and two end caps ($1.375 < |\eta| < 3.2$). The total thickness of both parts is 24 and 26 radiation lengths respectively¹. The granularity of the calorimeter cells $\Delta\eta \times \Delta\phi$ varies between 0.003×0.025 and 0.1×0.1 . The resolution of the energy is estimated $\Delta E/E \approx 11.5\%/\sqrt{E} \oplus 0.5\%$.

Hadronic Calorimeter

Hadronic showers have different, more complicated characteristics than EM showers. Furthermore, some hadrons decay into electrons or photons, e.g. $\pi^0 \rightarrow \gamma + \gamma$, so they also have electromagnetic components with a different response. This can be compensated for with software corrections. The main task required by HCAL is to reconstruct jets. For this, two techniques are applied. The Tile calorimeter, consisting of a central barrel

¹Radiation length X_0 is the mean distance over which high-energy electron loses all but $1/e$ of its energy, where e is the base of the natural logarithm.

and two extended barrels visible in Fig. 2.6, is made of iron as an absorber and scintillating plastic samplers. It covers the pseudorapidity range $|\eta| < 1.7$. It is complete with hadronic end caps (HEC), which span the range $1.5 < |\eta| < 3.2$. HEC is stored within the same cryostats as EMCAL end-caps and FCAL. Therefore, LAr can be used as the active medium and copper plates can be used as the absorber. The spatial resolution $\Delta\eta \times \Delta\phi$ for HEC varies between 0.1×0.1 and 0.2×0.2 . The energy resolution is approximately equal to $\Delta E/E \approx 50\%/\sqrt{E} \oplus 3\%$.



Figure 2.7: Characteristic accordion structure in EM calorimeter [64].

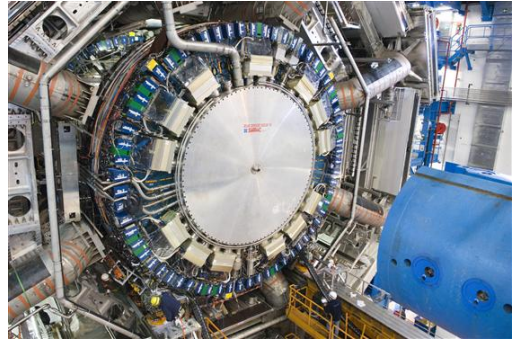


Figure 2.8: End-cap of Hadronic Calorimeter [65].

Forward Calorimeter

The last part of the ATLAS calorimeter system covers the forward pseudorapidity range $3.1 < |\eta| < 4.9$. It consists of one electromagnetic and two hadronic calorimeters. Both use LAr as an active material and copper and tungsten as absorbers for electromagnetic and hadronic parts, respectively. The energy resolution and granularity of η are limited, but the large coverage in η helps to analyse the particles in the area where tracking information is lacking.

2.3.4 Muon Spectrometer

Most of the high-energy muons pass through the Inner Detector and Calorimeters undetected. They are important for total energy calculation and are also the signature of many interesting physics events. To measure them, the ATLAS Muon Spectrometer was made up of 4000 muon chambers using four different technologies [66]. It covers the last layer, starting from a radius of 4.25 m close to the calorimeters to a radius of 11 m. The spectrometer is also exploited for muon identification, as a few other particles can pass calorimeters (neglecting neutrinos that leave ATLAS undetected). In general, the Inner Detector dominates the muon reconstruction in the range of p_T up to 30 GeV and the Muon Spectrometer in the region above 200 GeV [67].

2.3.5 Minimum Bias Trigger Scintillators

Minimum Bias Trigger Scintillators (MBTS) allow to trigger of most inelastic interactions with as little bias as possible [58, 42]. They are arranged in two disks at ± 3.56 m from

the IP and consist of eight inner and four outer azimuthally arranged sectors - Fig. 2.9. The former ring covers $2.82 < |\eta| < 3.84$ and the latter ring $2.09 < |\eta| < 2.82$.

Each sector is made of an independent polystyrene scintillating counter of 2 mm thickness. When the charged particle passes through the scintillator, the emitted light is detected by the WLS fibres² connected to the photomultipliers. The signal must pass a discriminating threshold to be registered as a particle hit.

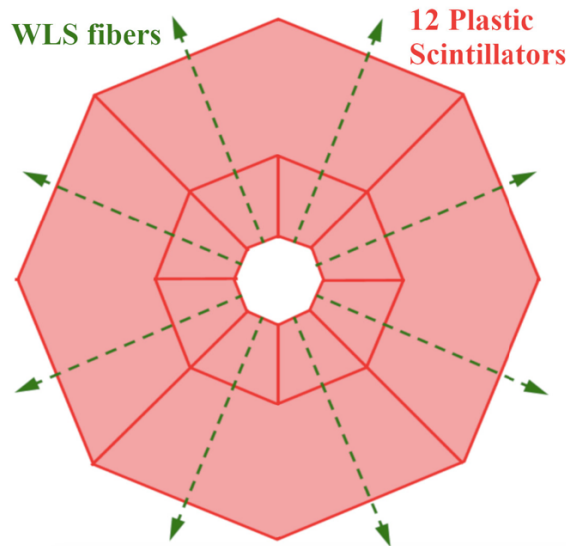


Figure 2.9: Scheme of MBTS sectors [28].

2.3.6 Forward Detectors

The ATLAS tracking system covers the pseudorapidity range $|\eta| < 2.5$ and the calorimetric system measures up to 4.9. To acquire acceptance with larger pseudorapidity, the detector is completed by the set of detectors in the forward region, located in the LHC tunnel on both sides of the interaction point:

- **LUCID** - detector used to monitor instantaneous luminosity as seen by the ATLAS detector, exploiting Cerenkov radiation, placed 17 m away from IP [69].
- **ZDC** - calorimeters placed 140 m from IP where the pipe is split into two tubes, detect neutrons and photons with $|\eta| > 8.3$, plays an important role in determining centrality in heavy-ion collisions [70].
- **AFP** - designed to detect beam protons scattered at small angles, located around 210 m from the IP, can operate during normal data collection [71].
- **ALFA** - scintillating detectors for measuring beam protons scattered at small angles, located at around 140 m from IP, operating only during dedicated LHC campaigns.

²Wave-Length Shifting (WLS) optical fibres are used to collect the light produced in the tiles, more details in [68].

2.3.7 Trigger and Data Acquisition systems

The amount of raw data recorded for a single event is on average at 1.5 MB [63]. The nominal bunch crossing rate at the LHC Run 2 was 40 MHz. This gives around 40 TB of data per second if all events are recorded, which is impossible to save. Furthermore, most of the events are not interesting to physicists. For that reason, ATLAS exploits two levels of triggers that can reduce the data rate to an acceptable level.

The first-level trigger (L1) collects limited information from Calorimeters and Muon Systems that can be calculated fast. It also incorporates other fast-responsive detectors, such as MBTS or ALFA. After that, L1 determines the location of the Regions-of-Interest (RoI). They are further forwarded if they meet the specified requirements. It also checks if some prescale should be applied (if prescale $n_{\text{psc}} > 1$, only one event from n_{psc} consecutive events that pass L1 requirements is stored). All decisions in L1 are hardware-based, in opposition to the next part - High-Level Trigger (HLT) - where decisions are determined with software after RoI full reconstructions. This mechanism reduces the event rate from 40 MHz to 100 kHz after L1 and 1 kHz after HLT. All events that pass triggers are fully reconstructed and stored for offline analysis.

2.4 Track and vertex reconstruction

The Inner Detector provides input for track reconstruction software that distinguishes the hits from different types of charged particles and therefore determines their trajectories after a proton-proton collision. The reconstruction process exploits measurements from the pixel, SCT, and TRT detectors. The intersection of the tracks determines the position of the vertices.

The particle generates, on average, signals in 4 pixels and 8 SCT hits close to the interaction point [62]. They represent precise 3D points from which the track candidates are built. Pattern recognition starts with finding track seedlings formed by combinations of three points. That seed can be extended using a fast Kalman filter. If a minimum of seven silicon hits are associated, then a candidate track is found [62]. Many candidates are incomplete or share hits. The ambiguity-solving process removes fake tracks by assigning a score to each candidate. In general, more hits correspond to a higher score. On the other hand, a missing signal in the detector elements decreases the score. Shared hits are removed from the track with a lower score. All tracks with less than 7 hits after the ambiguity-solving process is neglected. Additional 30 TRT hits at a larger distance provide an accurate measurement of track curvature.

A track in ATLAS is parameterised in terms of five parameters perigee at the point closest to the Z -axis [62]:

$$\eta(q/p, d_0, z_0, \phi_0, \theta_0), \quad (2.8)$$

where q/p expresses the particle charge divided by momentum, d_0, z_0 denote the transverse and longitudinal impact parameters and ϕ_0, θ_0 are the polar and azimuthal angle of the track at the perigee point. These track parameters can be propagated to different positions within the ATLAS detector by using the magnetic field map. Additional information about tracks, such as energy loss or a Muon Spectrometer output, can be utilised for particle identification.

Proton-proton collisions happen in a small region around the centre of the ATLAS detector known as the beam spot. For regular runs, it can be described by Gaussian distributions as a spheroid with nominal length $\sigma_z \approx 50$ mm and radius $\sigma_R \approx 20$ μm [58], but the size depends on the beam conditions. Most of the particle tracks from a single proton-proton collision in ATLAS originate from the interaction point (IP) and indicate the primary vertex of that collision. Leaving aside the multiple proton-proton interactions per bunch crossing, some particles can decay at a long distance from the primary vertex. The vertices-finding procedure identifies such decay as a secondary vertex. A typical primary vertex is an intersection of 20 or more tracks, while secondary vertices can often be fitted with 2 or 3 trajectories [62].

2.5 Topological clusters

The jets in ATLAS are reconstructed using the FASTJET software package [72, 73]. It can accept a number of different inputs: *track jets* formed by Inner Detector tracks or *calorimeter jets* exploiting topological clusters of calorimeter cells (TopoClusters). The former is limited to $|\eta| < 2.5$ and can utilise charged particles only. Therefore, calorimeter jets are used in most analyses³. For MC, *true jets* are based on stable particles that originate from the hard-scatter vertex and do not include particles from pile-up. Muons and neutrinos are also excluded because they do not leave significant deposits in calorimeters [75].

The topological clusters are built from adjacent calorimeter cells with significant deposited energy E . The seed cell is selected as the one with significance $S = E/\sigma > 4$, where σ is the noise per cell measured from randomly triggered events. Then a set of neighbouring cells with significance $S > 2$ is added to the seed and form cluster. Finally, cells that surround directly neighbouring cells are added to a cluster if their significance is $S > 0$. Fig. 2.10 shows the construction of a cluster within a single sampling layer, but the algorithm also merges cells from neighbouring layers. The threshold values: 4, 2 and 0, are selected to suppress the electronics and pile-up noise. Clusters can also be built from cells with negative energy, which ensures that the tails of noise distributions cancel on average.

The energy of TopoCluster is calculated as the sum of the energy of the associated cells. The energy can be calibrated at the electromagnetic scale (EM jets), which is a basic signal scale for accounting for the energy deposited by the electromagnetic showers. Clusters can be further calibrated using the local cell weighting (LCW) method [76]. This method is designed to give the correct scale for charged pions produced in collisions and to reduce the fluctuations. The mass of TopoClusters is set to zero and the direction (η and ϕ) is determined from the centre of the ATLAS detector to the barycenter of cells weighed in energy.

This thesis exploits jets built from TopoClusters at LCW scale, reconstructed with an anti- k_t algorithm with R parameter equal to 0.4. As a result of the energy loss in dead material and other detector inefficiencies, the raw jet energy is usually less than that of

³The combination of Inner Detector and calorimeters is exploited with newer analyses, with abstract objects known as the Particle Flow [74]

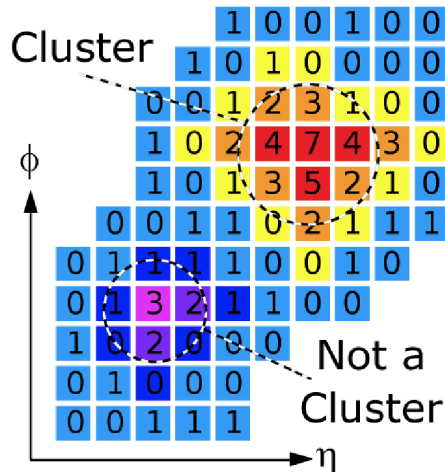


Figure 2.10: TopoCluster built from a group of seed (red), neighbouring (orange) and surrounding (yellow) cells in a single layer of a calorimeter [63]. The numbers correspond to the significance of the cells.

actual jets. The jet calibration process tries to apply correction factors as a function of the raw p_T and η . Correction factors are derived from the data and the comparison of the MC and also include additional adjustments *in situ*. More information about it is given in Section 5.4.

2.6 Data samples

Data were collected during a campaign in October 2015 when proton beams collided at centre-of-mass energy $\sqrt{s} = 13$ TeV. The eight special LHC runs used in this analysis were characterised by a large $\beta^* = 90$ m that allowed collecting a sample with an integrated luminosity of 725.0 nb^{-1} [77]. The crossing angle was equal to $\theta_c = 2 \times 50 \text{ } \mu\text{rad}$. The pile-up was very small with the average number of proton-proton interactions per bunch crossing $\mu \approx 0.1$ and the distance between subsequent bunches was $\Delta t = 100$ ns.

The main trigger exploited by this analysis is L1_J12_ALFA_ANY. It requires at least one hit in the ALFA trigger tile in coincidence with at least one calorimeter Region of Interest (RoI) with MET⁴ that passes the 12 GeV threshold. It reaches an efficiency greater than 10% for a single jet with $p_T = 30$ GeV and is enhanced by the second jet requirement. The ALFA triggers have been shown to have an efficiency of about 99.9% [78, 28]. This trigger provides 3.6M of diffractive dijet event candidates, but the majority come from an accidental background.

The SD analysis is supported by an additional "SD trigger" based on two streams: L1_MBTS_1_A_ALFA_C or L1_MBTS_1_C_ALFA_A, which required at least one MBTS counter in coincidence with a signal from the ALFA trigger on the opposite side.

⁴MET measures the energy imbalance in the plane transverse to the colliding proton beams - $\text{MET} = \sqrt{(\sum_{i=0}^n E_x^i)^2 + (\sum_{i=0}^n E_y^i)^2}$, where $E_{x(y)}^i$ are the energies of the i^{th} input object projected along the $x(y)$ -axis, respectively.

The MBTS provides 100% efficiency for SD jets, but was prescaled by 190 or 300 (depending on the run number). This sample can be used for the jet trigger efficiency estimation. Two highly prescaled triggers are exploited by accidental background studies. The first one is L1_MBTS_1, which requires at least one active MBTS counter and provides information about the central state that is not biased by the ALFA detector. The second one is L1_ALFA_ANY, which supplies information about events not biased by the central state conditions.

2.7 MC samples

The measured cross sections can be compared with model predictions and demonstrate a proper understanding of the observed results. Some MC samples can be used for acceptance study and detector effects. The simulation chain in the ATLAS experiment consists of the following steps, using the ATLAS software framework ATHENA [79, 80]:

- event generation using multipurpose MC generators;
- detector simulation using the GEANT4 package [81, 82];
- digitisation of the energy deposits of particles in the sensitive detectors' regions;
- reconstruction of observables, which are the same for data and MC simulated events.

The simulation of the ATLAS central detector follows all the steps mentioned above. However, the full simulation of the beam aperture is quite slow. Instead, the Forward-Tracker package from ATHENA is used for the protons propagation between the interaction point and the forward detectors [83]. If the proton was successfully transported, then the ALFA detector response is fully simulated with GEANT4.

Two simulations were used to prepare MC samples for the SD analysis. Pythia 8 provides four models that describe inelastic interactions separately (SD, CD, DD and ND). EPOS was used to generate one inclusive sample which contains all inelastic processes. Separation into different types of processes is performed after generation and is based on the characteristics of the event. It should be noted that EPOS does not provide the production of SD dijets because of the lack of a hard diffraction mechanism. However, many events are recognised as SD' (see Section 1.3).

All samples were enhanced with an SD dijet filter: one proton in the forward region ($\xi^P < 0.2$) and a minimum of two jets with the leading jet $p_T > 12$ GeV. An additional sample was produced for CD analysis using the Herwig generator. The filter was extended with the additional requirement of a second proton. The details about the generated samples are gathered in Table 2.1.

Generator	Process	Total cross-section predicted by model [mb]	Filter efficiency	Number of generated events
Pythia	SD	12.83	8.583e-04	297499
	CD	8.80	7.370e-06	10000
	DD	1.28	4.436e-05	10000
	ND	56.79	2.656e-05	149800
EPOS	inclusive	78.98	7.360e-05	597200
Herwig	CD	0.92	7.491e-05	10000

Table 2.1: Details of the generated MC samples. Filter efficiency corresponds to the fraction of accepted events.

Chapter 3

The ALFA detectors

Absolute luminosity at hadron colliders can be determined by using elastically scattered protons at very small angles using the optical theorem. This was the main purpose of designing the ALFA (**A**bsolute **L**uminosity **F**or **A**TLAS). The optical theorem connects the elastic scattering amplitude in the forward region with the total cross section: $\sigma_{tot}(pp \rightarrow X)$ [78]. In addition, other interesting physics topics, such as diffractive processes, may also be explored with protons measured in the forward region.

3.1 ALFA Roman Pots

The ALFA detector comprises eight subdetectors. They are installed in the outgoing beam pipe at stations around ± 237 m and ± 245 m from the ATLAS Interaction Point on both sides of the central ATLAS detector. Each station consists of two Roman Pots (RPs) - one above and one below the beam pipe. Both of them can be moved very close to the beam.

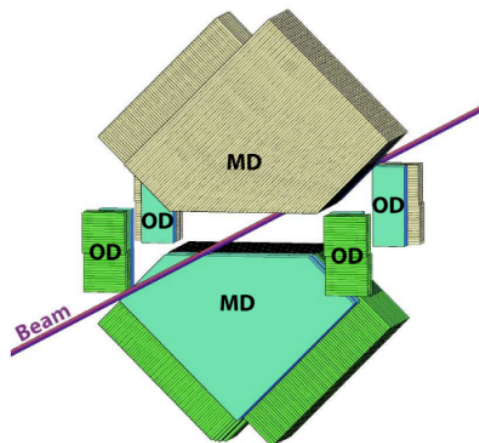


Figure 3.1: A schematic view of the ALFA station composed of upper and lower RPs [78]. Each RP contains one Main Detector (MD) and two Overlap Detectors (OD). The turquoise plates visible on the scheme in front of the lower MD and upper ODs are the trigger counters (for the upper MD and the lower ODs they are on the opposite side).

Each RP houses one Main Detector (MD) to track protons and two Overlap Detectors (OD) to measure the distance used in the alignment procedure - Fig. 3.1. Detectors are completed by trigger counters. They consist of 3 mm thick scintillator plates that cover the active areas of MDs and ODs. Each MD is equipped with two trigger counters, and their signals are used in coincidence to reduce noise contributions. ODs are covered by single trigger counters and each signal is recorded.

The nominal beam divergence is greater than the extremely small scattering angles (a few μrad) measured with the ALFA detector. Therefore, these measurements can be accomplished only with specially prepared beam conditions: high-beta (β^*) optics with reduced beam emittance (the so-called ALFA special runs) - Section 2.1. Moreover, the detectors have to be placed far from the interaction point and as close to the beam as possible. The problem is solved by the Roman Pot (RP) concept.

The RP idea is based on a detector volume (the pot) that is separated from the vacuum of the accelerator by a thin window. It is connected through the bellows to the beam pipe and thus can be moved close to the beam [58]. The RPs are made of stainless steel, with 0.2 and 0.5 mm thick windows on the bottom and front sides, which reduce the interactions of traversing protons. The concept of RP can be seen in Fig. 3.2, where the retracted and working positions are shown [84]. The working position brings the bottom surface of a pot to a minimal distance of a few σ from the circulating beam. The movement could be vertical only, due to the mechanical constraints imposed by the two horizontal beam pipes of the LHC. This can only occur during the high β^* operation during dedicated LHC runs, which corresponds to a very low instantaneous luminosity, and for this reason, no radiation hard technology is required for this specific set of detectors.

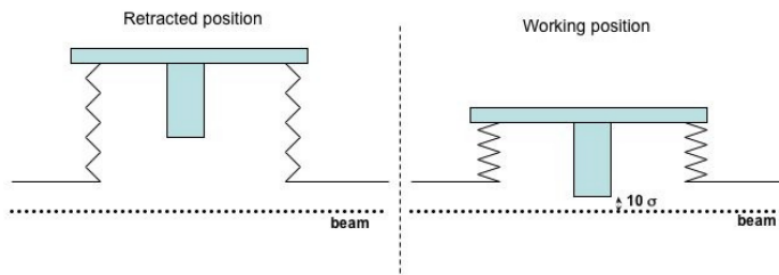


Figure 3.2: RP concept: on the left, the retracted position is shown where the Pot is placed out from the beam; on the right, the Pot in working position is approaching 10σ from the circulating beam [84].

Thanks to the RP technique, the ALFA detectors can be easily inserted into the beam pipe for special runs and retracted in other cases for safety. But each of those movements can introduce small misalignments. In addition to detector movements, the beam position can also vary between different LHC fills, due to minor changes in the conditions in the pipe. Therefore, the alignment procedure must be repeated for each fill to avoid bias due to possible beam movements. The alignment for diffractive runs collected in October 2015 used in this analysis is described in Chapter 4.

3.2 Naming convention

The arrangement of the ALFA system is presented in Fig. 3.3. The two stations on side A are called B7L1 and A7L1 (positive z) and the two on side C are named A7R1 and B7R1 (negative z), respectively. A7L1 and A7R1 are closer to IP - they are called inner or nearest - opposite to the outer or further stations B7L1 and B7R1. Each RP in a station has an additional letter in the name: U for upper RPs (positive y) and L for lower RPs (negative y). RPs are also denoted by the numbers 0 - 7 according to Fig. 3.3.

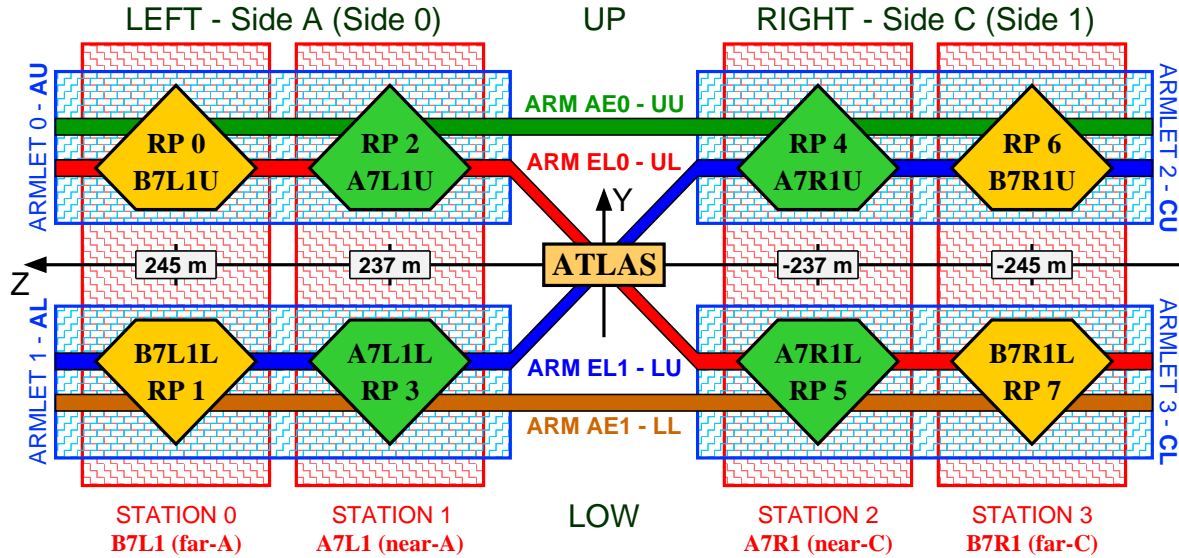


Figure 3.3: Naming convention for ALFA RPs and configurations used in this dissertation.

For diffractive analysis, the most important are pairs of RPs that measure the trajectory of a single proton. Armlets are marked with blue rectangles in Fig. 3.3. The acronyms for each armlet comprise side and level: AU for RPs 2-0, AL for 3-1, CU for 4-6, and CL for 5-7.

Two armlets on the opposite side form an arm marked with a solid line in Fig. 3.3. The RPs can be grouped into two arms for elastic-scattering event topologies (back-to-back). The first elastic arm has a configuration 0-2-5-7 and the second 1-3-4-6. The anti-elastic arms refer to the four RPs on the same level. The acronyms for elastic arms are UL and LU, and for anti elastic UU and LL. All configurations are also presented on Figs. 3.4 and 3.5.

3.3 Tracks reconstruction

The MD aims to track the protons scattered at a small angle. It is a high-precision scintillating fibre detector, using SCSF-78 S-type fibres, produced by Kuraray. They are manufactured into square fibres with 500 μm side length, with 10 μm thick cladding, and coated with aluminium to reduce crosstalk between the fibres. The plastic scintillator used for manufacture has an emission spectrum ranging from $\lambda = 415 \text{ nm}$ to 550 nm,

Single Proton Configurations

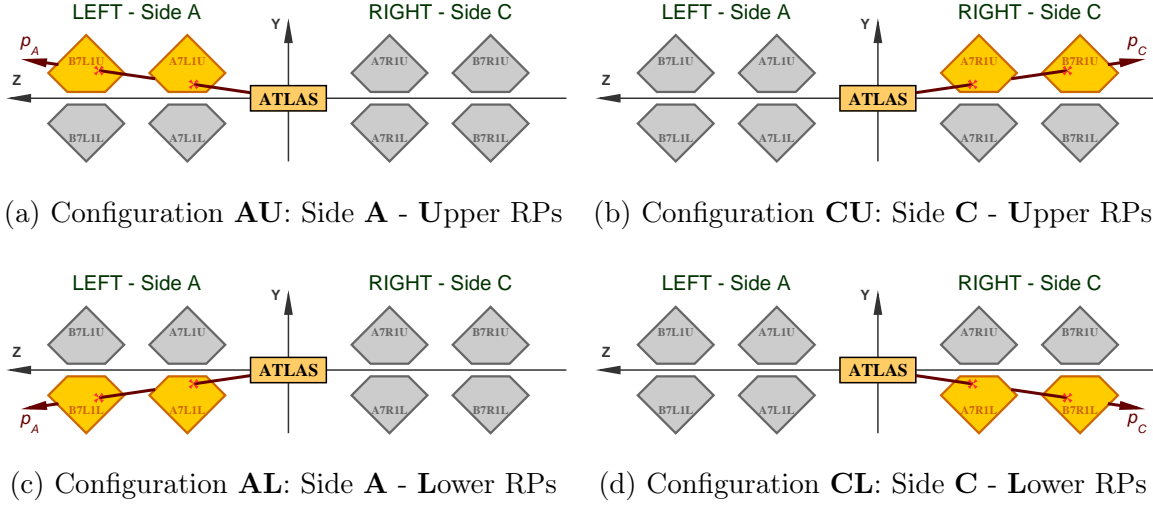


Figure 3.4: Four configurations of ALFA RPs that can measure single proton from SD process. The acronyms are composed of ATLAS side with the proton: **A** or **C**, and the level of the RPs with the signal: **U** - upper or **L** - lower.

Double Proton Configurations

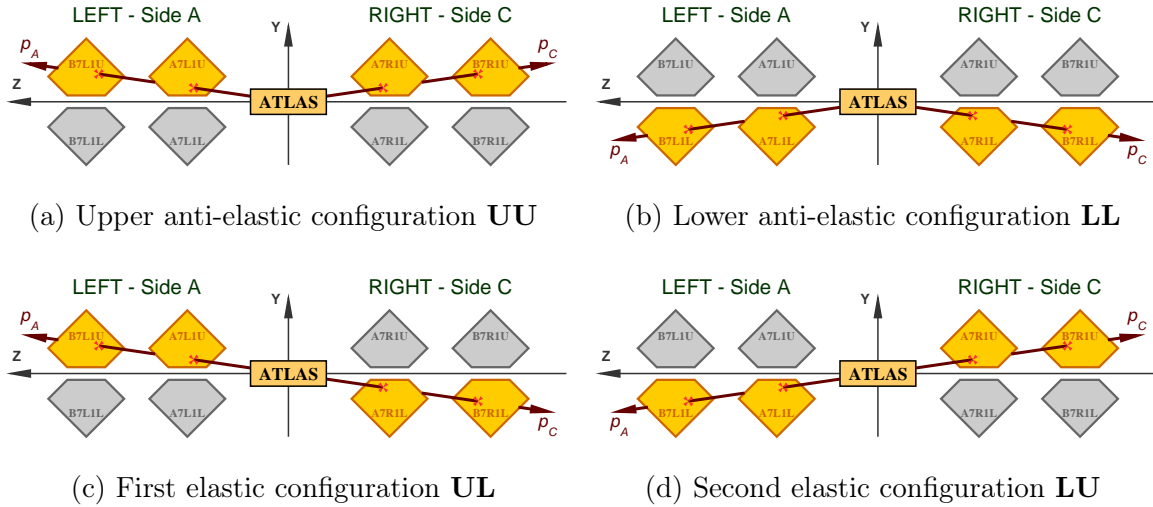


Figure 3.5: Four configurations of ALFA RPs that can measure two protons from the CD process. The acronyms are composed of the levels of the RPs with the signal on the side A and C: **U** - upper or **L** - lower.

with the peak emission occurring at $\lambda_{\max} \approx 440$ nm [84], which has a fast decay time of organic scintillators: 2.8 ns.

Each MD comprises 10 planes, each plane has two layers: u and v , with fibres arranged perpendicular to each other and tilted 45° relative to vertical - Fig. 3.6. Each layer has 64 fibres, but the effective area of the detector is somewhat smaller than the 32×32 mm² because 40 fibres are cut in 45° . Due to this arrangement, the inactive cladding material

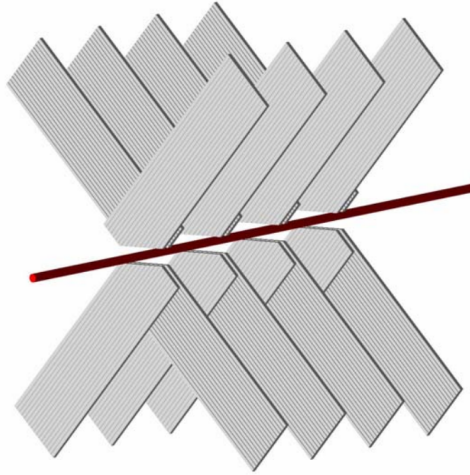


Figure 3.6: Schematic view of the orientation of the fibers [84]. Only eight of twenty planes are drawn.

does not form a dead zone at the detector edge. This is done to get the fibre as close as possible to the Roman Pot windows and consequently to the beam. The fibres are aligned and glued to a precision machined support structure made of titanium [58]. The positions of the fibres were measured in various stages of manufacture and used during track reconstruction.

The traversing proton generates light in the fibres. It is routed to multianode photomultipliers (MAPMT), which convert it into an electric signal. The MAPMTs have 64 channels, which are arranged in an eight-by-eight matrix, and are located outside the secondary vacuum in a five-by-five matrix, where 20 slots are filled with MD MAPMTs Fig. 3.7a. Due to the 45° arrangement, routing the fibres towards the MAPMTs does not require small bending radii. The middle slot is for structural support, three slots are filled with OD MAPMTs, and one slot is for the trigger MAPMT [84].

Protons scattered at a small angle go almost parallel to the beam, whereas the scintillating fibre layers are arranged perpendicular to the beam. The basic assumption for the reconstruction of the track is that the protons pass perpendicularly to the layers. An angle below one mrad in the normal direction has a minimal impact. Therefore, a natural way to reconstruct the track coordinates is by using the fact that the hit fibres overlap.

The first step of reconstruction is to determine the u and v coordinates of the two sets of ten layers that have the same orientation. They are related to the detector coordinate system (x, y) by the equation:

$$\begin{bmatrix} x \\ y \end{bmatrix} = \begin{bmatrix} \cos(45^\circ) & -\sin(45^\circ) \\ \sin(45^\circ) & \cos(45^\circ) \end{bmatrix} \begin{bmatrix} u \\ v \end{bmatrix}. \quad (3.1)$$

The metrology files provide the intercept and slope of each fibre in the (x, y) system. These parameters are used to project the fibres in a perpendicular plane, as shown in Fig. 3.8. The hit fibres are filled with blue. One can already distinguish the proton path from the pattern. The superposition of the hit fibres is shown on the right. The centre of the overlap region gives the u or v coordinates, while the width determines the resolution. The coordinates x and y are obtained using Eq. (3.1).

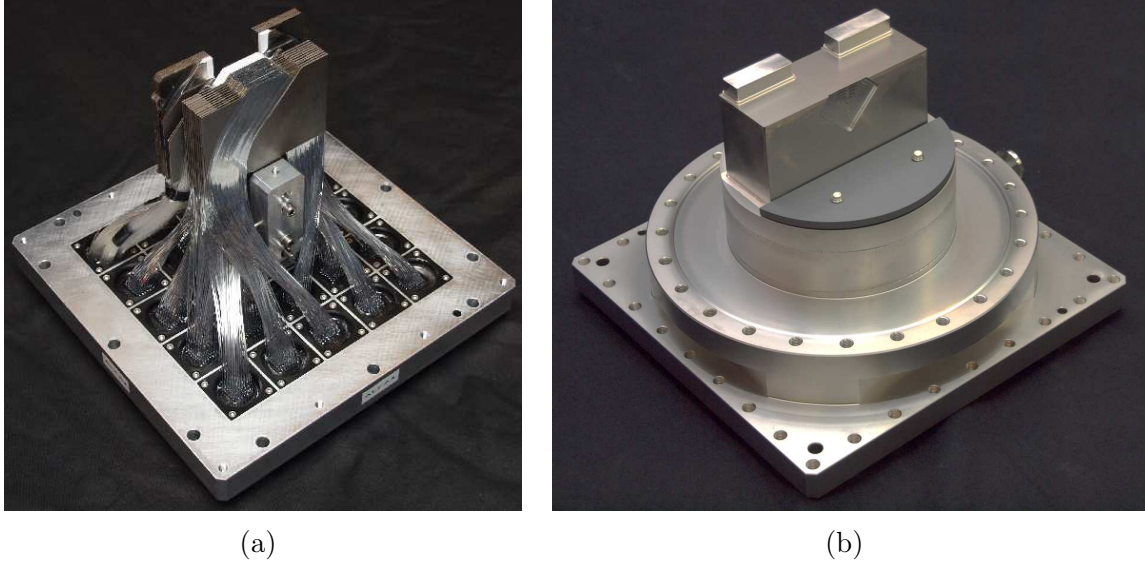


Figure 3.7: Photographs of ALFA RP. On the left one are visible scintillating fibres that are routed to plastic connectors in the grid of the base plate which on the other side is facing the MAPMTs. The right one shows an RP with a cover. On the side, the front window machined to the sensitive MD area is visible. Both pictures are taken from [85].

The accepted u and v coordinates for the spatial positions must be formed from at least three overlapping hit fibres. To exclude events with hadronic showers and layers with a high noise level, fibre layers with more than ten hits are not used in track reconstruction. Finally, at least three of the remaining layers must have between one and three hits [78].

The resolution of a single hit can be calculated using the standard deviation of the uniform distribution: $\sigma = d/\sqrt{12}$. For fibre width $d = 500 \mu\text{m}$, the resolution should be approximately $144 \mu\text{m}$, which is insufficient for the analysis. Therefore, the ALFA detector utilises 10 planes with the same orientation. Each plane is shifted by $1/10$ of the fibre width. This staggering reduces the effective pixel size ten times, leading to a resolution of $14.4 \mu\text{m}$, but only assuming perfect staggering and 100% fibre efficiency. The real resolution measured during the test beam campaign was found to be about $30 \mu\text{m}$ for both x and y for all detectors [86].

3.4 Efficiency of track reconstruction

The efficiency of ALFA track reconstruction for the diffractive campaign of October 2015 was studied in [87]. The analysis was performed using the same track requirements as in Section 7.3, therefore, it includes the ALFA selection efficiency. It involves elastic events $p + p \rightarrow p + p$ observed in the data and Pythia simulation. Protons should be detected in four RPs in a given elastic arm, and efficiency can be estimated by counting the events with missing signals at one or two ALFA stations. The background simulation is optimised with the overlay technique: the simulated signal is mixed with the detector response obtained from zero-bias data before digitisation. Such a procedure allows for pile-up simulation and provides a better understanding of actual experimental conditions.

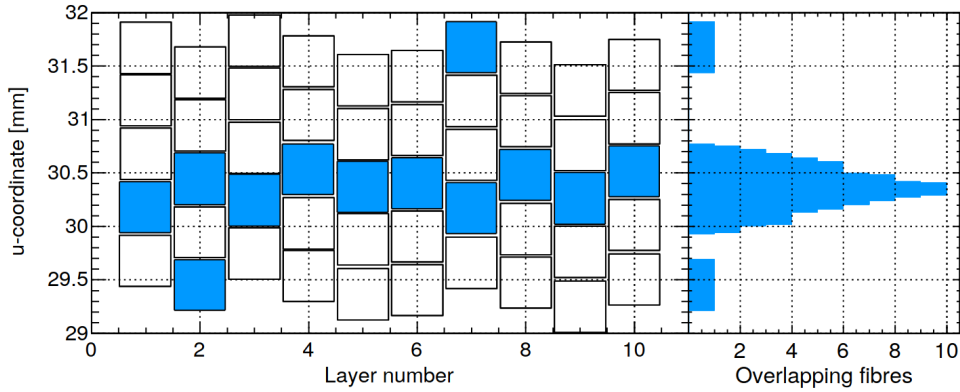


Figure 3.8: Hit pattern of a proton trajectory in the ten u -oriented layers [78]. The superposition of hit fibres is shown on the right. The position of maximum overlap is used to determine the track position.

Only 6 of 10 scintillating layers are required to reconstruct the track coordinate. The efficiency of a single layer is estimated at 90%, including the glue between the fibres [88], therefore, the overall efficiency should be around 99.6%. However, it is significantly reduced by the particle showers induced in the inner or outer station, resulting in the inability to reconstruct tracks in either one or two stations. The effect is larger near the detector edges. It can be seen in the top plot in Fig. 3.9, where the efficiency of the armlet AU is presented as a function of the y -coordinate.

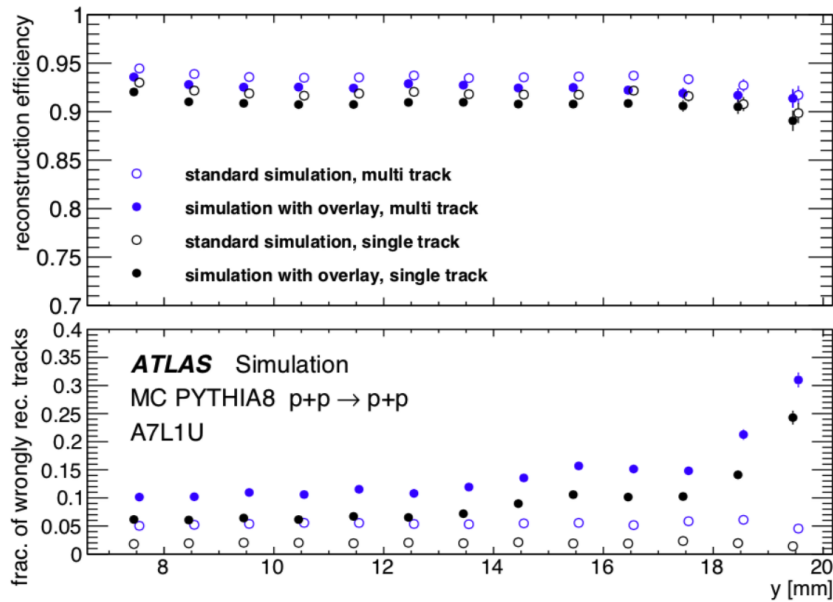


Figure 3.9: ALFA track reconstruction and selection efficiency (top) and the fraction of wrongly reconstructed tracks (bottom) in a function of y -coordinate for armlet AU. Plot taken from [87].

Configuration	Efficiency	Uncertainty
AU	0.91	± 0.02
AL	0.90	
CU	0.89	
CL	0.91	
UL	0.85	± 0.03
LU	0.82	
UU	0.83	
LL	0.84	

Table 3.1: ALFA track reconstruction and selection efficiency for each configuration [87].

The ALFA track reconstruction and selection efficiency was evaluated for each armlet and arm, elastic and anti-elastic. The numbers are presented in Table 3.1. The uncertainty is set to 2% for armlets (SD analysis) and 3% for arms (CD analysis), based on the variation in efficiency and overlay conditions.

The fraction of tracks that were incorrectly reconstructed in Fig. 3.9 is significant. But the impact of the fake protons is covered by the accidental background study in 6.2, therefore, they can be omitted in the corrections.

3.5 Proton transport and kinematic reconstruction

Two MDs in one branch can detect the same proton and provide information about the position and local angle of its track. This information is used to reconstruct the momentum of the scattered proton at the ATLAS IP. For this, the precise position of the detectors with respect to the beam must be known. The alignment procedure is summarised in Chapter 4.

The proton coordinates measured by the ALFA detectors, where u stands for x or y , depend on

- the position u^{IP} of the proton in IP;
- the ratio between the corresponding component of the transverse momentum of the proton in IP and the total momentum p_u^{IP}/p ;
- the functions of the loss of the momentum of the proton $\Delta p/p$:

$$u \left(u_{\text{IP}}, \frac{p_u^{\text{IP}}}{p}, \frac{\Delta p}{p} \right) = u_{\text{IP}} \cdot F_u \left(\frac{\Delta p}{p} \right) + \frac{p_u^{\text{IP}}}{p} \cdot G_u \left(\frac{\Delta p}{p} \right) + H_u \left(\frac{\Delta p}{p} \right) \quad (3.2)$$

A detailed description can be found in [83]. The F_u, G_u, H_u functions are quartic polynomials with constant parameters fitted to the MC simulation output. They depend on the collision energy, optics, and crossing angle. It can be seen that the coordinates x and y are decoupled. This is because the section between the ALFA and ATLAS Central Detector contains dipole and quadrupole magnets only.

This relation shown in Fig. 3.8 is exploited by the ALFAReco package [83, 89]. It is used to obtain initial proton momentum based on the positions of reconstructed tracks in the ALFA detector.

3.6 Vertical range estimation

Two vertical cuts help to reduce the impact of edge effects. The proton tracks are required to be at least 200 μm from the edge of the detector that is closer to the beam, to ensure full detection efficiency. The false tracks below the detector edge - Fig. 3.10a - are due to mismatched overlapping hits in the layers orientated u and v . Furthermore, the y coordinate is restricted to be at least 1 mm away from the edge of the beamline apertures, in order to minimise the impact from showers generated in the beam screen, a protection element of the quadrupoles.

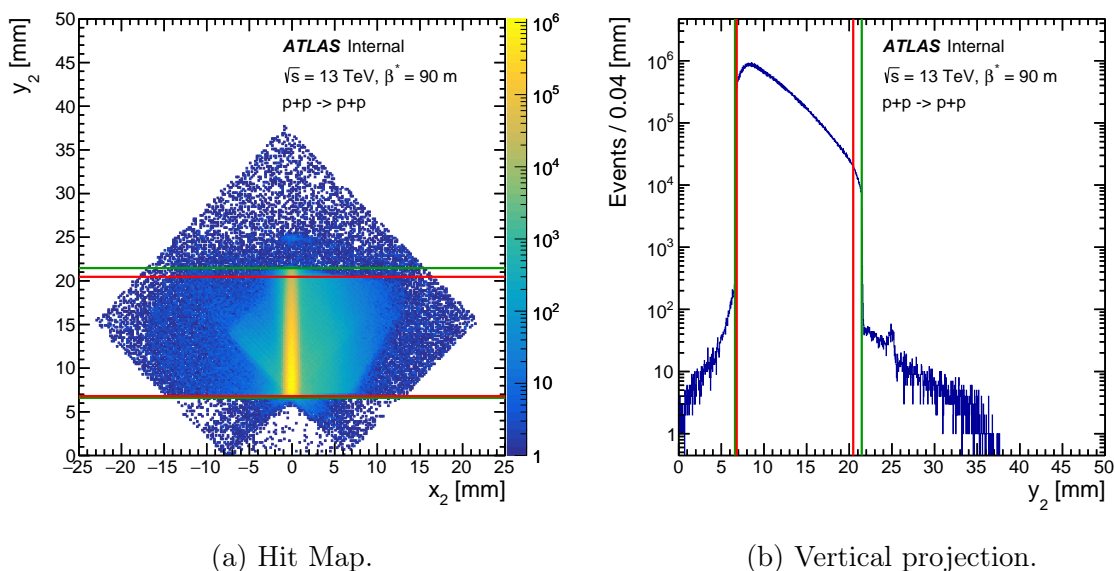


Figure 3.10: Distribution of tracks reconstructed in RP A7L1U for LHC fill 4509. The green lines indicate the inflexion points of vertical projection, and the red lines indicate the acceptance range.

The position of the detector edge near the beam and the shadow of the beam screen can be easily recognised in the y distribution in Fig. 3.10b, which is obtained for RP A7L1U from the sample without cuts. They are determined as the inflexion points of the distribution and indicated by the green lines. The red lines indicate the acceptance range. The fiducial cuts for LHC fill 4509 are presented in Table 3.2. The results for other fills are presented in Table A.1 in the appendix.

RP	B7L1U	B7L1L	A7L1U	A7L1L	A7R1U	A7R1L	B7R1U	B7R1L
Edge [mm]	6.095	-6.445	6.805	-7.145	6.695	-7.115	6.045	-6.445
Beam-screen [mm]	18.385	-18.405	20.465	-20.505	20.205	-20.415	18.165	-18.375

Table 3.2: The fiducial cuts for LHC fill 4509 in beam coordinate system.

3.7 Geometrical acceptance

To define the fiducial range of the measurements, the geometric acceptance of the ALFA detector was calculated on the basis of the Pythia SD sample. It is mostly limited by the geometrical coverage and vertical position of the RPs. Detectors cannot approach too close to the beamline, which leads to the minimum value for the vertical component of the momentum p_Y of scattered protons that can be reconstructed. The maximum value of p_Y is limited by the beam screens in front of the ALFA stations. The acceptance for p_X is almost unlimited but has some dependence on the proton energy E .

Therefore, acceptance is calculated in terms of ξ and t . It is defined as the probability that the proton reaches the ALFA detector and the reconstructed position passes the x and y requirements - they are restricted to be away from the edges of the RPs and LHC apertures - Section 4.4. Evaluations are performed for each ALFA configuration separately and are shown in Figs. 3.11 and 3.12. Due to the crossing angle between the LHC beams, the acceptance is higher in the upper branches, especially for large ξ . There is no visible difference between sides A and C.

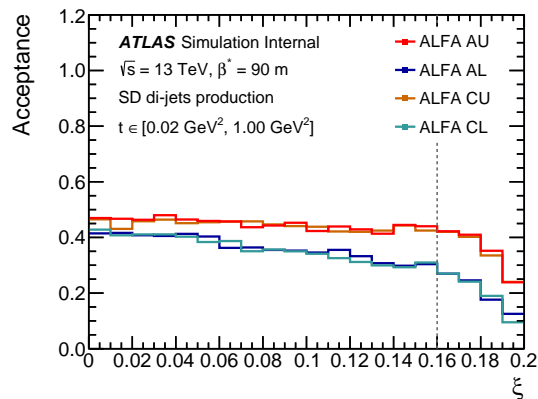
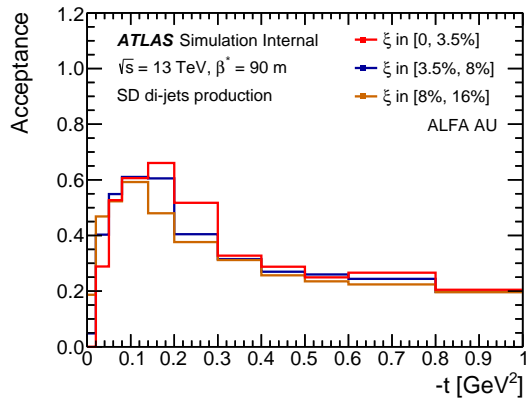
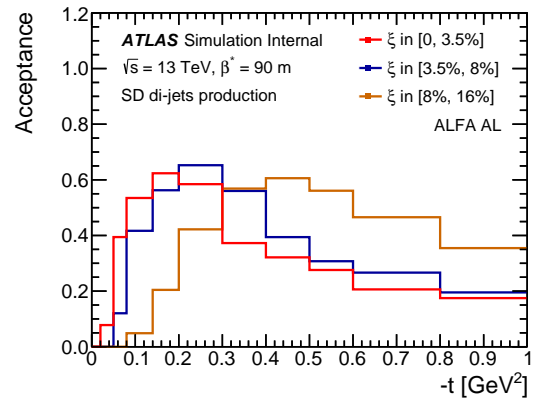


Figure 3.11: The ALFA acceptance as a function of ξ for all ALFA branches, based on the Pythia SD sample.

The acceptance starts to drop at $\xi \approx 0.16$ due to interactions between the forward scattered particles and the beamline apertures. It was not included in the provided MC samples; therefore, the fiducial region ends with ξ less than 0.16. The minimum value of proton p_Y forces the cut on $|t|$ to be greater than 0.02 GeV^2 .



(a) ALFA AU



(b) ALFA AL

Figure 3.12: The ALFA acceptance as a function of t for upper and lower ALFA branches on the ATLAS side A, based on the Pythia SD sample.

Chapter 4

Fast ALFA Alignment

ALFA Alignment procedure is necessary for the proton momentum reconstruction. Dedicated analysis was performed for data collected during the October 2015 campaign [90]. The results were used in this thesis and other diffractive analyses [28, 41, 42, 91].

4.1 Motivation

In elastic and diffractive analysis, with protons measured by the ALFA detector, the reconstructed position and local angle of the tracks can be used to calculate the proton momentum. For this, the precise position of the detectors with respect to the beam must be known.

Thanks to the RP concept (Fig. 3.2), the ALFA detectors can be inserted smoothly into the beam pipe for special runs and retracted in other cases for safety. But each of those movements can introduce small misalignments. In addition to detector movements, the beam position can also vary between different LHC fills, due to minor changes in the conditions in the pipe. Therefore, the alignment procedure must be repeated for each fill to avoid bias due to possible beam movements.

4.2 Alignment strategy

Each detector has three degrees of freedom in the XY plane:

- ΔX - horizontal position;
- ΔY - vertical position;
- θ_Z - rotation about the Z -axis.

Other possible degrees of freedom - ΔZ , θ_X , θ_Y - are negligible, as they do not significantly affect the measurements of the x and y coordinates.

The alignment procedure is based on the symmetry of the elastic event pattern, an ellipse elongated in the vertical direction Fig. 4.1. The horizontal position and rotation along the Z -axis can be determined from the pattern for each detector separately, but the

vertical axis of this ellipse does not overlap with the detectors. Consequently, the vertical position must be calculated from two values for both detectors at the one ALFA station:

- d - the distance between the upper and lower detectors;
- Y_{off} - vertical offset of the entire station, which is obtained from the comparison of the y distribution measured in the upper and lower detectors.

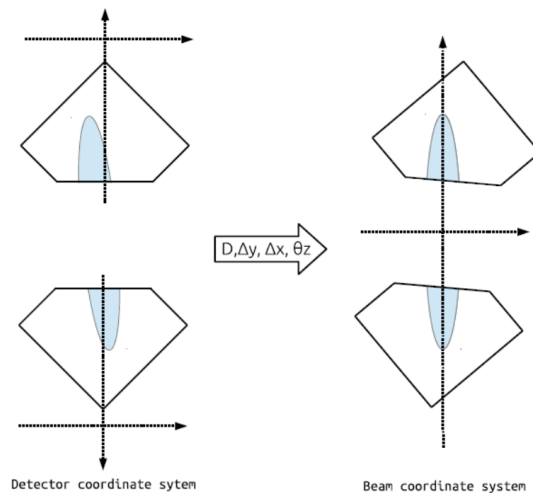


Figure 4.1: Principle of the ALFA alignment [78], based on four parameters: distance between the detectors, vertical offset of the entire station, horizontal offset and rotation angle of the detector. In the beam coordinate system, the elastic pattern of tracks is symmetrical. This property is used to align detectors.

Distance measurement is the first stage of ALFA alignment using OD-reconstructed beam halo particles or shower fragments. The principle is explained in Section 4.3.2. In the second stage, the offsets in x and y and the rotation are calculated on the basis of the distributions of elastic events. Elastic selection criteria are based on the position of the tracks and thus depend on the alignment. To reach a convergence, the procedure is repeated several times. Corrections are calculated in each iteration, and the results are applied to the alignment constants with a factor of 0.7 in the next iteration. The value of inertness 0.7 is arbitrarily chosen to improve the stability of the iterating procedure.

The coordinates of a proton from the different detectors in an ALFA arm are correlated. This can be used to develop optimisation for the Y_{off} offset which is most prone to errors. Correction Y_{opt} improves the reconstruction of the proton kinematics, which is more dependent on the relative positions of the tracks in different detectors (local angle).

Track coordinates in the detector coordinate system (x_{det}, y_{det}) can be converted to the beam coordinate system (x_{beam}, y_{beam}) with the matrix equation:

$$\begin{bmatrix} x_{beam} \\ y_{beam} \end{bmatrix} = \begin{bmatrix} \cos \theta_Z & -\sin \theta_Z \\ \sin \theta_Z & \cos \theta_Z \end{bmatrix} \begin{bmatrix} x_{det} - \Delta X \\ y_{det} + Y_{nom} \end{bmatrix} + \begin{bmatrix} 0 \\ Y_{edge} - Y_{nom} + d/2 - Y_{off} + Y_{opt} \end{bmatrix}. \quad (4.1)$$

The constant Y_{nom} is equal to the nominal position of the detector edge: $Y_{nom} = 135$ mm. The constant Y_{edge} is the actual position of the detector edge measured during the ALFA test beam campaign, shown in Table 4.1.

The randomisation process is used to limit problems with discontinuous nature of position measurement, which still remains significant due to imperfect staggering. Instead of taking the track position as the centre of the overlap region, the coordinates u and v are randomly selected, assuming a uniform distribution of the track position in the overlap region. Then, the randomised u and v can be transformed into the coordinates x and y . Randomisation is not enough to resolve all problems of significant staggering imperfection if the real distribution of tracks evolves rapidly in the widest overlap region. However, it can help to improve the stability of the alignment procedure.

4.3 Distance measurements

4.3.1 ALFA Overlapping Detectors

Two independent Overlapping Detectors (ODs) are complementary to the MD and measure the distance between the upper and lower RPs. They are attached on each side of both MDs, as sketched in Fig. 3.1. The ODs are built of the same scintillating fibres as MD, but with only 3 layers of 30 fibres each, and the ODs can measure only the vertical position of the track. Therefore, the reconstruction of the track for OD is like that for MD, but using only three layers - Fig. 4.2.

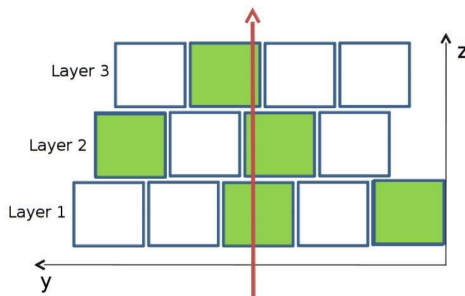


Figure 4.2: Sketch of a particle passing the 3 OD layers [85]. Real and noisy hits are filled with green colour.

Three layers of fibres in each OD are staggered by $1/3$ and $2/3$ fibre width to increase the resolution, similar to the staggering of the MD. The single-track resolution of this detector is $166 \mu\text{m} / \sqrt{12} \approx 48 \mu\text{m}$, and the precision of distance measurement by a single particle is approximately $\sqrt{2} \cdot 48 \mu\text{m} \approx 68 \mu\text{m}$. The staggering is not perfect; therefore, this value increases to about $100 \mu\text{m}$, which is not sufficient for a precise analysis. The effect was confirmed with simulations [85]. More coincidences between both ODs improve this precision to $100 \mu\text{m} / \sqrt{N}$, where N stands for a number of reconstructed tracks. Once the sample statistics exceeds a few thousand counts, the precision is dominated by the relative pitch error and the precision of the alignment of the fibre and overlap detectors so that the overall precision remains within the limit of $10 \mu\text{m}$ [86].

Detected protons are usually part of the beam halo. During the motion of proton bunches, some particles might interact with the LHC instruments or with the residual gas in the vacuum chambers. These processes create the beam halo - particles that stray

from the bunch structure of the beam but still circulate inside the LHC beam pipe. They are usually very problematic because they can damage the delicate accelerator equipment or introduce background - and are cleaned or absorbed. It is a fair assumption that they travel parallel to the beam.

When the distance between the upper and lower RPs is less than 17 mm, two ODs of both RPs overlap. Halo particles can traverse the overlapping part, and two independent measurements of the vertical position can be performed. The vertical coordinates of the tracks are related to the distance between the upper and lower edges of both main detectors.

However, a precise measurement of distance requires information on the relative positions of the ODs to the MD. This information was obtained from a test beam performed in 2010 in the North Area of CERN. The high-resolution beam telescope EDUET was installed in front of the ALFA detector. Then, the particles went through the telescope and MD or the telescope and ODs. The results of this measurement are summarised in Table 4.1. The combined uncertainty of the MD-OD calibration is obtained by adding different uncertainty contributions in quadrature: convoluted effect of the OD fibre positions, MD edge measurement, and alignment between EUDET and ALFA [85]. The high value for station B7L1 is because the upper RP, B7L1U, was not part of the test beam campaign, as it was already installed in the LHC tunnel.

Station	B7L1	A7L1	A7R1	B7R1
d_{up} [mm]	135.000	135.034	135.008	135.005
d_{low} [mm]	135.012	134.948	134.995	135.021
$u(d_{up} + d_{low})$ [mm]	± 0.081	± 0.017	± 0.012	± 0.022

Table 4.1: Relative position of the ODs and MDs measured during the ALFA test beam [78]. The combined uncertainty for the calibration of the entire station is shown.

Additional detectors that measure the positions of the RPs are Linear Variable Displacement Transducers (LVDT) which are calibrated in a laser survey regarding the geometrical centre of the beam pipe. The internal precision of these sensors is 10 μm . This measurement is used during data collection, for a preliminary setting of RPs positions. They are not calibrated precisely with the MDs; therefore, they cannot be used to obtain absolute distance. This is the reason why ODs are so important in distance measurement. Despite that, the LVDT can be used for relative measurements and to cross-check the OD analysis.

4.3.2 Measurement principle

The distance measurement is the first stage of ALFA alignment using traversing beam-halo particles or shower fragments reconstructed by ODs. The principle is presented in Fig. 4.3. The vertical coordinates of the tracks in the OD coordinate systems are D_{up} and D_{low} . The sum $D = D_{up} + D_{low}$ can also be described by the sum of the distance d and the positions d_{up} and d_{low} of both MD edges: $D = d + d_{up} + d_{low}$. Therefore, the distance

d between the MDs is given by:

$$d = D_{up} + D_{low} - (d_{up} + d_{low}). \quad (4.2)$$

The distance measurement is performed separately for both OD sides and then averaged. The primary source of the differences between the left and right sides comes from the rotation of the RPs around the Z-axis.

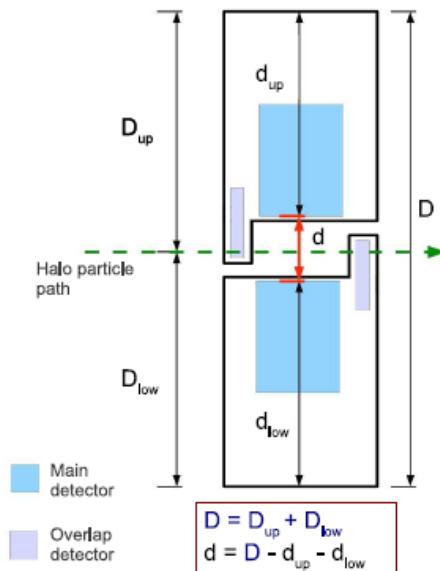


Figure 4.3: Distance d between upper and lower MD edges is calculated using the horizontal beam halo path, reconstructed by both ODs [85].

4.3.3 Events selection and measurement

The distance measurement uses traversing beam-halo particles, whose vertical position is measured by Overlapping Detectors. Exactly one track must be reconstructed in both ODs on the same side in one ALFA station. Multiple tracks may result in a mismatch and give the wrong distance. Besides the tracks coincidence requirement, a few additional selections can be applied to reject as much background and noise as possible, and keep high statistics for signal events:

1. The fibres bend outside the area covered by the OD trigger. Therefore, a signal is required in the corresponding OD triggers to ensure that the track is not reconstructed in the bent fibres.
2. A veto on trigger and fibre hits in ODs on the other side of the MD and limited activity in the MD (no more than five hit fibres) are used to reduce the chance of shower events. Showers present problems for distance analysis because they generate particles with large angles as well as uncorrelated signals in two ODs.

3. Tracks should be isolated; none of the five neighbouring fibres of the track should be hit. This selection can limit the effects of crosstalk between fibres.
4. At least one layer in each of the ODs should be clean - it should have only one fibre hit. This cut reduces the impact of uncorrelated tracks.
5. Only three fibres are hit in each OD, which are used for track reconstruction. This extends selections 3 and 4 and significantly improves the quality of the reconstructed tracks.
6. The requirement of an OD trigger signal in an adjacent ALFA station is very strict, but it can enchant the sample with perpendicular tracks.

Nominal selections are 1-4, they provide sufficient statistics with a limited background. A data sample without the veto (selection number 2) is the most inclusive sample possible, which is not dominated by background events. Selections 5 (clean tracks) and 6 (adjacent trigger) are used to produce samples used in uncertainty analysis.

The idea of distance measurement is simple: for all events in the nominal sample, the distance is calculated according to Eq. (4.2) and fills the histogram. The output for station A7L1 for LHC fill 4509 is shown in Fig. 4.4. The distribution is fitted with the Gaussian function as a signal, and a fourth-degree polynomial as the background. The distance is estimated as the position of the Gaussian centre.

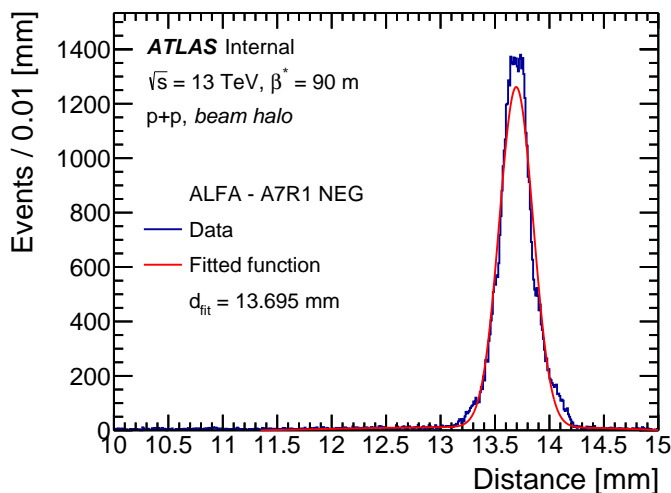


Figure 4.4: Distance plot for nominal selections with randomisation - station A7L1 negative side, LHC fill 4509.

The distribution of the vertical coordinates reconstructed with OD is not contiguous but discrete - the tracks reveal the same combination of fibres for a given range of y . ODs have only three layers, and the combination of hit fibres has a wider overlapping region compared to MD. Furthermore, layers staggering is poor for some ODs; therefore, the overlap region can vary between $1 \mu\text{m}$ and $380 \mu\text{m}$.

The distribution of distance obtained from the discrete track positions is also discrete. It can be seen in Fig. 4.5a. Each peak around the true distance comes from a valid

combination of hit fibres and cannot be neglected. However, it is impossible to estimate the precise distance from this plot; e.g. the fit would be very unstable.

A randomisation process is introduced to improve the stability of the fit. For both ODs - upper and lower - the position of the reconstructed track is chosen randomly from the overlapping region. The uniform distribution is assumed. The distance distribution obtained with randomised positions is shown in Fig. 4.4, and the fit is stable.

The distribution from Fig. 4.4 does not have an exact bell shape. The main reason for this is the imperfection of the randomisation method. The positions in the upper and lower ODs are randomised independently, ignoring the correlation between them. For example, if the true position of the particle was shifted to the left in the upper OD, there is a higher probability that the true position in the lower OD was also shifted to the left. Unfortunately, the correlation is not trivial and depends on the actual distance and the arrangement of hit fibres.

To cross-check the results obtained with randomisation, another approach is prepared for histogram smoothing. The raw distribution of Fig. 4.5a is convoluted with a normalised Gaussian function with $\sigma = 0.500$ mm. This produces a very smooth histogram with a bell shape that is presented in Fig. 4.5b. However, the results can be influenced by background events. The difference between the randomisation and convolution approaches is of the order of a few μm , which implies the correctness of the methods used. Furthermore, it is also confirmed with the fast simulation.

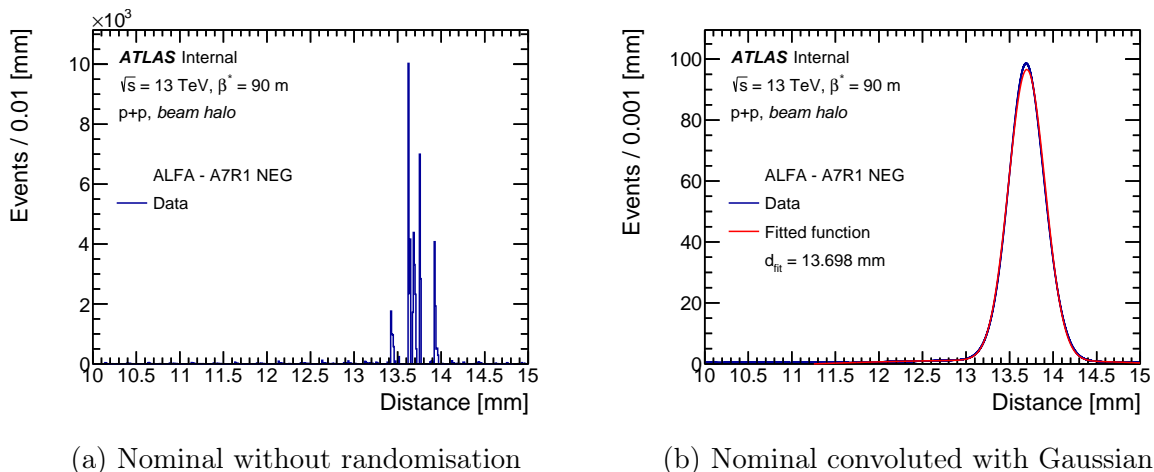


Figure 4.5: Distance measured with different methods - station A7L1 negative side, LHC fill 4509.

4.3.4 Simulation

A fast simulation of two ODs is performed to test the described method of distance measurement. Each OD is modelled as a set of three layers with scintillating fibres. The width of the fibre is equal to $480 \mu\text{m}$, and between two fibres is approximately $20 \mu\text{m}$ of inactive glue. Two models of staggering are tested:

- Ideal staggering - the distance between two consecutive fibres in one layer equals exactly $500 \mu\text{m}$ and the shift between two layers is $500/3 \mu\text{m} \approx 166.67 \mu\text{m}$.

- Random staggering - the position of the next fibre is determined by Gaussian distribution with $\mu = 500 \mu\text{m}$ and $\sigma = 5 \mu\text{m}$.

The particle is assumed to traverse the layers perpendicularly - the position is generated using uniform distribution - and only one dimension is considered besides layer number. The fibre is hit when the position of the particle is within the range of $480 \mu\text{m}$. Hitting the glue does not create a signal in the layer. Visualisation of some events is shown in Fig. 4.6.

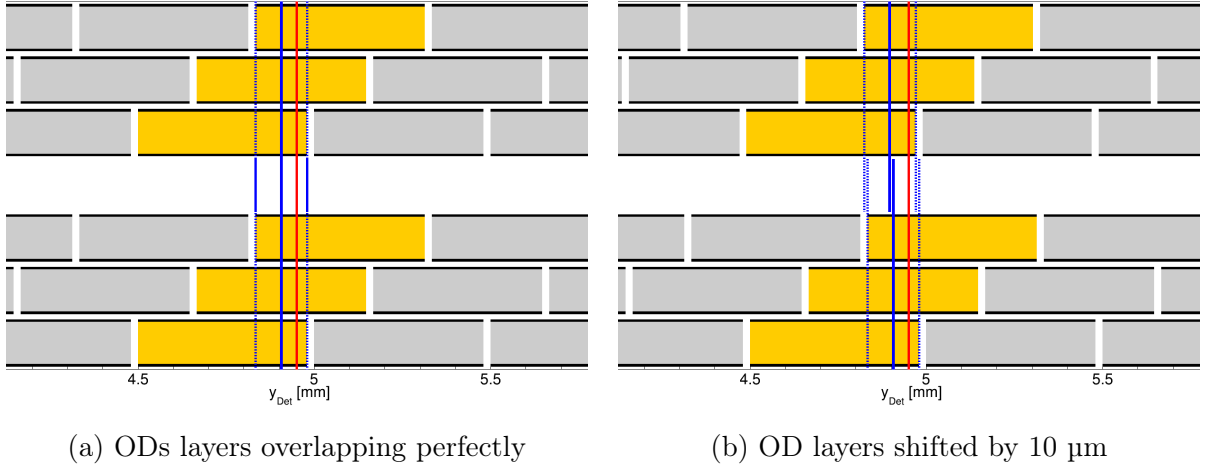


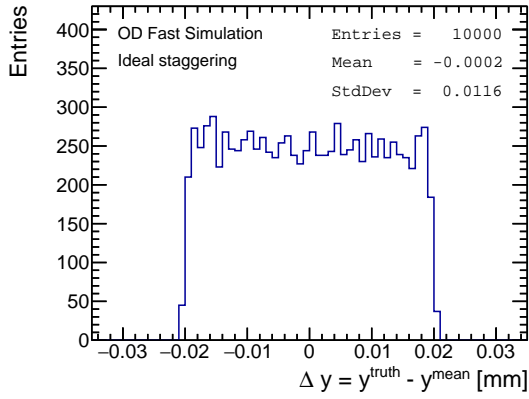
Figure 4.6: Scintillating fibres in two ODs with the ideal staggering model [88]. The traversing particle is marked with the red line and the blue lines indicate the positions reconstructed in upper and lower ODs.

The positions of both ODs were randomly selected for each experiment. Then, 100 thousand particles were generated uniformly and events with a signal in all six layers were used to determine the distance. The experiment was carried out 10 thousand times and the differences between the truth and the determined values are shown in Fig. 4.7. The simulation shows two sources of errors in distance measurement:

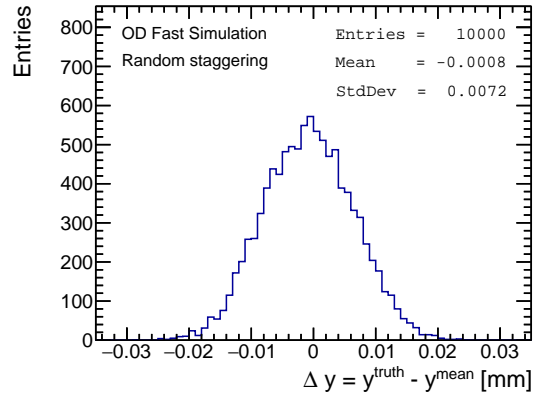
- inactive gap (glue) between fibres;
- imperfection of randomisation.

The first source of errors is clearly visible for the ideal staggering model in Fig. 4.7a, where the difference between the truth distance and the distance calculated as the arithmetic mean of all events is shown. For a simulation with no background events, the mean is not biased and can be used as the best estimation of distance. The distribution is uniform in the range $[-20, 20] \mu\text{m}$, which corresponds to the width of the inactive gap.

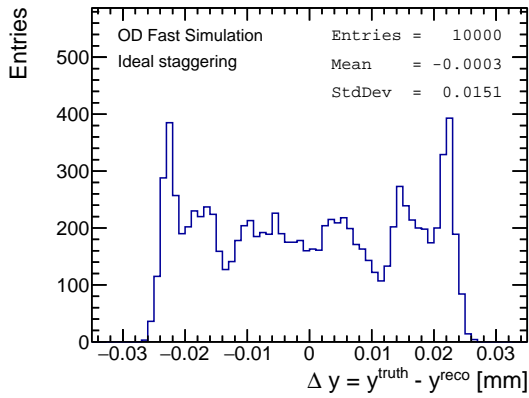
For ideal staggering, there is the possibility that two sets of layers overlap perfectly, Fig. 4.6a. In that case, all particles have the same position reconstructed in both ODs, and the distance is measured without error. When the upper OD is shifted by $10 \mu\text{m}$ - Fig. 4.6b - the reconstructed distance is exactly the same as for Fig. 4.6a, but the error is equal to $10 \mu\text{m}$. This situation continues with a shift up to $20 \mu\text{m}$. Above $20 \mu\text{m}$,



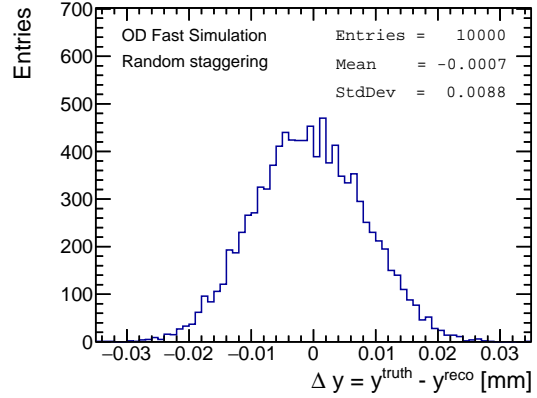
(a) $y^{truth} - y^{mean}$ for ideal staggering



(b) $y^{truth} - y^{mean}$ for random staggering



(c) $y^{truth} - y^{reco}$ for ideal staggering



(d) $y^{truth} - y^{reco}$ for random staggering

Figure 4.7: Distribution of errors received in the OD simulation. The upper plots show the difference between the true distance and the distance calculated as the arithmetic mean of all events. The lower plots show the difference between the true distance and the distance calculated with Gaussian fit.

the set of three overlapping fibres in the lower OD can coincide with two different sets of fibres in the upper OD, and the error decreases. In summary, the inactive gap width and the requirement of three enlightened fibres for track reconstruction result in errors in the range $[-20, 20]$ μm . The situation improves for random staggering - Fig. 4.7b - where the standard deviation for the $y^{truth} - y^{mean}$ distribution is 7.2 μm , compared to $2 \cdot 20 / \sqrt{12}$ $\mu\text{m} \approx 11.6$ μm for ideal staggering.

The imperfection of the randomisation process increases the error of distance estimation. The plots in Fig. 4.7c and Fig. 4.7d show the errors obtained from Gaussian fits to the randomised positions of the reconstructed particles. This increases the standard deviation to 15.1 μm for ideal staggering and 8.8 μm for random staggering.

4.3.5 Results

Detailed results of distance measurement for LHC fill 4509 are presented in Table 4.2. The results for other fills are presented in Appendix A.

Station	B7L1	A7L1	A7R1	B7R1
Distance [mm]	12.590	13.741	13.685	12.549
Statistical [mm]	±0.001	±0.001	±0.002	±0.002
MD-OD calibration [mm]	±0.080	±0.008	±0.009	±0.008
Inactive gap and randomisation [mm]	±0.011	±0.011	±0.011	±0.011
Event selection [mm]	±0.007	±0.006	±0.003	±0.008
Method [mm]	±0.001	±0.001	±0.003	±0.002
Total systematic [mm]	±0.082	±0.015	±0.015	±0.016

Table 4.2: Distances with uncertainties between ALFA MDs edges for LHC fill 4509.

The distance for an ALFA station is found as the average of the two OD sides. The difference between sides can be up to 200 μm (station B7L1) due to the rotation of the RPs. The statistical uncertainty is estimated with the bootstrap method at around 1 or 2 μm . Compared to the systematic effects, it is not significant although very tight selection criteria are used. The combined systematic uncertainty is at a level similar to that of elastic analysis [78], despite the two fundamentally different methods used.

The systematic uncertainties are determined for each side of the ALFA station separately. Then, they are combined into one value according to the propagation of uncertainty for the arithmetic mean:

$$u_{station} = \frac{1}{2} \sqrt{u_L^2 + u_R^2}. \quad (4.3)$$

The main sources of uncertainty include:

- **MD-OD calibration** - the relative position of ODs is not important in physics analysis. It is used to obtain the distance between the edges of the upper and lower MDs, but this method requires calibration between the MD and the ODs. The calibration was done in the test beam campaign, and the uncertainties for the stations can be found in Table 4.1.
- **Inactive gap and imperfection of randomisation** - the simulation shows the impact of inactive gap (glue) between the fibres on the distance measurement. It is estimated together with the imperfection of the randomisation process at 15 μm , so the uncertainty for the entire station is $15/\sqrt{2}$ $\mu\text{m} \approx 11$ μm .
- **Event selection** - background effects are estimated by the difference between the maximal and minimal distance for samples with different selection criteria (described in Section 4.3.3):
 - nominal sample - selections: 1-4;
 - most inclusive sample - selections: 1, 3, 4;
 - clean track sample - selections: 1-5;
 - nominal sample with an adjacent trigger - selections: 1-4, 6;
 - most inclusive sample with an adjacent trigger - selections: 1, 3, 4, 6.

- **Method** - randomisation process ignores the nontrivial correlation between corrections in the upper and lower ODs. The convolution with normalised Gaussian is used as a cross-check, and the uncertainty is defined as the difference between both methods.

Nontrivial methods that do not suffer from inactive gap effects are used in the elastic analysis that requires precise determination of distance. Other sources of systematic uncertainty, such as vertical and horizontal distributions of particles, are analysed in [78]. However, they can be ignored compared to the sources listed here.

Additional detectors that measure the positions of the ALFA detectors are Linear Variable Displacement Transducers (LVDT) which were calibrated in a laser survey. This measurement is used for a preliminary set of distances between ALFA detectors during data collection. It can also be used to cross-check the results from OD analysis. The correlation between both measurements for station A7R1 for the LHC fills analysed is presented in Fig. 4.8.

The difference between the LVDT and OD measurements for all the filled stations analysed is constant for each station; this difference is equal to 613 μm for station A7R1. The correlation shows excellent precision for the relative changes in distance. Hence, any potential source of errors can come from calibration; for example, the relative position of the ODs and MD could change during the installation of ALFA in the LHC tunnel.

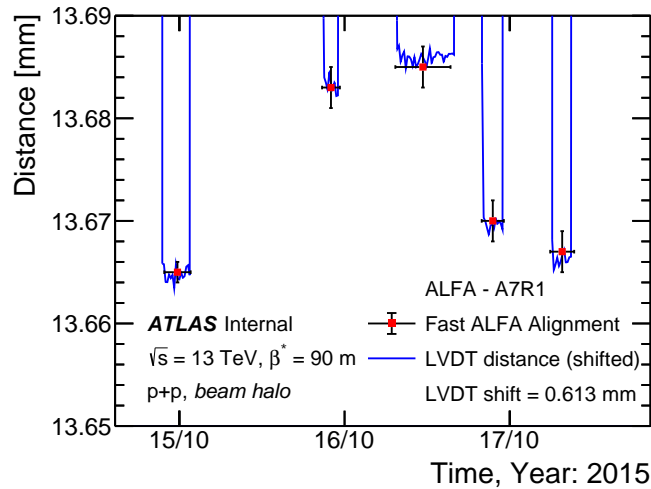


Figure 4.8: Correlation between the received distance and the LVDT measurement for station A7R1 for the analysed LHC fills. Vertical error bars show the statistical uncertainty while the horizontal bars correspond to the fill length. The LVDT results are shifted by 613 μm to match the OD analysis results (for easier comparison).

4.4 Elastic selection

The second part of ALFA alignment is based on the distributions of elastically scattered protons that are measured in MDs. The selection criteria exploit the back-to-back topology of elastically scattered events - Fig. 4.9. The base requirements for the analysis are

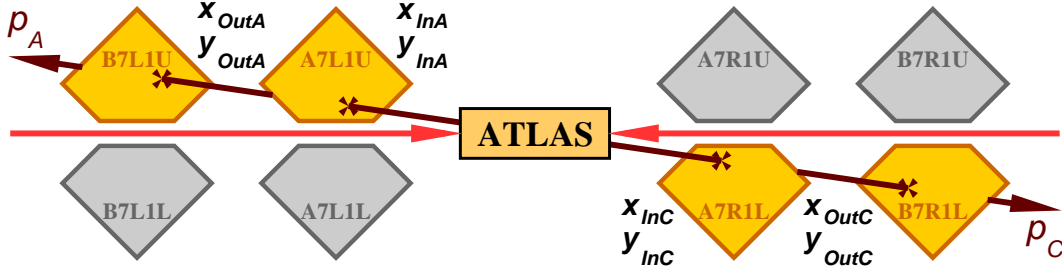


Figure 4.9: Elastic scattered protons measured in ALFA arm 0.

the trigger signal and at least one reconstructed track for all detectors in the ALFA arm analysed. The tracks are required to have at least six overlapping fibres in each U and V plane. In the case of multiple track candidates in one detector, the longest track is used for the analysis.

Because of the back-to-back topology, the positions of protons in opposite detectors should be correlated. This means that:

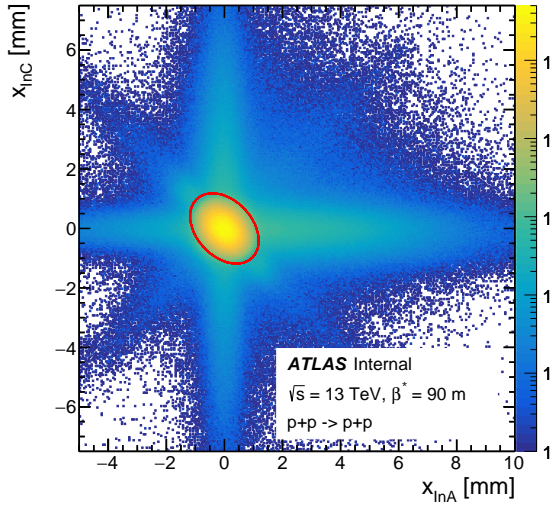
$$\begin{cases} x_{InA} \approx x_{InC} \\ y_{InA} \approx y_{InC} \end{cases} \quad \text{and} \quad \begin{cases} x_{OutA} \approx x_{OutC} \\ y_{OutA} \approx y_{OutC} \end{cases} . \quad (4.4)$$

Correlation plots for inner positions are shown in Fig. 4.10a for the horizontal coordinate and in Fig. 4.10b for the vertical coordinate. The horizontal coordinates are required to lie inside the red ellipse - within 3.5σ of its resolution determined by the 2D Gaussian fit. The rectangular cut is used for the vertical coordinates, because only part of the ellipse can be seen on the plot in Fig. 4.10b. The cut is the same as for elastic analysis [78]: $|y_{InA} + y_{InC}| < 3$ mm. Selection criteria for outer detectors are defined in the same way.

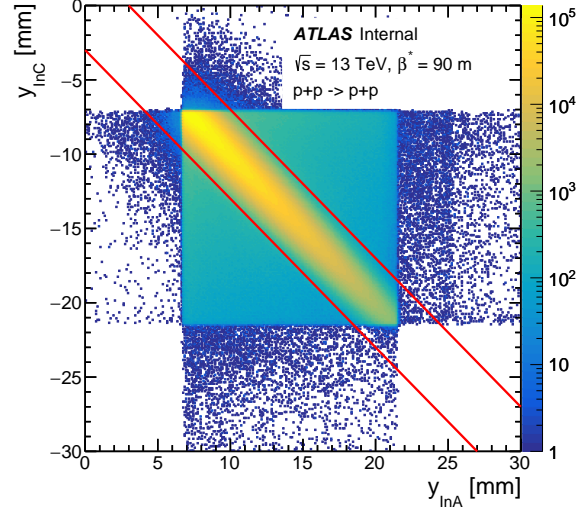
An efficient cut against the non-elastic background is obtained from the correlation of the local angle¹ and the average of horizontal or vertical positions in two adjacent detectors - that are shown in Fig. 4.11a or Fig. 4.11b respectively. The elastic events are focused inside a narrow ellipse with the positive slope in Fig. 4.11a. Other patterns correspond to different kinds of backgrounds, e.g., the unsymmetrical pattern in the top-left corner is due to diffractive events. The parameters of the cuts in Fig. 4.11b are obtained from the fit to the slices projected along the X -axis. This plot can be used as the cross-check for vertical alignment, because the correlation offset should be zero for aligned data.

When the described selection criteria are applied, the nonelastic background is reduced significantly. The distributions are sufficiently symmetric for fast ALFA alignment. Selections are not used in physical analysis besides alignment. Hence, the efficiency is of no interest as long as the statistics is large enough. Some improvements can be investigated in future analysis, such as a veto on MBTS signals that could reduce the diffractive background.

¹The local angle can be measured from difference in coordinates from adjacent detectors: $\theta_X = \arctan(\Delta x/\Delta z) \approx \Delta x/\Delta z$, where Δz is the distance between detectors.

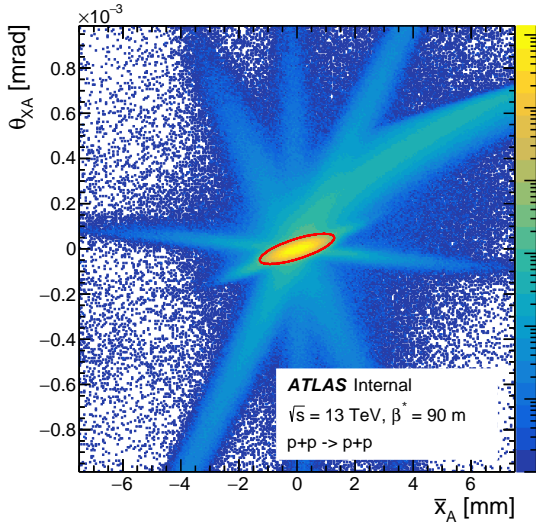


(a) Horizontal coordinate.

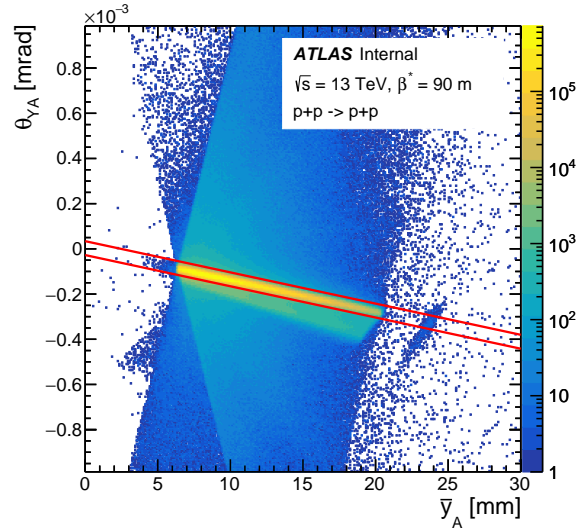


(b) Vertical coordinate.

Figure 4.10: The correlation of measured position of protons in the inner detectors in ALFA arm 0. The plots are generated from aligned data for LHC fill 4509. Elastic events must lie inside the red ellipse or between the red lines.



(a) Horizontal local angle.



(b) Vertical local angle.

Figure 4.11: The correlation of measured local angle for protons on the side A in ALFA arm 0. The plots are generated from aligned data for LHC fill 4509. Elastic events must lie inside the red ellipse or between the red lines.

4.5 Track based alignment

4.5.1 Horizontal Offset

The horizontal offset is determined from the centre of the elastic protons x distribution. The centre can be calculated using three methods:

- **arithmetic mean**;
- **median value**;
- **Gaussian mean** - a Gaussian distribution is fitted to the data.

All three methods are prone to error. The arithmetic mean can be sensitive to outliers. On the other hand, the median is sensitive to the fibre pattern close to the centre of the distribution. The measured distribution does not have an ideal Gaussian shape (e.g., non-Gaussian tails, fibre patterns). The arithmetic mean is chosen as the default method because it has the best stability among all. The difference between methods is used to estimate the systematic uncertainty.

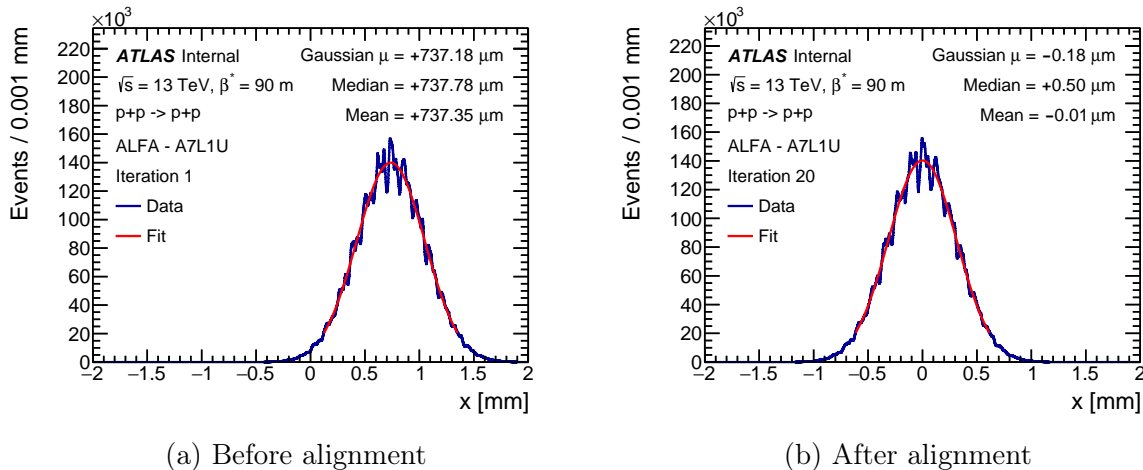


Figure 4.12: Distribution of horizontal positions measured in RP A7L1U for LHC fill 4509, before and after alignment.

Fig. 4.12 presents the horizontal positions of the elastic protons for RP A7L1U, before and after applying corrections. The fibre pattern is visible. The fit is plotted in red, and the offsets for all methods are given in the labels. The results for the LHC fill 4509 are summarised in Table 4.3. Results for other fills are presented in Appendix A. The statistical uncertainty is estimated using the bootstrap method. The systematic uncertainties are based on:

- **Event selection** - the impact of the elastic selection criteria is estimated using different thresholds for the correlations described in Section 4.4 from 3.0σ to 4.5σ in steps of 0.5σ . A new offset is calculated for the aligned detector using a new selection threshold, and the uncertainty is taken as half the difference between the maximal and minimal offsets for different thresholds.

- **Method** - the fibre pattern has a significant impact on the results. It is the dominant source of systematic uncertainty and it is estimated by the difference between the arithmetic mean, the median value and Gaussian mean in the last iteration of the alignment procedure.
- **y-range** - the results can be biased by detector edge effects, e.g., interactions with the RP housing, and different efficiency between the left and right side of the detector edge. To suppress them, the new offsets are calculated in a limited range of y. The range is lessened on both sides by 0.5, 1.0 and 1.5 mm (together and separately).

RP	B7L1U	B7L1L	A7L1U	A7L1L	A7R1U	A7R1L	B7R1U	B7R1L
Horizontal offset [μm]	620.08	-136.58	726.53	507.69	172.63	214.58	207.40	317.47
Statistical [μm]	± 0.04	± 0.04	± 0.03	± 0.03	± 0.03	± 0.03	± 0.04	± 0.04
Event selection	± 0.10	± 0.10	± 0.03	± 0.02	± 0.05	± 0.01	± 0.03	± 0.06
Method [μm]	± 0.73	± 0.64	± 0.68	± 0.73	± 0.48	± 0.40	± 0.71	± 1.93
y range [μm]	± 0.14	± 0.07	± 0.12	± 0.40	± 0.15	± 0.09	± 0.21	± 0.27
Total systematic [μm]	± 0.75	± 0.66	± 0.69	± 0.84	± 0.51	± 0.41	± 0.75	± 1.95
Time dependency [μm]	± 6.34	± 6.34	± 6.34	± 6.34	± 2.83	± 2.83	± 2.83	± 2.83

Table 4.3: Horizontal offsets of the ALFA RPs with their uncertainties for LHC fill 4509.

The total systematic uncertainty is obtained by adding all contributions in quadrature. The alignment parameters change over time as a result of the movement of the beam. This can be considered an additional source of systematic uncertainty. The effect is described in Section 4.5.4.

The iterative instability effect - the impossibility of reaching full coverage despite many iterations, described in [78] - is not observed in this analysis. The residual offset is negligible compared to the other sources of uncertainty. It is due to the randomisation procedure that significantly increases the stability.

4.5.2 Vertical Offset

The vertical offset of the entire station is the second part of the vertical alignment. Together with the distance between the upper and lower RPs which is known from the OD analysis, they provide the vertical position of each detector. The position of the mid-point between both RPs in the beam coordinate system is obtained by comparing the y distributions in the upper and lower detectors.

Due to the up-down symmetry of the elastically scattered protons, the upper and lower y distributions should have the same shape. Therefore, the ratio between both distributions is y-independent (constant). Any misalignment for nonlinear y distributions will make the ratio y dependent. In particular, a constant shift of the approximate e^{-by^2} distribution is expected for elastic events effects in the ratio that linearly depends on y with a slope proportional to the misalignment. This simple method is confirmed by MC

simulation as described in Section 4.7. Different efficiency in ALFA elastic arms 0 and 1 causes different scales in the upper and lower y distributions and the ratio does not equal 1.0, but it should preserve the shape. The ratio is not constant for the misaligned detectors.

The comparison is made with a very simple technique. One of the distributions is shifted left, and the other right by the same amount to achieve a constant ratio between distributions. The linear function is fitted to the ratio - a zero slope indicates the aligned RPs. It can be seen in Fig. 4.13b, where plots for aligned detectors are shown. In the first alignment iteration, the slope is significant, Fig. 4.13a. The shift measures the Y offset between the centre of the ALFA station and the actual beam position.

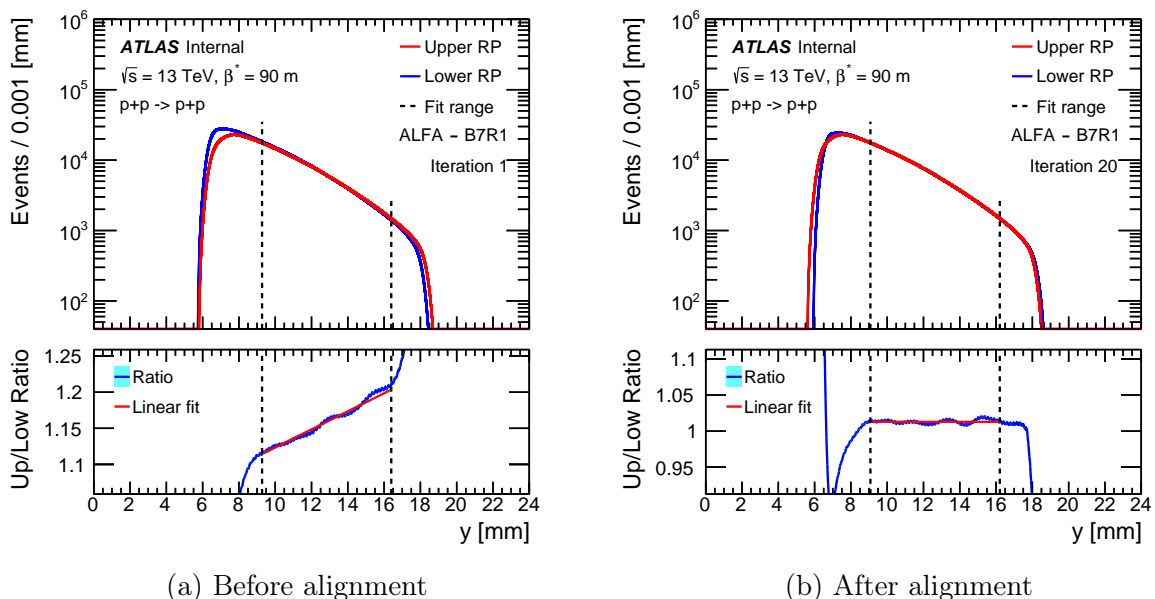


Figure 4.13: Distribution of vertical positions measured in station B7R1 for LHC fill 4509, before and after alignment. The distribution for lower RP is reversed and scaled for easier comparison. The ratio between distributions is shown, and the red line indicates a linear fit.

The ratio fluctuates due to the imperfect fibres staggering. To improve stability, convolution with the Gaussian function is applied to smooth the y distributions. Due to edge effects, the fit is performed in a limited range: the lower limit is increased by 3 mm and the upper limit is decreased by 2 mm.

The results for the LHC fill 4509 are summarised in Table 4.4. The results for other fills are presented in Appendix A. The statistical uncertainty is estimated using the bootstrap method. The systematic uncertainties are based on:

- **Event selection** - see description for horizontal offset - Section 4.5.1
- **y-range** - due to the ratio fluctuations, the fit is sensitive to the y range. To estimate this effect, the new offsets are calculated with the range lessening on both sides by 0.5, 1.0 and 1.5 mm (together and separately). The uncertainty is taken as half the difference between the maximum and minimum offsets.

- **Convolution** - the convolution with Gaussian function improves the stability of the fit, but can bias the results. The uncertainty is estimated as offset calculated without convolution for aligned detectors.
- **Limited events** - the method can be sensitive to the value of the ratio between the upper and lower RPs. The effect can be studied by discarding 50% of random events in the elastic arm 0 or 1. This can change ratios drastically, but the offsets remain on a similar level.

RP	B7L1	A7L1	A7R1	B7R1
Vertical offset [μm]	138.9	111.9	118.4	175.5
Statistical [μm]	± 1.4	± 1.3	± 1.1	± 1.3
Event selection [μm]	± 2.5	± 2.5	± 0.3	± 0.3
y range [μm]	± 18.3	± 19.5	± 9.8	± 8.5
Convolution [μm]	± 26.0	± 8.0	± 2.0	± 8.0
Limited events [μm]	± 0.5	± 7.0	± 6.0	± 6.0
Total systematic [μm]	± 32.0	± 22.4	± 11.7	± 13.4
Time dependency [μm]	± 11.5	± 11.5	± 7.5	± 7.5

Table 4.4: Vertical offsets of the ALFA stations with their uncertainties for LHC fill 4509.

The sliding window technique used for the elastic analysis is more precise but requires reconstruction efficiency for ALFA elastic arms. The ratios between ALFA elastic arms 0 and 1 received in this analysis are consistent for all stations. For LHC fill 4509 they are 0.980, 0.981, 0.980 and 0.987. However, they cannot be used for the track reconstruction efficiency estimation due to simplified selection criteria.

4.5.3 Rotation

The elastic pattern measured by the ALFA detector is an ellipse vertically elongated. The semimajor axis can be determined as the correlation between the vertical positions and the average horizontal positions of the elastic protons. The profiles of these distributions measured in the RP A7L1U for LHC fill 4509, before and after alignment, are presented in Fig. 4.14.

For aligned detectors, the profile should be parallel to the Y -axis. The rotation angle around the middle of the lower detector edge is obtained from the slope of the linear fit to the profile. Fluctuations are due to fibre patterns.

The results for the LHC fill 4509 are summarised in Table 4.5. The results for other fills are presented in Appendix A. The statistical uncertainty is estimated using the bootstrap method. The sources considered for the systematic uncertainty are the following:

- **Event selection** - see description for horizontal offset - Section 4.5.1
- **y-range** - due to the ratio fluctuations, the fit is sensitive to the y range. In order to estimate this effect, the new rotation angles are calculated with the range lessening

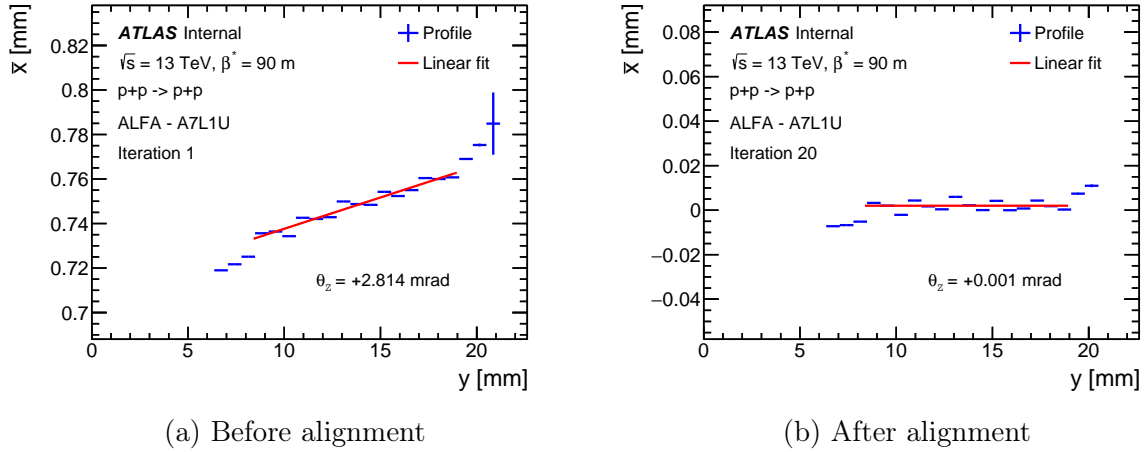


Figure 4.14: Correlation between the vertical positions and average horizontal positions of elastic protons measured in RP A7L1U for LHC fill 4509, before and after alignment. The line shows the linear fit used for the rotation angle estimation.

on both sides by 0.5, 1.0 and 1.5 mm (together and separately). The uncertainty is taken as half the difference between the maximum and minimum rotation.

- **Binning** - besides the fit range, the result is sensitive to histogram binning. The uncertainty is estimated by calculating the rotation angle for the aligned detectors, with the binning shifted by offset from $0.2w$ to $1.0w$ in steps of $0.2w$, where w denotes the width of the bin.

RP	B7L1U	B7L1L	A7L1U	A7L1L	A7R1U	A7R1L	B7R1U	B7R1L
Rotation angle [mrad]	4.65	1.27	2.88	1.85	-1.05	-0.52	0.55	-0.38
Statistical [mrad]	± 0.03	± 0.03	± 0.02	± 0.02	± 0.02	± 0.02	± 0.03	± 0.03
Event selection [mrad]	± 0.01	± 0.01	± 0.02	± 0.01	± 0.02	± 0.01	± 0.04	± 0.03
y range [mrad]	± 0.32	± 0.08	± 0.25	± 0.23	± 0.25	± 0.17	± 0.34	± 0.36
Binning [mrad]	± 0.15	± 0.10	± 0.13	± 0.08	± 0.13	± 0.17	± 0.18	± 0.24
Total systematic [mrad]	± 0.35	± 0.13	± 0.28	± 0.25	± 0.28	± 0.24	± 0.39	± 0.43
Time dependency [mrad]	± 0.12	± 0.12	± 0.12	± 0.12	± 0.13	± 0.13	± 0.13	± 0.13

Table 4.5: Rotation angles θ_z of the ALFA RPs with their uncertainties for LHC fill 4509.

4.5.4 Time dependency

The ALFA alignment is performed with respect to the position of the beam. Therefore, any movement of the beam affects the alignment corrections. In order to study this, the time evolution of each parameter must be investigated.

The full data sample of elastic events is divided into 20 parts according to time. Each subsample has at least 10 million events. Then, using the alignment parameters obtained

for the full sample, the analysis is processed separately for each of the sub-samples. The residual alignment parameters for the ALFA RPs/stations on side A are presented in Fig. 4.15 as a function of time. Statistic uncertainties are estimated for each subsample separately and marked with error bars.

The most significant time dependence is observed for the horizontal offsets - Fig. 4.15a and Fig. 4.15b. The statistical uncertainties are much smaller compared to the offset changes. The trend is very similar for all RPs on the same side, indicating the movements of the beam during the fill duration.

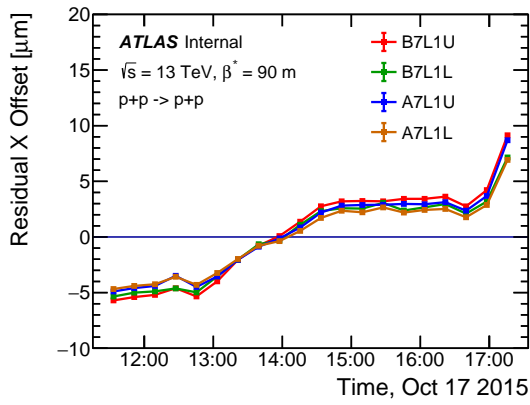
A hint of some trend may be visible for vertical offsets - Fig. 4.15c and Fig. 4.15d - but it fluctuates more than the horizontal offset. They may be derived from changes in the vertical beam position during LHC fill or alignment sensitivity. However, the fluctuations are consistent for both stations on the same side. This fact is important in the optimisation process.

The situation is different for rotations, Fig. 4.15e and Fig. 4.15f. The θ_Z fluctuates around 0 with a constant variation of about 0.1 mrad for all detectors and different fills. No indication of a significant time dependence for this parameter is observed.

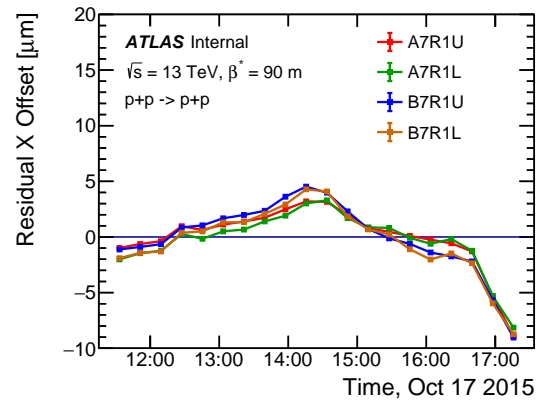
For precise analysis, such as elastic analysis, the transformation from the detector to the beam coordinate system can be made time-dependent. It is important for the horizontal offset, where the trend is clear and the changes are larger even than the systematic uncertainties.

In diffractive analysis, the variation of the residuals of the alignment parameter can be considered to be one of the systematic uncertainties sources. The uncertainty is estimated by the interquartile range calculated from the residuals. The residuals are similar for all ALFA RPs/stations on the same side; hence, they can be grouped together. The box plots present the results for the analyzed LHC fills in Fig. 4.16 . The numbers are added to Tables A.3 to A.5.

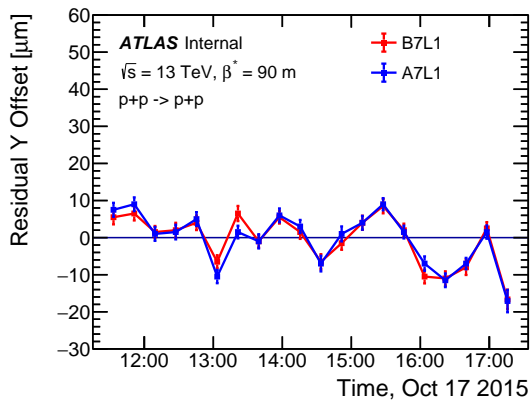
The relative values of the alignment parameters for different LHC fills are presented in Fig. 4.17. For easier comparison, the average over all fills of each parameter is subtracted for each ALFA RP/station. Relative offsets in x are very similar for all detectors on the same side. This suggests that the effect may be related to the different positions of the beam during each LHC fill. Vertical offsets are also sensitive to the different positions of the ALFA stations indicated by the LVDT sensors. The fill dependence for rotation is negligible.



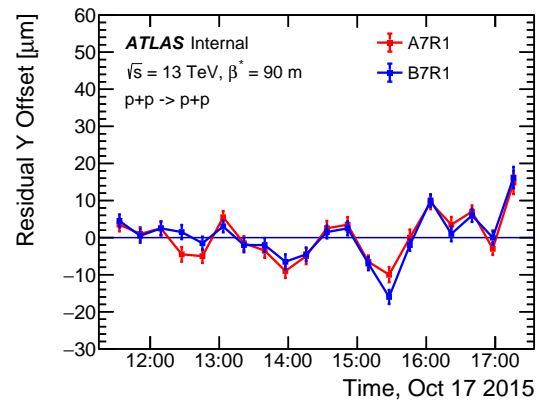
(a) X Offset - Side A



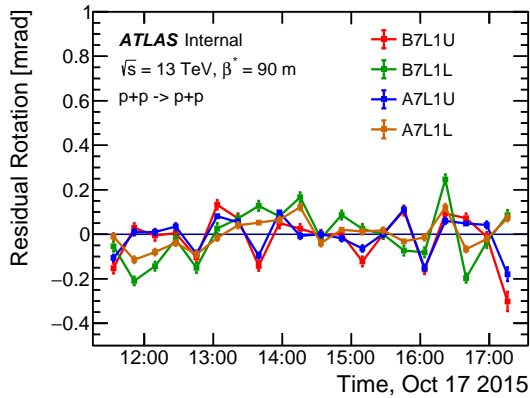
(b) X Offset - Side C



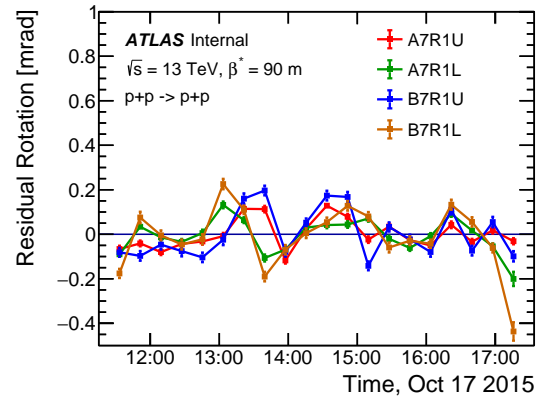
(c) Y Offset - Side A



(d) Y Offset - Side C

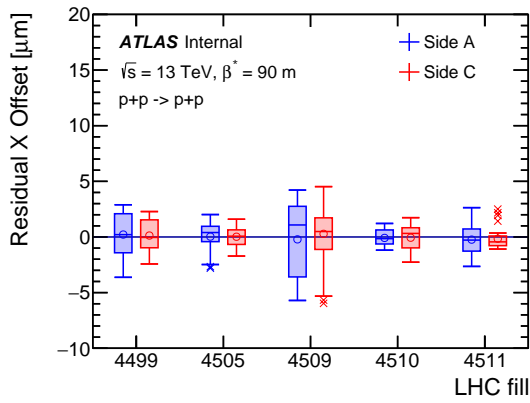


(e) Rotation - Side A

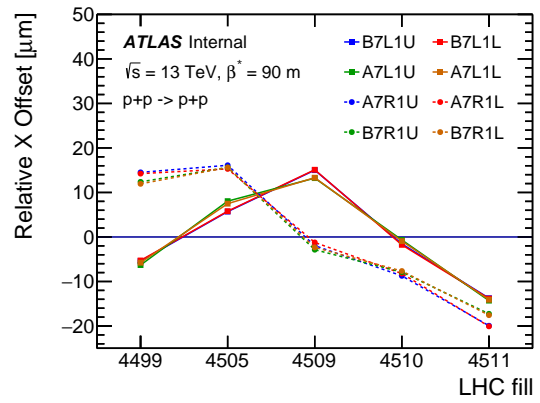


(f) Rotation - Side C

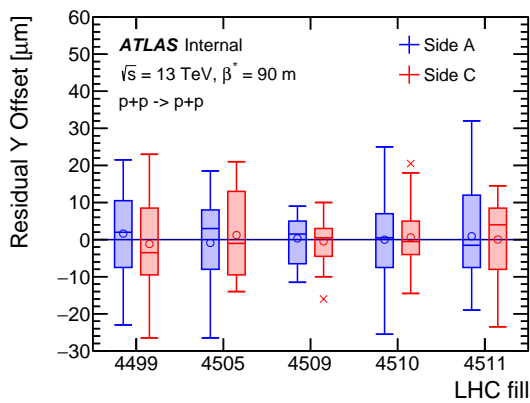
Figure 4.15: Evolution of ALFA alignment parameters for RPs/stations for LHC fill 4509. Only statistical uncertainties are shown.



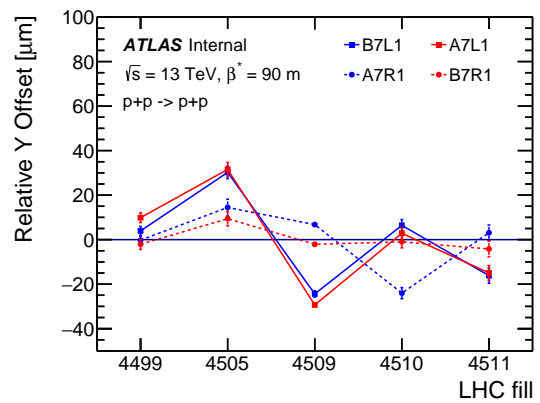
(a) X Offset



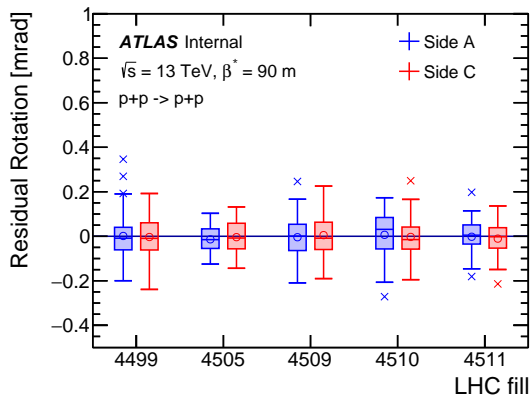
(a) X Offset



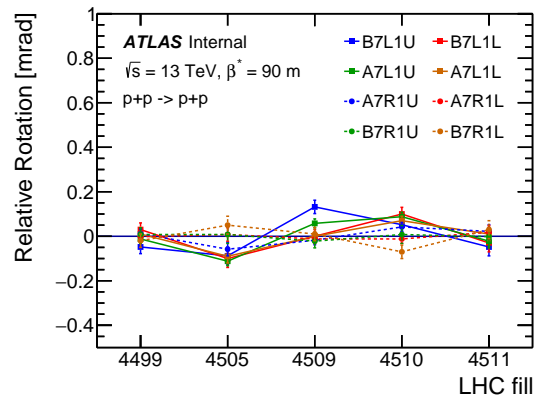
(b) Y Offset



(b) Y Offset



(c) Rotation



(c) Rotation

Figure 4.16: Box plots of the alignment parameters residuals for the sub-samples from the time dependence analysis. The residuals are similar for all ALFA RPs/stations on the same side; hence they are grouped together.

Figure 4.17: ALFA alignment parameters for different LHC fills. For easier comparison, the average over all fills of each parameter is subtracted for each ALFA RP/station. Only statistical uncertainties are shown.

4.6 Optimisation

4.6.1 Kinematic reconstruction and alignment

The ALFA detector measures the position and local angle of the protons scattered forward. The measurements can be used as input for the ALFAReco package to obtain the energy and momentum of protons at the interaction point. The diffractive analysis is usually performed as a function of the proton relative energy loss ξ or the four-momentum transfer squared t - Section 7.4.

The reconstruction of the variables ξ and t depends on the precision of the alignment parameters. Fig. 4.18 shows the errors for ξ reconstruction after adding $\Delta x = 20 \mu\text{m}$ to the horizontal position of the outer RP. The sample enhanced with diffractive events is analysed, but many accidental elastic events remain around $\xi = 0$. The average error for small ξ is approximately 0.001 and decreases for larger ξ . Fig. 4.19 presents average errors for different values of Δx . The error is proportional to the value added to the horizontal position. Therefore, the error of ξ for $\Delta x = 2 \mu\text{m}$ - the typical value of horizontal offset uncertainty - is around 10^{-4} .

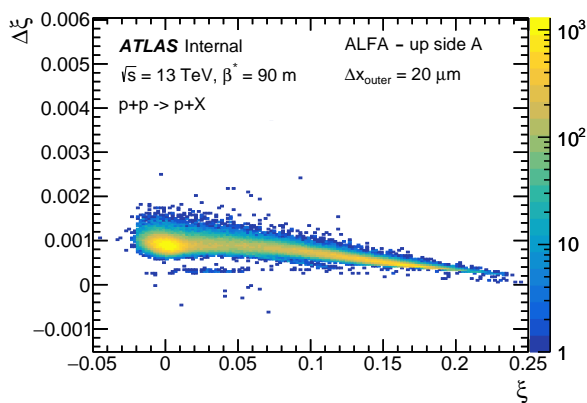


Figure 4.18: The errors for ξ reconstruction after adding $\Delta x = 20 \mu\text{m}$ to the horizontal position of outer RP. Sample enhanced with diffractive events is analysed.

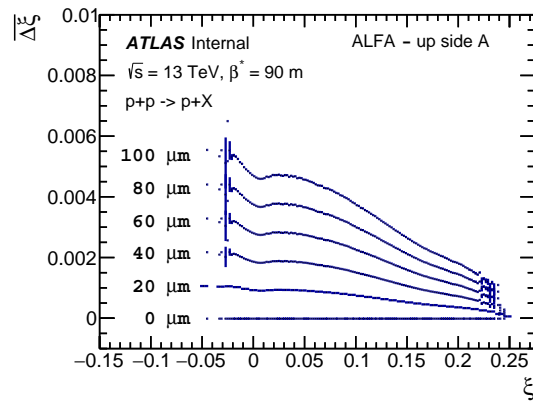
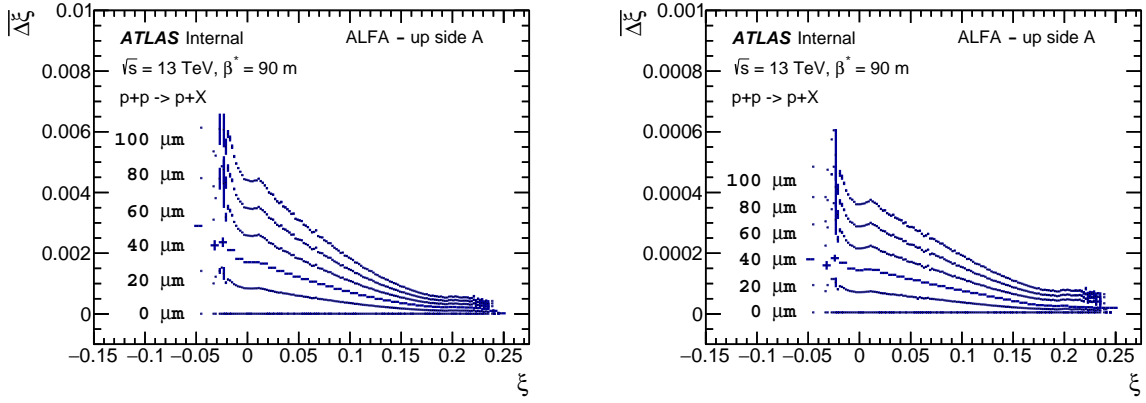


Figure 4.19: Average ξ reconstruction error in the function of ξ , for different values, added to the horizontal position of outer RP.

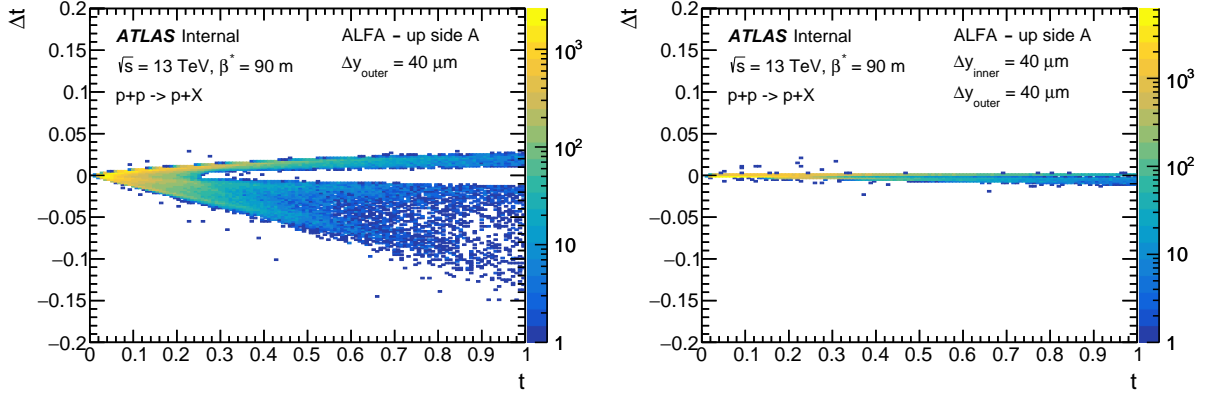
The vertical position error has a similar impact on the reconstruction ξ - Fig. 4.20a presents average errors for different values of Δy . Unfortunately, the uncertainty of the vertical position is about 10 times greater than that of the horizontal position. The situation changes when Δy is added to the positions of both RPs in one ALFA branch - Fig. 4.20b. After that, the relative positions of both RPs are still well determined and the local angle of the proton θ_y remains unchanged. The errors received in this situation are more than 10 times smaller compared to the previous ones.

The effect is also visible for the variable t . Fig. 4.21 shows the errors for t reconstruction after adding $\Delta y = 40 \mu\text{m}$ to the vertical position of one and both RPs. The errors are much smaller when the local angle is unchanged.



(a) Shift added to the position of outer RP (b) Shift added to the positions of both RPs

Figure 4.20: Average ξ reconstruction error in the function of ξ , for different values added to the vertical position of outer RP or to the vertical positions of both RPs in one ALFA branch. The vertical scale is 10 times smaller on the right plot.



(a) Shift added to the position of outer RP (b) Shift added to the positions of both RPs

Figure 4.21: The errors for t reconstruction after adding $\Delta y = 40 \mu\text{m}$ to the vertical position of outer RP or to the vertical positions of both RPs in one ALFA branch. Sample enhanced with diffractive events is analyzed.

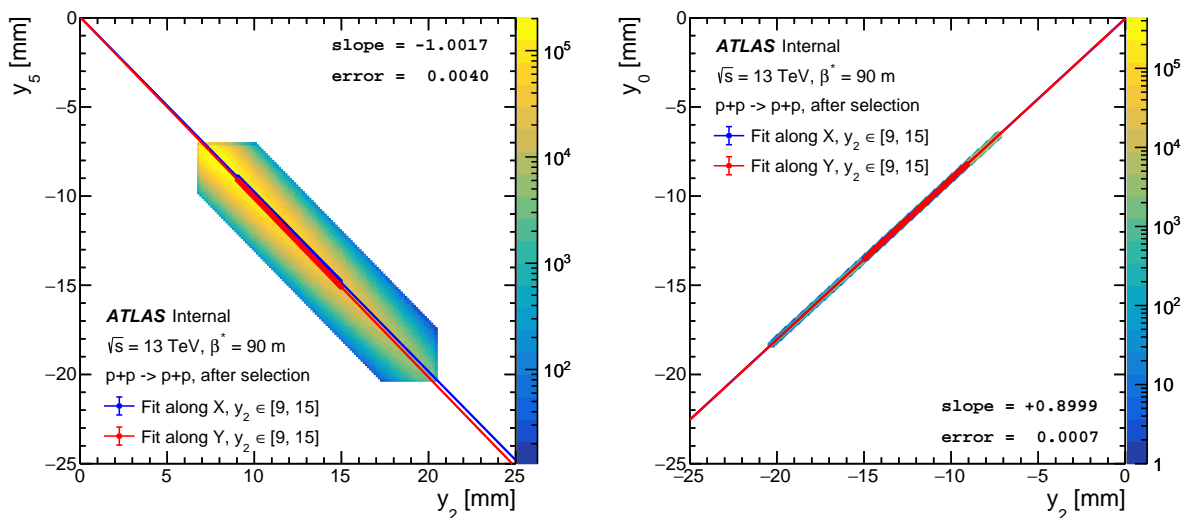
The plots show that the vertical local angle is more important for the kinematics reconstruction than the vertical position itself. Optimisation helps to improve the precision of the relative vertical positions and the reconstruction. The effect is smaller for the horizontal position.

4.6.2 Vertical optimisation

The positions of elastically scattered protons are constrained by LHC optics and the kinematics of an individual elastic event. This leads to the correlations between the vertical position of the elastic tracks in four detectors. The correlation is especially strong for two RPs on the same side, but the back-to-back topology of elastic events makes the

sums of vertical positions measured in the inner ALFA stations centred around zero. A similar effect is observed for the outer stations, but it is interfered with, e.g., interaction with the detector housing.

Fig. 4.22a presents the correlation between vertical positions measured in opposite RPs: A7L1U and A7R1L. The slope α_{25} is calculated as the average of two slopes from fits along the X and Y axes, and the systematic uncertainty is estimated to be half the difference between them. The fit is performed in the range $y \in [9, 15]$ mm in the case of some detector edge effects. As predicted, the value is very close to -1, but it has a large relative uncertainty due to the wide distribution. The correlation between two adjacent RPs on side A, A7L1U and B7L1U, is shown in Fig. 4.22b. The slope α_{20} is positive and the value is approximately 0.9 with a small relative uncertainty for all ALFA branches. All values are collected in Table 4.6.



(a) Correlation between inner RPs:
A7L1U and A7R1L

(b) Correlation between adjacent RPs:
A7L1U and B7L1U

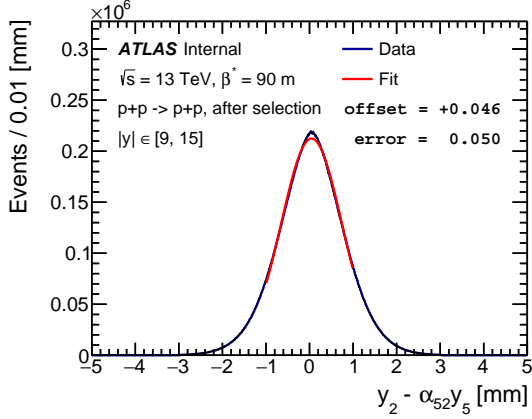
Figure 4.22: The correlation between vertical positions measured in ALFA RPs. The elastic event candidates after selections are shown. The values of the slopes with the uncertainty are added in labels.

	Opposite RPs		Adjacent RPs			
	α_{52}	α_{43}	α_{20}	α_{31}	α_{46}	α_{57}
Slope	-1.0017	-1.0003	0.8999	0.9000	0.9017	0.9002
Stat. uncertainty	± 0.0040	± 0.0042	± 0.0007	± 0.0007	± 0.0008	± 0.0007

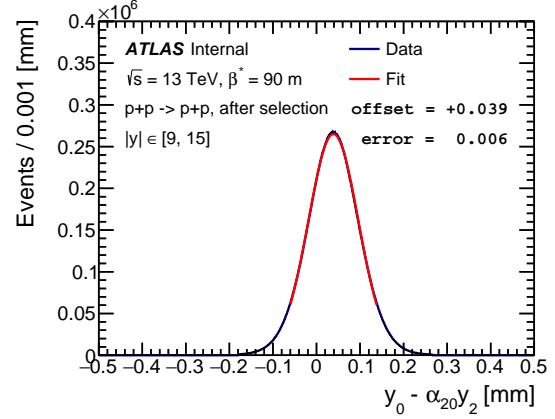
Table 4.6: The slopes for correlations between different ALFA RPs for LHC fill 4509.

The difference between the extrapolated and measured positions indicates misaligned detectors. The extrapolation between RPs i and j is made using the measured slope α_{ij} :

$$y_j = \alpha_{ij} \cdot y_i. \quad (4.5)$$



(a) Extrapolation between inner RPs:
A7L1U and A7R1L



(b) Extrapolation between adjacent RPs:
A7L1U and B7L1U

Figure 4.23: The difference between extrapolated and measured vertical positions for two inner RPs and two adjacent RPs. The elastic event candidates after selections are shown. The offset is measured with Gaussian fit marked by the red line. The values of offsets with the uncertainty are added in labels.

	Opposite RPs		Adjacent RPs			
	2 - 5	3 - 4	0 - 2	1 - 3	6 - 4	7 - 5
Residual [μm]	46 ± 50	-26 ± 52	39 ± 6	-43 ± 6	39 ± 8	-77 ± 7

Table 4.7: Residuals for correlations between different ALFA RPs with uncertainties.

The distributions of the differences are shown in Fig. 4.23. The offset of the distribution corresponds to the misalignment between two RPs. All residuals are collected in Table 4.7.

The residual values for opposite RPs are compatible with zero. The large uncertainties come from the significant uncertainties of the corresponding slopes. However, for the RPs on the same side, the relative shifts are significantly larger than the uncertainties. In conclusion, knowing the importance of precise vertical local angle measurement for the kinematic reconstruction, optimisation must be applied.

The information that comes from the correlation between RPs can be exploited in several ways. Two approaches are considered: nominal and inner. In the nominal scenario, the vertical positions of the inner RPs are shifted by half of the obtained residuals. Then, the positions of the outer RPs are aligned with the inner RPs according to the corresponding slopes and residuals. For uncertainty analysis, the corrections for the outer RPs can be modified by residual uncertainty.

The second one is based on the fact that the residuals for opposite RPs are smaller than the uncertainties. The extrapolation to the other side of ATLAS does not increase the precision. This is especially true for single diffraction analysis, where the correlation left-to-right is lost. For this approach, the inner RPs are fixed and the optimisation is based on the extrapolation between adjacent RPs. This method can be modified for uncertainty analysis. The corrections for inner stations can be increased or decreased by vertical offset uncertainty, and the outer RPs are aligned according to the new inner

RP	B7L1U	B7L1L	A7L1U	A7L1L	A7R1U	A7R1L	B7R1U	B7R1L
Nominal [μm]	-60	56	-23	13	13	-23	-27	55
Inner [μm]	-39	43	0	0	0	0	-39	77

Table 4.8: The corrections for a vertical position in nominal and inner scenarios of the optimization procedure for LHC fill 4509.

positions. The corrections obtained for both approaches are stored in Table 4.8.

Corrections for the vertical position can also be transformed into effective corrections for distance and vertical offset, Table 4.9. The changes for the distance are much greater than for the offsets. The effect is also observed for elastic analysis [78]. Besides, the differences between the LHC fills analysed for the optimisation results are smaller than the statistical uncertainty of vertical alignment, which allows one to apply the same optimisation correction for all the LHC fills analysed. This suggests a problem with the OD calibration; for example, the relative position of the ODs and MD could change during the ALFA installation in the LHC tunnel. For this reason, it is recommended to increase the uncertainty of distance measurement to 100 μm [78].

Station	B7L1	A7L1	A7R1	B7R1
Distance [μm]	116	38	-38	82
Vertical offset [μm]	-2	-5	-5	14

Table 4.9: The effective corrections for distance and vertical offset in the nominal optimization procedure.

4.7 Alignment in MC

4.7.1 Introduction

The Monte Carlo elastic sample was prepared with the PYTHIA 8 generator with A2 tune (based on MSTW2008LO PDFs). The protons generated by PYTHIA were transported from the interaction point to $z \approx 20$ m by GEANT4. Then, the Forward Transport package is used to propagate the particles through the LHC beamline. Finally, the ALFA detector simulation is performed by GEANT4 for all protons that are in the ALFA acceptance.

This is the first alignment of an MC sample with the full ALFA simulation. The alignment results can be compared with the input positions of the detectors. The ALFA RPs are aligned to the position of the beam with a precision of 10 μm - not to the Z-axis of the LHC coordinate system. Because the beam halo is not simulated in this sample, the distance measurement cannot be performed. However, rotation, horizontal, and vertical offsets were calculated in the track-based part of the alignment.

The generated sample contains about 400 thousand elastic candidates with protons inside the ALFA acceptance region. This is about 100 times smaller than the shortest of analysed LHC fills. In order to improve the stability, every event is used 20 times (with

different randomisation, see Section 4.2). But even so, the fluctuations are still visible. This results in considerable uncertainties.

4.7.2 Track-based alignment for MC sample

The MC and data samples are processed with the same track-based alignment software. Results for horizontal offset are presented in Table 4.10. The values are compared with the input positions. The differences are up to 7.49 μm , which is less than the precision of the beam position.

RP	B7L1U	B7L1L	A7L1U	A7L1L	A7R1U	A7R1L	B7R1U	B7R1L
Horizontal offset [μm]	613.08	-149.17	715.50	508.62	166.50	212.71	200.70	323.53
u_{stat} [μm]	± 0.94	± 0.82	± 0.70	± 0.74	± 0.72	± 0.69	± 0.99	± 1.00
u_{syst} [μm]	± 1.75	± 1.37	± 0.84	± 1.18	± 0.86	± 0.83	± 2.06	± 1.27
Input [μm]	615.57	-141.68	718.12	512.78	165.31	212.22	200.75	324.59
Δ [μm]	2.49	7.49	2.62	4.15	-1.19	-0.49	0.05	1.06

Table 4.10: Horizontal offset with uncertainties for the MC sample. The input values for the simulation are shown for comparison.

Fig. 4.24 shows the vertical position distributions for station B7R1 that are used to estimate the offset. Compared to Fig. 4.13, the ratio fluctuates significantly. For this reason, the uncertainties for the MC are greater than for the data. The summary of vertical alignment is given in Table 4.11. The results are comparable to the input. Small statistics for the MC sample make it difficult to determine the source of the differences: alignment error or simulation conditions. For example, the central magnetic field simulated by GEANT4 shifts the beam by about 30 μm on side A and by 10 μm on side C. This effect is not added to the input.

The rotation also agrees well with the input, Table 4.12. The fit range is shorter than for the data, which further increases the uncertainties.

Station	B7L1	A7L1	A7R1	B7R1
Vertical offset [μm]	232.4	164.5	115.5	158.7
u_{stat} [μm]	± 32.2	± 30.4	± 45.2	± 41.5
u_{syst} [μm]	± 74.3	± 78.2	± 66.6	± 90.9
Input [μm]	138.3	112.3	121.9	167.2
Δ [μm]	-94.1	-52.2	6.4	8.5
CMF effect [μm]	-30.0	-30.0	10.0	10.0

Table 4.11: Vertical offset with uncertainties for the MC sample. The input values for simulation and central magnetic field effect are shown for comparison.

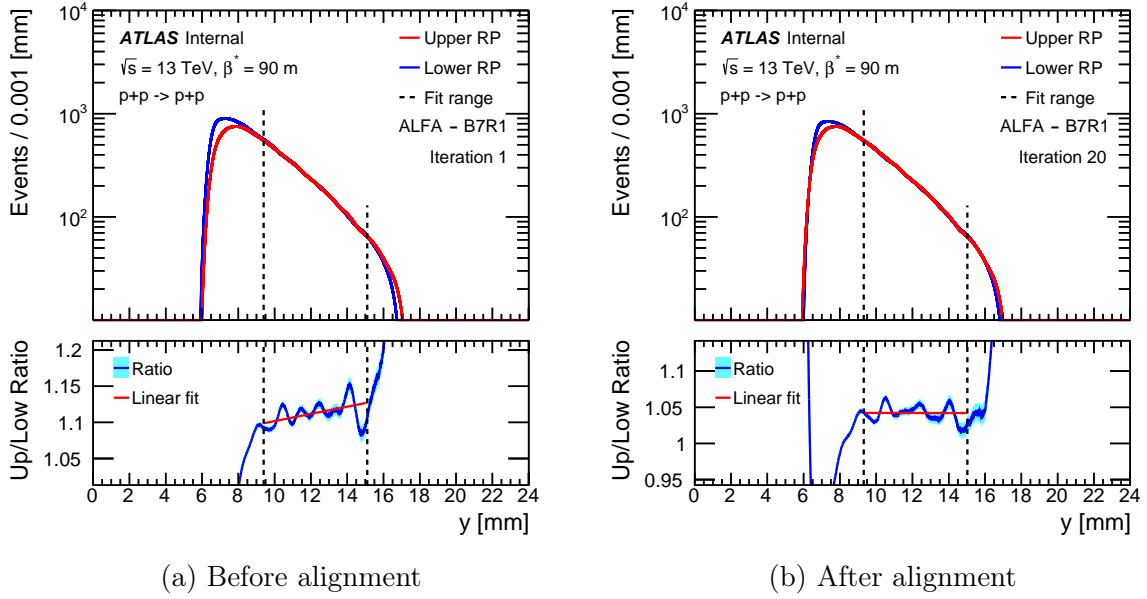


Figure 4.24: Distribution of vertical positions measured in station B7R1 for the MC sample, before and after alignment. The ratio between distributions with statistical uncertainty is shown, and the red line indicates linear fit.

RP	B7L1U	B7L1L	A7L1U	A7L1L	A7R1U	A7R1L	B7R1U	B7R1L
Rotation angle [mrad]	3.940	0.676	2.879	1.253	-1.178	-0.925	0.705	-0.925
u_{stat} [mrad]	± 0.764	± 0.720	± 0.349	± 0.483	± 0.506	± 0.492	± 0.788	± 0.788
u_{syst} [mrad]	± 1.169	± 1.295	± 0.971	± 0.721	± 0.807	± 1.106	± 1.265	± 1.322
Input [mrad]	5.223	1.151	3.113	1.712	-1.051	-0.857	0.296	-0.217
Δ [mrad]	1.283	0.475	0.234	0.459	0.127	0.068	-0.409	0.708

Table 4.12: Rotation angles with uncertainties for the MC sample. The input values for the simulation are shown for comparison.

4.8 Summary

Fast ALFA Alignment software provides alignment parameters for diffractive data. It is based on a similar analysis for elastic data [78]. The results are satisfactory. The precision of the implemented procedure is enough for diffractive analysis. The results for different LHC fills are stable. The impact of alignment uncertainty on proton kinematic reconstruction (ξ and t) is shown. Fast ALFA alignment can be used as a preliminary input for elastic analysis or the main input for diffractive analysis.

To estimate the effect of alignment uncertainty on diffractive analysis, a complete analysis can be performed with several alignment sets. The envelope of deviations from the nominal set for each type of uncertainty is taken as a systematic uncertainty. At first approximation, the parameters should be independent (horizontal offset and rotation, etc.). Then the total alignment uncertainty can be calculated with all parameter uncertainties summed in squares. The recommended sets reflect the alignment uncertainty:

1. Horizontal set - allows for estimating the correlations between horizontal positions in different RPs:
 - horizontal offsets in inner and outer RPs varied by their uncertainties;
 - horizontal offsets in inner RPs increased by their uncertainties and decreased by their uncertainty in outer RPs.
2. Vertical set - optimisation binds vertical position in inner and outer RPs; this allows for the following strategy to estimate the sensitivity to the distance, vertical offset and optimisation uncertainties:
 - vertical offsets in inner and outer RPs varied by the sum of the uncertainty of inner vertical offset and half of uncertainty of distance measurement (according to recommendations it is increased to $1/2 \cdot 100 \mu\text{m}$);
 - vertical offsets in outer RPs varied by the uncertainty of optimisation residuals from Table 4.8;
 - the optimisation based on the extrapolation between adjacent RPs only (the inner RPs are fixed); rest parameters as default.
3. Rotation set - the same changes as for horizontal offset.

Chapter 5

Jets based corrections

The measurement of jets from TopoClusters on the LCW scale is subject to many corrections. These include the efficiency of triggering on jets, the jets' cleaning and the jets' reconstruction efficiency. The energy of the reconstructed jet is different from that of the corresponding jet at a stable particle level; therefore, it requires special calibration.

5.1 Trigger efficiency

At the trigger level, events were selected with the combination of two signals: L1_J12 jet trigger and ALFA_ANY trigger. The second corresponds to the signal from any ALFA RP. Elastic analysis shows that the efficiency of ALFA scintillators in detecting scattered protons is approximately equal to 99.9%, which has been proven several times [78, 28]. Therefore, only the effectiveness of the jet trigger should be examined.

The L1_J12 is a level-one trigger that is based on hardware. It can be used independently or as the foundation for software high-level trigger HLT [92]. L1 exploits trigger towers made of calorimeter elements that have a size of approximately 0.1×0.1 in the (η, ϕ) space, grouped into so-called jet elements with a granularity of 0.2×0.2 . The region of interest (RoI) is formed by the sliding window technique when the sum of online E_T in the window of 4×4 jet elements is greater than the threshold (12 GeV for L1_J12). A jet can exceed this value in more than one window, so it is required that a 2×2 core is a local maximum; this is used to resolve ambiguities and determine the RoI location [93].

The L1_J12 requires at least one RoI. The efficiency of the trigger for a single jet ϵ_{jet} is estimated as a function of the raw jet p_T and η at the detector level before calibration. In this way, it is more stable as it is free from any calibration imperfections. More jets in a single event increase the trigger efficiency because each jet can independently exceed the threshold E_T . In the case of non-isolated offline jets ($\Delta R < 0.8$), the softer ones are excluded from the estimation. The efficiency for events with multiple jets is equal:

$$\epsilon_{multijet} = 1 - \prod_i (1 - \epsilon_{jet}(p_T^i, \eta^i)). \quad (5.1)$$

For clean dijet events, Eq. (5.1) transforms into:

$$\epsilon_{dijet} = \epsilon_{jet}(p_T^{LJ}, \eta^{LJ}) + \epsilon_{jet}(p_T^{SJ}, \eta^{SJ}) - \epsilon_{jet}(p_T^{LJ}, \eta^{LJ}) \cdot \epsilon_{jet}(p_T^{SJ}, \eta^{SJ}). \quad (5.2)$$

Unfortunately, the forward jet trigger was not exploited in ALFA diffractive runs in the 2015 campaign. For this reason, the pseudorapidity of the leading jet in this analysis is limited to $|\eta^{\text{LJ}}| < 3.0$. However, this does not mean there are no jets outside these regions. Therefore, secondary jets are accepted with $|\eta^{\text{SJ}}| < 4.0$.

Offline jets are tested to determine if a jet trigger has been fired for the jet by matching it to any L1 RoI with $\Delta R < 0.4$. Efficiency is measured for jets with the tag-and-probe method:

$$\epsilon_{\text{jet}} = \frac{N(\text{jet \& jet matched to any L1_J12 RoI})}{N(\text{jet})}. \quad (5.3)$$

Two approaches can be used to count the tag and probe jets. The first one uses multijet events from a non-scaled L1_J12 sample, which provides excellent statistics. In this case, the jet can be tagged if there is at least one RoI outside the matching region: $\Delta R > 0.4$. It is based on the assumption that multiple jets can trigger independently. In the case of two non-isolated jets, the softer one is omitted from the count as it may be incorrectly assigned to the RoI of the jet with the higher p_{T} . The one-dimensional efficiency plots in terms of jet p_{T} and η are shown in Fig. 5.1. The reduction in efficiency for $|\eta| \in [1.3, 1.7]$ is caused by transition regions between calorimeter parts. High statistics increase the resolution, and allow us to calculate efficiency based on the two-dimensional distribution shown in Fig. 5.2.

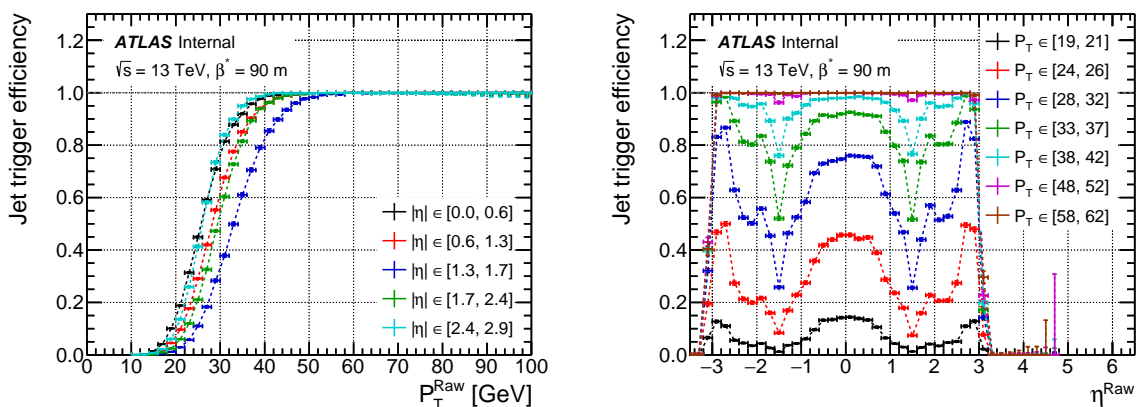


Figure 5.1: Trigger efficiencies as a function of p_{T} and η in different kinematic regions.

The second approach to the tag-and-probe jets uses events from the MBTS+ALFA sample that is prepared with an independent trigger: L1_MBTS_1_A(C)_ALFA_C(A). The ALFA part does not influence the jets, and the MBTS trigger is fully efficient for dijet events [47]. Therefore, all jets can be used as tags (if they are not close to jets with higher p_{T}). Unfortunately, due to the high prescale in this sample, the statistic is small, and this method is only used as a cross-check for the previous one. The MBTS-triggered sample without ALFA was not used because of an even higher prescaling. The difference between both methods is shown in Fig. 5.3. No statistical discrepancy is visible.

Fig. 5.4 shows the trigger efficiency as a function of the calibrated jet p_{T} , corrected for the detector effects. The efficiency of L1_J12 reaches the 99% plateau for p_{T} around 50-60 GeV. This level is too high for the dijet diffraction analysis, where the cross section decreases exponentially with p_{T} . For this reason, this analysis exploits jets below the

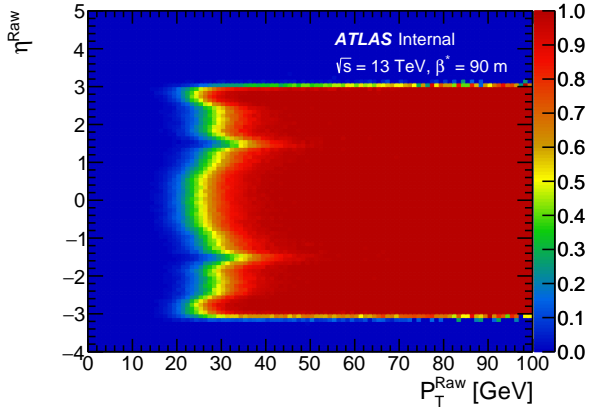


Figure 5.2: Trigger efficiencies as a two-dimensional function of raw jet p_T and η .

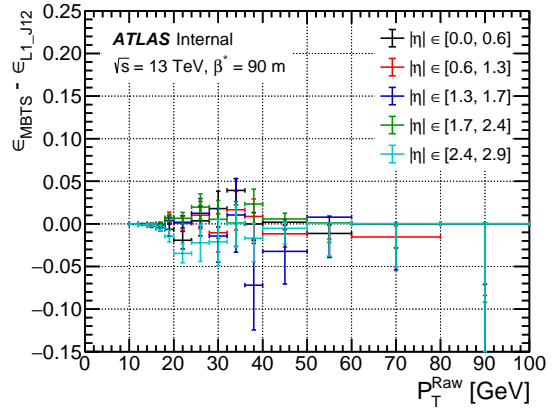


Figure 5.3: Difference between efficiencies calculated from L1_J12 and MBTS+ALFA samples.

plateau. The minimum for the leading jet p_T^{LJ} is set at 30 GeV, where the efficiency of a single jet is greater than 10% for $1.3 < |\eta| < 1.7$ (the lowest of the efficiency ranges) and has small uncertainties. An additional requirement of secondary jet $p_T^{SJ} > 20$ GeV increases the overall efficiency for a single event. The selections are verified by the closure tests.

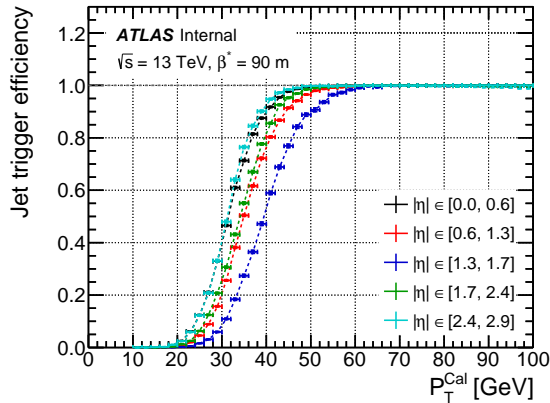


Figure 5.4: Trigger efficiencies as a function of calibrated jet p_T .

Trigger selection was not applied to MC. Instead, the inefficiencies of L1_J12 are accounted for by reweighting the data events by the factor $1/\epsilon$, based on the value calculated from the jets with Eq. (5.1). The analysis is verified with closure tests performed on the MBTS+ALFA sample presented in Fig. 5.5, which are obtained for the leading and secondary jets p_T and η . Base dijets selections from the analysis are applied: $p_T^{LJ} > 30$ GeV, $|\eta^{LJ}| < 3.0$, $p_T^{SJ} > 20$ GeV, $|\eta^{SJ}| < 4.0$. All events that pass this selection (black dots) are compared with L1_J12 events that are reweighted by the factor $1/\epsilon$ (blue dots). The ratio between both distributions is plotted below. The results of this trigger closure test show that efficiency is well evaluated. Some discrepancies within 2% for $p_T^{SJ} < 40$ GeV are

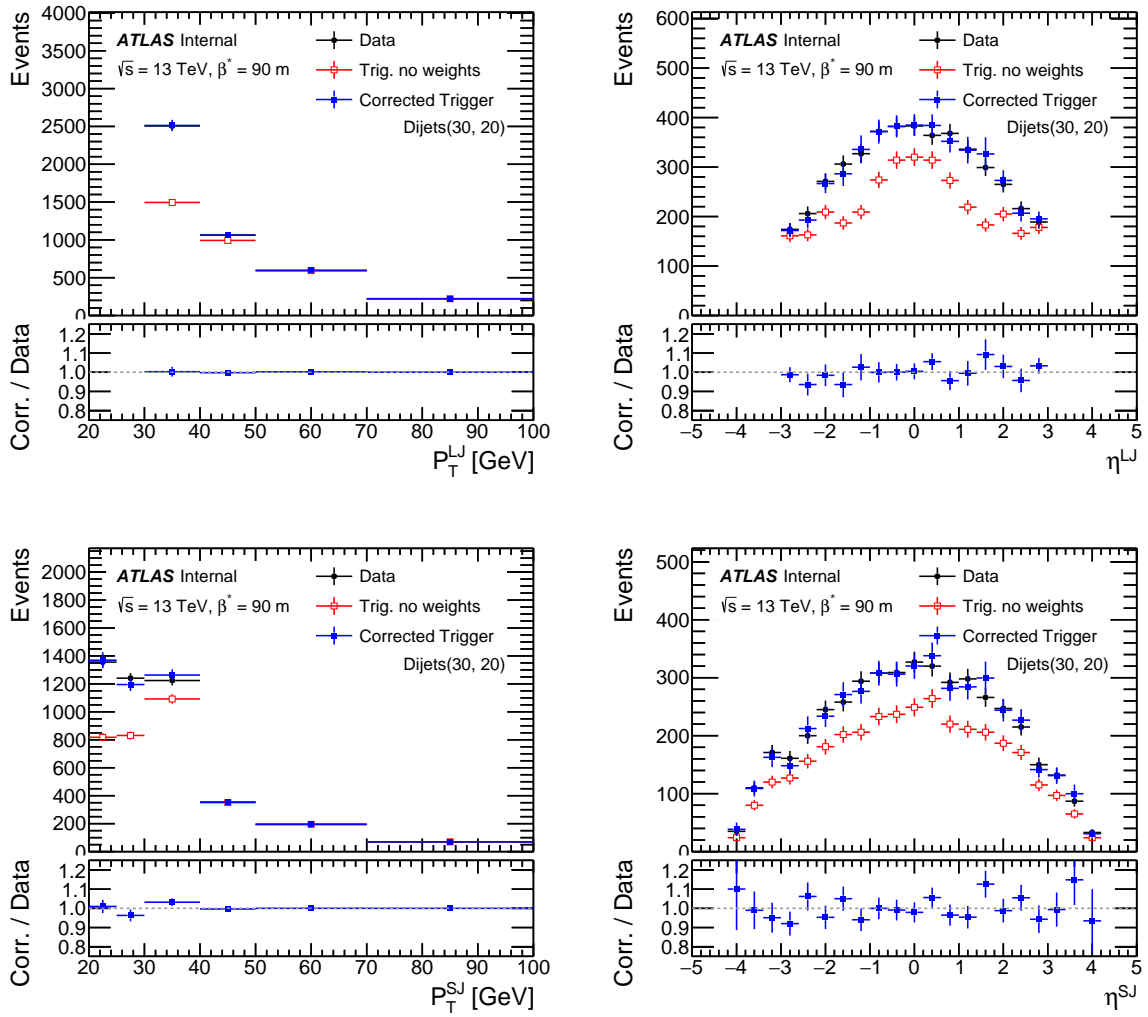
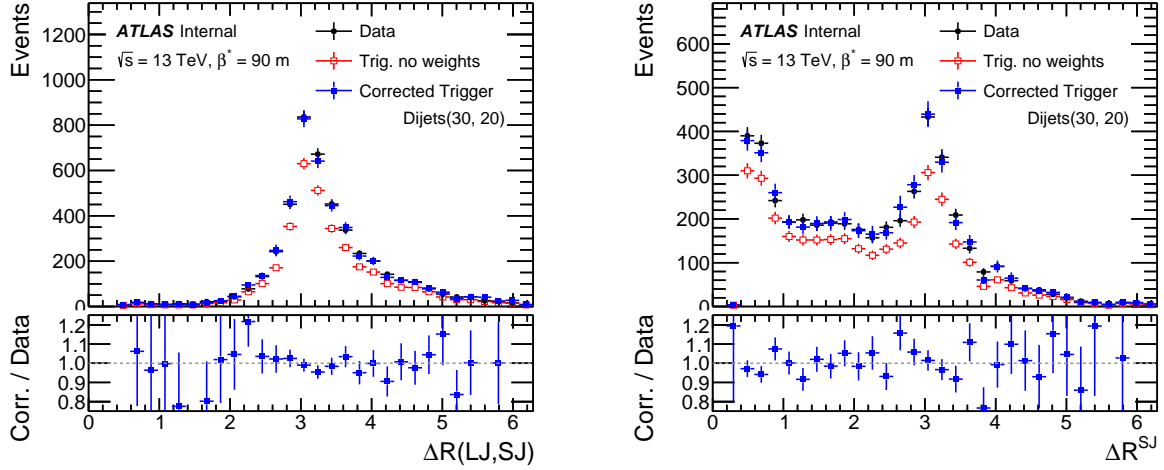


Figure 5.5: Trigger closure test for fiducial jets selection in terms of leading and secondary jets p_T and η . The test is based on the MBTS+ALFA sample. Black dots corresponds to all dijet events recorded in the MBTS+ALFA sample with $p_T^{LJ} > 30$ GeV, $p_T^{SJ} > 20$ GeV. Red dots are the L1_J12 triggered events without correction and blue dots are reweighted events. The ratios between the corrected distribution and all dijet events are added below. Only statistical uncertainties are shown.

taken into account in the estimation of the systematic uncertainty. Distributions without scaling but with the L1_J12 trigger are also drawn (red dots).

Other trigger closure tests confirm that the non-isolated jets are treated correctly. Fig. 5.6a shows the distance in the (η, ϕ) space between the leading and secondary jets. They have a large influence on the efficiency of the trigger. However, for most events, these two jets are well separated. The distributions in Fig. 5.6b show the distance ΔR between the secondary and the nearest jet. This test closes even for non-isolated jets with $\Delta R < 0.8$.

The sensitivity of the trigger efficiency to the shape of the distributions measured from the scattered protons ξ^P and t is shown in Fig. 5.7. Additional antiaccidentals selection



(a) Distance between leading and secondary jets (b) Distance between secondary and closest jets

Figure 5.6: Trigger closure test for fiducial jets selection in terms of ΔR between leading jet and secondary jet (left) and in terms of ΔR between secondary jet and closest jet (right). The description of plots is the same as for Fig. 5.5.

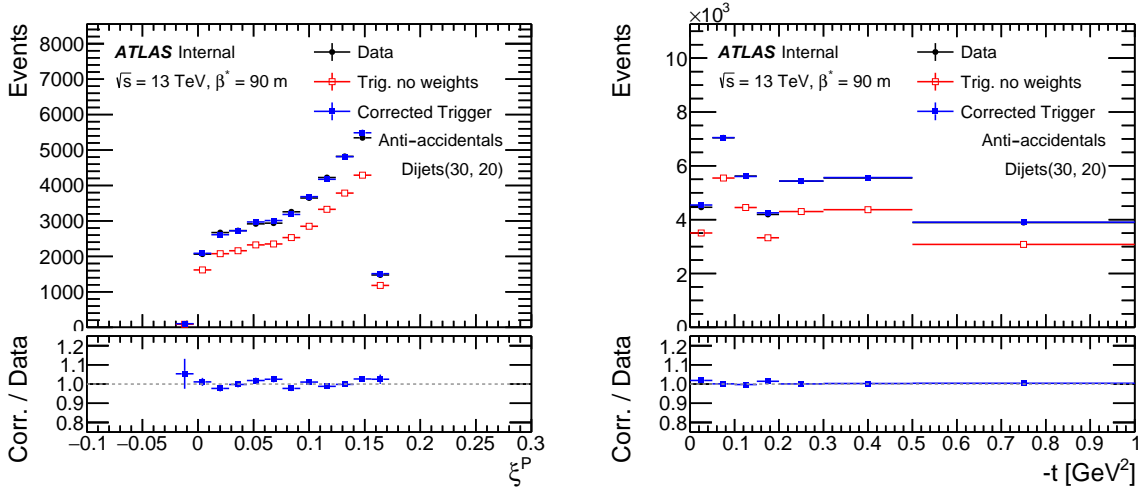


Figure 5.7: Trigger closure test for fiducial jets selection and anti-accidentals cuts for ξ^P and t calculated from the scattered proton. The test is based on the data sample with a probing trigger signal for the leading jet. The description of plots is the same as for Fig. 5.5.

between ξ^P and $\tilde{\xi}_{\text{CAL}}^X$ is added, helping to enrich the sample with diffractive events; in the other case, the distributions are dominated by accidental protons with $\xi^P \approx 0$. The statistic is not sufficient for such selection in the MBTS + ALFA sample. Therefore, events with at least one triggered signal outside the leading jet radius are exploited, based on the not prescaled L1_J12 sample. They are compared with events in which the leading jet triggers, weighted by $1/\epsilon_{\text{LJ}}$. The results for both ξ^P and t indicate the stability of both distributions compared to the trigger efficiency.

5.2 Jets cleaning

Many cleaning selections exist to improve the quality of jets. Standard jet analysis in the ATLAS experiment utilises three cleaning tools: a general Jet Cleaning Tool (JCT) [94], Overlap Removal [95], and Jet Vertex Tagger [96]. The impact of each tool was studied, and only the second one applies to this analysis.

JCT exploits jet quality variables such as signal pulse shape in LAr calorimeters, energy ratio between different parts of calorimeters, or ID track-based variables. They are effective at limiting the calorimeter noise, in addition to rejecting cosmic and beam-induced background. Two sets of jet quality criteria are defined in ATLAS [94]. The loose selection level is designed to ensure a high efficiency above 99.5% for jets with $p_T > 20$ GeV. The tight selection level allows for further rejection of spurious jets for analysis sensitive to the noncollision background, but the efficiency is only 95%. It is not recommended for the October 2015 diffractive campaign with a low noncollision background, especially after antiaccidental selection. This is confirmed by the Fig. 5.8a, where the pass rate of the JCT loose level is plotted as a function of the jet p_T , for data and Pythia samples (without pile-up simulation). The efficiency is similar and close to 99.9% for $p_T > 20$ GeV for both samples, so JCT does not need to be applied in this analysis.

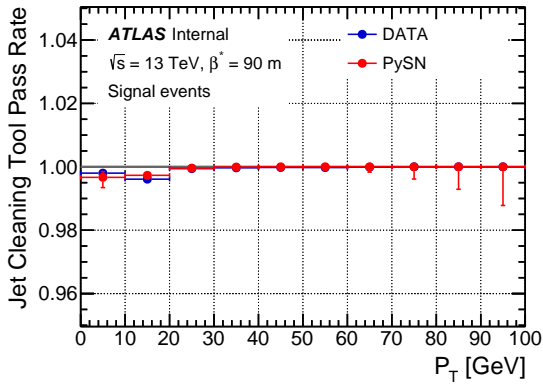
The next tool, Overlap Removal (OR), is applied to remove ambiguities when the same object is reconstructed by multiple algorithms. It follows the recommended removal steps [97]. Leptons, especially electrons, can produce signals in the calorimeter that are incorrectly observed as jets. In this analysis, the OR matches leptons and jets in terms of (η, ϕ) space. The jet is discarded if there is an electron or muon with $\Delta R < 0.2$ and lepton carries most of the jet momentum: $p_T^{\text{lepton}}/p_T^{\text{jet}} > 0.6$. About 2% of the jets in the data and about 1% of the jets in the simulation are incorrectly reconstructed - Fig. 5.8b. The differences are investigated in the estimation of the systematic uncertainty.

One of the most useful tools in the standard jet analysis is the Jet Vertex Tagger (JVT), which helps remove pile-up jets [96]. It applies requirements to the JVT variable, which is based on the ratio between the sums of the transverse momentum of tracks associated with the jet: the ones originating from the primary vertex and all associated tracks. According to the recommendations, a jet is considered a pile-up if it has $JVT < 0.59$. JVT is used only for small jets with $p_T < 60$ GeV which lie inside the tracking range $|\eta| < 2.4$.

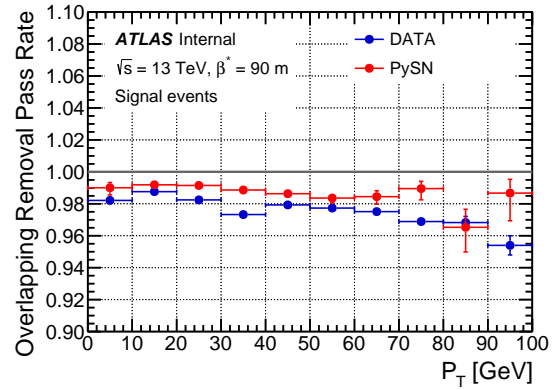
However, the acquisition conditions for the data used in this analysis ensure a low pile-up ($\mu = 0.1$). The distribution of the JVT variable for the data is similar to the simulation without pile-up, which can be seen in Fig. 5.8c. The efficiency of the JVT requirement is around 93% - Fig. 5.8d - a lot of good jets would be mistreated as pile-ups if the JVT is applied. Therefore, it was decided to not use this tool in diffractive dijets analysis.

5.3 Jets reconstruction efficiency

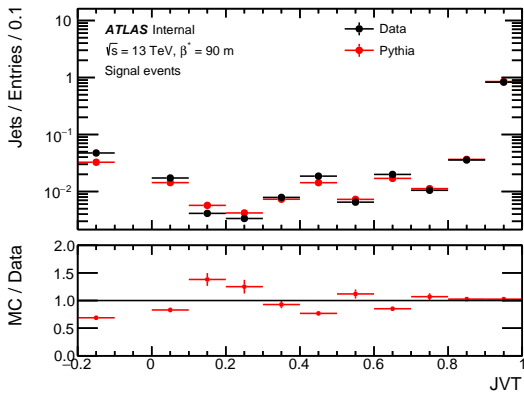
The jet reconstruction efficiency is evaluated in the Monte Carlo simulation by counting how many truth jets are matched to the calorimeter jet. Standard ΔR matching is performed, with a requirement of $\Delta R < 0.4$. Fig. 5.9a shows the jet reconstruction efficiency



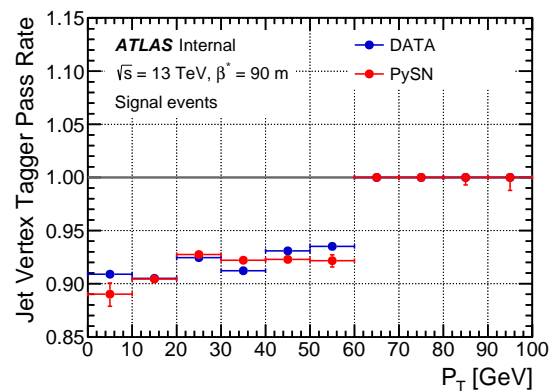
(a) JCT pass rate



(b) OR pass rate



(c) JVT distribution



(d) JVT pass rate

Figure 5.8: Pass rate in function of p_T for jets after Jet Cleaning Tool (a), Overlap Removal (b), Jet Vertex Tagger (d). Figure (c) shows the distribution of the Jet Vertex Factor, where a negative value corresponds to the undetermined JVT. Distributions are presented for data (blue) and Pythia (red) samples after the anti-accidental selection.

for anti- k_t LCTopo jets with radius $R = 0.4$. It is expressed in terms of the transverse momentum of the truth jet. The efficiency reaches 99% for $p_T > 20$ GeV.

The simulation can only be used to determine the efficiency when the agreement between the data and the simulation is confirmed by *in situ* methods. The validation is processed using track jets¹ that provide an independent reference; the tracking system is simulated with high precision, which has been confirmed by other analyses [98]. A tag-and-probe technique is used:

- Track jets are limited to region $p_T > 5$ GeV and $|\eta| < 1.9$.
- The track jet with the highest p_T is defined as the reference object. It is required to have $p_T > 15$ GeV and match with a calorimeter jet with $p_T > 7$ GeV in terms of ΔR . This definition of reference object provides stable results [98].

¹Jets reconstructed from ID tracks.

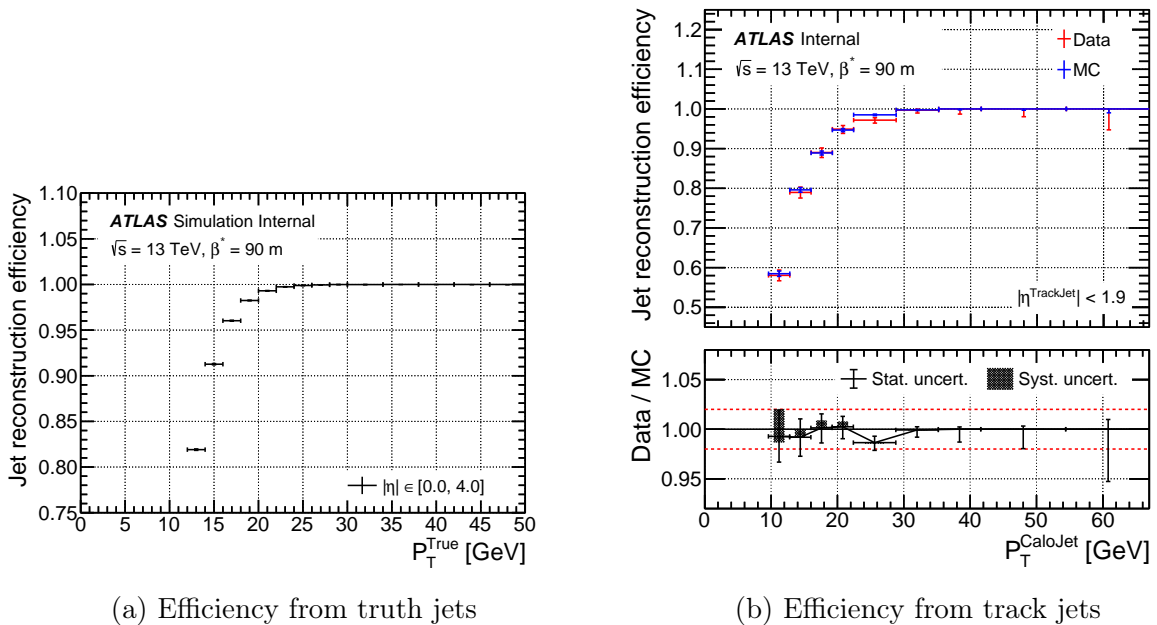


Figure 5.9: Calorimeter jet reconstruction efficiency with respect to truth jets (a) and track jets (b), as a function of the truth jet (a) or the calorimeter jet (b) p_T for anti- k_r LCTopo Jets. The ratio of data to simulation is added for figure (b). The hatched area corresponds to the systematic uncertainty obtained by variations in the *in situ* method. Red lines mark 1 ± 0.02 values.

- The probe track jet must be back-to-back in ϕ with the reference object, with $|\Delta\phi| > 2.8$ rad. Events with more than one track jet within $|\Delta\phi| > 2.8$ rad are excluded.
- The calorimeter reconstruction efficiency with respect to track jets is defined as the fraction of probe jets that are matched to a calorimeter jet with $\Delta R < 0.4$, compared to all probe jets.

Relative reconstruction efficiency is measured for data and compared to a simulation. Initially, it is measured in terms of the track jet p_T , but it can be converted to the calorimeter jet p_T using a known relationship between the average track jets and the transverse momenta of the average calorimeter jets. The results as a function of the calorimeter jet p_T are presented in Fig. 5.9b, with a plateau of 100% above 30 GeV. Data and simulation show good overall agreement with a small discrepancy below 30 GeV. Systematic uncertainties are obtained by varying the event selection requirements for both the data and the MC: the back-to-back angle $|\Delta\phi|$ accepted range, the distance ΔR requirements between the tag/probe jet and the matched calorimeter jet. They are shown in the lower part of Fig. 5.9b.

The total systematic uncertainty for calorimeter jet efficiency reconstruction is set to 2% for jets with $p_T < 30$ GeV. It is negligible for the higher jet p_T , where full efficiency is observed.

5.4 Jets calibration

Jets reconstructed from calorimeter energy deposits are sensitive to the detector effects. The calibration procedure allows correction of the transverse momentum and rapidity. Due to the special detector conditions in the October 2015 diffractive campaign of October 2015, the standard calibration procedure cannot be applied to the data used in this analysis. Instead, a dedicated procedure was prepared, based on the standard approach described in [98, 99, 100].

5.4.1 Motivation

The same algorithm for reconstructing jets (anti- k_t) is used to form jets in data and simulations. The input to the algorithm is typically energy deposits in calorimeters *calorimeter jets*, but Inner Detector track *track jets* or stable particles at the true level in the MC *true jets* can also be used. Due to the following detector effects, the energy of the reconstructed jets differs from that of the corresponding jets at a stable particle level [99]:

- **Calorimeter non-compensation:** the difference between energy scales in hadronic and EM showers.
- **Dead material:** energy loss in inactive areas of calorimeters.
- **Leakage:** jets reaching the outer edge of the detector.
- **Out-of-calorimeter jet:** energy contributions of stable particles not detected by the calorimeter.
- **Small energy deposits:** energy from particles that do not form clusters because of the noise suppression mechanism.
- **Pile-up:** energy deposition in jets due to multiple pp collisions and residual signals from previous bunch crossings.

The reconstruction underestimated the energy and momentum of the jet, which is shown in Fig. 5.10a. The calibration process helps to unify the energy on the reconstruction and true levels. In addition, the rapidity of jets near the calorimeter transition regions is also corrected. Unfortunately, the standard calibration was not applicable due to the special detector conditions in the October 2015 diffractive campaign. It overestimates the transverse momentum of the jets, especially for small p_T , as shown in Fig. 5.10b. For this reason, a dedicated procedure is prepared for the data and MC samples used in this thesis (described in Section 2.6). It focuses on jets reconstructed with the anti- k_t algorithm with $R = 0.4$ on the LCW scale, which is the subject of the analysis.

5.4.2 Calibration strategy

The calibration strategy follows the standard approach. However, the analysed data and MC samples have insufficient statistics, so some steps had to be changed. The dedicated procedure starts with two corrections based on the simulation: η and energy correction,

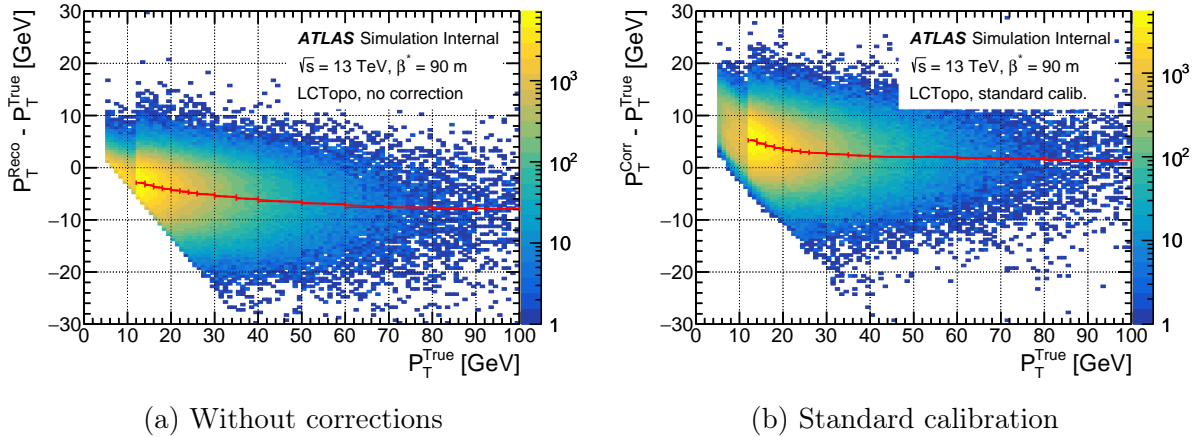


Figure 5.10: Comparison between the transverse momentum of the jets on the real and reconstructed (left) and calibrated (right) levels. Reconstructed jets without calibration have an underestimated energy, while the standard calibration overestimates this energy. The cuts applied to the jets momentum are visible: $p_T^{\text{True}} > 5$ GeV and $p_T^{\text{Reco}} > 7$ GeV. Red lines correspond to the profile of 2D distributions. Based on the Pythia sample

which are derived from the comparison of the true and reconstructed levels. They are followed by two *in situ* corrections applied to the data only, which unify the energy scale in the data and the MC. To ensure that the resolution of jet energy is well simulated, additional studies were carried out. More details on each step can be found in the following sections. The algorithms for data and MC are presented in Fig. 5.11.

After calibration, the jet four-momentum is specified by the following:

$$(p_T, \eta, \phi, E) = (c_{\text{calib}} \cdot p_T^{\text{Reco}}, \eta^{\text{Reco}} + \Delta\eta, \phi^{\text{Reco}}, c_{\text{calib}} \cdot E^{\text{Reco}}), \quad (5.4)$$

where $\Delta\eta$ is pseudorapidity correction based on MC and c_{calib} is a four-momentum scale factor that combines all calibration steps:

$$c_{\text{calib}} = \begin{cases} c_{\text{JES}} \cdot c_{\eta} \cdot c_{\text{abs}} & \text{for data,} \\ c_{\text{JES}} \cdot c_{\text{JER}} & \text{for MC simulation.} \end{cases} \quad (5.5)$$

Here, the c_{JES} is the so-called *Jet Energy Scale* correction and is based on MC (Section 5.4.3), applied to the reconstructed jets for data and MC. The pseudorapidity intercalibration c_{η} and the absolute *in situ* calibration c_{abs} are two *in situ* corrections applied to the data only (Sections 5.4.5 and 5.4.6). The *Jet Energy Resolution* c_{JER} ensures that the resolution in MC is the same as in the data (Section 5.4.4). The corrections are functions of jet momentum and pseudorapidity.

The standard process consists of a few more steps compared to the algorithm presented. The first is the jet origin correction. Topo-clusters used for reconstruction have their directions defined from the centre of the ATLAS detector, but the angular coordinates can be adjusted to originate from the primary vertex. After that, the corrected jet four-momentum is the sum of the updated topo-cluster momenta. A clear improvement can be

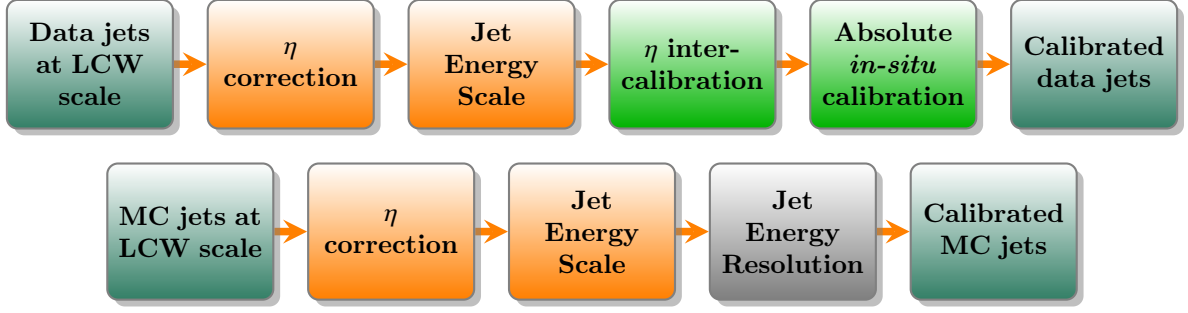


Figure 5.11: Calibration flow for data and MC jets.

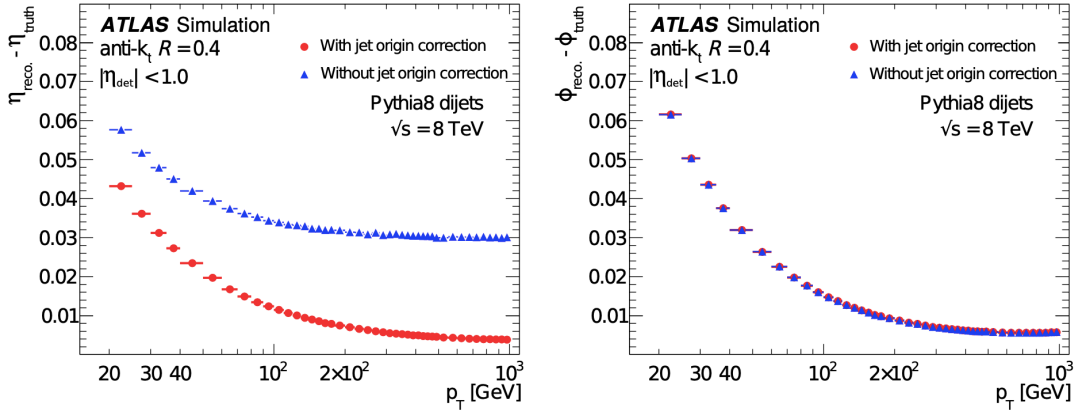


Figure 5.12: Jet angular resolution as a function of transverse momentum, defined by the spread of the difference between the calorimeter jet axis and the axis of the matched true jet. The resolution is shown both with (red circles) and without (blue triangles) the jet origin correction. Plots taken from [99].

seen for the pseudorapidity resolution, which can be seen in Fig. 5.12. But even without correction, the resolution is more than five times smaller compared to the η bins used in this thesis.

The dedicated calibration does not consider the impact of pile-up (not simulated in MC), which is a significant correction in the standard procedure. Nevertheless, the pile-up in the analysed data sample is very low ($\mu = 0.1$) and the analysis applies a veto to the secondary vertices. Therefore, the effect of energy deposition in a single jet from multiple pp collisions is negligible. Furthermore, the bunch separation is four times greater than the nominal (100 ns), and the residual signal from the previous bunch crossing is insignificant.

The standard calibration is designed to be used for nearly all of the data. Therefore, additional corrections are made, known as global sequential calibration. It takes advantage of some properties of the jet, such as the topology of energy deposits or tracking information, and can improve the calibration dependence on so-called *jets flavour*, i.e. the physical process in which the jet was generated. For example, a distinction is made between quark-initiated and gluon-induced jets. When calibrating for a specific process (such as diffractive dijet production), this step is unnecessary.

5.4.3 Monte Carlo based calibration

The first part of the calibration is based on Monte Carlo. For this, it is necessary to match a true jet to the reconstructed jet. This analysis exploits simple angular (η, ϕ) matching, with a distance requirement of $\Delta R < 0.3$ (the distance is defined by Eq. (2.5)). This criterion is smaller than the jet radius parameter $R = 0.4$, but much larger than the jet angular resolution (Fig. 5.12). To ensure a good match, a separation between jets is introduced: reconstructed jets are required to have no other reconstructed jets with $p_T > 7$ GeV within $\Delta R < 0.6$. For true jets the separation is increased to $\Delta R < 1.0$.

The calibration begins with a simple additive correction for η , which improves the jet pseudorapidity around the calorimeter transition regions. The magnitude of this correction is negligible in the middle regions and can reach values as large as 0.05 near the edge of the forward calorimeters. It is symmetrical as a function of η but with the opposite sign. The correction does not depend significantly on the momentum; therefore, it is calculated only in three p_T ranges. Fig. 5.13 shows the comparison between η on the true level and the level of reconstruction of jets with $p_T \in [20, 40]$ GeV. Profiles for different p_T ranges are shown on the right. Pseudorapidity correction is based on the Pythia sample, but the EPOS shows consistent results.

The most significant correction in the calibration procedure is the Jet Energy Scale (JES). It dominates c_{calib} in Eq. (5.5). Jets that pass isolation criteria are divided into bins of η with a width of 0.4 - this width is set to deal with a limited statistic in MC samples. For each bin, the correlation between the reconstructed and true jet transverse momentum is plotted, e.g. Fig. 5.14. Then, the detector response is fitted with a Gaussian in the bins of p_T^{True} . After that, the average response for $p_T^{\text{True}} > 15$ GeV is fitted with the function:

$$\tilde{p}_T^{\text{Reco}} = A \times p_T^{\text{True}} + B + \frac{C}{p_T^{\text{True}}}, \quad (5.6)$$

and linear extrapolation is used for $p_T^{\text{True}} < 15$ GeV. The inverse function provides the

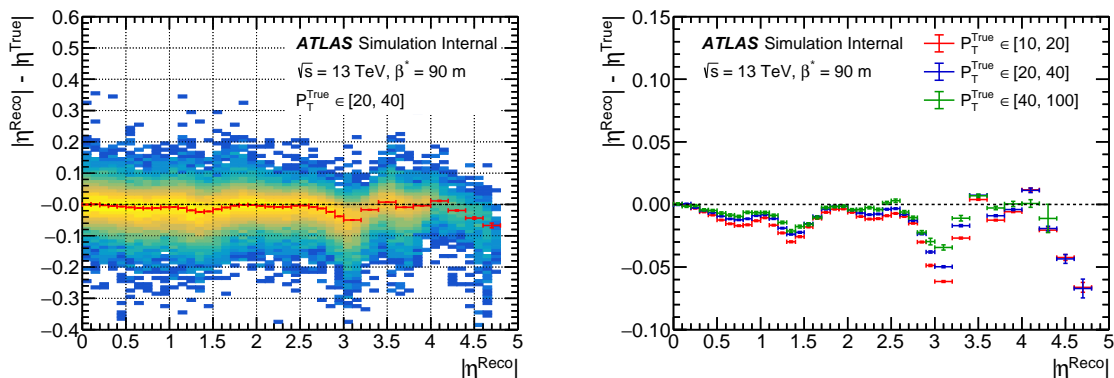


Figure 5.13: Comparison between jet pseudorapidity on true and reconstruction levels in the function of $|\eta^{\text{Reco}}|$. The left plot shows 2D distribution for $p_T \in [20, 40]$ GeV and the right plot shows the average shift for each p_T range. The systematic shifts around transition regions can be observed. Based on the Pythia sample.

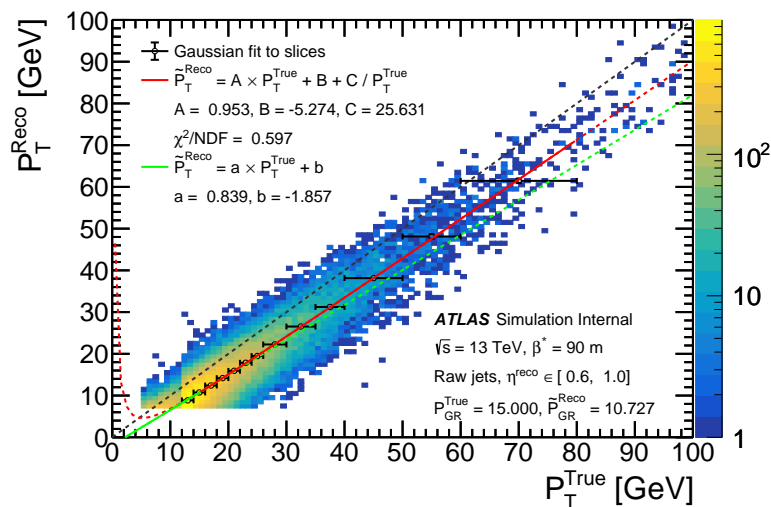


Figure 5.14: The correlation between jet reconstructed and true jet transverse momentum. The black points mark the Gaussian mean in each p_T^{True} range. The red and green lines correspond to the fit and linear extrapolation below 15 GeV. Based on the Pythia sample.

calibration factor c_{JES} . After applying this correction ($p_T^{\text{Reco}} \rightarrow c_{\text{JES}} p_T^{\text{Reco}} = p_T^{\text{Corr}}$) the jet response is close to unity.

Small residuals - the difference between p_T^{True} and p_T^{Corr} - contribute to the JES uncertainties. The uncertainty of the model is defined as the difference between c_{JES} determined from the Pythia and EPOS samples. The type of interaction can also have an impact on the detector response. Therefore, the JES estimation for the SD and ND samples was performed separately, and the difference is considered another source of uncertainty. The last source of systematic uncertainty considered is the response of a single particle interacting in the ATLAS calorimeter. A detailed estimate can be found in [98], and is based on the measurements performed in the 2004 combined test beam, where a full slice of the ATLAS detector was exposed to pion beams. The relative uncertainty for this source was established at 2%, which is the upper limit of this uncertainty presented in the article (for the range p_T considered). Results are presented in Fig. 5.15, together with statistical uncertainty, which is evaluated using the bootstrap method.

5.4.4 Jet Energy Resolution

Determining the calibration factor based on MC obliges measuring the response and resolution of the jet *in situ*. Only this procedure can quantify the agreement between simulation and data and correct any discrepancy. This section focuses on the Jet Energy Resolution (JER) measurement, determined by the dijet asymmetry method. All results presented in this and the following sections were obtained after applying the η and JES corrections.

The resolution of the jet energy or transverse momentum in the simulation can be determined simply as the dispersion of the difference between the corrected momentum p_T^{Corr} and the matched true jet momentum p_T^{True} . The method for determining JER in

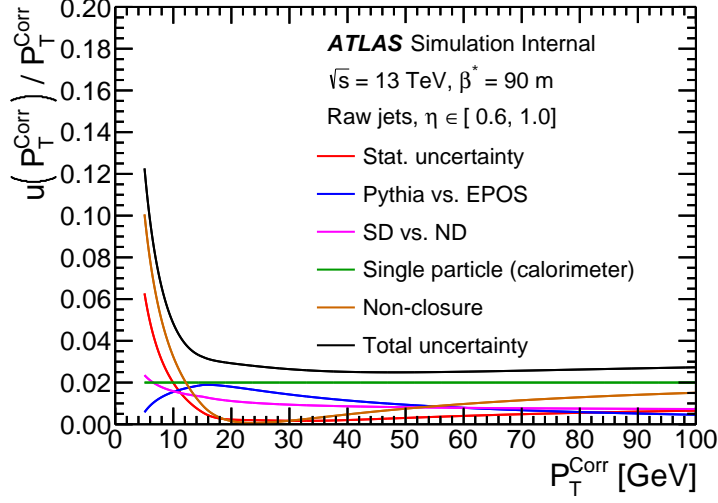


Figure 5.15: JES relative uncertainties in function of the corrected p_T (after JES), for jets with $\eta \in [0.6, 1.0]$. The total uncertainty is the square root of the sum in the quadrature of the individual components.

the data is based on the symmetry between jets in dijet events: both jets should have a back-to-back topology with the same transverse momentum, which is only affected by the p_T resolution. The balance p_T between two η regions, reference and probe, is expressed by the dijet asymmetry:

$$\mathcal{A} = \frac{p_T^{\text{probe}} - p_T^{\text{ref}}}{p_T^{\text{avg}}}, \quad (5.7)$$

where p_T^{ref} is the transverse momentum of a jet in a reference region, p_T^{probe} is the transverse momentum of a jet in a region under investigation, and p_T^{avg} is the arithmetic average of the previous two. The standard deviation of asymmetry distribution $\sigma_{\mathcal{A}}^{\text{probe}}$ in a given $(p_T^{\text{avg}}, \eta^{\text{probe}})$ bin can be expressed as²:

$$\sigma_{\mathcal{A}}^{\text{probe}} = \frac{\sigma_{p_T}^{\text{probe}} \oplus \sigma_{p_T}^{\text{ref}}}{p_T^{\text{avg}}} = \left\langle \frac{\sigma_{p_T}}{p_T} \right\rangle_{\text{probe}} \oplus \left\langle \frac{\sigma_{p_T}}{p_T} \right\rangle_{\text{ref}}, \quad (5.8)$$

where $\sigma_{p_T}^{\text{probe}}$ and $\sigma_{p_T}^{\text{ref}}$ are the standard deviations of p_T^{probe} and p_T^{ref} , respectively.

The relative resolution in the reference region can be derived from events where both jets fall into this region. In this case, the reference region is being probed: the reference and probe jets are randomly selected. Therefore, both terms on the right side of Eq. (5.8) are equal, giving:

$$\left\langle \frac{\sigma_{p_T}}{p_T} \right\rangle_{\text{ref}} = \frac{\sigma_{\mathcal{A}}^{\text{ref}}}{\sqrt{2}} \quad (5.9)$$

²The operator \oplus and \ominus are defined in this section as $a \oplus b = \sqrt{a^2 + b^2}$, $a \ominus b = \sqrt{a^2 - b^2}$.

The reference region is set to be in the centre of the calorimeter $|\eta^{\text{ref}}| < 0.8$. The standard calibration of the probe jets p_{T} with $|\eta^{\text{ref}}| > 0.8$ can be derived from Eq. (5.8):

$$\left\langle \frac{\sigma_{p_{\text{T}}}}{p_{\text{T}}} \right\rangle_{\text{probe}} = \sigma_{\mathcal{A}}^{\text{probe}} \ominus \left\langle \frac{\sigma_{p_{\text{T}}}}{p_{\text{T}}} \right\rangle_{\text{ref}}. \quad (5.10)$$

The balance p_{T} between two jets is not strictly maintained. It is affected on an event-by-event basis by a few effects. Hadronisation, MPI effects, and additional quark/gluon radiations cause particle losses or additions to the jets and break the balance. This effect can be estimated from the standard deviation of the dijet asymmetry $\sigma_{\mathcal{A}}^{\text{True}}$ which is measured for true jets. It increases the standard deviation of the detector smearing $\sigma_{\mathcal{A}}^{\text{det}}$, therefore, the latter can be expressed as follows:

$$\sigma_{\mathcal{A}}^{\text{det}} = \sigma_{\mathcal{A}}^{\text{Reco}} \ominus \sigma_{\mathcal{A}}^{\text{True}}, \quad (5.11)$$

where $\sigma_{\mathcal{A}}^{\text{Reco}}$ is obtained from a Gaussian fit to the core of the asymmetry distribution. Therefore, the final values of JER can be calculated with Eqs. (5.9) and (5.10) after first correcting for the asymmetry spreads $\sigma_{\mathcal{A}}^{\text{ref}}$ and $\sigma_{\mathcal{A}}^{\text{probe}}$ according to Eq. (5.11).

Events with dijet topology are selected with the following requirements:

- the azimuthal angle between the reference and probe jets has to be $\Delta\phi^{12} > 2.5$;
- the third jet (if present) cannot have transverse momentum $p_{\text{T}}^{\text{J3}} > 0.4 p_{\text{T}}^{\text{avg}}$;
- the transverse momenta of the two leading jets are greater than 20 GeV.

The first two requirements are fulfilled by most of the events. However, despite this, the statistic in the data is quite poor for systematic analysis: most of the systematic uncertainties have associated statistical uncertainty (i.e. an "uncertainty on the uncertainty") greater than themselves. Thus, only statistical uncertainties are evaluated. They are significant, much larger than the systematic uncertainties evaluated in the standard calibration of Run 1 and 2 [98, 99].

The results are shown in Fig. 5.16. Data and MC are compatible: the differences between data and truth level are less than 25% for all points. This value is used as the nominal uncertainty for JER; the impact on analysis can be determined by additional smearing of the jet p_{T} in MC by 25% of the nominal $\sigma_{p_{\text{T}}}$.

5.4.5 η -intercalibration

The relative *in situ* calibration is expressed in terms of the pseudorapidity; therefore, it is called η -intercalibration. The aim is to unify the energy scale in different parts of the calorimeter. Together with the absolute energy scale calibration (Section 5.4.6), both *in situ* corrections are applied to data only. It also exploits the dijets asymmetry, similar to JER, but it measures the mean asymmetry instead of the spread.

The average calorimeter response relative to the reference region $1/c_{\eta}$ is defined in terms of the mean asymmetry distribution for a given bin of $p_{\text{T}}^{\text{avg}}$ and η^{probe} :

$$\frac{1}{c_{\eta}} = \frac{2 + \langle \mathcal{A} \rangle}{2 - \langle \mathcal{A} \rangle} \approx \frac{\langle p_{\text{T}}^{\text{probe}} \rangle}{\langle p_{\text{T}}^{\text{ref}} \rangle}. \quad (5.12)$$

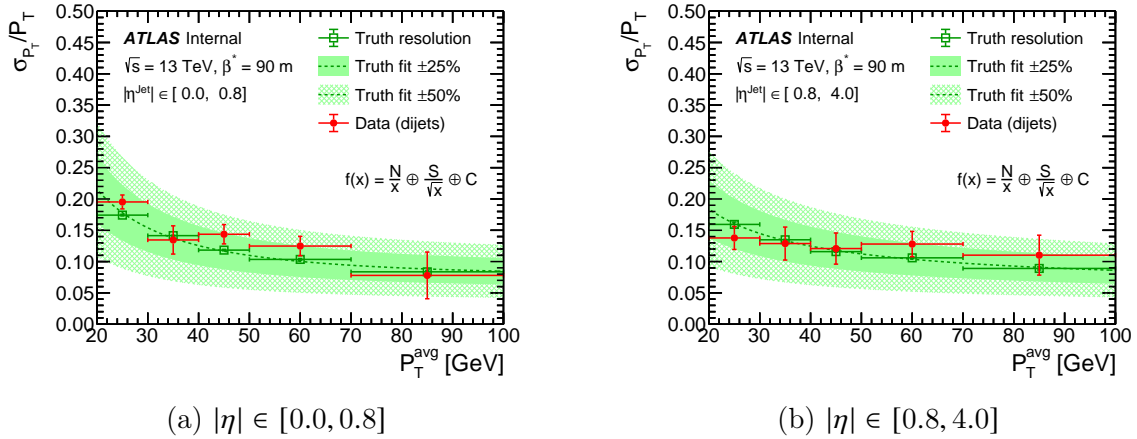


Figure 5.16: Jet energy resolution for pseudorapidity inside and outside of central region $|\eta| < 0.8$. The bands show the fits to the true resolution, with width $\pm 25\%$ and $\pm 50\%$ accordingly.

The approximation can be obtained by inserting the expectation value of a Taylor expansion of Eq. (5.7), giving $\langle \mathcal{A} \rangle \approx 2 \left(\langle p_T^{\text{probe}} \rangle - \langle p_T^{\text{ref}} \rangle \right) / \left(\langle p_T^{\text{probe}} \rangle + \langle p_T^{\text{ref}} \rangle \right)$.

The calculated response for the data is normalised to the response in MC. Limited statistics impose larger η bins compared to the JES analysis, with $\Delta\eta = 0.8$. No statistically significant differences are observed for positive and negative η , justifying parameterisation over $|\eta|$, which increases the statistical power. For the same reason, the MC analysis is based on the sum of Pythia and EPOS samples, but the difference is used to estimate the systematic uncertainty. Dijets selection is the same as for JER analysis. The responses for the data and the MC are presented in Fig. 5.17.

The ratio between MC and the data for $p_T \in [30, 40]$ is presented in Fig. 5.18. Detailed uncertainties are added to the right. The impact of the model is estimated as the difference between Pythia and EPOS. The uncertainty based on JER is determined by the additional smearing of the jet p_T in the MC by 25% of the nominal σ_{p_T} . The influence of the dijet selection criteria is assessed by shifting the parameters by ± 0.3 rad for $\Delta\phi^{12}$ and ± 0.1 for p_T^{J3} . Statistical uncertainty is estimated using the bootstrap method. The uncertainty for the reference region $|\eta| < 0.8$ is set to 0 by the definition.

The analysis was limited to $p_T > 20$ GeV, which is sufficient for typical analysis. But the results presented in Fig. 5.17 show that the corrections do not depend significantly on p_T , especially in the central part of the calorimeter ($|\eta| < 3.0$). Therefore, it can be assumed that the corrections can be applied for $p_T < 20$ GeV, with the same values as for $p_T \in [20, 30]$ GeV. The uncertainties can be conservatively doubled in this range.

5.4.6 Absolute Energy Scale

The final jet calibration corrects the absolute energy scale of the jets in the data to achieve a data-to-MC agreement. This *in situ* analysis uses a well-calibrated object as a reference and compares the data with the simulation. The standard calibration uses the transverse momentum balance between a jet and a photon or a bozon Z that decays leptonically

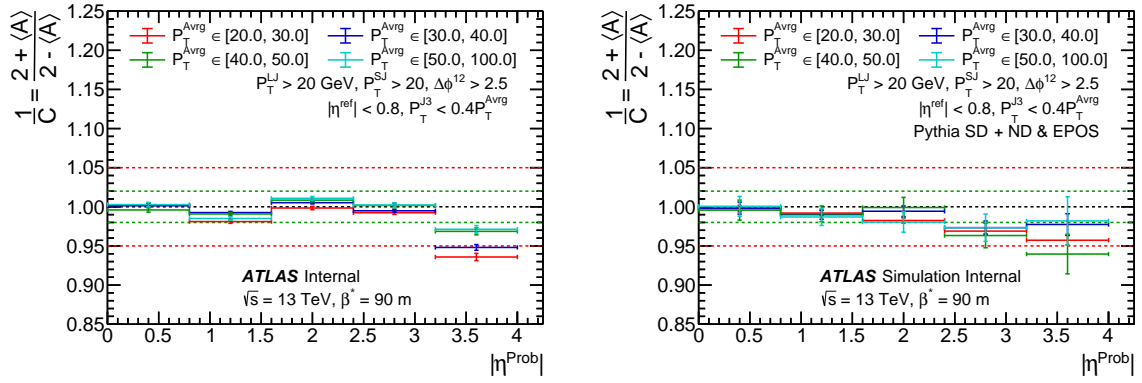


Figure 5.17: The average calorimeter response relative to the reference region $|\eta| < 0.8$ for data (left) and simulation (right). Only statistical errors are presented. The dashed lines indicate 1 ± 0.02 and 1 ± 0.05 .

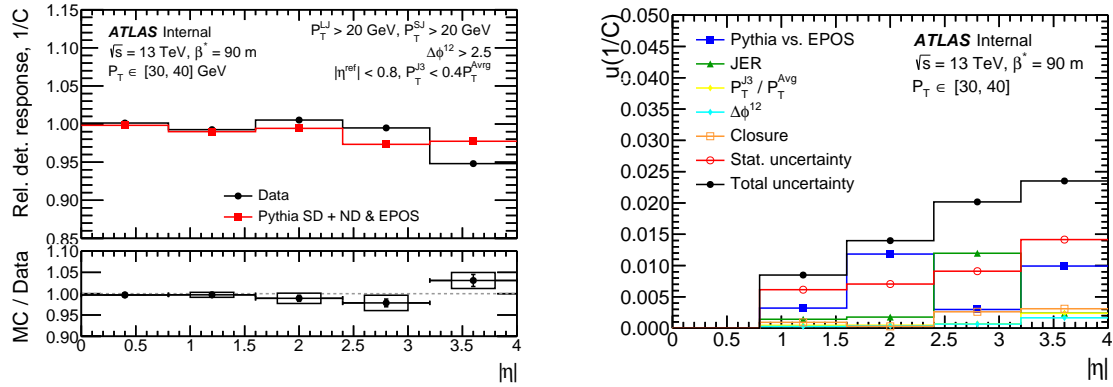


Figure 5.18: The average calorimeter response relative to the reference region $|\eta| < 0.8$ normalised to MC, for $p_T \in [30, 40]$ GeV. Detailed uncertainties are shown on the right.

[99], but the amount of such events in the October 2015 diffractive data is not sufficient. Instead, this analysis exploits the momentum carried by Inner Detector tracks associated with a jet as the reference object. The tracking system provides a measurement that is independent of the calorimeter. Since the tracks in the data and MC are well-modelled and calibrated, they can be used to determine the calorimeter energy scale [98].

Tracks are associated with a jet in (η, ϕ) space, the distance has to be less than the jet reconstruction radius: $\Delta R < 0.4$. Only well-defined tracks are selected (in terms of Pixel/SCT hits and impact parameters - the same as in Section 7.5). In addition, only tracks with $p_T^{\text{track}} > 1$ GeV are selected - this requirement allows tracks from fragmentation to be selected rather than those from soft and diffuse interactions. The tracking system imposes the limit on jet pseudorapidity: $|\eta| < 2.1$. If two jets overlap ($\Delta R < 0.8$) then the softer jet is not considered in the analysis. Each jet needs to be associated with at least one track.

Jets and tracks can be compared by the charged-to-total momentum ratio:

$$r_{\text{ID}} = \frac{\sum p_{\text{T}}^{\text{track}}}{p_{\text{T}}^{\text{jet}}}. \quad (5.13)$$

Then, the calibration constant c_{abs} for given p_{T} bin is defined as the double ratio of the mean r_{ID} observed for the distributions in the data and simulation:

$$\frac{1}{c_{\text{abs}}} = \frac{\langle r_{\text{ID}}^{\text{Data}} \rangle}{\langle r_{\text{ID}}^{\text{MC}} \rangle} \quad (5.14)$$

Typical distributions of r_{ID} are shown for data and Pythia sample in Fig. 5.19a. The agreement between simulation and data is good, although the data distribution is somewhat wider than the MC. Fig. 5.19b presents the values of double ratio for different p_{T} bins for two MC models. The final values of $1/c_{\text{abs}}$ are calculated as the arithmetic mean of those two and are summarised in Fig. 5.19c.

The following sources of systematic uncertainty are considered:

- MC model - half of the difference between the results obtained with Pythia and EPOS samples;
- tracking efficiency - estimated by removing part of the tracks in MC according to the uncertainty of the tracking reconstruction efficiency;
- the sensitivity of the selection - evaluated by increasing the requirement of associated track multiplicity to 2;
- JER based uncertainty - determined by the additional smearing of the jet p_{T} in the MC by 25% of the nominal $\sigma_{p_{\text{T}}}$;
- residuals - the difference between $1/c_{\text{abs}}$ and unity after applying the correction.

All of them are collected in Fig. 5.19d. The most significant source of uncertainty comes from the tracking efficiency, which dominates the lowest p_{T} bins. For a higher p_{T} , the impact of the JER uncertainty is visible.

5.4.7 JES and *in situ* combined uncertainty

Jet calibration uncertainties consist of the JES uncertainties combined with the *in situ* results. They are collected in Fig. 5.20 for a few different pseudorapidity ranges as a function of jet p_{T} . The most significant part comes from the absolute scale uncertainty (cyan). The calorimeter uncertainty from single particle propagation (green) provides the largest contribution from JES uncertainties. The η -intercalibration (grey) is crucial for the forward region.

The total fractional uncertainty, calculated as the quadrature sum of individual contributions, is shown as the solid light-shaded area. Typical values are between 3% and 4%, except for the forward calorimeter where inter-calibration dominates. They are higher, but comparable to the results of standard calibration (1.5-3%, [100]). The uncertainties for $p_{\text{T}} < 20$ GeV are conservatively estimated.

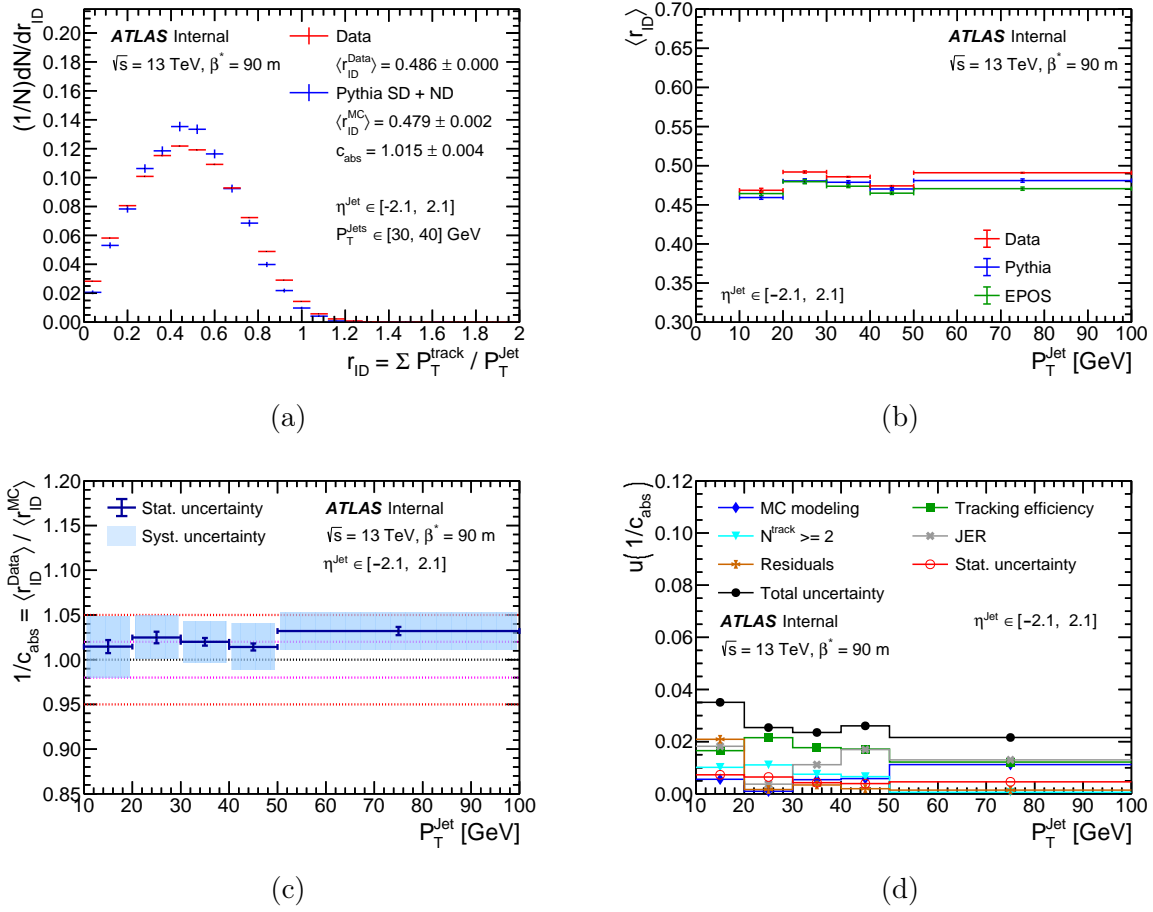


Figure 5.19: The results for absolute energy scale correction: the distribution of the charged-to-total momentum ratio r_{ID} for $p_{\text{T}} \in [30, 40] \text{ GeV}$ (a); the average charged-to-total momentum ratio $\langle r_{\text{ID}} \rangle$ for data and two MC models as a function of jet p_{T} (b); the calibration constant $1/c_{\text{abs}}$ - the ratio of $\langle r_{\text{ID}} \rangle$ for data and simulation together with statistical and total systematic uncertainties (c); the relative uncertainties on the $1/c_{\text{abs}}$ from different sources.

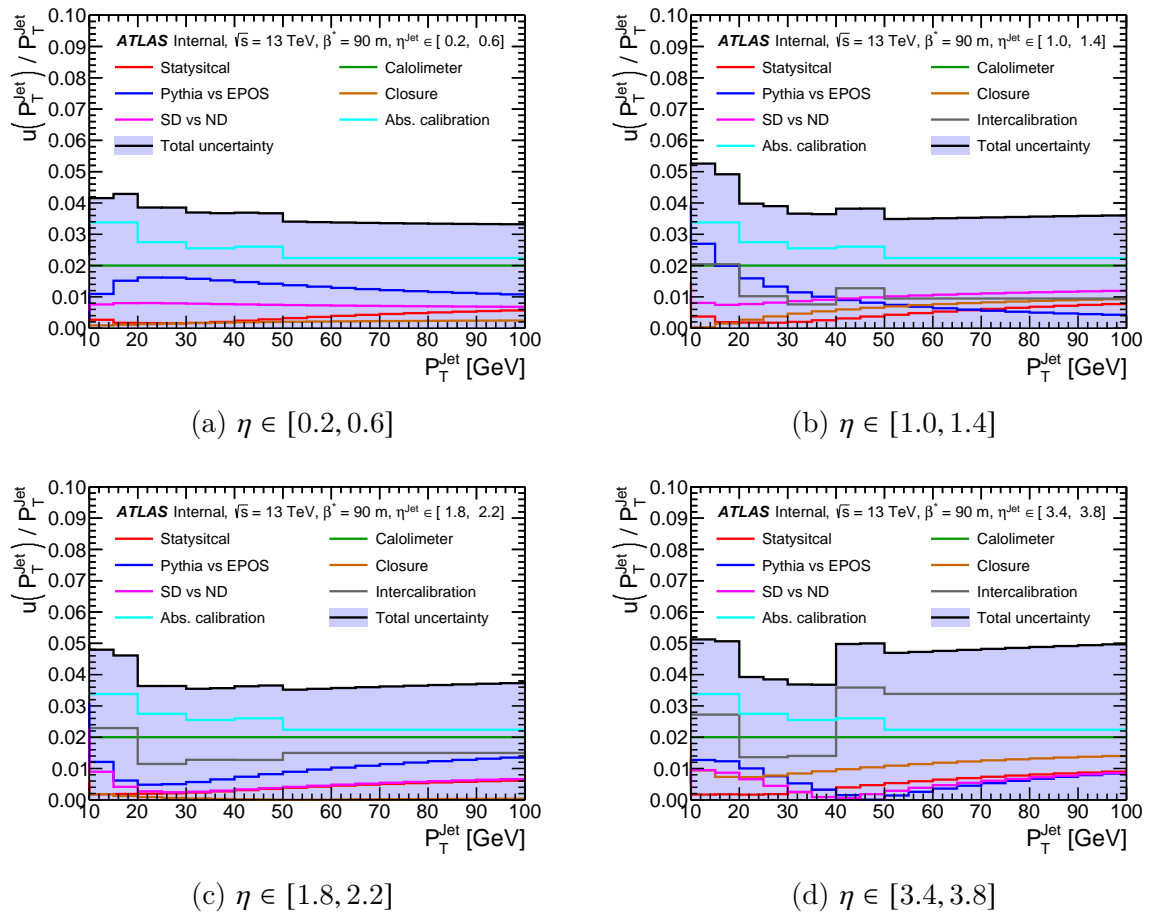


Figure 5.20: JES and *in situ* combined uncertainty in terms of p_T for different η bins. The total fractional uncertainty, calculated as the quadrature sum of individual contributions, is shown as the solid light-shaded area.

Chapter 6

Background contribution

The data sample is contaminated with events that mimic the topology of single or central diffractive dijet production. The background contribution must be modelled and subtracted from the data distribution prior to unfolding. This section describes two sources of background. An accidental background refers to the overlay of two or more unrelated events in the central ATLAS detector and in ALFA. These events originate from different collisions (pile-up). The second type of background comes from single inelastic processes, such as the production of ND and DD dijets, because of the formation of protons in hadronic showers. This type also includes the background of CD for SD analysis when only one of the intact protons is detected in ALFA.

6.1 Correlation between ξ^P and $\tilde{\xi}_{\text{CAL}}^X$

The relation between ξ^P and $\tilde{\xi}_{\text{CAL}}^X$ is one of the basic tools in SD analyses. The value of $\tilde{\xi}_{\text{CAL}}^X$ is calculated according to Eq. (1.21), with the sum over calorimeter clusters. According to the momentum conservation, both quantities should be equal, but it is biased due to detector effects, such as:

- energy scale calibration;
- calorimeter inefficiency for particle detection;
- particles with $|\eta| > 5.0$ that escape the calorimeter;
- finite resolutions of the ALFA detector and of the ATLAS calorimeter.

For these reasons, $\tilde{\xi}_{\text{CAL}}^X$ is generally lower than ξ^P . However, it can sometimes be slightly larger as a result of the finite detector resolution. The observed relationship is given by:

$$0.85\xi^P + 0.02 > \tilde{\xi}_{\text{CAL}}^X \quad (6.1)$$

This relation is based on the distribution shown in Fig. 6.1a. Corresponding plots for MC are presented in Fig. 6.15. Events that fulfil Eq. (6.1) lie below the solid red line. Above this line are events that occur from accidental coincidences, centred around the vertical line $\xi^P = 0$, dominated by elastically scattered protons or beam halo. The slope of 0.85

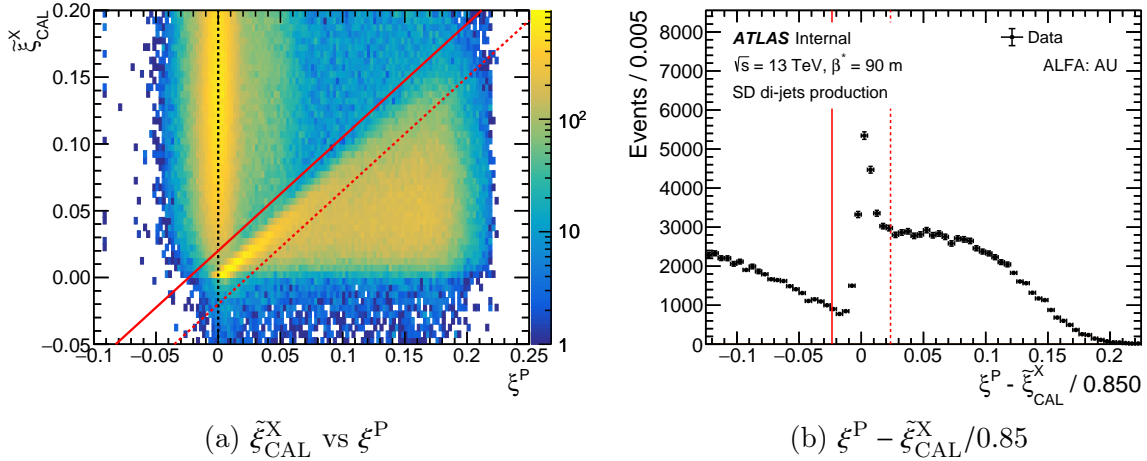


Figure 6.1: (a) Correlation between ξ^{P} and $\tilde{\xi}_{\text{CAL}}^{\text{X}}$ for data sample without cuts. The solid red line indicates the signal selection. The dashed line corresponds to the separation between correlated and uncorrelated regions. (b) Shown is the profile parallel to the red lines of (a).

represents the underestimated energy deposited in the calorimeter. The offset of 0.02 was added to preserve the full efficiency of the SD signal.

Signal events seem to group themselves into two regions: correlated and uncorrelated. The dashed line $0.85\xi^{\text{P}} - 0.02 = \tilde{\xi}_{\text{CAL}}^{\text{X}}$ is set *ad hoc* to separate both regions. The effect is more obvious on the 1D profile parallel to these lines in Fig. 6.1b. The dashed line separates the peak around 0 and the plateau for higher ξ differences. The source of this effect is not fully understood. Detector effects may affect the distribution, e.g. more particles escape detector acceptance at higher ξ . However, this may also be an indication of a subprocess involved in SD dijet production. This requires a better simulation of the SD and ND processes.

The typical selection for CD analysis (especially exclusive processes) is carried out in terms of ξ^{X} and ξ^{PP} , according to Eq. (1.27). The relation between these two quantities is presented in Fig. 6.2. With a large contribution of accidental events and the limited detector resolution, separation is difficult to perform. Instead, selection can be based on the relationship between ξ^{P} and $\tilde{\xi}_{\text{CAL}}^{\text{X}}$, similarly to SD analysis, simultaneously on ATLAS sides A and C:

$$0.85\xi^{\text{PA}} + 0.02 > \tilde{\xi}_{\text{CAL}}^{\text{XA}} \quad \wedge \quad 0.85\xi^{\text{PC}} + 0.02 > \tilde{\xi}_{\text{CAL}}^{\text{XC}} \quad (6.2)$$

The MC plots confirm these relations (Section 6.3.2). Unfortunately, the CD topology is heavily contaminated by elastically scattered protons. The plots in Fig. 6.3 show the correlation of ξ^{PA} and ξ^{PC} before and after the above selection. After this selection, a substantial number of accidental events still remain, with both $\xi^{\text{P}} \approx 0$. For this reason, the selection for inclusive CD analysis is extended to anti-elastic cuts:

$$\xi^{\text{PA}} > 0.02 \quad \vee \quad \xi^{\text{PC}} > 0.02. \quad (6.3)$$

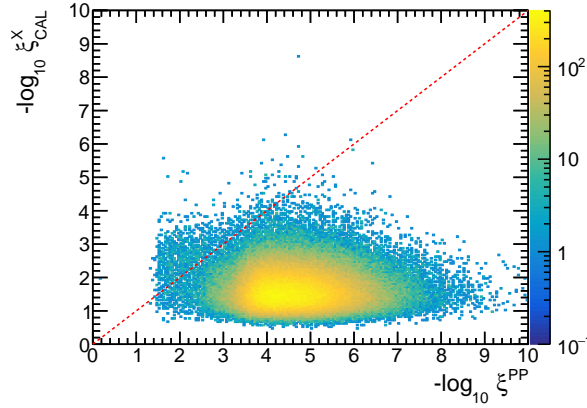
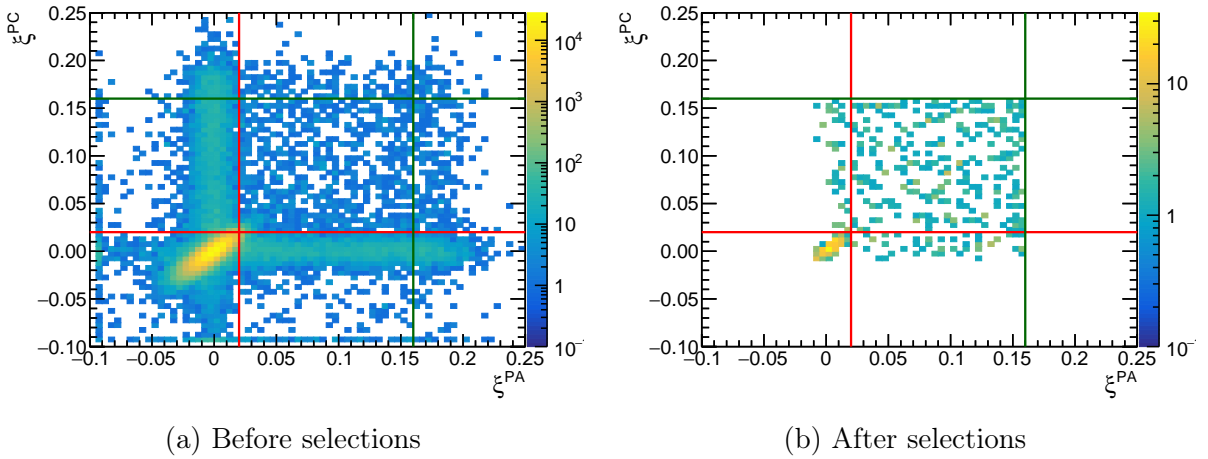


Figure 6.2: The relation between ξ^X and ξ^{PP} . The red line marks the line $\xi^X = \xi^{PP}$.



(a) Before selections

(b) After selections

Figure 6.3: Correlation between ξ^{PA} and ξ^{PC} for data before any selection (left) and after applying ξ^P vs. ξ_{CAL}^X cuts simultaneously on both ATLAS sides (right). The right plot is also limited by the fiducial region: $\xi^P < 0.16$.

6.2 Accidental background

6.2.1 Accidentals with one proton topology

The topology of SD dijet production consists of one proton detected by the ALFA detector and at least two dijets detected by the ATLAS central detector system. This topology can be easily mimicked by the coincidence of two unrelated processes with high cross sections. Possible sources of background protons include beam-halo events, elastic scattering in which a proton is missing, and non-jet SD events. Dijets can be produced in any inelastic collision, but the largest contribution of jets in ATLAS is due to ND. Fig. 6.4 presents how the overlay mimics the signal. It meets all the base selection criteria from Section 7.3.

The contribution of such background is estimated with a fully data-driven method. The accidental SD sample was prepared as a mixture of the following templates:

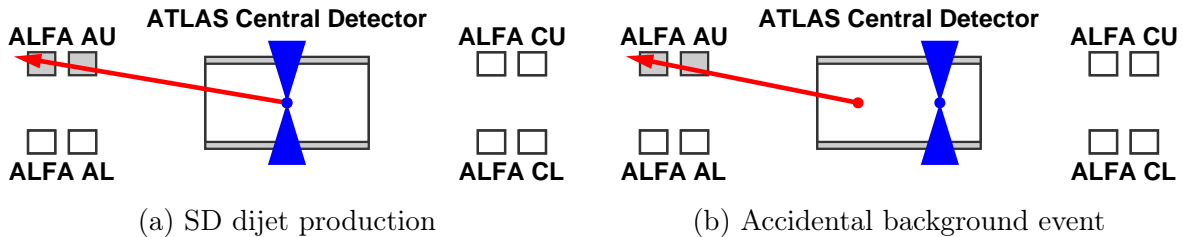


Figure 6.4: SD dijets production and accidental background events that mimic the topology of the signal event. Solid red lines indicate intact protons and blue cones indicate a central state with two jets.

1. Exactly one reconstructed proton in the ALFA detector and no jets in the ATLAS central detector. The veto on the primary vertex is also required. The template is based on the trigger L1_ALFA_ANY.
2. Veto on the signal in the ALFA detector and two jets and a primary vertex in the central detector. The jets need to fulfil the same criteria as for the signal mentioned in Section 7.3. The template is based on the trigger L1_MBTS_1.

The first template provides the proton characteristics, and the second carries information about the central state (Inner Detector, Calorimeters, and MBTS). An important advantage of this method is model independence, especially when diffractive models provide poor normalisation and shape of physics distributions. It is exploited even when the statistic is low, due to the high prescaling of the MBTS trigger in the analysed data.

The region enriched with accidentals is selected with the cut $-0.015 < \xi^P < 0.010$ because this is a region dominated by elastically scattered protons. The effect is strengthened with x vs θ_X cut - within an ellipse corresponding to elastic events - see Section 4.4. The data are fitted in terms of $\tilde{\xi}_{\text{ID}}^X$, defined as the sum over ID tracks, in the range $[0.01, 0.06]$. Due to narrower η coverage of the ID, $\tilde{\xi}_{\text{ID}}^X$ is biased; this region corresponds to $\tilde{\xi}_{\text{CAL}}^X > 0.05$. However, the fit is more stable in terms of $\tilde{\xi}_{\text{ID}}^X$ compared to $\tilde{\xi}_{\text{CAL}}^X$. Due to the correlation between ξ^P and $\tilde{\xi}_{\text{CAL}}^X$ for diffractive events, no signal is expected in this region. Normalisation was obtained for each ALFA armlet separately. Fig. 6.5 shows the $\tilde{\xi}_{\text{ID}}^X$ distribution with the accidental contribution fitted for the ALFA armlet AU.

The distributions of ξ^P and $\tilde{\xi}_{\text{CAL}}^X$ are used as a cross-check for the normalisation procedure Fig. 6.6. Accidentals' distributions are scaled by the number obtained from the ID fit. In the region where signal events are not expected, $\tilde{\xi}_{\text{ID}}^X > 0.01$, the template describes well ξ^P below -0.02 . A similar situation is observed for $\tilde{\xi}_{\text{CAL}}^X$ above 0.05 , validating the method used. The differences are taken into account when estimating systematic uncertainty. The correlation between ξ^P and $\tilde{\xi}_{\text{CAL}}^X$ for mixed accidental templates is shown in Fig. 6.7a. Accidentals concentrate along the line $\xi^P = 0$ and have high values of $\tilde{\xi}_{\text{CAL}}^X$. Most events lie above the red lines that correspond to the selection cuts (described in Section 6.1), therefore, they do not overlap with the SD signal region. It is more visible in the plot showing the difference in Fig. 6.7b.

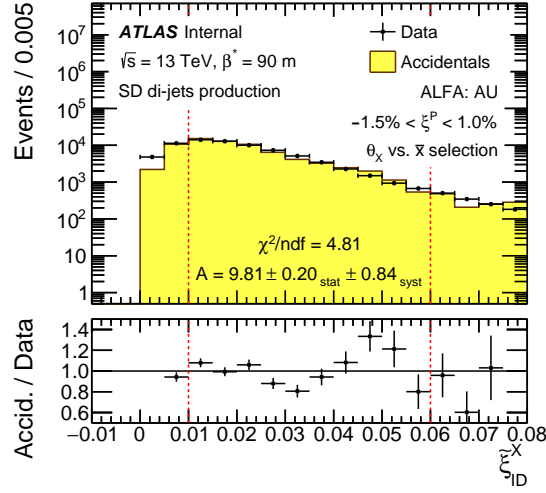


Figure 6.5: Raw distribution of $\tilde{\xi}_{ID}^X$ for configuration AU in accidentals enriched region. The red lines indicate the fit range, and the result of accidentals to data normalisation is also shown. The ratio of accidentals to data is drawn in the bottom pad.

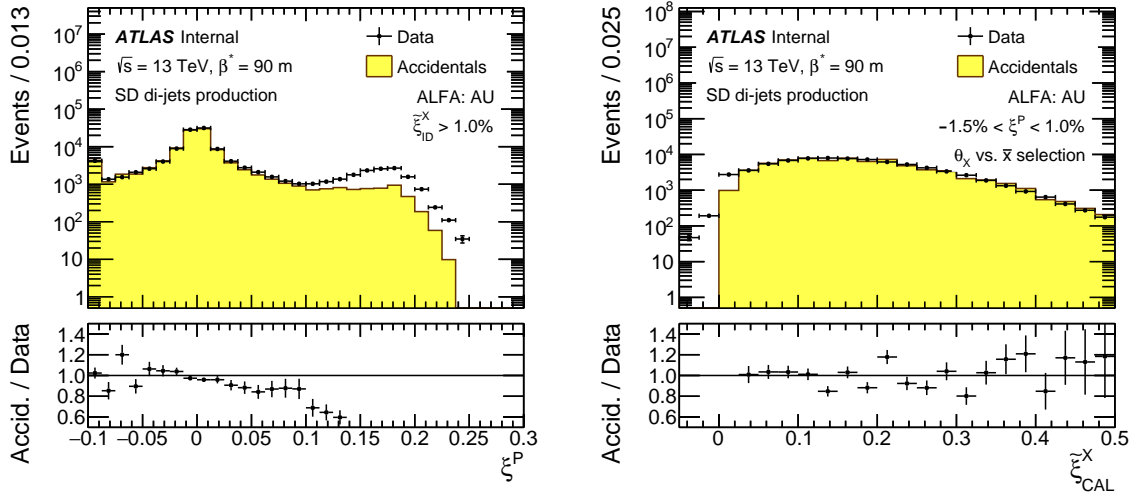


Figure 6.6: Raw distribution of ξ^P and $\tilde{\xi}_{CAL}^X$ for configuration AU in accidentals enriched region, used as cross-checking for normalisation.

6.2.2 Accidentals with two protons topology

In CD dijet production, two protons make the accidentals analysis more complicated. Four types of coincidence mimic the CD topology of two protons and a dijet:

- **PP + J** - two protons + dijet production;
- **P + J + P** - one proton on side A + dijet production + one proton on side C;
- **PJ + P** - dijet production with a proton on side A + one proton on side C;
- **P + PJ** - one proton on side A + dijet production with a proton on side C.

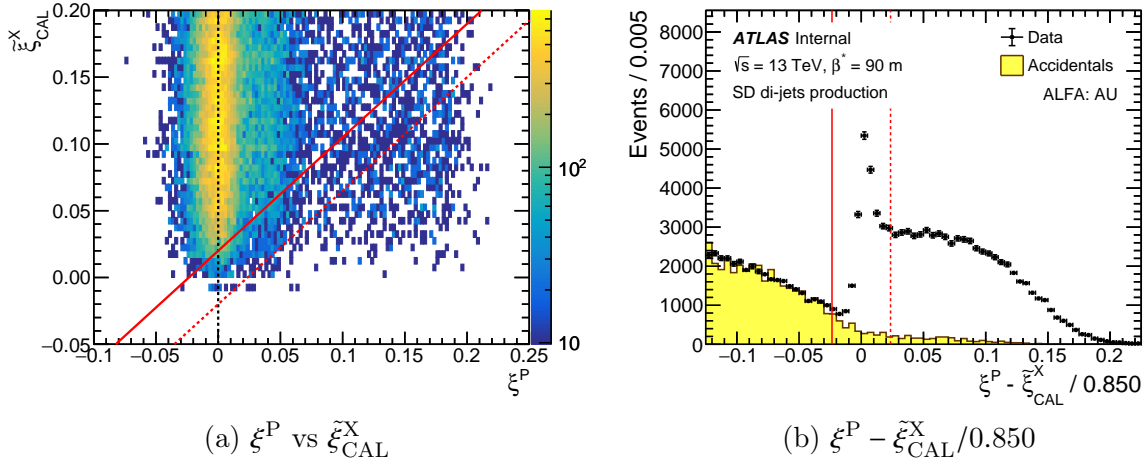


Figure 6.7: Correlation between ξ^{P} and $\tilde{\xi}_{\text{CAL}}^{\text{X}}$ for mixed SD accidental templates. Red lines indicate signal selection described in Section 6.1. The right plot shows the profile parallel to that lines.

Contributions from other possibilities are negligible. CD signal and four types of accidental background with protons in armlets AU and CL are presented in Fig. 6.8. In the **PP** + **J** scenario both protons come from the same interaction (such as elastic scattering) and for **P** + **J** + **P** they have different sources. In both cases, the dijets are produced in separate processes, usually ND. The remaining types are the result of a coincidence between SD dijet productions and protons from other interactions. The dijet may share a source with the proton on side A (**PJ** + **P**) or side C (**P** + **PJ**).

Four samples are required for CD accidentals analysis:

- I. Sample generated with templates similar to those for SD analysis, but the first template uses events with two reconstructed protons instead of one. This sample contains accidental events **PP** + **J** and **P** + **J** + **P**.
- II. Sample generated from templates used for the SD accidentals sample, but the first template is used twice instead of once. Events with a single proton on side A are mixed with events with a single proton on side C. This sample contains only **P** + **J** + **P** accidental events.
- III. The first template for SD-based backgrounds is generated from a subsample of data that passed selections for the SD signal: exactly one proton on side A, at least two jets, and the primary vertex. That template is mixed with protons on side C from the first template in SD accidentals analysis. This sample provides events of the types **PJ** + **P** and **P** + **J** + **P**.
- IV. The sample with **P** + **PJ** events is produced with the same scheme as the previous one, but SD data is used as the source of events with a proton on the C side. It is mixed with protons on side A from the L1_ALFA_ANY sample. Such a sample contains a significant amount of **P** + **J** + **P** events.

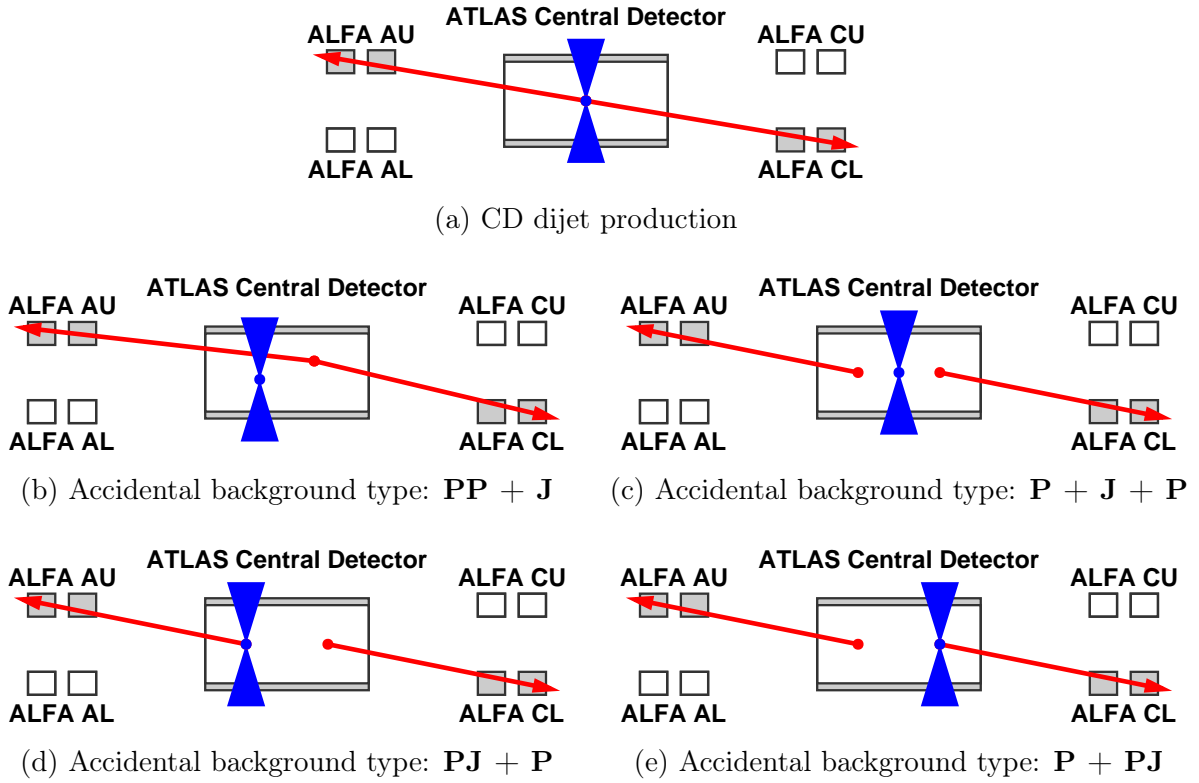


Figure 6.8: There are four types of accidental background events for CD analysis with different connections between protons and jets. Solid red lines indicate intact protons and blue cones indicate a central state with two jets.

The first two accidental background types are dominant (especially for elastic configurations). They are analysed together with CD accidental sample I. There is no simple way to distinguish the $\mathbf{PP} + \mathbf{J}$ and $\mathbf{P} + \mathbf{J} + \mathbf{P}$ events. Nevertheless, data-based templates provide correct normalisation between both types of accidental sources.

Normalisation is performed as a function of $\log_{10} \xi_{\text{ID}}^{\text{X}}$ for each ALFA configuration separately. The accidentals are enriched with elastic events by the cut $-0.015 < \xi^{\text{P}} < 0.010$ that both protons have to pass. This ensures that $\xi^{\text{PP}} < 10^{-4}$. Additional elastic selection on x vs. θ_X is also applied. Then the fit can be made in the range $\xi_{\text{ID}}^{\text{X}} \in [10^{-4}, 10^{-3}]$ where the signal or the SD-based background is not expected. The statistic is small for the anti-elastic configuration shown in 6.9a because it originates mainly from $\mathbf{P} + \mathbf{J} + \mathbf{P}$ events. About 100 times more events are observed for the elastic configuration - 6.9b. The cross-check is performed for ξ^{PP} and $\xi_{\text{CAL}}^{\text{X}}$ distributions. The differences are taken into account for systematic uncertainties, similar to SD background analysis.

Samples III and IV, prepared for SD-based backgrounds, contain a significant amount of $\mathbf{P} + \mathbf{J} + \mathbf{P}$ accidentals that must be subtracted prior to normalisation. For this purpose, sample II is normalised to SD-based accidental samples in terms of $\xi_{\text{ID}}^{\text{X}}$ in the same way as for SD accidental analysis. Finally, the difference between normalised samples III and II (or IV and II) is derived from the $\mathbf{PJ} + \mathbf{P}$ (or $\mathbf{P} + \mathbf{PJ}$) distributions. They are denoted as III' and IV', respectively.

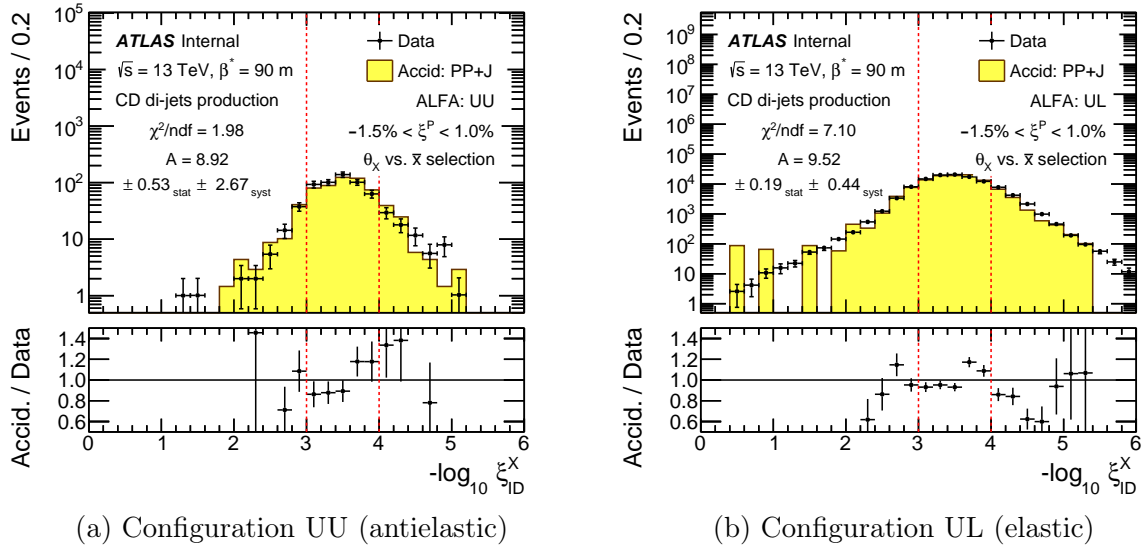


Figure 6.9: Raw distribution of $\log_{10} \xi_{\text{ID}}^{\text{X}}$ for configurations UU (a) and UL (b) in accidentals' enriched region. The red lines indicate the fit range, and the results of accidentals to data normalisation are also displayed. Ratios of accidentals to data are drawn in the bottom pads.

The correlation between ξ^{P} and $\tilde{\xi}_{\text{CAL}}^{\text{X}}$ can be used to select regions for normalisation. It is fulfilled on side A for the $\mathbf{PJ} + \mathbf{P}$ background, on side C for the $\mathbf{P} + \mathbf{PJ}$, and on both sides for the CD signal - Fig. 6.10. A combination of two conditions: $0.85\xi^{\text{PA}} + 0.02 > \tilde{\xi}_{\text{CAL}}^{\text{XA}}$ and $0.85\xi^{\text{PC}} + 0.02 < \tilde{\xi}_{\text{CAL}}^{\text{XC}}$, provides a region with only the $\mathbf{PJ} + \mathbf{P}$ events, where sample III' can be normalised to the signal sample. The slope 0.85 and offset 0.02 come from detector resolution and are taken from the SD analysis. Reverse conditions are used for sample IV' and $\mathbf{P} + \mathbf{PJ}$ background.

The samples III' and IV' are normalised to the difference between data and sample I. This excludes the $\mathbf{PP} + \mathbf{J}$ and $\mathbf{P} + \mathbf{J} + \mathbf{P}$ events from the analysis. The fit is performed for both samples separately: as a function of ξ^{PA} for $\mathbf{PJ} + \mathbf{P}$ or ξ^{PC} for $\mathbf{P} + \mathbf{PJ}$ in the common range of [0.02, 0.16]. Systematic effects are estimated by varying the limits by one bin width on each side. The results of the normalisation of sample IV' for UU and UL configurations are shown in Fig. 6.11. The quality of the fit is poor, but it shows that the SD-based accidentals have a small contribution to the data sample.

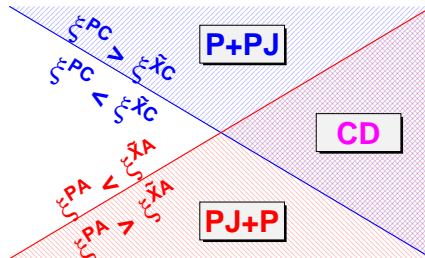
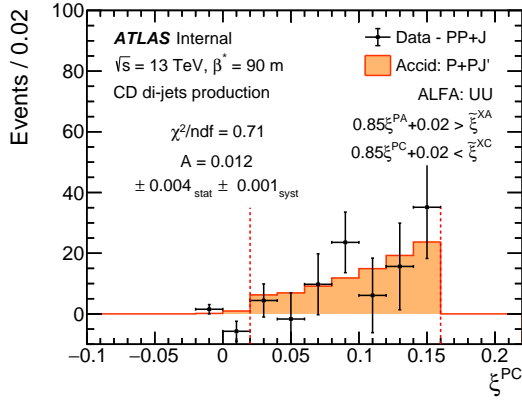
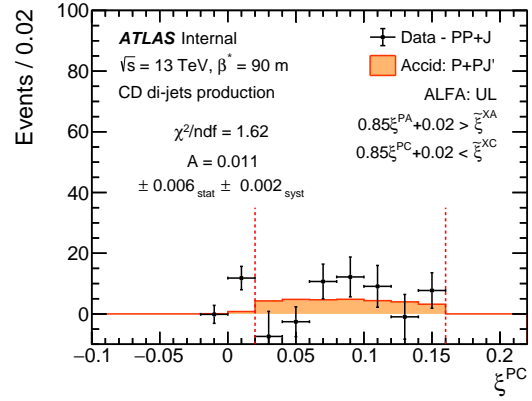


Figure 6.10: The red and blue regions mark events that pass the correlation between ξ^{P} and $\tilde{\xi}_{\text{CAL}}^{\text{X}}$ on side A and C, respectively. CD signal events fulfil both conditions.



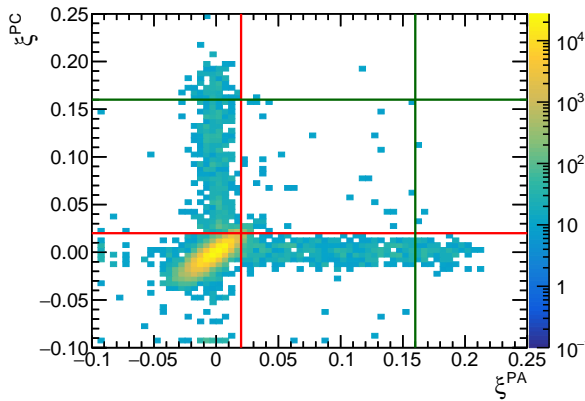
(a) Configuration UU (antielastic)



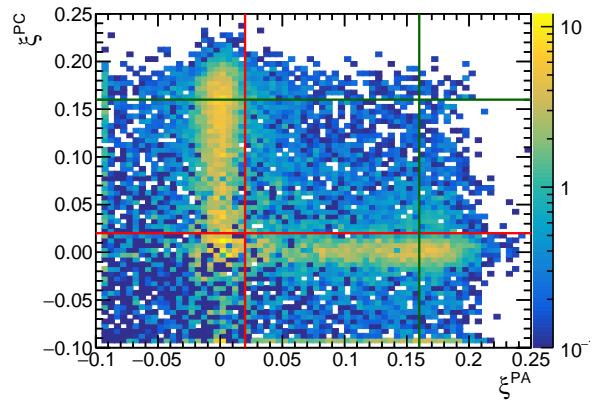
(b) Configuration UL (elastic)

Figure 6.11: Raw distribution of ξ^{PC} for configurations UU (left) and UL (right) in $\mathbf{P}+\mathbf{PJ}$ enriched region. The vertical red lines indicate the fit range and the results of accidentals to data normalisation are also displayed.

In the following sections, $\mathbf{PP} + \mathbf{J}$ and $\mathbf{P} + \mathbf{J} + \mathbf{P}$ are denoted together as elastic accidental background because it is the main source of the protons. Similarly, the term SD accidental background is used for the sum of $\mathbf{PJ} + \mathbf{P}$ and $\mathbf{P} + \mathbf{PJ}$. The distribution of ξ^{PA} vs. ξ^{PC} for mixed CD accidental templates is shown in Fig. 6.12. The red and green lines indicate $\xi^{\text{P}} = 0.02$ and $\xi^{\text{P}} = 0.16$ which correspond to the selection described in Section 6.1. Elastic accidentals dominate the sample, but they are concentrated around the point (0, 0). Some residuals from the $\mathbf{P} + \mathbf{J} + \mathbf{P}$ events are visible along the X and Y axes. SD accidentals are also concentrated, $\mathbf{PJ} + \mathbf{P}$ around the X axis and $\mathbf{P} + \mathbf{PJ}$ around the Y axis, but there are more coincidences of two protons with larger ξ . They constitute the main source of accidental background in CD analysis because they cannot be separated from the signal with ξ^{P} vs ξ^{X} selection.



(a) Elastic accidentals



(b) SD accidentals

Figure 6.12: Distribution of ξ^{PA} vs ξ^{PC} for mixed CD accidental templates. Red and green lines indicate signal selection described in Section 6.1.

6.3 Inelastic background

6.3.1 Inelastic events with one detected proton topology

In contrast to accidental events, the inelastic background for SD dijet production originates from single process events and involves CD, DD, and ND. The background of CD is observed when ALFA detects only one of the intact protons - Fig. 6.13a, when the production of ND or DD dijets can be misidentified as SD due to the formation of forward protons in hadronic showers - Fig. 6.13b. There is no simple way to separate these processes from SD based only on the data, and MC simulation needs to be used. The simulation of high ξ requires accurate modelling of the secondary interaction between forward scattered particles and beamline apertures. It was not included in the available samples. Therefore, the fiducial region ends at $\xi \lesssim 0.16$.

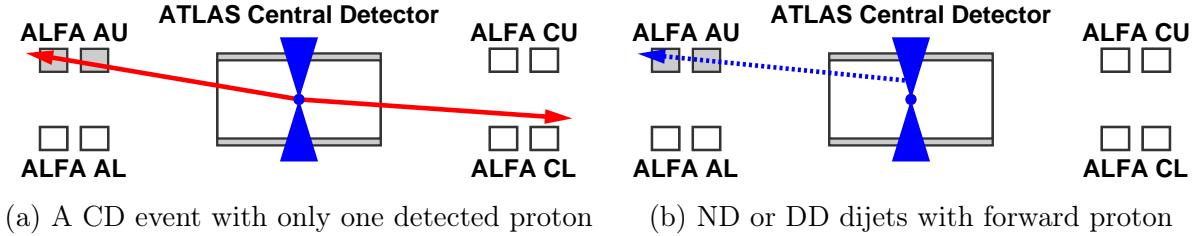
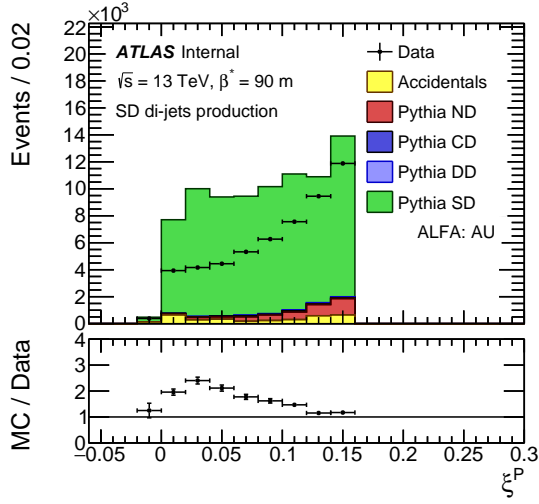


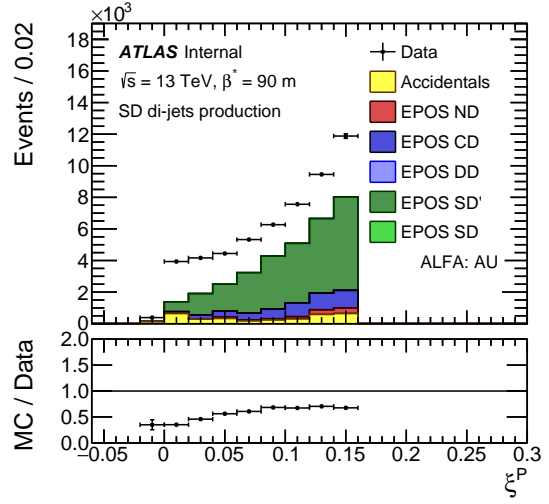
Figure 6.13: Inelastic background for SD dijets analysis. Solid red lines indicate intact protons and blue cones indicate a central state with two jets. The dashed blue line indicates a proton that was created in hadronic showers.

Fig. 6.14 shows uncorrected ξ^P distributions in the data compared to two MC models: PYTHIA and EPOS. MC distributions are separated into SD, CD, DD, and ND components (with SD' for EPOS). MC is normalised to an integrated luminosity based on the cross sections provided by the generators. All selections are applied, including anti-accidentals cut $0.85\xi^P + 0.02 > \tilde{\xi}_{\text{CAL}}^X$. Two ALFA configurations are presented from side A: upper AU and lower AL. Due to the beam-crossing angle, more protons with high ξ^P are reconstructed in the upper RPs. For small ξ^P the numbers of events are similar. However, the MC/data ratio is the same in the upper and lower configurations.

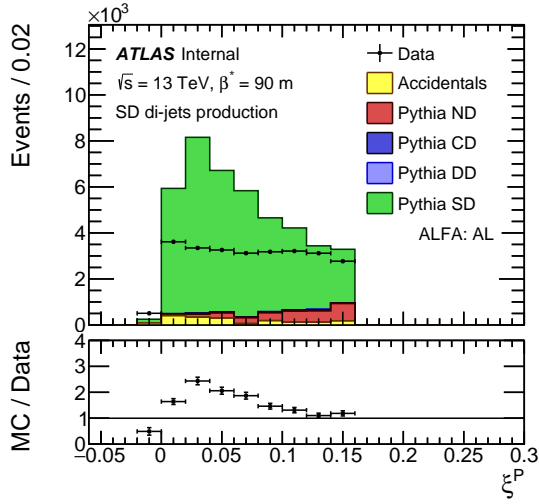
The correlation of ξ^P and $\tilde{\xi}_{\text{CAL}}^X$ for different process types of process predicted by Pythia and EPOS is presented in Fig. 6.15. For high ξ events, most particles escape central detector acceptance, leading to underestimated values of $\tilde{\xi}_{\text{CAL}}^X$. It is interesting to compare these distributions in correlated and uncorrelated regions separately. The corresponding plots for Pythia and EPOS are gathered in Figs. 6.16 and 6.17. The ratio of MC to data is constant for Pythia in both regions, but has different values: Pythia overestimates the data in the correlated region by 2.5 times (left plots), but agrees with the data in the uncorrelated region (right plots). Due to the SD' mechanism, the agreement for EPOS is not so bad even in the uncorrelated region (but decreases for higher ξ^P). However, not as many correlated events are predicted - about 2.5 fewer than in the data. The effect can also be examined using the distribution of the difference $\xi^P - \tilde{\xi}_{\text{CAL}}^X/0.85$, as shown in Fig. 6.18. The red line separates correlated and uncorrelated regions.



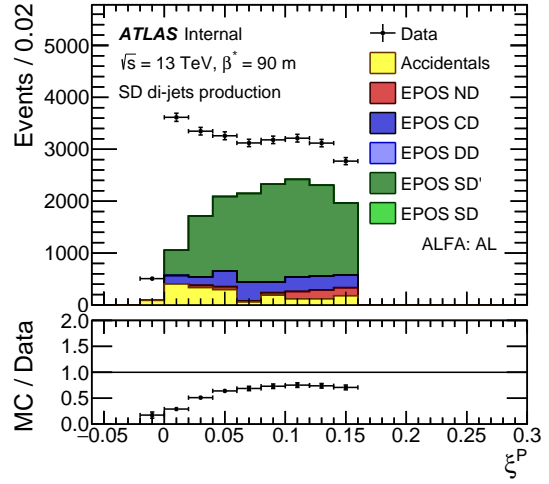
(a) Pythia - ALFA AU



(b) EPOS - ALFA AU



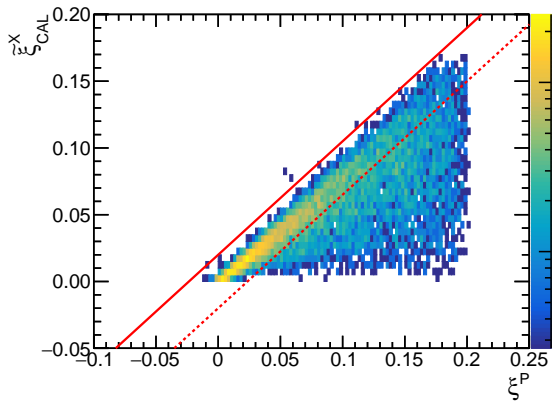
(c) Pythia - ALFA AL



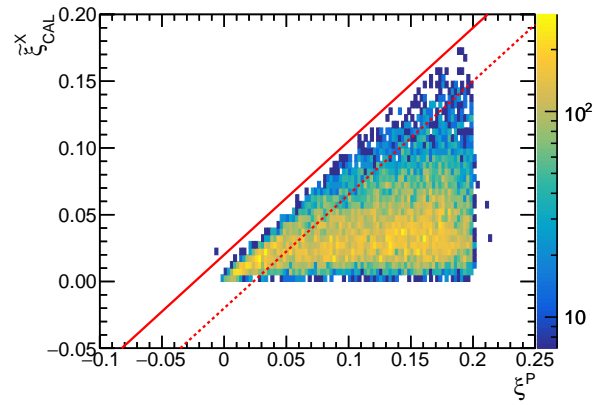
(d) EPOS - ALFA AL

Figure 6.14: Uncorrected distribution of ξ^P for configurations AU and AL in the signal enriched region, compared to MC models: PYTHIA (left) and EPOS (right). The ratios of MC prediction to data are shown in the bottom panels (with statistical uncertainty).

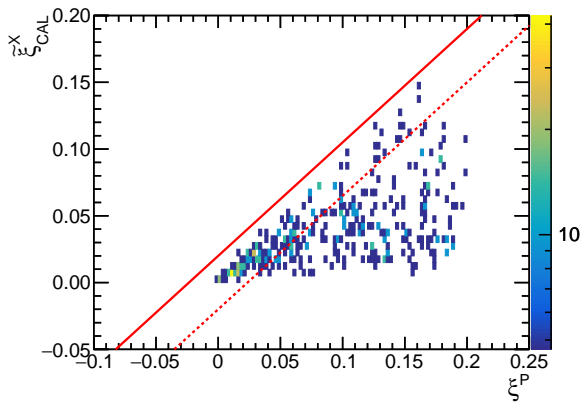
The predictions of both generators do not agree well with the data: Pythia overestimates the data, while EPOS underestimates it. Moreover, the shapes are different. Pythia yields significantly more events with low ξ^P thanks to the hard diffraction model implemented in it. On the other hand, EPOS lacks this mechanism. The MC /data ratio decreases for small ξ^P and does not predict normal SD dijets at all. Most of the events are of SD' type. It is important to note that both generators predict small contributions from non-SD/SD' processes. The probability of the formation of a forward proton with low ξ^P in ND is small. The number of DD events is also negligible. EPOS predicts a higher contribution from CD events than Pythia, which is also known from other analyses [42].



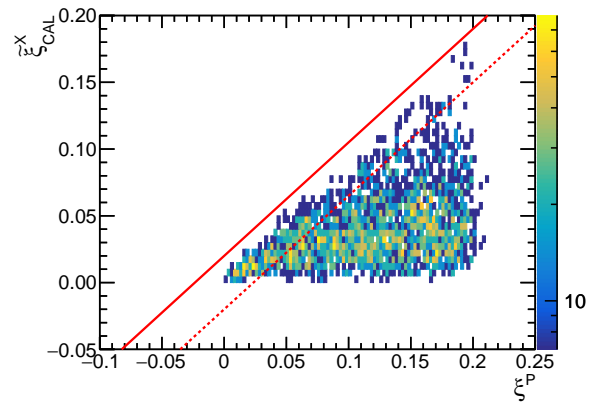
(a) Pythia SD



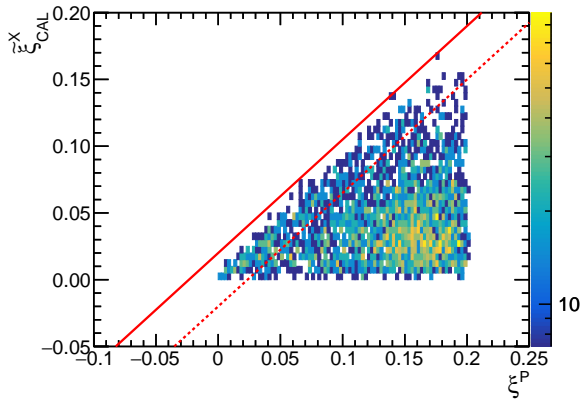
(b) EPOS SD'



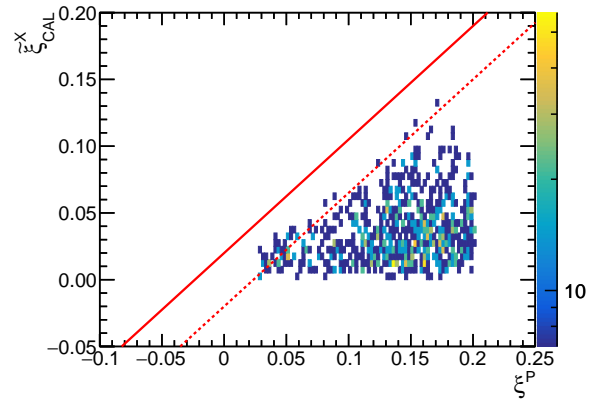
(c) Pythia CD



(d) EPOS CD

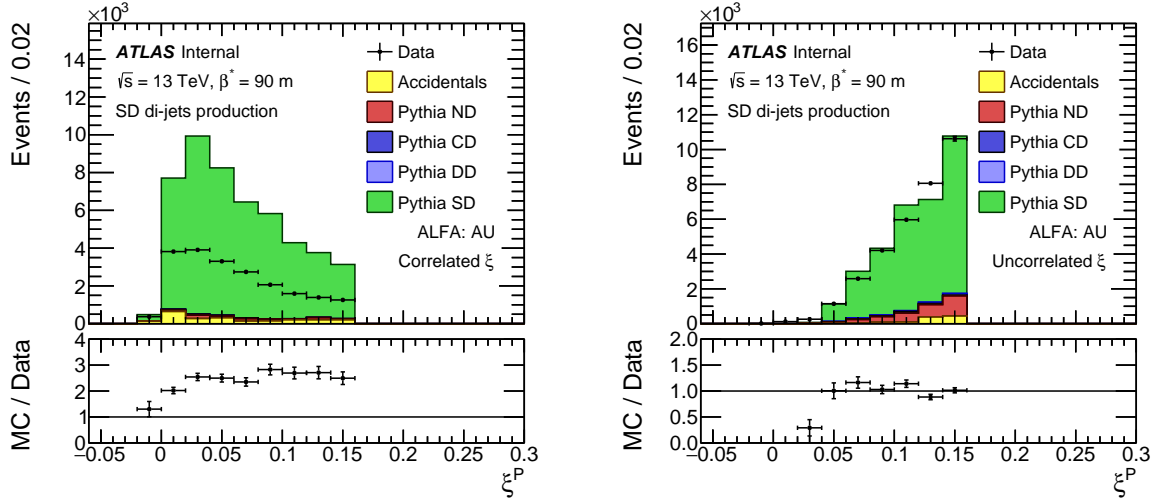


(e) Pythia ND



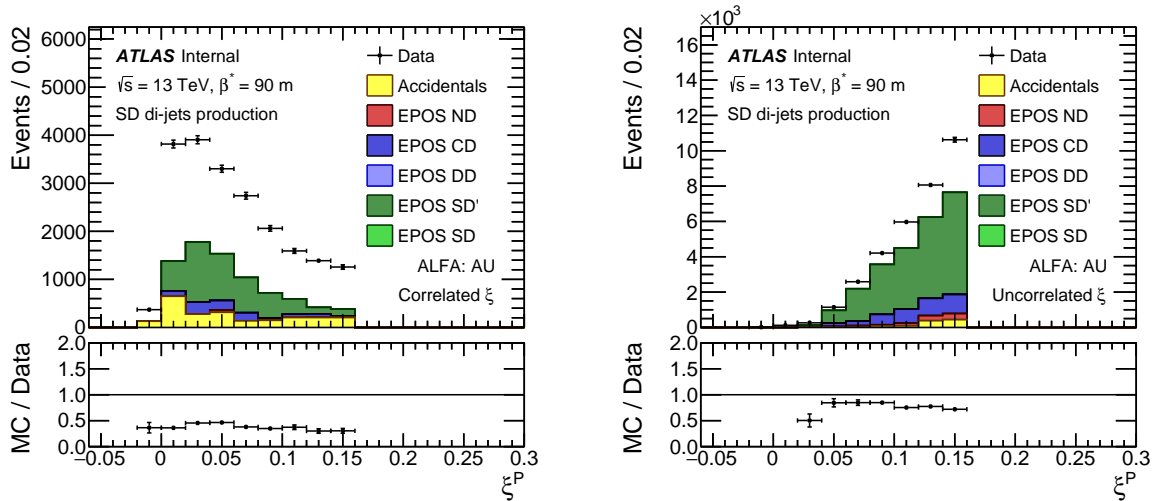
(f) EPOS ND

Figure 6.15: Correlation between ξ^P and ξ_{CAL}^X for different processes simulated with Pythia and EPOS generators. Both generators predict negligible numbers of DD events. For EPOS, the SD' events are shown instead of SD (EPOS does not predict SD dijets at all). Red lines indicate signal selection described in Section 6.1.



(a) Pythia - ALFA AU - Correlated region (b) Pythia - ALFA AU - Uncorrelated region

Figure 6.16: Uncorrected distribution of ξ_P for configuration AU in correlated (left) and uncorrelated (right) regions compared to Pythia predictions.



(a) EPOS - ALFA AU - Correlated region (b) EPOS - ALFA AU - Uncorrelated region

Figure 6.17: Uncorrected distribution of ξ_P for configuration AU in correlated (left) and uncorrelated (right) regions compared to EPOS predictions.

The reason for the difference between the data and the MC is rather complex and remains unclear at this time. Neither generator is yet fully tuned to diffractive data. However, some problems are known to occur in all diffractive analyses, e.g. [42]. Pythia is known to have problems with high ξ , probably due to the crossing angle. In addition, it yields more particles with higher rapidity - Fig. 6.19. This leads to higher ξ_{CAL}^X compared to the data. Dijets have a larger η , and more events pass the selection criteria. For EPOS, the main reason for the difference is the lack of a hard diffraction model. There is no simple way to reweight the simulation to match it to the data in the correlated and uncorrelated regions.

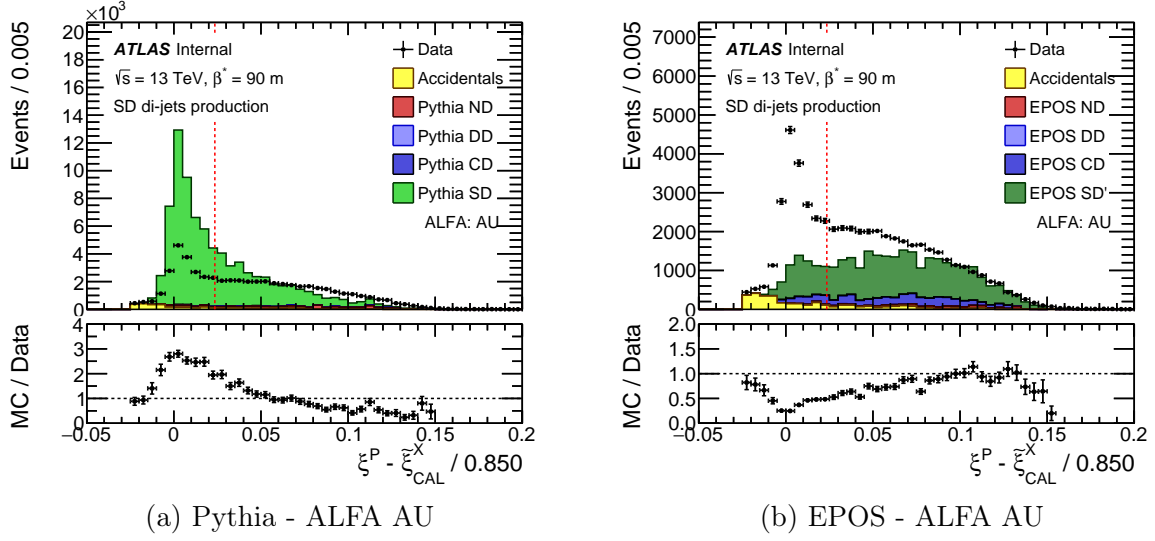


Figure 6.18: Difference between ξ variable reconstructed from the forward scattered proton and the central state for configuration AU compared to Pythia and EPOS predictions. The scaling factor, 0.850, applied to ξ_{CAL}^X comes from the correlation slope in 2D distributions (see Fig. 6.1a). The red lines separate correlated and uncorrelated regions.

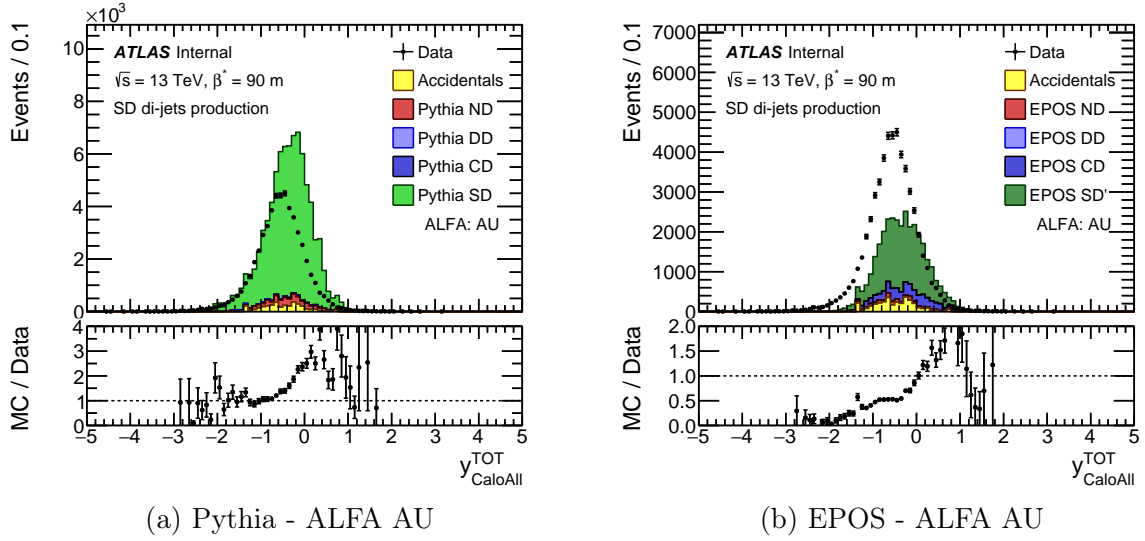


Figure 6.19: Rapidity of central state reconstructed from calorimeter clusters for configuration AU compared to Pythia and EPOS predictions.

6.3.2 Inelastic events with two protons topology

The main source of inelastic background for CD dijet production is SD events with additional forward protons created in the central state. The topology of such an event is presented in Fig. 6.20a. A similar topology originating from DD or ND events is less likely to occur -Fig. 6.20b. It requires the simultaneous production of two protons with small ξ in the hadronic process.

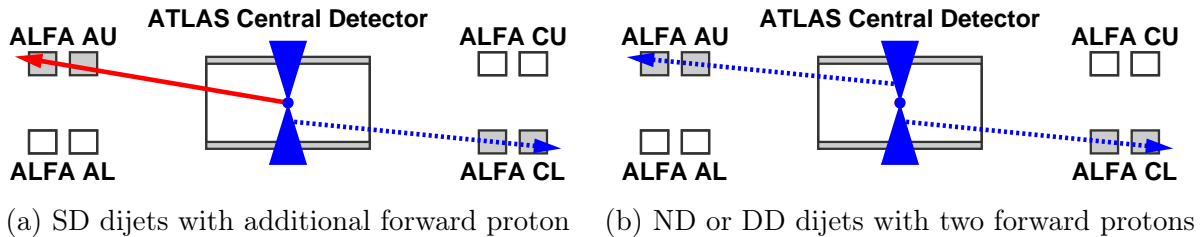


Figure 6.20: Inelastic background for CD dijets analysis. Solid red lines indicate intact protons and blue cones indicate a central state with two jets. Dashed blue lines indicate protons that are created in hadronic showers.

Three MC generators are used to study the production of CD dijets: Pythia, EPOS (with SD' mechanism) and Herwig. Herwig provides only one CD sample. The cross section for the production of CD dijets is much smaller than that for SD. The available samples contain a small number of events with two protons reconstructed in the ALFA detector. Therefore, a partial reconstruction was used for inelastic background estimation. For this, all protons in the forward region on the true level ($\xi < 0.16$) are used in the analysis. The central detector response is still fully simulated. Distributions are normalised to the full simulation according to the number of entries. This mechanism increases the statistics about 4-6 times.

Table 6.1 gathers the numbers of events reconstructed in each MC sample, with full-simulation and partial-reconstruction approaches. The last column shows the effective number of events that is equal to the number of events scaled by the normalisation factor. It is based on the cross section provided by generators and ALFA acceptance - Section 2.7.

Generator	Process	Events with two true forward protons	Events with two reconstructed protons	Effective number of reconstructed events
Pythia	SD	18	2	60.5
	CD	177	32	138.7
	DD	0	0	0.0
	ND	1	0	1.2
EPOS	SD	0	0	0.0
	CD	178	18	190.6
	DD	0	0	0.0
	ND	1	0	0.7
Herwig	SD'	17	2	11.9
	CD	289	72	226.1

Table 6.1: The number of events with two forward protons in MC samples that pass the base CD dijets events criteria. The effective number of reconstructed events is equal to the number of events with two true protons in the forward region scaled by a normalisation factor (based on the cross section provided by generators and ALFA acceptance - Section 2.7).

According to these figures, the contributions from DD and ND are negligible. However, the SD contribution is substantial, about 25% of events according to Pythia and 15% based on EPOS, and cannot be easily separated from CD events.

Fig. 6.21 shows the two-dimensional distributions of ξ produced with the Herwig CD sample. No cuts are applied. MC does not predict events with both $\xi^P < 0.02$ (red lines in Fig. 6.21a) where most elastic accidentals concentrate. The plot in Fig. 6.21b confirms that protons on side A meet the SD relation $0.85\xi^{\text{PA}} + 0.02 > \tilde{\xi}_{\text{CAL}}^{\text{XA}}$. It looks similar to side C. The same conclusion about selection also comes from other MC generators.

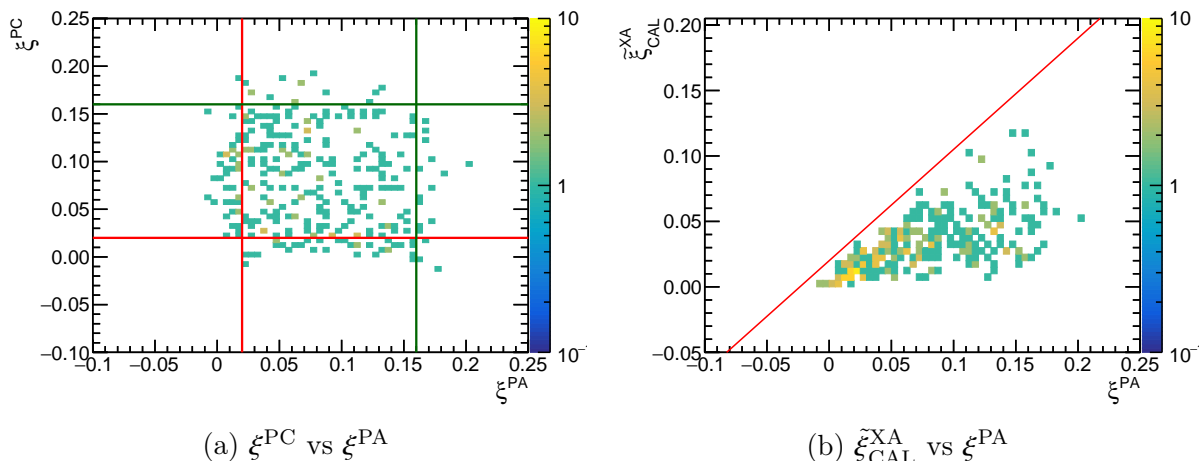


Figure 6.21: Two-dimensional distributions of ξ produced with Herwig sample without selections. Red and green lines indicate signal cuts described in Section 6.1.

The comparison between data and simulation as a function of $\log \xi^{\text{PP}}$ is shown in Fig. 6.22. All generators do not describe the data very well. Pythia underestimates the cross section of CD, and the effect is also known in diffractive charged particle analysis [42]. EPOS also underestimates CD dijet production. Herwig describes the lower ξ^{PP} part better than other models but underestimates it at higher ξ^{PP} .

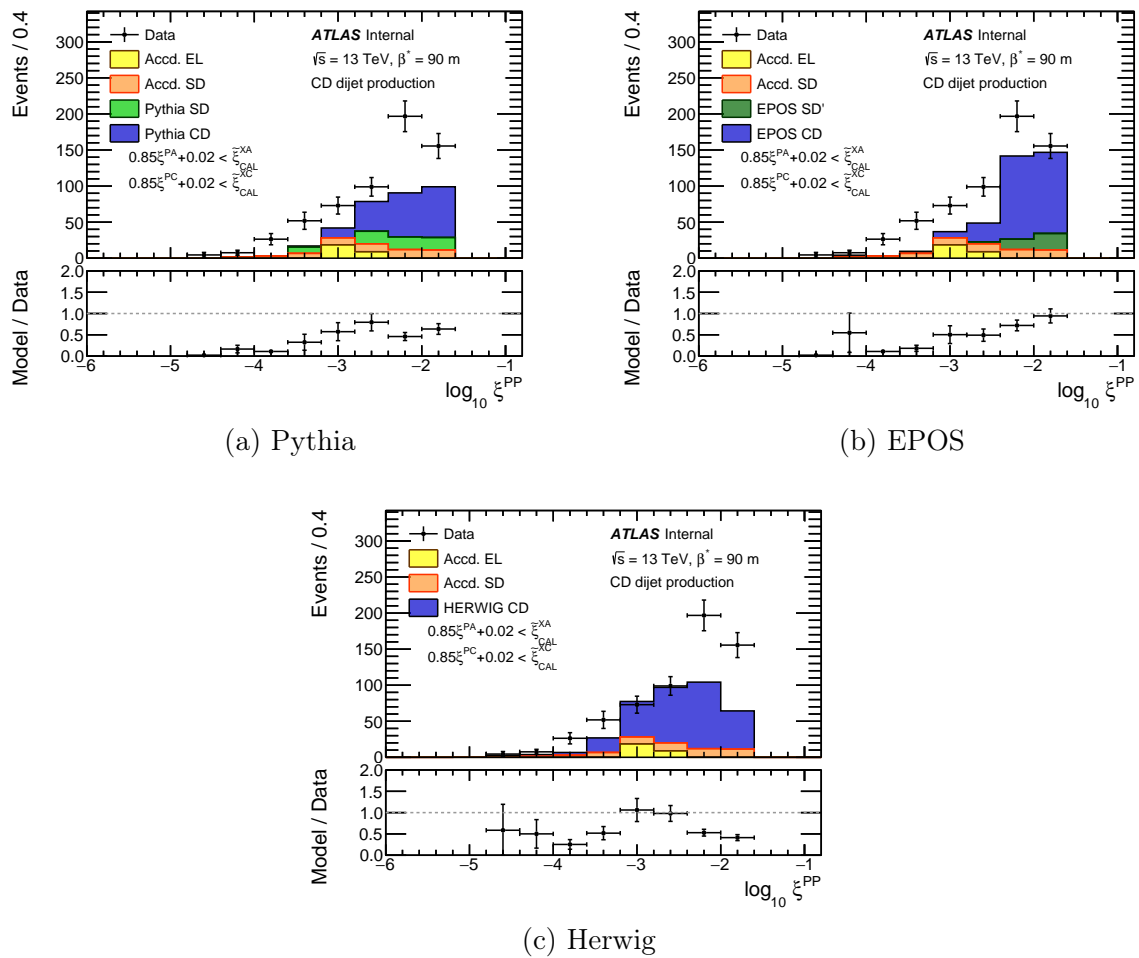


Figure 6.22: Uncorrected distribution of $\log \xi^{PP}$ after selections compared to MC models: PYTHIA (left), EPOS (right), and Herwig (bottom). All ALFA configurations are summed together.

Chapter 7

Event selection and unfolding

The data sample was collected using the L1_J12_ALFA_ANY trigger. Event selection is extended offline by the list of required cuts described in this chapter. It significantly restricts the background but preserves almost all signal events. The selection is based on the beam conditions, the quality of the jets, and measurements in the ALFA detectors.

The analysis focuses on measurements of several differential cross sections for dijet production in single and central diffraction. Each of these cross sections must be evaluated with appropriate binning. Then, a procedure known as unfolding needs to be applied in order to find the distributions at the hadron level. This allows for a direct comparison between the measurements and other experimental results or theoretical predictions.

7.1 Reconstructed vertex requirement and pileup

Only events with a single vertex with at least 4 or more associated tracks are analysed. In order to reduce pile-up, a veto is applied for events with additional vertices associated with 4 or more tracks. In this way, a clean sample is created for diffractive analysis, but it also leads to some inefficiency.

The impact of primary vertex selection is slight: the portion of events without primary vertex is approximately 0.5% in the data and less than 0.1% in the MC when other selection criteria are met. These small values can be understood as a result of the presence of two jets with more than enough particles for vertex reconstruction. Therefore, no correction is applied due to the primary vertex requirement, but this fact is considered in systematic analysis.

Events without pile-up vertices are dominant in both the data and the MC, but pile-up suppression has a greater effect than the previous requirement. Once the selection criteria for dijets are met, the veto on additional vertices removes 12.4% of data events. Part of this fraction comes from the inelastic interaction that overlaps with the signal events during single bunch crossing. It can be estimated using Poisson statistics as the probability of occurrence of at least one additional interaction:

$$P(n \geq 1) = 1 - P(0) = 1 - e^{-\mu} \approx 9.5\%, \quad (7.1)$$

where μ denotes the average number of inelastic interactions per bunch crossing and is equal to 0.1. Eq. (7.1) is justified by the high independence of additional interactions

in a single bunch crossing. Studies based on MBTS samples show that about 10% of the interactions do not meet the requirements for vertex reconstruction. Therefore, the probability of observing an additional vertex is smaller and is approximately 8.6%.

Additional vertices can also occur because of decays of short- and long-lived particles within a single interaction. They are wrongly rejected with pile-up suppression cuts. In MC samples, the fraction of rejected events stands at 3.2% and 1.7% for Pythia and EPOS respectively (the simulation does not include pile-up). Together with the real pile-up correction, the sum is close to the observed value. Data are scaled by factor 1.142, which is equal to $(1.124)^{-1}$. The difference between the observed and estimated values is taken into account in the systematic uncertainty. Vertex requirements are not applied to MC; therefore, MC samples are not scaled.

7.2 Fiducial region

The fiducial regions for this analysis are defined in terms of jet and diffractive variables. The former comes from trigger efficiency. The kinematics of the jets must ensure satisfactory jet trigger efficiency - Section 5.1. Therefore, the kinematic limits for jets are as follows:

- $p_T^{LJ} > 30 \text{ GeV}$, $|\eta^{LJ}| < 3.0$,
- $p_T^{SJ} > 20 \text{ GeV}$, $|\eta^{SJ}| < 4.0$.

The latter is based on the geometric acceptance of the ALFA detector. Furthermore, the lower ξ limit was imposed by requiring two jets with $p_T > 30/20 \text{ GeV}$. The plot in Fig. 7.1 shows the relative fraction of simulated events containing such jets, based on the Pythia SD sample. The distribution is normalised to unity for $\xi \in [0.10, 0.20]$. The fraction is less than 50% for $\xi < 0.002$. However, the limit of $\xi > 0.002$ applies only to unfolded cross-section distributions. The selection of the reconstructed ξ^P has to be shifted due to the finite resolution of the detector. It is set to $\xi^P > -0.005$.

Additionally, due to the exponential dependence on t , the high $|t|$ distributions suffer from statistical fluctuations. The upper limit for $|t|$ is set to 1.0 GeV^2 . Therefore, measurements are performed for forward protons in the fiducial region:

- $\xi \in [0.002, 0.160]$,
- $t \in [0.02, 1.00] \text{ GeV}^2$.

For the CD region, both protons must meet those conditions.

Furthermore, the distributions for SD dijets are presented in three ξ regions. The limiting values correspond to the acceptance of the AFP detector which overlaps with the middle region. This may be helpful for a possible comparison of the AFP and ALFA analyses. The regions are defined as:

- $\xi^I \in [0.002, 0.035]$,
- $\xi^{II} \in [0.035, 0.080]$,
- $\xi^{III} \in [0.080, 0.160]$.

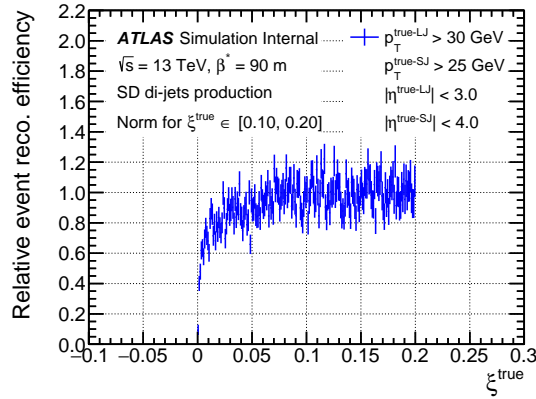


Figure 7.1: The fraction of simulated events containing two jets that pass fiducial cuts, based on the Pythia SD sample. The fraction is normalised to unity for $\xi \in [0.10, 0.20]$.

7.3 Event selection

The diffractive dijet event candidates were selected online using the L1_J12_ALFA_ANY trigger. To ensure good event quality, additional cuts must be applied offline. The complete list of 12 cuts is given below:

- C1.** Stable conditions for the beam and detectors. This cut removes some of the lumi-blocks, especially at the beginning and end of each run.
- C2.** Reconstruction of the primary vertex with four or more associated tracks.
- C3.** Veto for pileup vertices (associated with four or more tracks). The number of pile-up events is not large ($\mu = 0.1$), but thanks to this veto, it is further reduced.
- C4.** At least two jets reconstructed with the anti- k_t algorithm and parameter $R = 0.4$. The input consists of clusters of calorimeter cells after Local Cluster Weighting [101].
- C5.** The kinematics of the jets must ensure a satisfactory jet trigger efficiency, which is evaluated in Section 5.1. L1_J12 achieves an efficiency of more than 10% for a single jet with $p_T = 30$ GeV. Unfortunately, forward calorimeters were not used for triggering and the pseudorapidity range must be constrained. The kinematic cuts for leading and secondary were defined as follows:
 - $p_T^{\text{LJ}} > 30$ GeV and $|\eta^{\text{LJ}}| < 3.0$;
 - $p_T^{\text{SJ}} > 20$ GeV and $|\eta^{\text{SJ}}| < 4.0$.
- C6.** Jets must pass the cleaning selection as described in Ref. [102].
- C7.** Exactly one or two protons were reconstructed in the ALFA detectors for SD/CD analysis. Tracks must have at least six active layers of the ten possible in both U and V planes used for reconstruction. No more than one track per RP is accepted.
- C8.** Veto the signal in the ALFA trigger tiles in RPs without protons.

C9. The coordinates of ALFA tracks are restricted to be away from the edges of the RPs and LHC beamline apertures. These cuts are slightly different for each RPs. The details are described in Section 4.4.

- $|x| \lesssim 10$ mm and 6 mm $\lesssim |y| \lesssim 20$ mm

C10. The plots in Fig. 7.2 show the correlation between the local angle in the XZ plane θ_X and the average horizontal position \bar{x} of the tracks in the inner and outer RPs. The local angle can be evaluated as $\theta_X = \Delta x / \Delta z$, where Δx and Δz denote the differences between the track positions in the outer and inner RPs. Interactions with the RP cover, the showers inside the detectors, and the beam-halo protons generate abnormal patterns visible in the data in Fig. 7.2a. They are parts of the accidental background, which is studied in Section 6.2. Nevertheless, they can be reduced by following cuts:

- $\bar{x} > 2.5$ mm,
- $\theta_X > \bar{x} \times 0.05 \frac{\text{mrad}}{\text{mm}} - 0.05$ mrad.

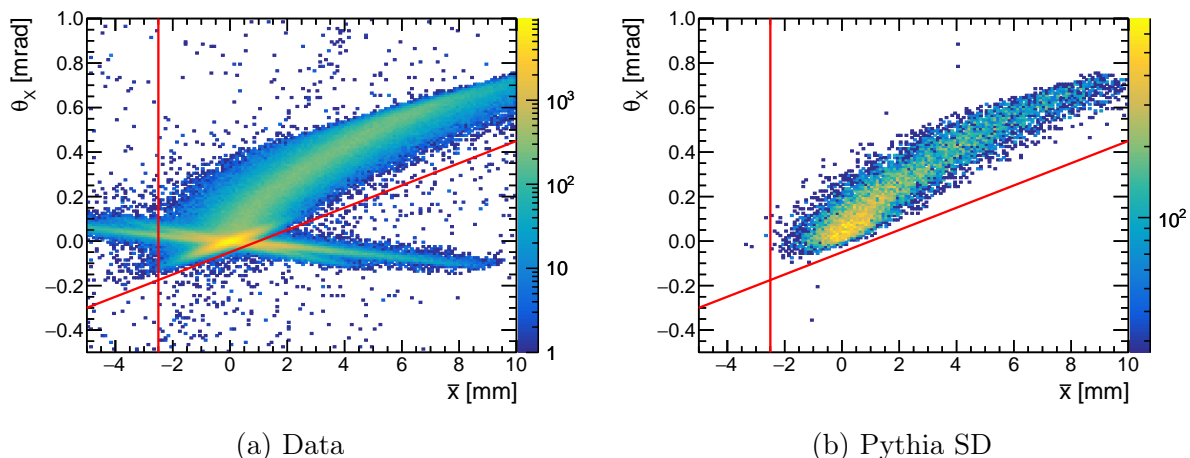


Figure 7.2: Correlations between \bar{x} and θ_X for data and Pythia SD samples. Red lines indicate the accepted region described in cut **C10**.

C11. The remaining events are contaminated by significant amounts of accidental coincidences (especially elastically scattered protons and ND dijets). Cuts that suppress this background in SD analysis are based on the relationship between ξ^P and $\tilde{\xi}_{\text{CAL}}^X$:

- $0.85\xi^P + 0.02 > \tilde{\xi}_{\text{CAL}}^X$.

The cuts used to reduce the accidental background in CD analysis are based on the relationship between ξ^P and $\tilde{\xi}_{\text{CAL}}^X$, similar to SD analysis, simultaneously on ATLAS side A and C. Because the CD topology is heavily contaminated by elastically scattered protons, a significant number of accidental events remain after this selection. Requiring ξ^{PA} or ξ^{PC} greater than 0.02 allows suppression of elastic residuals:

- $0.85\xi^{\text{PA}} + 0.02 > \tilde{\xi}_{\text{CAL}}^{\text{XA}}$;
- $0.85\xi^{\text{PC}} + 0.02 > \tilde{\xi}_{\text{CAL}}^{\text{XC}}$;
- $\xi^{\text{PA}} > 0.02 \vee \xi^{\text{PC}} > 0.02$.

C12. The last part of the selection cuts is related to the fiducial region and the acceptance of the ALFA detector. The conditions for the reconstructed protons ξ^{P} and $|t|$ are covered in Sections 3.7 and 7.2:

- $\xi^{\text{P}} \in [-0.005, 0.160]$,
- $t \in [0.02, 1.00] \text{ GeV}^2$.

7.4 Resolution of kinematic variables and bin widths

The resolutions of analysed variables can be used to determine the bin widths. For transverse momentum of leading jet p_{T}^{LJ} , the values obtained in the calibration process can be exploited, described in Section 5.4.4. Other resolutions are presented here.

Section 1.2.2 provides a straightforward way to evaluate t , ξ , and β^{JJ} in SD events. Figs. 7.3 to 7.5 show the difference between values measured in ALFA and those calculated from the truth-level proton energy using the Pythia SD sample. The resolutions are shown on the right. The ALFA reconstruction provides a good correlation of ξ^{P} which improves with increasing ξ^{True} . It should be however noted that at very small $\xi \lesssim 0.01$, the nonphysical negative values can be reconstructed due to finite detector resolution.

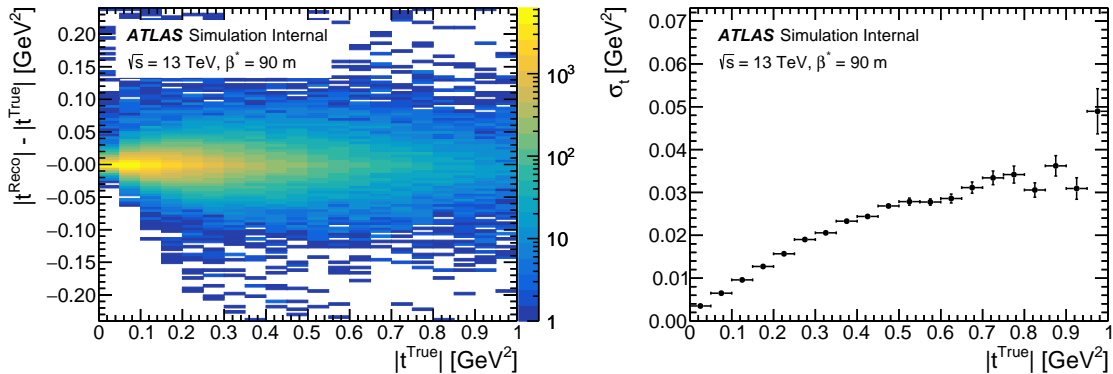


Figure 7.3: Difference between true and reconstructed t in the function of t^{True} . The right plot shows the resolution of t in the function of t^{True} . Based on the Pythia SD sample.

The resolution and bias of $\tilde{\xi}^{\text{X}}$ depend mainly on the limited geometrical acceptance of the detector, but also on the energy resolution of the calorimeter clusters or Inner Detector sensitivity to charged particles. It is worth pointing out that for $\tilde{\xi}_{\text{CAL}}^{\text{X}}$ calculation, no cell significance selection is required - any negative energy noise cluster used in the summation (with negative p_{T}) will statistically cancel similar positive noise contributions - the calorimeter noise has a Gaussian distribution with a mean of zero [47].

The bias is visible in Fig. 7.6, where $\tilde{\xi}^{\text{X}}$ is compared with ξ^{True} . The plot on the left shows $\tilde{\xi}_{\text{CAL}}^{\text{X}}$. The reconstruction is acceptable only for very low ξ^{True} , where most of the particles are within the geometric acceptance of calorimeters. When ξ^{True} increases,

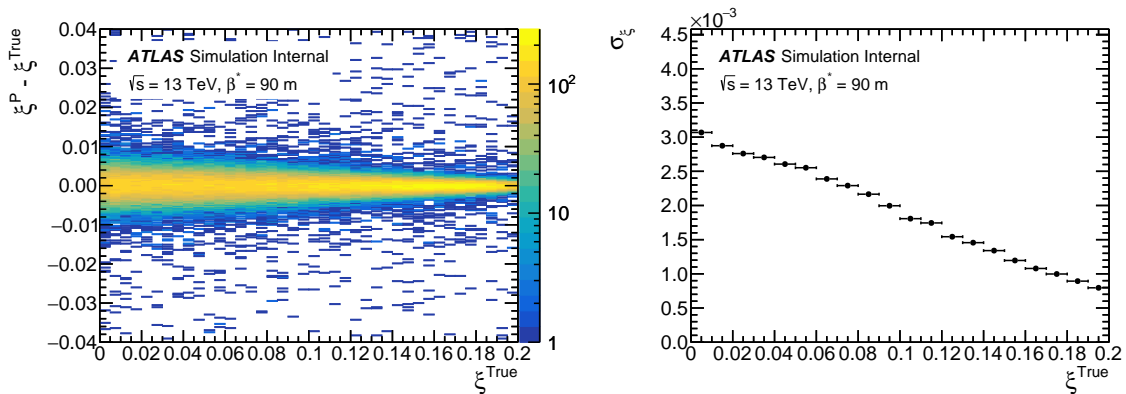


Figure 7.4: Difference between reconstructed and true ξ as a function of ξ^{True} . Right plot shows the resolution of ξ^P in the function of ξ^{True} . Based on the Pythia SD sample.

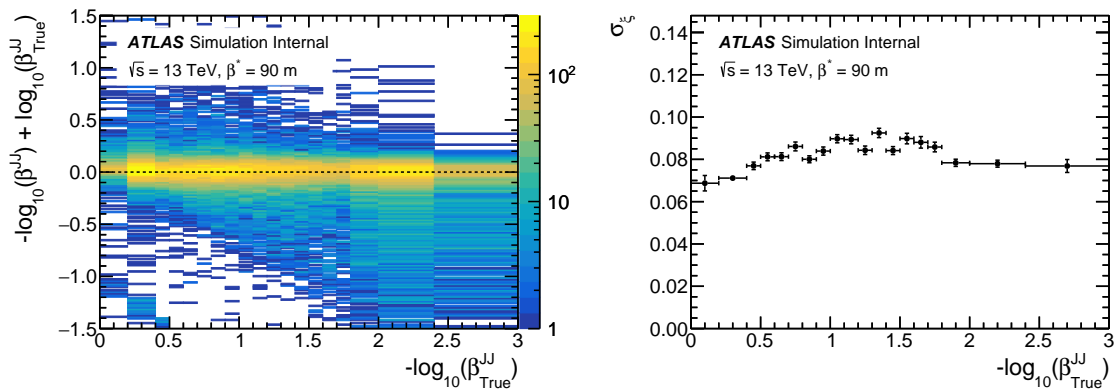


Figure 7.5: Difference between reconstructed and true level β^{JJ} as the function of $-\log_{10}\beta^{\text{JJ, True}}$. Right plot shows the resolution of β^{JJ} in the function of $-\log_{10}\beta^{\text{JJ, True}}$. Based on the Pythia SD sample.

more particles escape the detector on the same side as the proton, and the $\tilde{\xi}_{\text{CAL}}^{\text{X}}$ becomes underestimated. For this reason, the ξ^P evaluated from the proton detected by ALFA is used as input in the unfolding truth-level ξ distribution. Nevertheless, the correlation of $\tilde{\xi}_{\text{CAL}}^{\text{X}}$ and ξ^P helps to significantly limit the accidental background in Section 6.1.

ID covers narrow η -range, and the $\tilde{\xi}_{\text{ID}}^{\text{X}}$ calculated from tracks is highly biased. For analysis that focus on the lower ξ range (e.g. $\xi < 0.01$ in [103]), $\tilde{\xi}_{\text{ID}}^{\text{X}}$ provides better resolution than ξ^P . But it is not useful for dijet analyses with relatively high ξ . It is exploited only for accidental background normalisation since the fit is more stable in terms of $\tilde{\xi}_{\text{ID}}^{\text{X}}$ than $\tilde{\xi}_{\text{CAL}}^{\text{X}}$.

7.5 Rapidity gap $\Delta\eta$ reconstruction

Due to limited detector acceptance, it is often difficult to measure the real rapidity gap between the central state and forward scattered particle. Instead, the experiment mea-

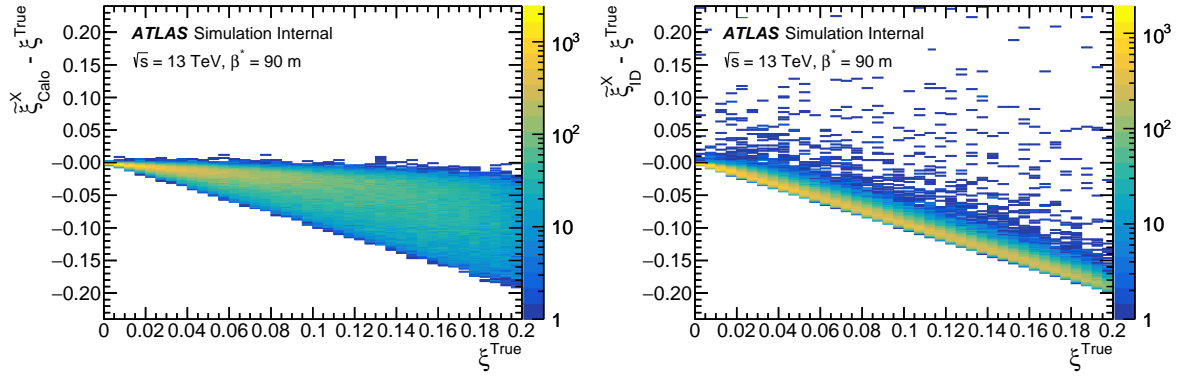


Figure 7.6: Difference between reconstructed ξ^X and true level ξ^{True} as the function of ξ^{True} . The left plot shows the ξ_{CAL}^X calculated from calorimeter clusters and the right plot shows ξ_{ID}^X based on Inner Detector tracks. Based on the Pythia SD sample.

sures the so-called observed rapidity gap - Fig. 7.7. It is calculated relative to the side of the ATLAS detector with the scattered proton between the edge of the calorimeter and the closest Inner Detector track or calorimeter cluster.

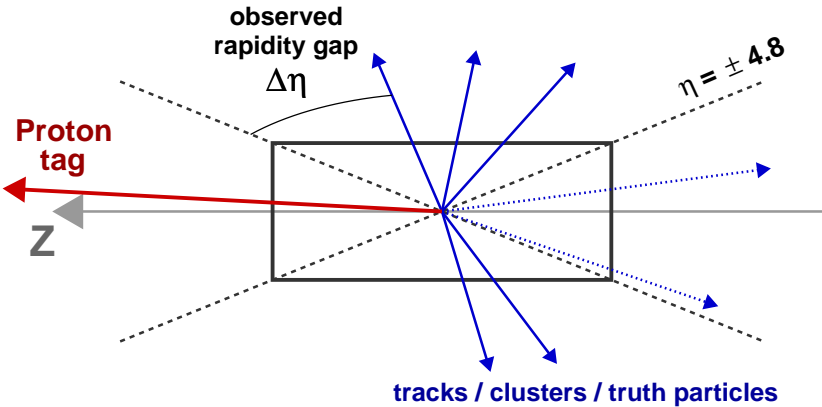


Figure 7.7: The observed rapidity gap is calculated as the difference between the pseudorapidity of the calorimeter edge and the closest corresponding object. The side with the proton determines the sign of the Z-axis.

According to the ATLAS rapidity gap dijet analysis [47], a reasonable selection of the considered objects is necessary. Otherwise, the noise would dominate the signal. The calculations are based on a hybrid method using the information from Inner Detector and calorimeter system. The observed rapidity gap based on the hybrid method is denoted by $\Delta\eta^{\text{Hyb}}$. Tracks are required to satisfy the following cuts; based on the analysis of charged particle production in diffractive scattering [42]:

- p_{T} of a track must be greater than 0.2 GeV;
- a track must be in region of $|\eta| < 2.5$;

- at least one hit in the Pixel layer;
- at least 2 hits in SCT layer for $p_T \in [0.2 \text{ GeV}, 0.3 \text{ GeV}]$, at least 4 SCT hit for $p_T \in [0.3 \text{ GeV}, 0.4 \text{ GeV}]$ and at least 6 SCT for $p_T > 0.4 \text{ GeV}$;
- $|d_0| \leq 1.5 \text{ mm}$, where d_0 is the transverse impact parameter with respect to the primary vertex;
- $|z_0 \sin \theta| \leq 1.5 \text{ mm}$, where z_0 is the longitudinal impact parameter with respect to the primary vertex and θ is the polar angle of the track;
- for tracks with $p_T > 10 \text{ GeV}$, the χ^2 fit probability must be at least 0.01.

These cuts allow for rejecting low-quality tracks. The cuts on d_0 and $z_0 \sin \theta$ allow removing tracks that do not originate from the primary vertex.

For clusters, the energy significance $S = |E|/\sigma_{noise}$ is required to be greater than 5.5. The value is the average significance threshold in the ATLAS rapidity gap dijet analysis [47]. Additional $|\eta| < 4.8$ cut is introduced, as very few clusters are reconstructed close to the edge of detector acceptance. The p_T cut is not necessary due to the significance cut.

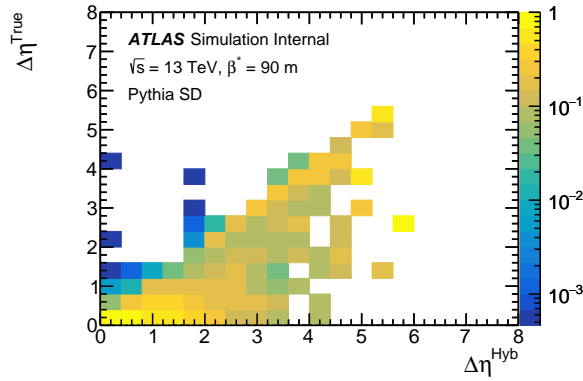


Figure 7.8: Observed rapidity gap at reconstructed vs true level for Pythia SD sample. Columns are normalised to unity.

At the truth level, the requirement is $p > 0.5 \text{ GeV}$ for neutral particles and $p > 0.5 \text{ GeV}$ or $p_T > 0.2 \text{ GeV}$ for charged particles. The difference in momentum cuts for neutral and charged particles matches the range in which the particles are likely to be reconstructed by the detector system [47]. The comparison between true and reconstructed levels is shown in Fig. 7.8. The plot reveals a detector effect around $\Delta\eta^{\text{Hyb}} \approx 1.5$. This value corresponds to $|\eta| = 3.3$, which is the boundary of the Forward Calorimeter. The clusters' noise in this region is larger than in the surrounding parts of the calorimeter system; therefore, it takes a larger energy deposition to pass the significance cut. As a consequence, events migrate from smaller to larger $\Delta\eta^{\text{Hyb}}$.

Comparison between SD and ND processes on the true level is shown in Fig. 7.9. For SD the correlation between $\Delta\eta^{\text{True}}$ and $\log \xi^{\text{True}}$ is visible for small ξ , but it is limited by the detector acceptance for large ξ^{True} . The rapidity gap for ND is exponentially suppressed. Nevertheless, small statistics, detector effects, and limited acceptance of high ξ^{True} make it difficult to exploit the observed rapidity gap in this analysis.

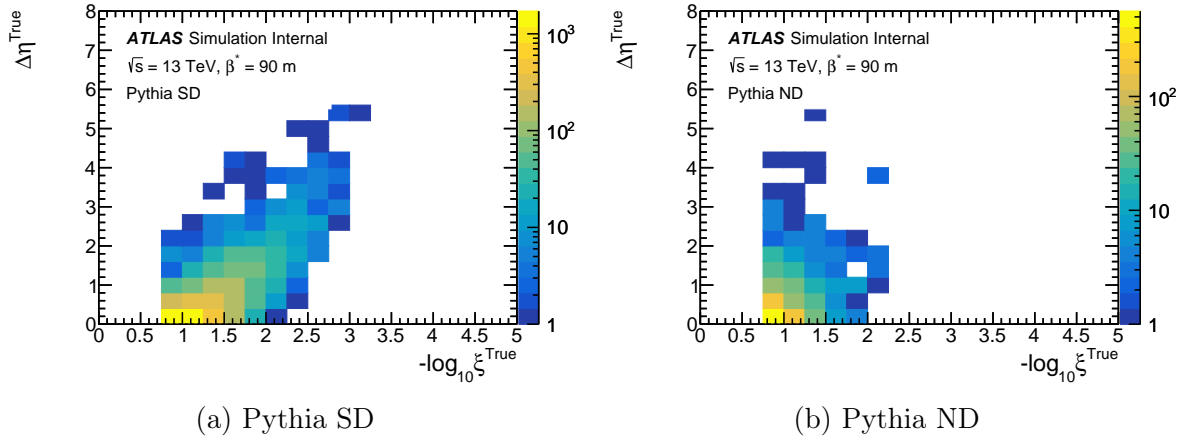


Figure 7.9: Observed rapidity gap at true level vs ξ^{True} for SD and ND Pythia simulation.

7.6 Unfolding for SD analysis

7.6.1 The concept of unfolding

Reconstruction of data is affected by detector effects, such as limited acceptance or finite resolution. Therefore, measured distributions are distorted compared to the true level counterparts. To find the hadron-level distributions, the data have to be corrected for these effects through a process called unfolding. It allows a direct comparison between measurements and other experimental results or theoretical predictions. The measured distribution \vec{m} is considered as the smeared truth level distribution \vec{t} :

$$\mathbf{R}\vec{t} = \vec{m}, \quad (7.2)$$

where \mathbf{R} is called the response matrix. It corresponds to the probability $P(m_j|t_i)$, that with a certain true value t_i the observed one will be m_j .

There are several methods for the unfolding process. The simplest is the bin-by-bin unfolding [104], which estimates the efficiency of the measurement by the ratio of the reconstructed and true distributions in the MC simulation. The data distribution can be divided by this ratio to obtain the unfolded results. Since migrations between bins are not considered, this method requires a high purity of measurement - most of the events must belong to the diagonal of the response matrix. It is equivalent to the binning of the measured distribution being a few times larger than the resolution. Both ξ and t plots meet these conditions, therefore, they can be unfolded with the bin-by-bin method.

The resolution of jet transverse momentum is comparable with the histogram binning. There are significant migrations that require subtle procedures. The most commonly used method is iterative Bayesian unfolding [105, 106], which is chosen to unfold the p_T^{LJ} and β^{JJ} distributions. It corrects the data in each iteration, accepting the response matrix prepared with MC as the base. The number of iterations needs to be chosen carefully. In the case of many iterations, statistical fluctuations explode due to positive feedback throughout each iteration [106]. Stability is achieved by stopping the iteration prematurely before convergence.

7.6.2 Bin-by-bin corrections for ξ and t

The resolutions of ξ and t summarised in Section 7.4 are at least a few times smaller than the corresponding bin widths. The correlation between true and reconstructed levels is presented in the plots in Fig. 7.10, where red lines correspond to the edges of the bins. It is important to note that the first ξ bin is wider on the reconstruction level - it covers $\xi^P \in [-0.005, 0.035]$.

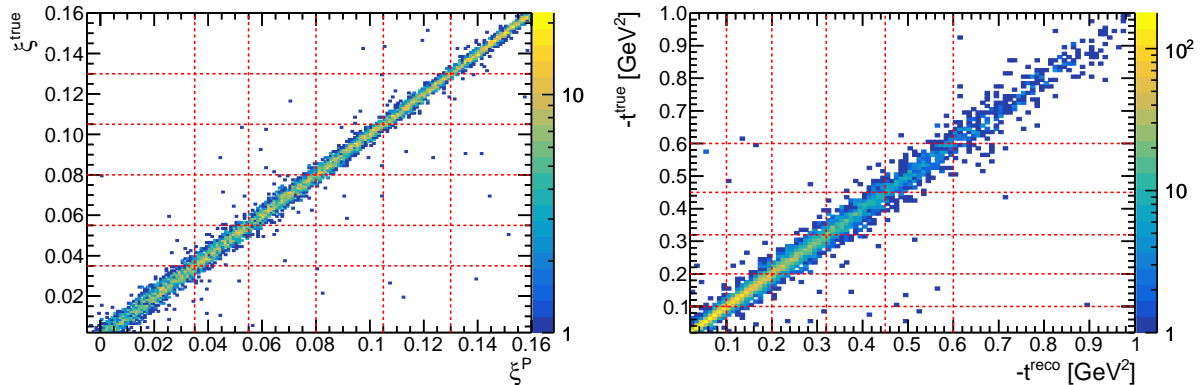
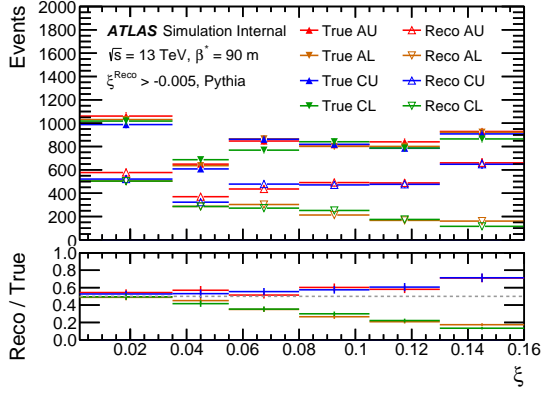


Figure 7.10: Correlation between true and reconstructed levels for proton variables ξ and t . The red lines correspond to the bin edges. It is important to note that the first ξ bin is wider on the reconstruction level - it covers $\xi^P \in [-0.005, 0.035]$.

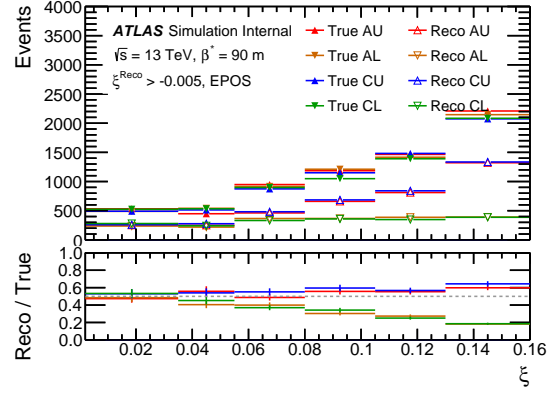
There are not many migrations outside the diagonal; therefore, simple bin-by-bin corrections suffice to unfold the true distributions from reconstructed levels. The unfolding for ξ and t was performed separately for each ALFA armlet. This makes it possible to compare the results from each armlet. The plots in Fig. 7.11 show the ratios between the ξ distributions at the reconstructed and true levels, for each ALFA armlet and for two MC generators. Events pass all selections described in Section 7.3. Despite the different shapes of the generated ξ distributions, both MC models yield similar results, and the difference is taken into account in the uncertainty analysis. There is no significant difference between sides A and C, and the difference between the upper and lower armlets is due to the crossing angle. The ratio is used to unfold the distributions obtained from the collected data. A similar procedure was carried out for t . The corresponding plots for Pythia and EPOS are presented in Fig. 7.12.

7.6.3 Iterative Bayesian unfolding for jet variables

The resolution of the jet transverse momentum causes a fluctuation in the value of the momentum measured for each jet. It causes more effects than simple p_T migrations because the leading and secondary jets can be interchanged on the detector level. Simple bin-by-bin corrections are insufficient to handle jet variables. This analysis exploits the *RooUnfold* implementation of iterative Bayesian unfolding [107]. The input consists of the response matrix as well as true and reconstructed distributions of jet variables, which permits the inclusion of inefficiencies and spurious jets in analysis. Response matrices

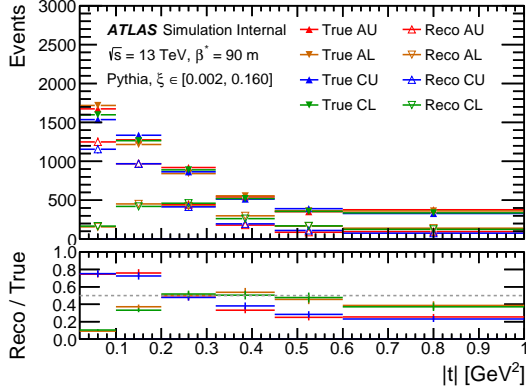


(a) Pythia

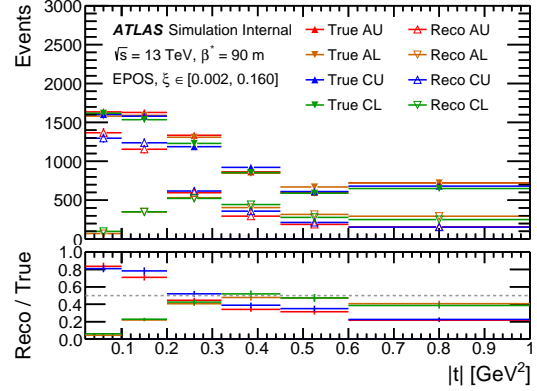


(b) EPOS

Figure 7.11: Ratios between ξ distributions on reconstructed and true level, for each ALFA armlet and for two MC generators. Only statistical uncertainties are shown.



(a) Pythia



(b) EPOS

Figure 7.12: Ratios between t distributions on reconstructed and true level, for each ALFA armlet and for two MC generators. Only statistical uncertainties are shown.

are presented in Fig. 7.13, Fig. 7.14 and Fig. 7.15, for p_T^{LJ} , η^{LJ} and β^{JJ} respectively, where events pass all proton selections with $\xi \in [0.002, 0.160]^1$, but the unfolding is performed for three smaller ξ ranges also. Two-dimensional unfolding is not required because of the small migration in ξ . Pythia is used as the default in this analysis because it has implemented the hard diffraction model. EPOS is used as a cross-check for the uncertainty analysis.

A basic closure test shows that the unfolding tools have been configured correctly. It consists of a single unfolding iteration, where the input is the same reconstructed MC distribution as the one used to train the tool. All detector effects should be perfectly erased, and the unfolded distribution should be overlaid with the truth level. Fig. 7.16 shows the result of this basic test: the reconstructed distribution transforms into the

¹The lower limit for reconstructed ξ^P is lowered to -0.005.

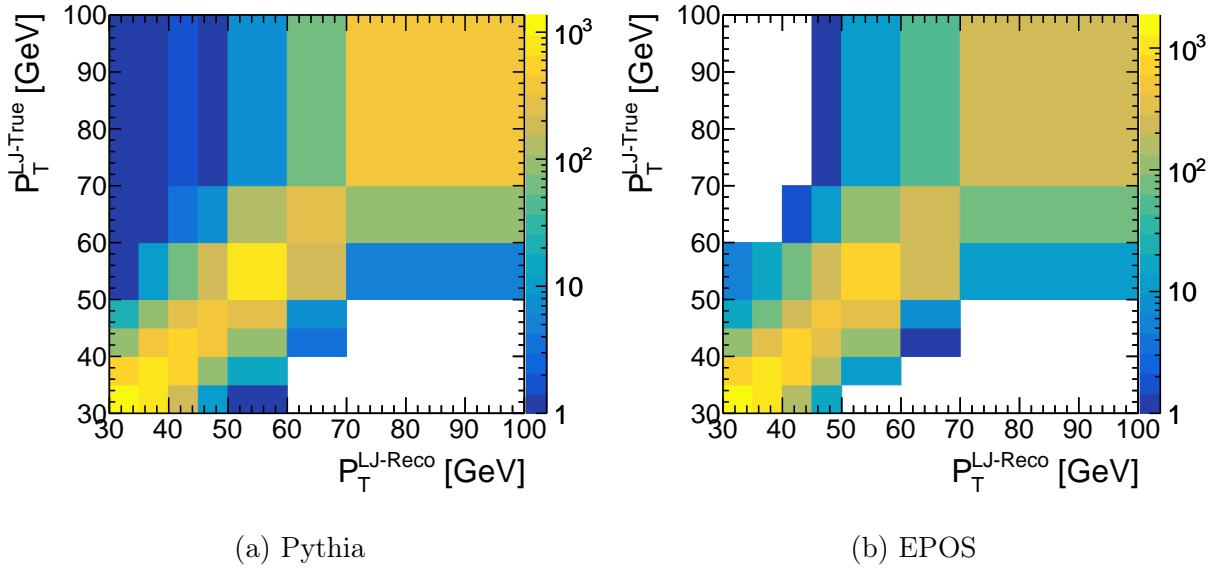


Figure 7.13: Response matrices for leading jet transverse momentum p_T^{LJ} generated with two MC models. Events pass all proton selections with $\xi \in [0.002, 0.160]$.

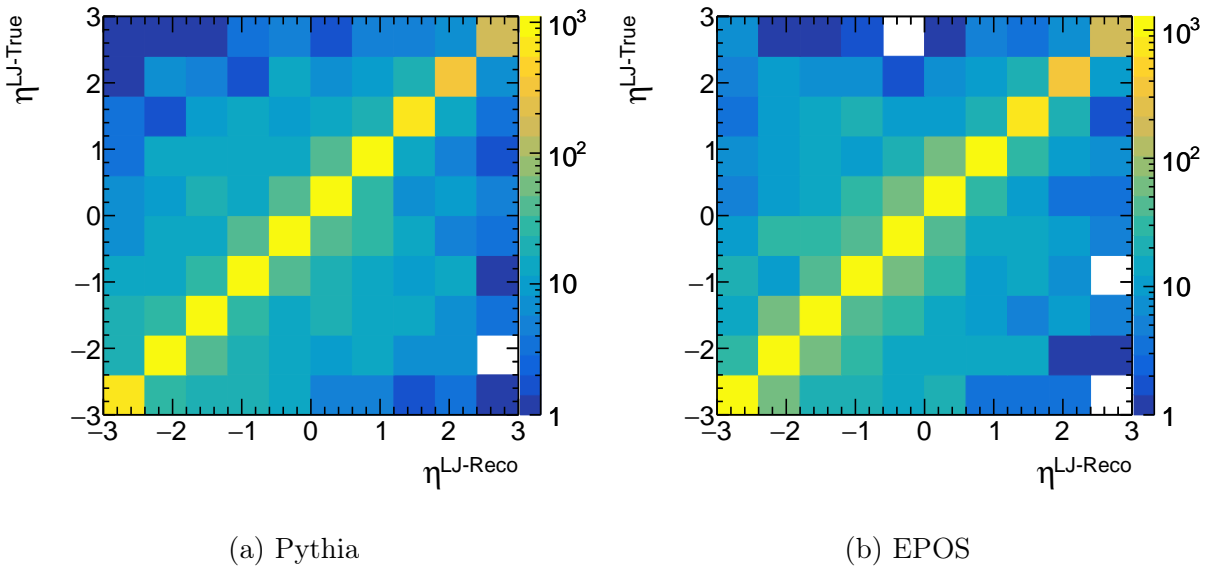


Figure 7.14: Response matrices for fraction of the Pomeron momentum carried by jets η^{LJ} generated with two MC models. Events pass all proton selections with $\xi \in [0.002, 0.160]$.

truth, which means that the unfolding is implemented correctly.

Two other tests exploit uncorrelated samples and help determine the best number of iterations. In the first test, a sample of MC is divided into two parts, with events randomly assigned to one of the subsamples. Then, unfolding is trained on the first subsample and is exploited to unfold the second subsample. The second approach trains unfolding with one

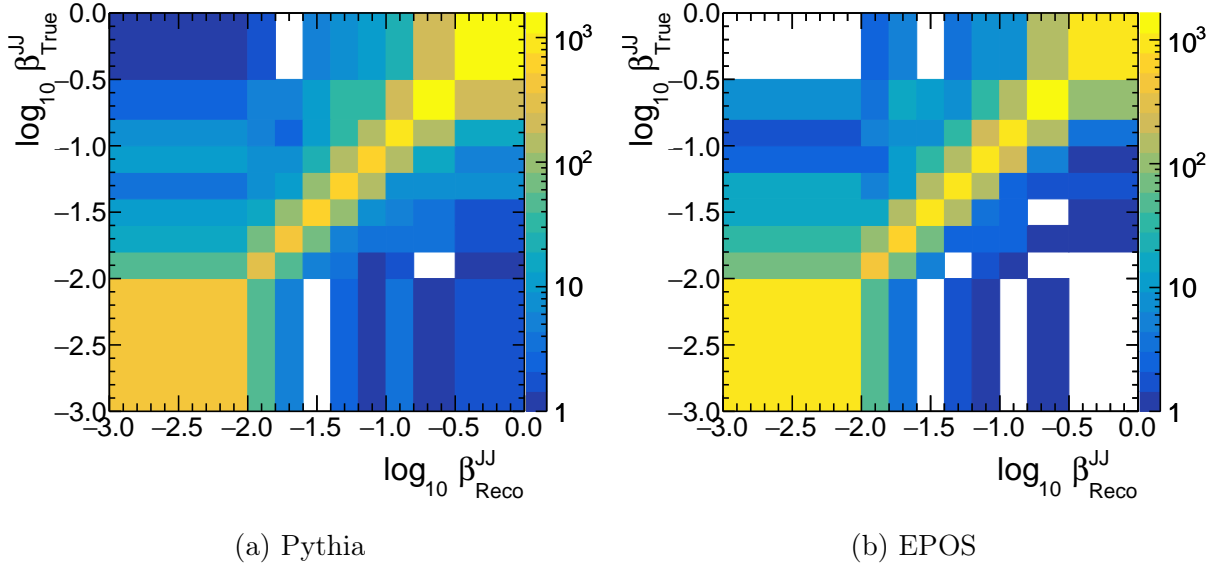


Figure 7.15: Response matrices for fraction of the Pomeron momentum carried by jets β^{JJ} generated with two MC models. Events pass all proton selections with $\xi \in [0.002, 0.160]$.

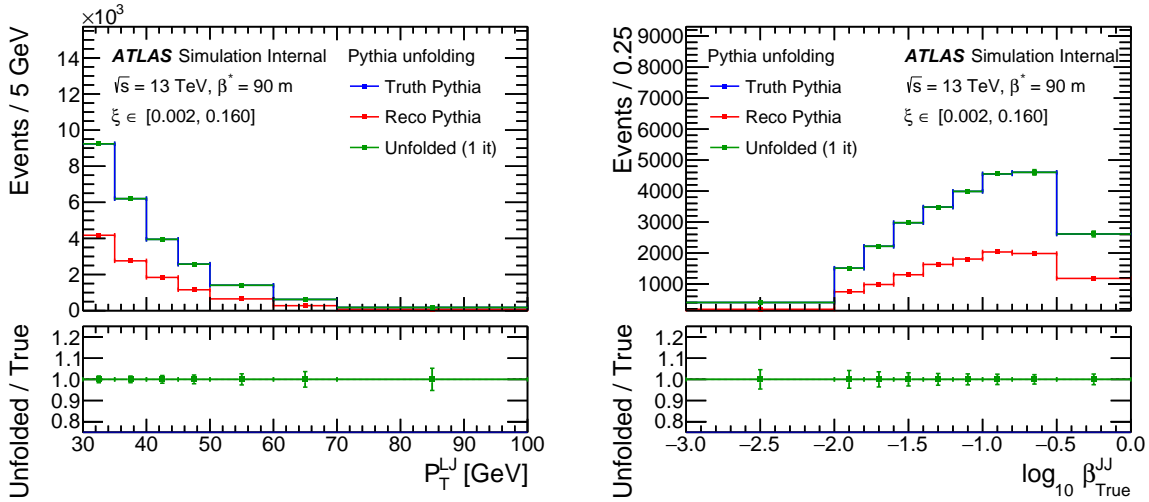


Figure 7.16: A simple closure test for unfolding. The unfolded distributions match the truth distributions, which demonstrates the *RooUnfold* package is exploited correctly.

MC generator, e.g. Pythia, and attempts to unfold the distribution generated by other MC generators, e.g. EPOS. In both cases, the output should resemble the truth level distributions. The results of both closure tests are presented in Fig. 7.17 and Fig. 7.18, for one, three, and five iterations, respectively. The tests show that the best number of iterations for p_T^{LJ} is 3, and for η^{LJ} and β^{JJ} is 1, based on the difference between the true and the unfolded distributions.

The systematic uncertainty arising from the unfolding can be estimated using the following approach. First, the Pythia sample is reweighted on the truth level with a

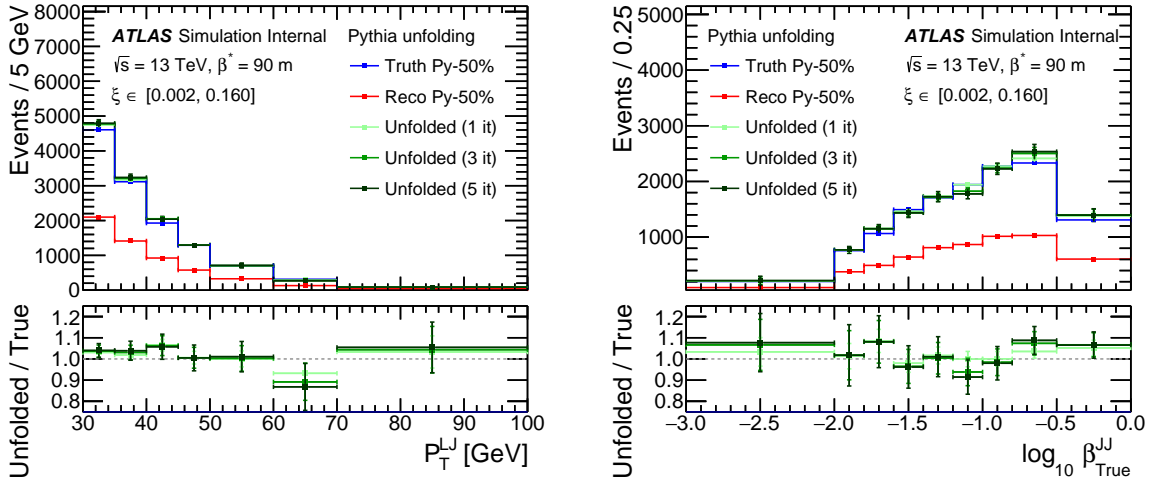


Figure 7.17: First, third and fifth iteration of unfolding for closure test based on two independent samples generated with the same MC model (Pythia). Events pass all proton selections with $\xi \in [0.002, 0.160]$. Only statistical uncertainties are shown.

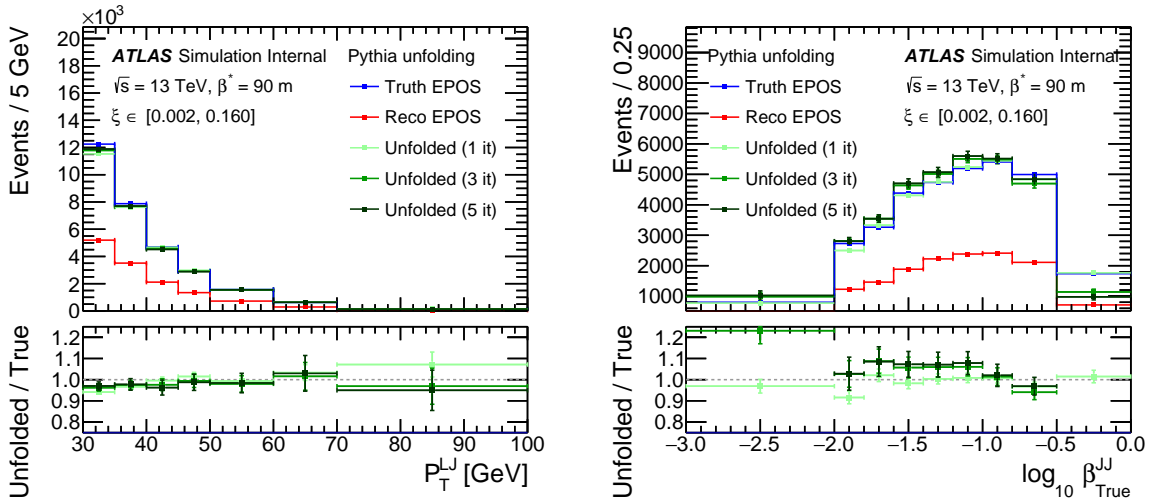


Figure 7.18: First, third and fifth iteration of unfolding for closure test based on two samples generated with two different MC models. The unfolding was based on the response matrix produced by Pythia and the unfolded distributions were generated with EPOS. Events pass all proton selections with $\xi \in [0.002, 0.160]$. Only statistical uncertainties are shown.

smooth function to match the reconstructed distribution with the corresponding data distributions. Then, the reweighted reconstructed distribution can be unfolded and compared with the reweighted truth level. The difference between the unfolded/truth ratio and unity can be considered as the systematic uncertainty arising from unfolding. The plots in Figs. 7.19 to 7.21 show the results in all ranges of ξ . The best number of iterations is consistent with the previous findings. The highest discrepancies are observed for $\xi \in [0.002, 0.160]$, where the statistic is the lowest. For other ranges, the discrepancies

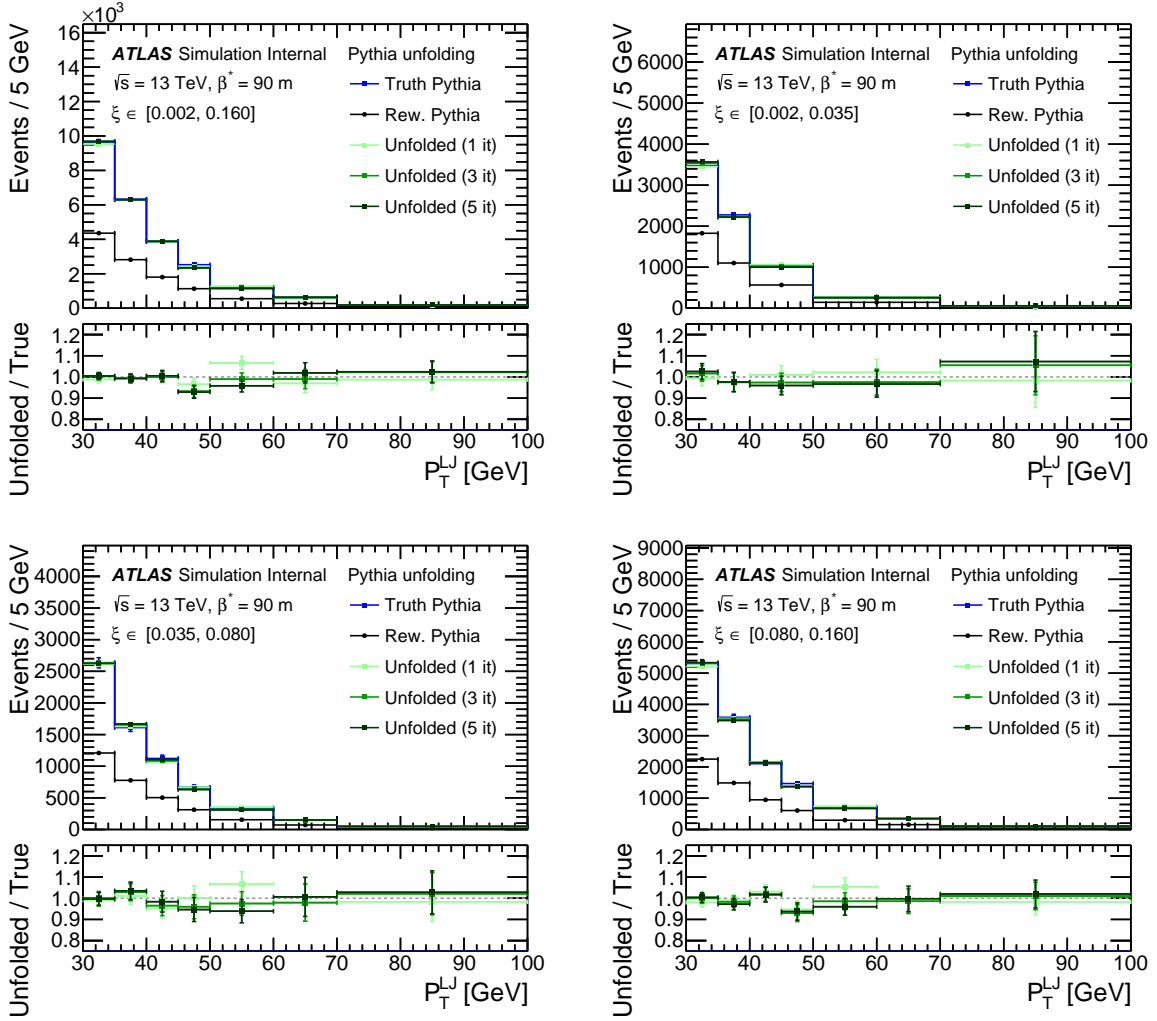


Figure 7.19: Closure tests for unfolding the p_T^{LJ} in four ξ bins. The Pythia sample is reweighed at the true level to match the reconstructed data. The best match between unfolded and reweighed truth distribution is assessed for the third iteration. The difference between unfolded/truth ratio and unity is considered as the systematic uncertainty arising from unfolding. Only statistical uncertainties are shown.

are generally smaller than 5%. The difference between unfolding data with Pythia and EPOS gives the uncertainty estimate that arises from the influence of the MC model.

7.7 Unfolding for CD analysis

Two distributions are studied for the CD process: differential cross sections in terms of relative energy loss $\xi^{PP} = \xi^A \times \xi^C$ and transverse momentum of leading jet p_T^{LJ} . Pythia and EPOS productions were optimised for SD dijet analysis; therefore, the statistic for CD analysis is limited. The Herwig sample was prepared with a two-forward-protons filter; therefore, it provides the highest number of simulated CD dijet events. Still, the sample is

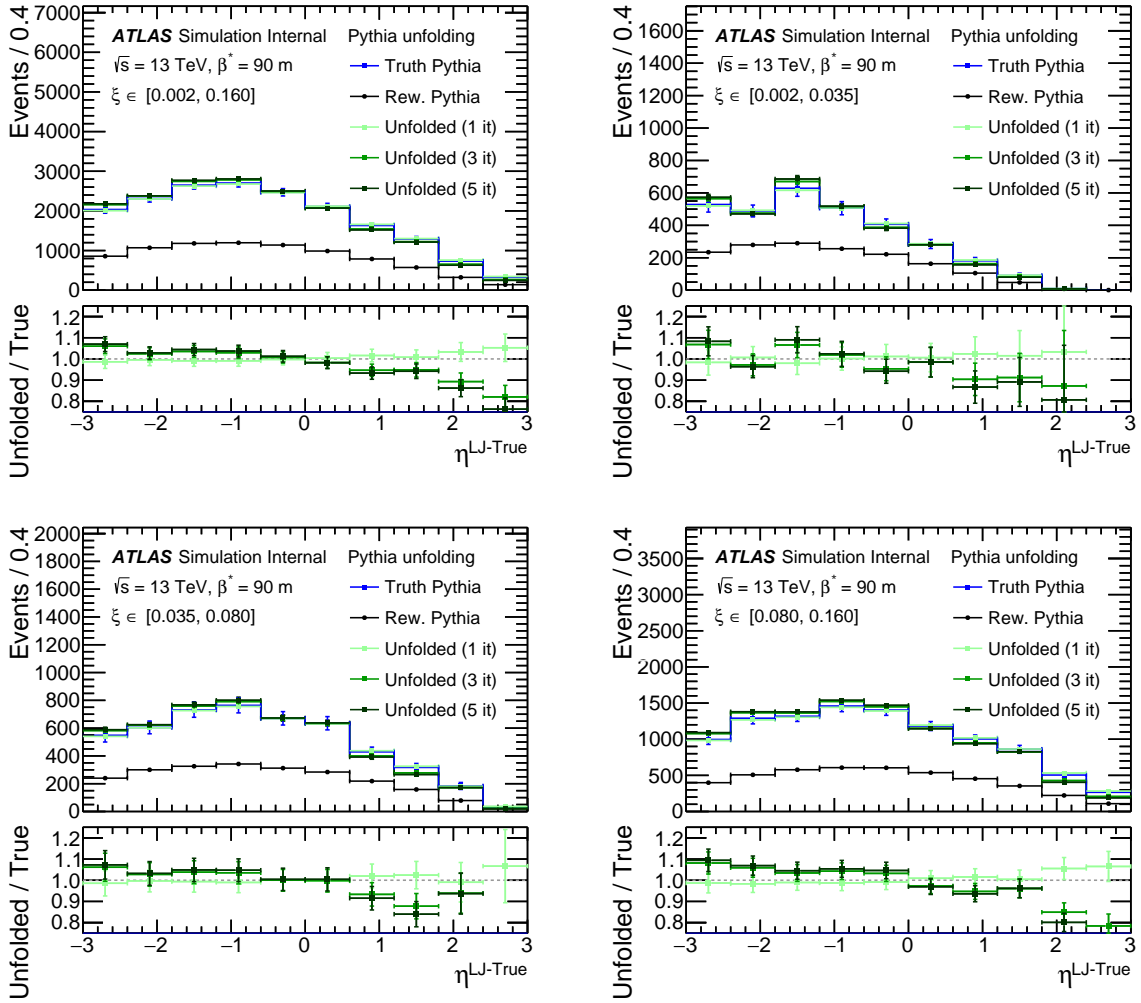


Figure 7.20: Closure tests for unfolding the η^{LJ} in four ξ bins. The Pythia sample is reweighed at the true level to match the reconstructed data. The best match between unfolded and reweighed truth distribution is assessed for the third iteration. The difference between unfolded/truth ratio and unity is considered as the systematic uncertainty arising from unfolding. Only statistical uncertainties are shown.

small and contains only 72/289 events that pass the selections on the reconstruction/truth level. Therefore, the fluctuations make the Bayesian unfolding impractical. Instead, simple bin-by-bin corrections are used. There are no problems with the analysis of ξ^{PP} , because the resolution of this variable is very good. But the bins for p_T^{LJ} have to be larger than those of the SD analysis due to the migrations for p_T^{LJ} .

The ratio between the reconstructed and the true level for both variables is shown in Fig. 7.22. The ratio is used to unfold the distributions obtained from the collected data. The plots show that the ratio is nearly constant and approaches 0.25, which is the ratio between the total number of reconstruction/truth events. It is indicated by a grey dashed line on the lower pad. The obtained value agrees with the SD analysis: the acceptance of ALFA measured for a single proton is about 0.5. This value must be squared for CD,

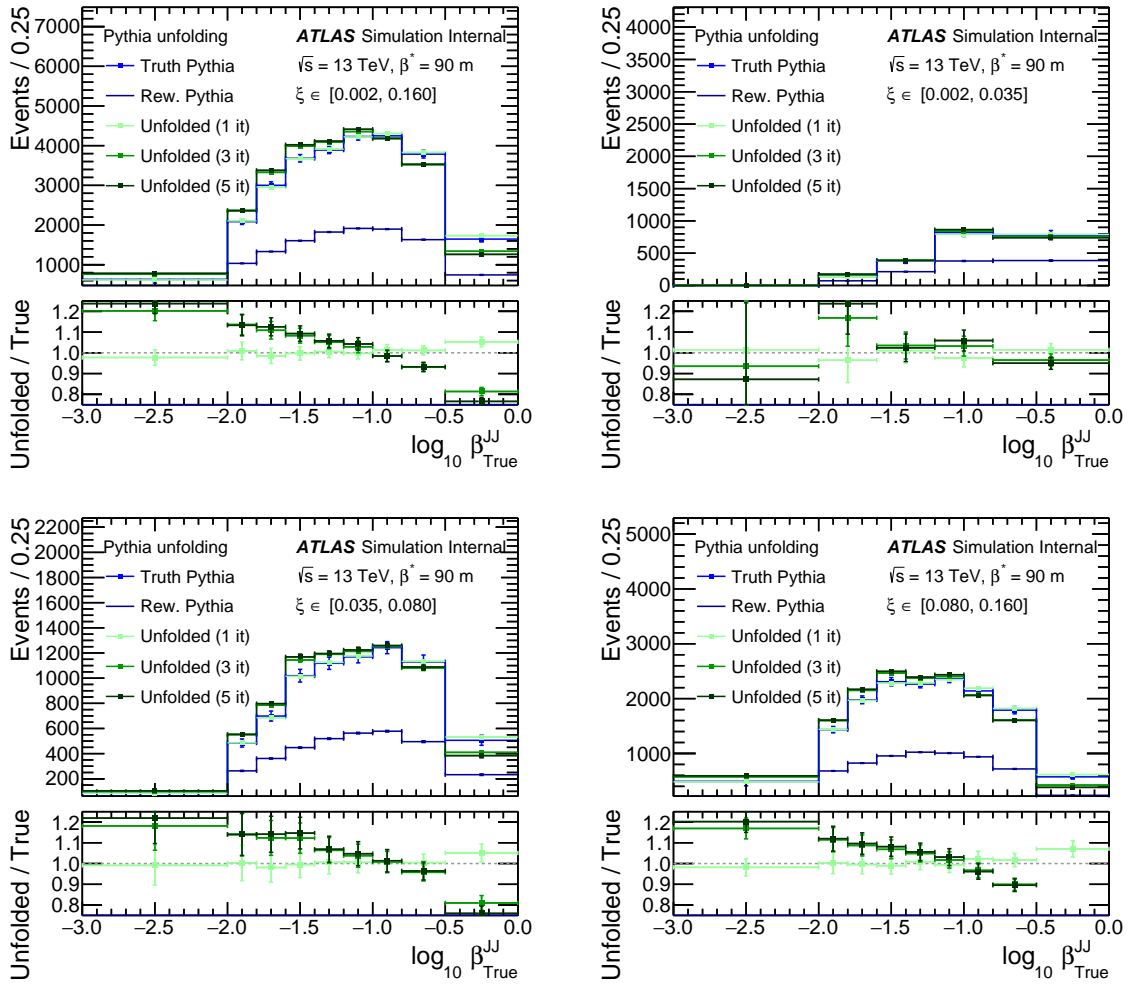


Figure 7.21: Closure tests for unfolding the β^{JJ} in four ξ bins. The Pythia sample is reweighed at the true level to match the reconstructed data. The best match between unfolded and reweighed truth distribution is assessed for the third iteration. The difference between unfolded/truth ratio and unity is considered as the systematic uncertainty arising from unfolding. Only statistical uncertainties are shown.

since the two protons are uncorrelated in an inclusive process to a first approximation. Therefore, a normalisation scale of 0.25 is used to correct for the CD distributions, and the deviations in Fig. 7.22 are used as a systematic uncertainty.

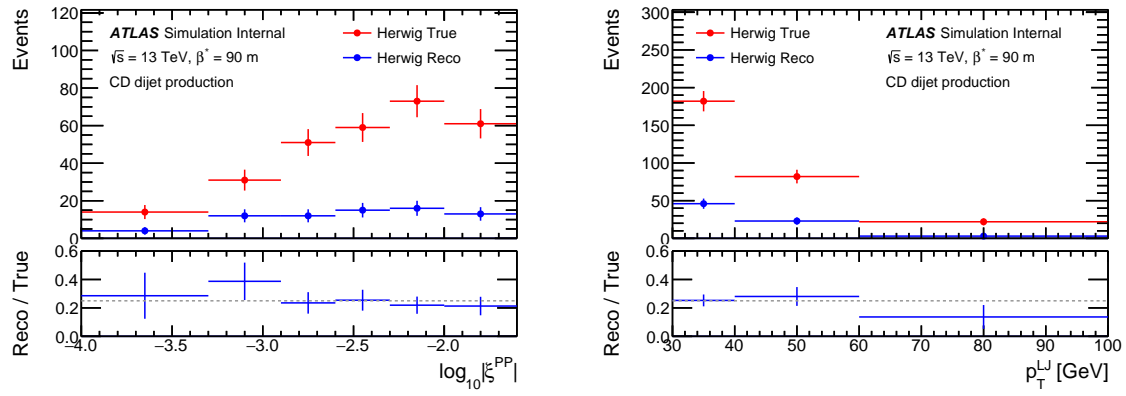


Figure 7.22: Reconstructed and true level distributions of $\log_{10} |\xi^{PP}|$ and p_T^{LJ} in the CD samples generated with Herwig. The dashed lines in the ratio panels mark the 0.25 level corresponding to the ratio of the total numbers of reconstruction/truth events that pass selections.

Chapter 8

Systematic uncertainties

Each part of this analysis introduces separate systematic errors in the final results. This section shows the methods by which the main sources of systematic uncertainties are assessed. They are grouped into six categories: trigger, jet calibration, jet efficiencies, ALFA systematics, unfolding, and remaining sources. Since systematic uncertainties from different sources are not correlated here, in the end together, they are added in the quadrature to obtain the total systematic uncertainty of the measurement.

Jet calibration dominates the total uncertainty. Other sources can be slightly overestimated, as long as they are significantly smaller than the calibration impact. For most sources, the analysis is repeated twice with the parameter in question varied away from the nominal value in both directions. The difference between the obtained results provides an estimate of the uncertainty for a given source. The impact of each source is presented in detail for two parameters: ξ and p_T^{LJ} for SD analysis. The remaining variables, including p_T^{LJ} for different ranges of ξ and the analysis of CD, are presented in the summary of this section.

8.1 Jet trigger uncertainties

This analysis exploits the events with jets below the trigger efficiency plateau. The base uncertainty for the tag-and-probe method is derived from Bayesian statistics, implemented in *TEfficiency* class with *ROOT* framework [108]. The trigger efficiency is estimated for each bin separately; therefore, statistical uncertainties are not correlated. For events with multiple jets, the uncertainty of efficiency can be determined by applying the uncertainty propagation rule to Eq. (5.1) [109]:

$$u(\epsilon_{\text{multijet}}) = \sqrt{\sum_i \left(u(\epsilon_{\text{jet}}^i) \cdot \prod_{j \neq i} (1 - \epsilon_{\text{jet}}^j) \right)^2}, \quad (8.1)$$

where ϵ_{jet}^i is the efficiency of the i -th jet. The $u(\epsilon_{\text{multijet}})$ has the same properties as the uncertainty for a single jet, and the value $\epsilon_{\text{multijet}} \pm u(\epsilon_{\text{multijet}})$ falls in the range $[0, 1]$ by definition. The Eq. (8.1) is correct for both the lower and upper bounds.

The propagation of the Bayesian uncertainty of the trigger is estimated by varying the efficiency by $u(\epsilon_{\text{multijet}})$ in both directions. Changes have the greatest impact on events

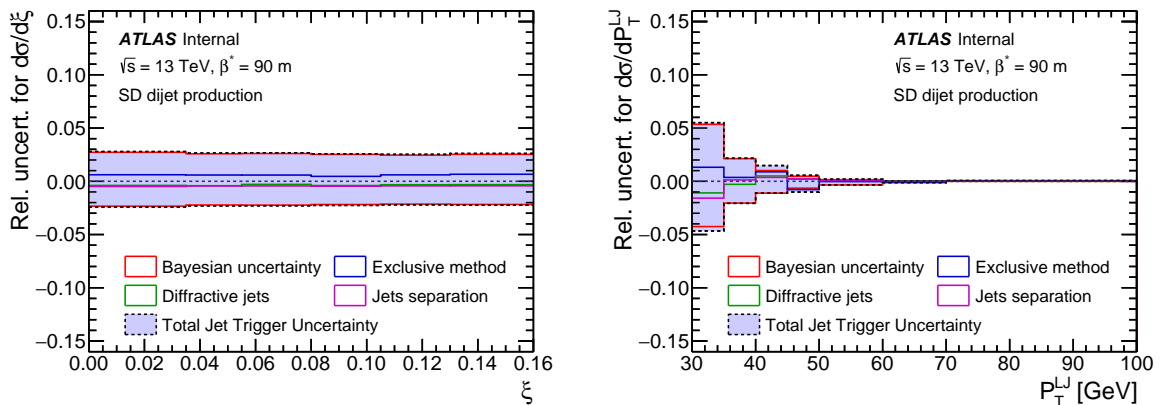


Figure 8.1: The propagation of trigger uncertainty in the functions of ξ and p_T^{LJ} for SD analysis. The livid distribution shows the total jet trigger uncertainty, which overlaps with the dominating Bayesian uncertainty.

with a low p_T^{LJ} , up to 5%, as can be seen in Fig. 8.1. It decreases for higher p_T^{LJ} , where efficiency reaches 100%. For other variables, which are less correlated with p_T^{LJ} , e.g. ξ in Fig. 8.1, the uncertainty is usually constant and less than 2.5%.

Fig. 8.1 shows also the studies of different models used during the estimation of trigger efficiency. The red line corresponds to the difference between exclusive and inclusive methods: the first utilises all jets in the MBTS sample and the second exploits multijet events in the L1_J12 triggered sample (default). The sample is dominated by accidental events and ND jets. Therefore, an additional test is performed to verify if the trigger is sensitive to the type of process. The blue line shows the difference in efficiencies calculated with an SD-enriched sample with anti-accidental cuts. Small values, usually less than 1%, reveal that the jet trigger is practically model-independent. The last study is about jet separation - the green line expresses the results when all jets are exploited, including non-isolated jets.

The livid distribution in Fig. 8.1 shows the total uncertainty of the jet trigger, calculated as the sum in the quadrature. It overlaps with Bayesian uncertainty, which dominates over other sources of uncertainty. The ALFA triggers are not investigated, as the efficiency is proved to be approximately equal to 99.9% [78, 28].

8.2 Jet calibration uncertainties

Due to the exponential and rapid decrease in jet transverse momenta in diffractive processes, cross-sectional measurements are sensitive to the jet calibration coefficients. A small variation causes a significant migration of events into and out of the fiducial region with requirements of p_T , as well as migrations between different bins of p_T^{LJ} .

Jet calibration uncertainties consist of the JES uncertainties combined with the *in situ* results: inter-calibration and absolute scale, and are summarised in Section 5.4.7. The propagation is presented in Fig. 8.2. The uncertainty distributions are regular and have values in the range of 15-20%. The most significant are the absolute calibration (cyan),

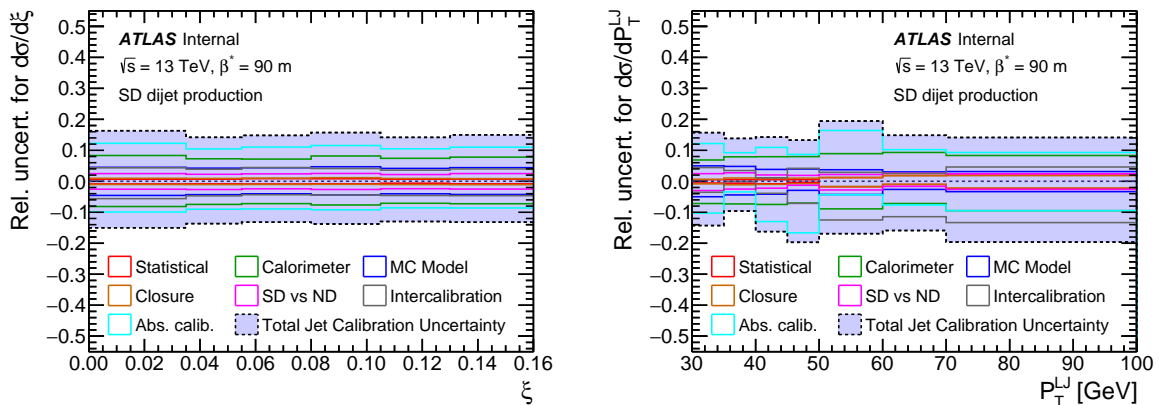


Figure 8.2: The propagation of jet calibration uncertainty in the functions of ξ and p_T^{LJ} for SD analysis. The livid distribution shows the total jet calibration uncertainty. The scale is larger compared to most plots in this chapter. The lines' colours correspond to the colours in the Section 5.4.7.

calorimeter (green), and inter-calibration (grey). The livid strips correspond to the total jet calibration uncertainty, relative to the measured differential cross sections. Jet Energy Resolution propagation is not shown, because it is included in the *in situ* uncertainties.

8.3 Jet efficiencies uncertainties

Jet-based uncertainties are complemented by studies of jet efficiency with results in Fig. 8.3. Two factors are considered: jet cleaning efficiency and jet reconstruction efficiency. The first is estimated with a variation of the overlapping removal parameters by 0.1: the momentum ratio $p_T^{\text{lepton}}/p_T^{\text{jet}}$ (red) and the distance between the jet and the lepton ΔR (blue). The second parameter has negligible impact, but the cross section is significantly dependent on the overlap removal ratio parameter; the uncertainty is up to 5%. Additional distinction rules between jets and leptons could improve this value.

The propagation of the efficiency of jet reconstruction is based on the results summarised in Section 5.3. The effect is small - around 1% - because the jet reconstruction is fully efficient for leading jets with $p_T^{\text{LJ}} > 30$ GeV and about 99% efficient for secondary jets with $p_T^{\text{SJ}} > 20$ GeV. The uncertainties are summed in quadrature, and the total uncertainty of the jet efficiency is shown as a livid strip in Fig. 8.3.

8.4 ALFA based uncertainties

Three sources of ALFA systematic uncertainties are considered. The first is the efficiency of the ALFA reconstruction. This propagates to the normalisation factors for single and double proton distributions with 2% and 3% respectively.

ALFAProton package is used for the reconstruction of proton energy and momentum, and it provides uncertainties of the reconstructed values. Due to this, estimation of the impact of proton kinematic reconstruction is possible. It is done by varying the evaluated

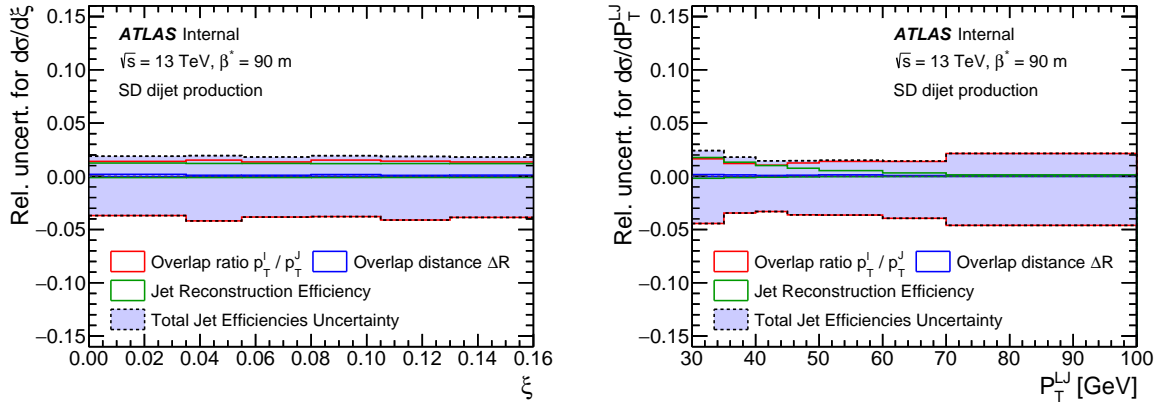


Figure 8.3: The propagation of jet efficiencies uncertainty in the functions of ξ and p_T^{LJ} for SD analysis. The livid distribution shows the total jet efficiency uncertainty.

energy or proton momentum by the uncertainty in both directions. The examples for ξ and p_T^{LJ} are presented in Fig. 8.4. As expected, the uncertainty of energy has the greatest impact for the smallest ξ bins, including the p_T^{LJ} and β^{JJ} distributions for $\xi \in [0.002, 0.035]$. The uncertainty of proton momentum has negligible impact except for the t distribution, where it can be up to 5%.

To estimate the effect of alignment uncertainty on diffractive analysis, the complete analysis can be performed with several alignment sets, according to Section 4.8. The envelope of the deviations from the nominal set for each alignment parameter is taken as the systematic uncertainty. At first approximation, the parameters should be independent. Then the total alignment uncertainty can be calculated with all parameter uncertainties summed in squares. The total effect is small for all plots, less than 2%.

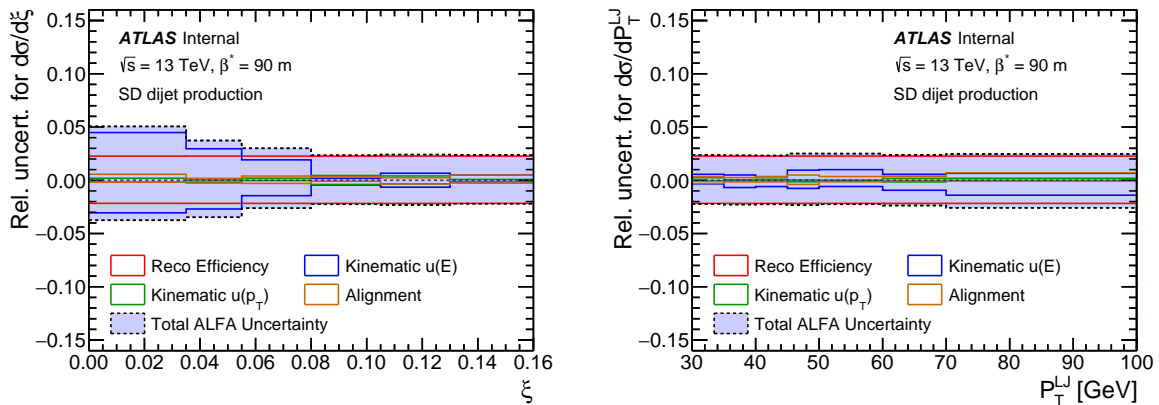


Figure 8.4: The propagation of ALFA uncertainties in the functions of ξ and p_T^{LJ} for SD analysis. The livid distribution shows the total ALFA systematic uncertainty.

8.5 Unfolding uncertainties

The uncertainties of the unfolding procedure are estimated differently for the distributions. Both ξ and t exploit the bin-by-bin corrections. The statistical uncertainty for the reconstructed/true level ratio is used as the first estimation of unfolding. The correlation between both levels is neglected, which overestimates the uncertainty. However, the values are 3-5% and are much lower than the jet calibration uncertainties. The difference between the data corrected with Pythia and EPOS is used as the second input to the estimation. Both sources are presented for ξ in Fig. 8.5 on the left.

The dependence of the MC model is also the source of unfolding uncertainty for p_T^{LJ} and β^{JJ} . The difference between data corrected with Pythia and EPOS is usually less than 10% - Fig. 8.5 on the right. The Bayesian unfolding is also verified with closure tests. The MC sample is reweighed at the true level to match the reconstructed and data distributions, and the differences between the unfolded and true distributions are used as an estimate of the unfolding procedure.

For CD plots, there is no statistic for the Bayesian unfolding process, and the constant normalisation factor of 0.25 is used to correct the data. The uncertainty is estimated as the deviation between 0.25 and the reconstructed/true ratio presented in Fig. 7.22.

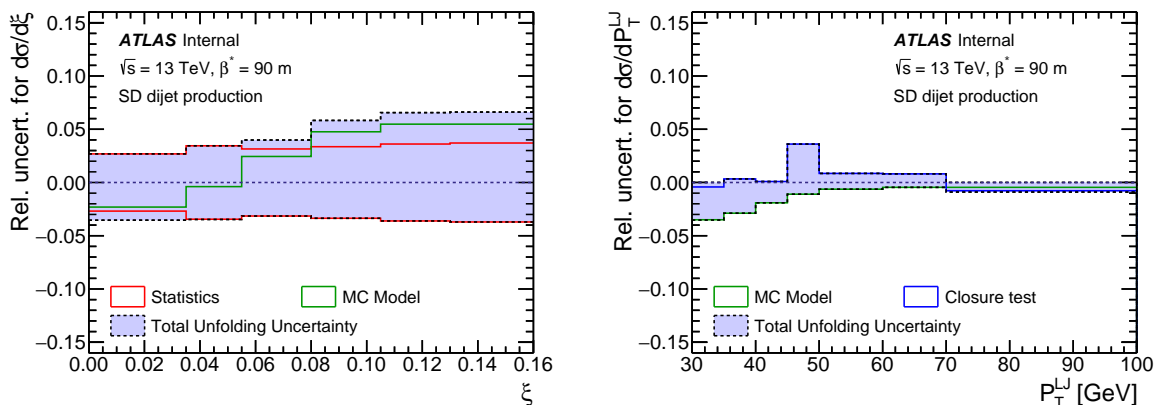


Figure 8.5: The propagation of unfolding uncertainties in the functions of ξ and p_T^{LJ} for SD analysis. The livid distribution shows the total unfolding systematic uncertainty.

8.6 Other systematic uncertainties

A few remaining systematic uncertainty sources are not included in previous groups:

- Luminosity - the ALFA diffractive campaign in October 2015 collected data with an integrated luminosity of 725.0 nb⁻¹. This value was estimated by ATLAS measurements with 2.1% uncertainty [77], which is propagated to cross section as the uncertainty of the normalisation constant.
- Accidental background - the background is normalised to the data with methods described in Section 6.2. The normalisation factors have about 10% uncertainties for

SD analysis and 20% for CD analysis. The background is reduced by anti-accidental selection; therefore, it has a small impact on the final results, about 1%.

- Primary vertex - two requirements are applied to vertices: the requirement on the primary vertex and veto on additional pileup vertices. Both help improve the quality of the sample but can introduce bias. The effect of the first requirement is studied by allowing events without primary vertices. It is small, only 0.5% of events do not have vertices, because the analysis requires two jets.
- Pileup correction - Section 7.1 describes the normalisation that must be applied to the data to compensate for pileup veto inefficiencies. The difference between the observed and estimated values is used as the uncertainty of the normalisation constant. It equals 2.4%.
- Left-right asymmetry - some detector effects can manifest with left-right asymmetry. Therefore, the SD sample is divided into two groups according to the side with the reconstructed protons. Differences between both groups are usually less than 2%.

The total of the other systematic uncertainties is calculated as the sum in quadrature of the other systematic uncertainties mentioned above. All of them are presented in Fig. 8.6. The values are less than 4% for all distributions.

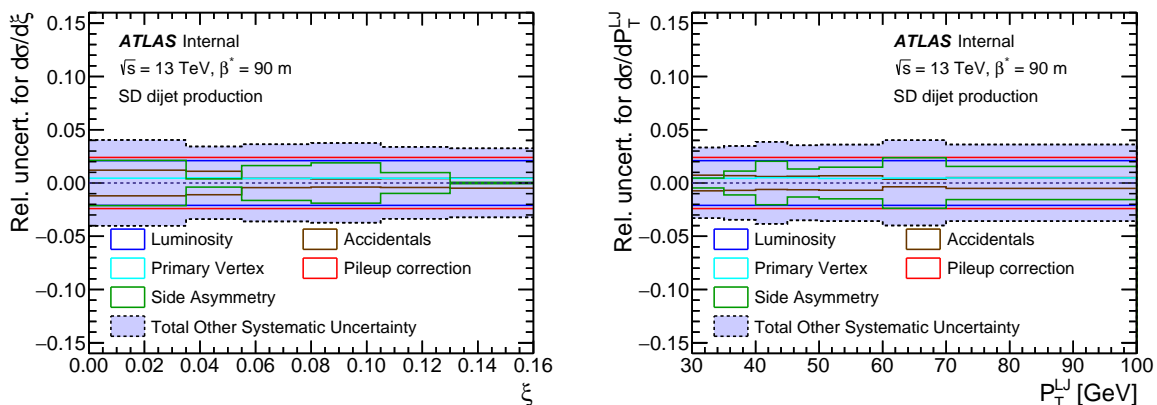


Figure 8.6: The propagation of remaining uncertainties in the functions of ξ and p_T^{LJ} for SD analysis. The livid distribution shows the total other systematic uncertainty.

8.7 Uncertainties summary

Plots in Figs. 8.7 to 8.11 present the total systematic uncertainties for each of the differential cross sections analysed. The total uncertainty is calculated as the sum in quadrature of each of the uncertainties mentioned.

For most variables, the main source of uncertainty is due to jet calibration, with about 15-20%, while others are typically less than 10%. The exceptions are the p_T^{LJ} and β^{JJ} distributions for the smallest bin of the ξ and CD distributions, where the uncertainties of proton energy or unfolding are also significant. The total systematic uncertainty for these plots can reach 40%.

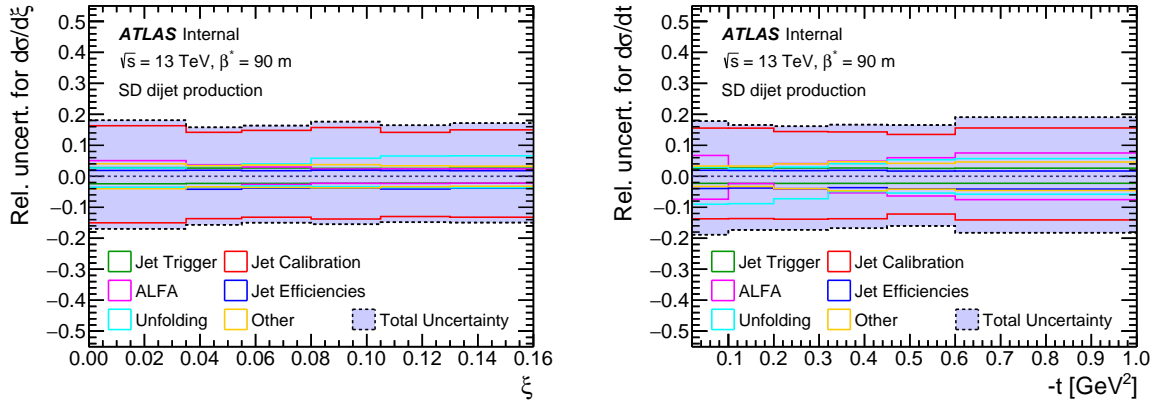


Figure 8.7: The propagation of uncertainties in the functions of ξ and t for SD analysis. The livid distribution shows the total systematic uncertainty.

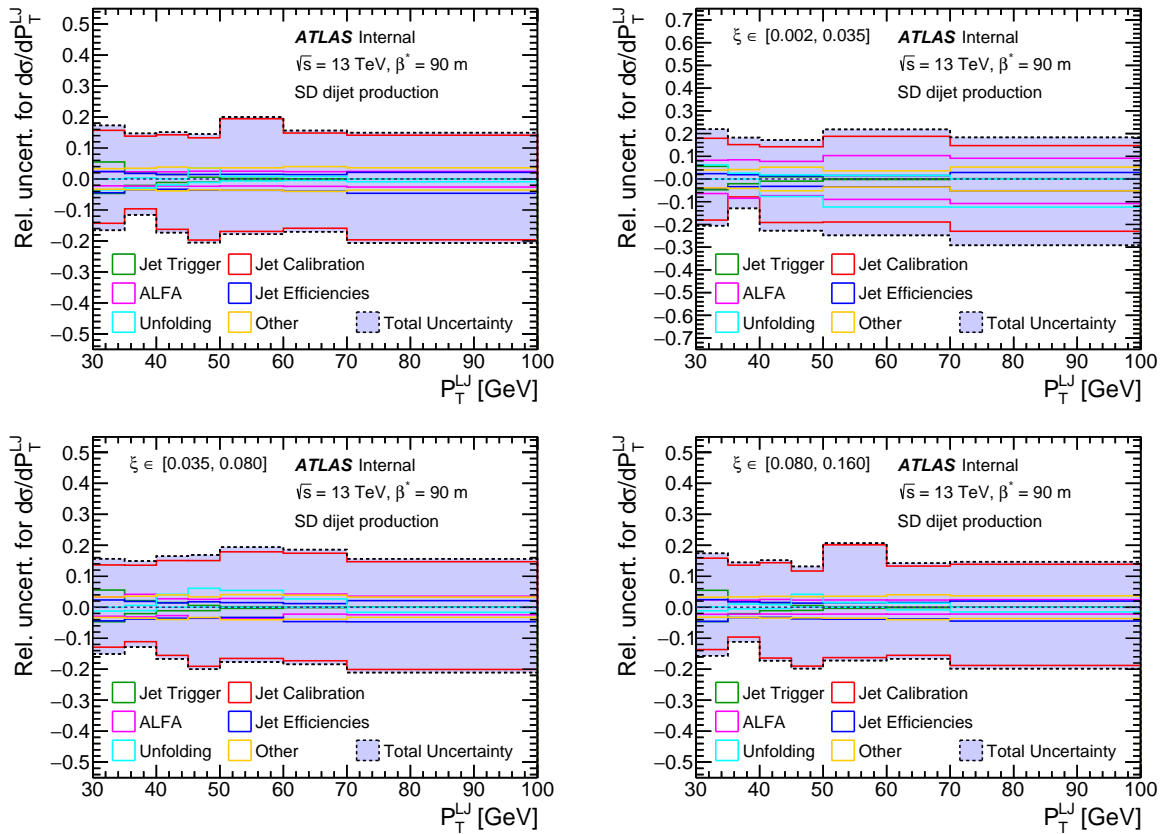


Figure 8.8: The propagation of uncertainties in the functions of p_T^{LJ} for SD analysis in different bins of ξ . The livid distribution shows the total systematic uncertainty.

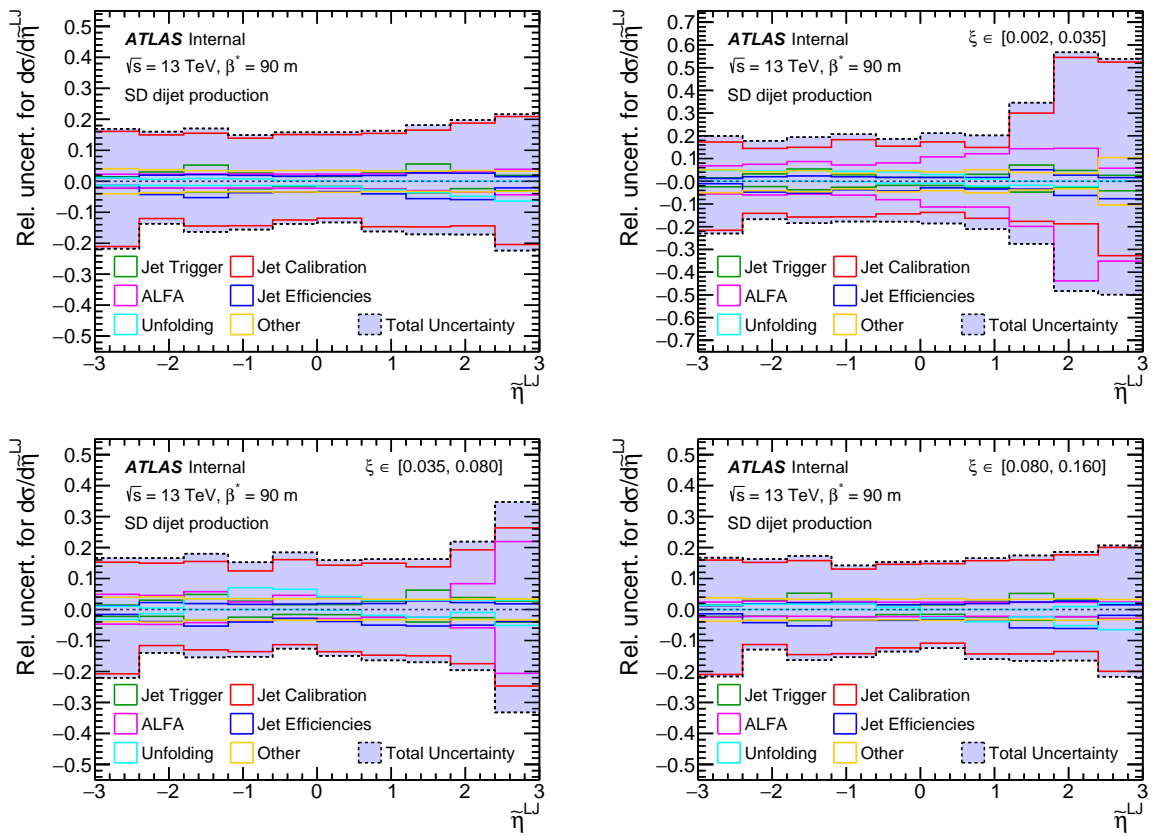


Figure 8.9: The propagation of uncertainties in the functions of η^{LJ} for SD analysis in different bins of ξ . The livid distribution shows the total systematic uncertainty. The high uncertainties for positive η^{LJ} for small ξ are observed in not populated region.

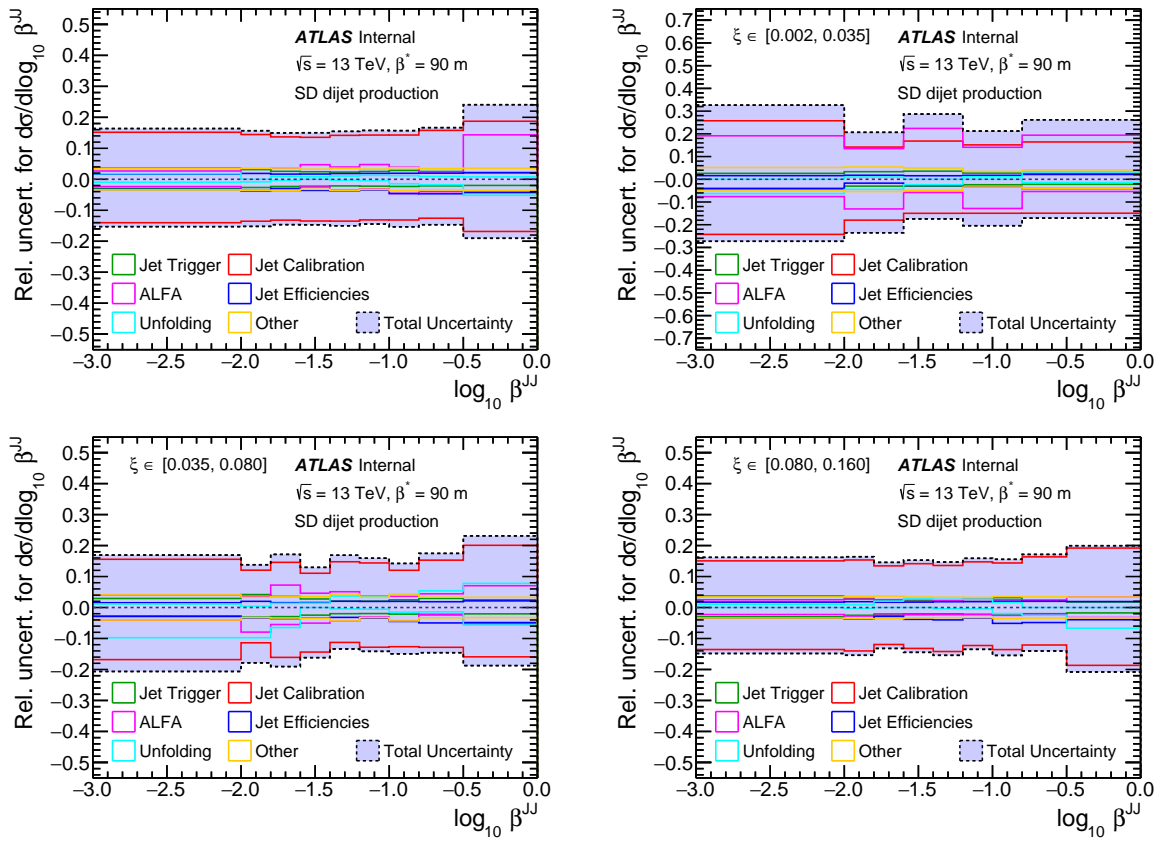


Figure 8.10: The propagation of uncertainties in the functions of β^{JJ} for SD analysis in different bins of ξ . The livid distribution shows the total systematic uncertainty.

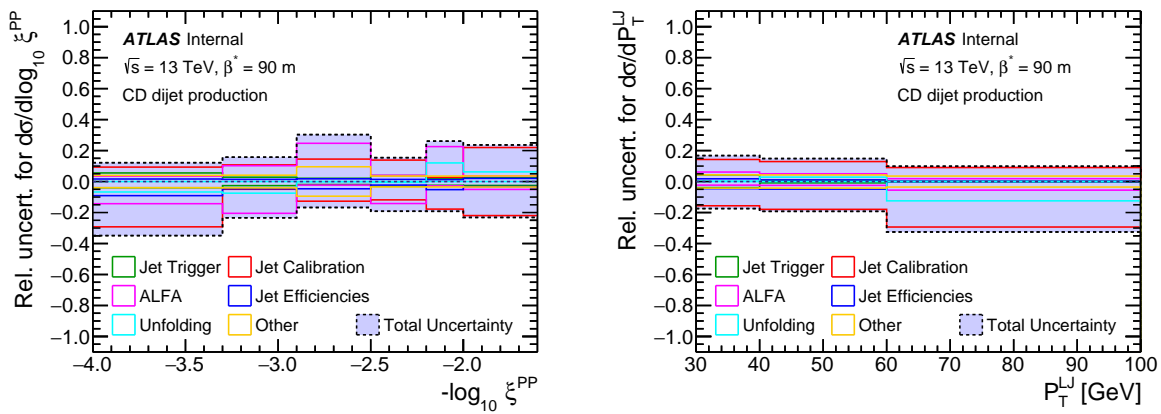


Figure 8.11: The propagation of uncertainties in the functions of ξ^{PP} and p_T^{LJ} for CD analysis. The livid distribution shows the total systematic uncertainty.

Chapter 9

Results

This chapter presents the outcome of diffractive dijet measurement with proton tagging, for single and central diffractive events. The main results for SD analysis are differential cross sections obtained for key proton variables ξ and t and jet-based variables p_T^{LJ} , η^{LJ} and β^{JJ} . For CD, the differential cross sections are presented in terms of ξ^{PP} and p_T^{LJ} .

The differential cross sections measured as a function of a general variable X and in bins of width ΔX are obtained as follows:

$$\frac{d\sigma}{dX} = \frac{\mathcal{U}\{N_{DATA} - N_{BKGD}\}}{\Delta X \int \mathcal{L} dt}. \quad (9.1)$$

The numerator expresses the unfolded numbers of signal events in a particular bin of X , after correcting for detector effects. Integral $\int \mathcal{L} dt$ denotes the luminosity of the analysed data sample. The total cross section for a process can then be calculated as the integral:

$$\sigma_{tot} = \int_X \frac{d\sigma}{dX} dX. \quad (9.2)$$

In the following figures, which present differential cross sections, black points represent the unfolded data, with vertical lines corresponding to the statistical uncertainties. The total systematic uncertainties are shown as the livid-coloured bands. The signal is compared with the predictions of MC generators: Pythia 8 (red), EPOS (blue), and Herwig (green, for CD analysis only). All results are obtained for the fiducial selection criteria:

- $\xi \in [0.002, 0.160]$, $t \in [0.02, 1.00] \text{ GeV}^2$,
- $p_T^{LJ} > 30 \text{ GeV}$, $|\eta^{LJ}| < 3.0$,
- $p_T^{SJ} > 20 \text{ GeV}$, $|\eta^{SJ}| < 4.0$.

For the CD process, both protons must meet the first condition.

9.1 Dijets production in single diffraction

9.1.1 Differential cross section

Bin widths for differential cross sections are determined based on the resolution of each variable, available statistics, and unfolding stability. No additional studies were performed

to optimise the edges of the bins. No subtle distribution structures are expected, and the bins can be wider. For the variable ξ , the ranges of common acceptance of ALFA and AFP (described in Section 7.2) were taken into account. The following bin edges for SD analysis were chosen:

- relative energy loss ξ : 0.002, 0.035, 0.055, 0.080, 0.105, 0.130, 0.160;
- squared four-momentum transfer t : 0.02, 0.10, 0.20, 0.32, 0.45, 0.60, 1.00 [GeV²];
- transverse momentum of leading jet p_T^{LJ} : 30, 35, 40, 45, 50, 60, 70, 100 [GeV];
- pseudorapidity of leading jet η^{LJ} : -3.0, -2.4, -1.8, -1.2, -0.6, 0.0, 0.6, 1.2, 1.8, 2.4, 3.0;
- fraction of the Pomeron momentum carried by jets $\log_{10} \beta^{\text{JJ}}$: -3.0, -2.0, -1.8, -1.6, -1.4, -1.2, -1.0, -0.8, -0.5, 0.0.

For the smallest ξ region, $\xi^I \in [0.002, 0.035]$, statistics is insufficient to provide the stability of some variables. Therefore, the bins are wider for:

- p_T^{LJ} : 30, 35, 40, 50, 70, 100 [GeV];
- $\log_{10} \beta^{\text{JJ}}$: -3.0, -2.0, -1.6, -1.2, -0.8, 0.0.

The differential cross sections in terms of proton variables: ξ and t are presented in Fig. 9.1. Statistical fluctuations are small, and the systematic uncertainty for each bin is about 20%. The data distribution in terms of ξ is flat for low ξ but increases for larger ξ , which was not observed for lower energies [52]. MC does not describe the data very well,

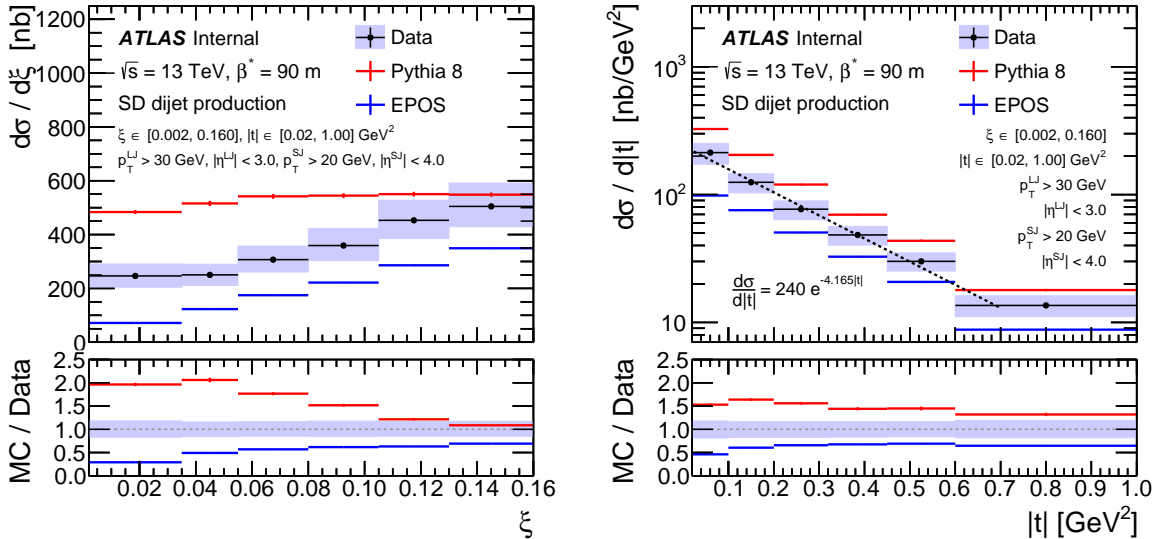


Figure 9.1: The differential cross sections as functions of the proton variables ξ and t for SD dijet production. Data is compared to two MC models, Pythia 8 (red) and EPOS (blue). The exponential fit result for $d\sigma/dt$ is shown in the right plot.

both the normalisation and the shape. Compared to the data, Pythia 8 provides an almost flat distribution. For the lowest ξ , the ratio MC/data is equal to two and decreases to one for higher ξ . On the other hand, EPOS underestimates data about twice, but predicts a rising distribution. Both generators have unique mechanisms (hard diffraction in Pythia and SD' events in EPOS), but probably simultaneous use of both mechanisms is required to describe the data. There is also a possibility that the rapidity gap survival probability S^2 depends on ξ .

The differential cross section in terms of t is well described by the exponential function, shown in Eq. (1.37). The parameter B is proportional to the obstacle size in the scattering process. The fit to data provides the following value:

$$B = 4.168 \pm 0.041 \text{ (stat)} \begin{matrix} +0.195 \\ -0.229 \end{matrix} \text{ (syst)} \text{ GeV}^{-2}. \quad (9.3)$$

Systematic uncertainty contains all the sources described in Chapter 8, extended by the one based on the fit range. The nominal fit includes all bins except the last one; the uncertainty was estimated by also excluding the first bin or including the last one. For MC, only the statistical error is estimated. The values are:

$$B^{\text{Pythia8}} = 4.514 \pm 0.051 \text{ (stat)} \text{ GeV}^{-2}, \quad (9.4)$$

and

$$B^{\text{EPOS}} = 3.390 \pm 0.039 \text{ (stat)} \text{ GeV}^{-2}. \quad (9.5)$$

The measured value is between the predicted values. It is also smaller than the results provided by TOTEM measurement for $\sqrt{s} = 8 \text{ TeV}$ [52]:

$$B^{\text{TOTEM}} = 5.8 \pm 0.5 \text{ (stat)} \begin{matrix} +1.0 \\ -1.0 \end{matrix} \text{ (syst)} \text{ GeV}^{-2}. \quad (9.6)$$

The plots in Figs. 9.2 and 9.3 show the differential cross section in terms of the leading jet variables: p_T^{LJ} and $\tilde{\eta}_T^{\text{LJ}}$, and Fig. 9.4 show β^{JJ} . All the mentioned distributions are provided in the full range and in three subranges of ξ . The most prominent dependency on ξ is observed for $\tilde{\eta}_T^{\text{LJ}}$. The distributions shift to larger $\tilde{\eta}_T^{\text{LJ}}$ for higher ξ range (the positive $\tilde{\eta}_T^{\text{LJ}}$ means that the jet has the same direction as the measured proton). In addition, the MC/data ratio changes significantly for each ξ range.

9.1.2 Total cross section

The value of the total cross section for SD dijet production in the fiducial region calculated from the data equals:

$$\sigma_{\text{JJ}}^{\text{SD}} = 57.2 \pm 0.8 \text{ (stat)} \begin{matrix} +9.6 \\ -8.7 \end{matrix} \text{ (syst)} \text{ nb}. \quad (9.7)$$

The systematic contributions to the uncertainties are provided in Table 9.1. The values of total systematic uncertainties are calculated by adding different uncertainty contributions in quadrature. The high systematic uncertainty is due to jet calibration, about 15% of the total value.

For MC, only statistical uncertainties are evaluated. Pythia 8 overestimates this total cross section:

$$\sigma_{\text{JJ}}^{\text{SD-Pythia8}} = 83.6 \pm 1.6 \text{ (stat)} \text{ nb}, \quad (9.8)$$

when EPOS underestimates it about twice:

$$\sigma_{\text{JJ}}^{\text{SD-EPOS}} = 32.4 \pm 0.7 \text{ (stat)} \text{ nb}. \quad (9.9)$$

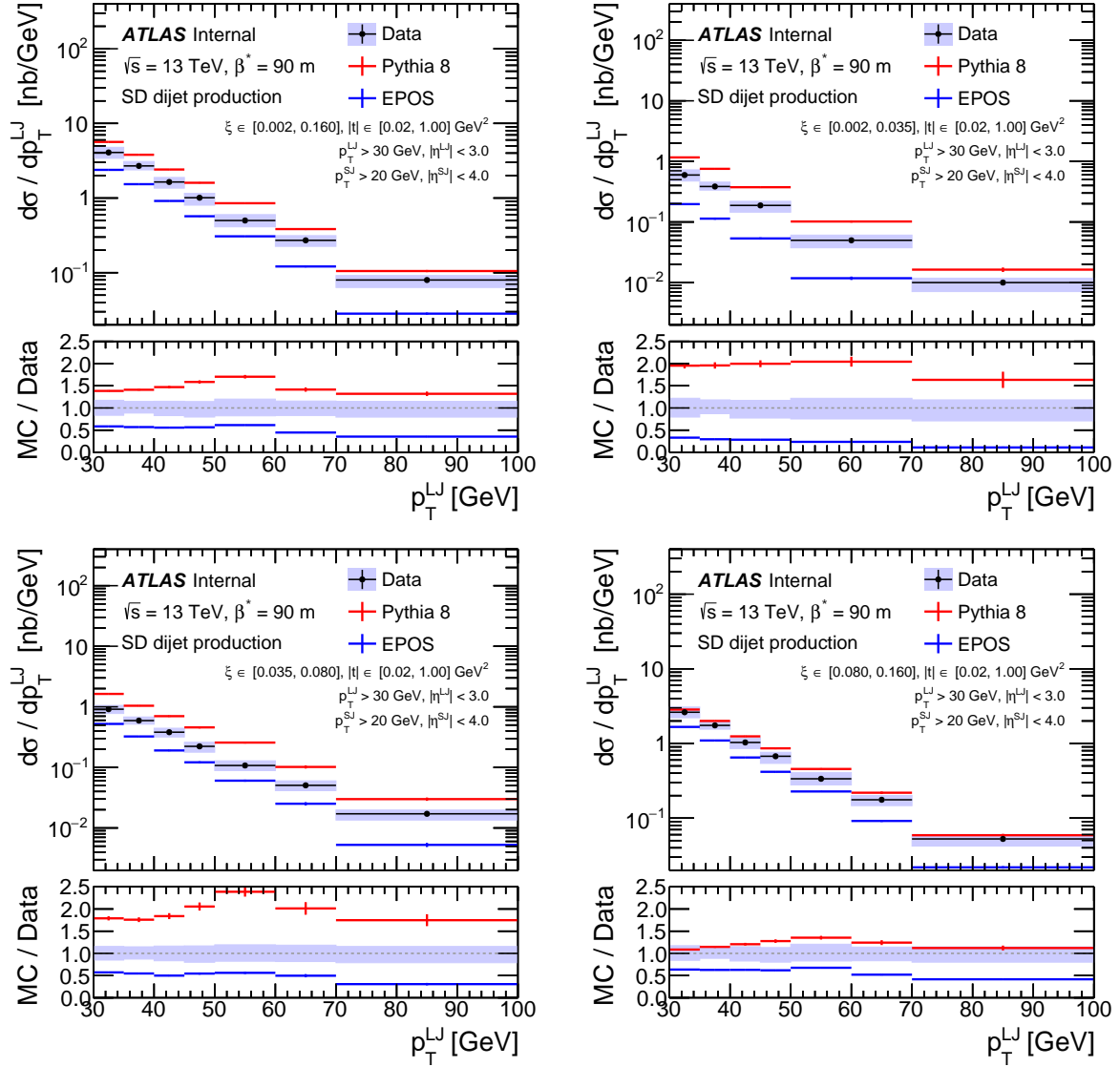


Figure 9.2: The differential cross section for leading jet transverse momentum p_T^{LJ} for SD dijet production, shown for full range and three subranges of ξ . Data is compared to two MC models, Pythia 8 (red) and EPOS (blue).

9.1.3 Contribution of the SD component

To further improve the description of the data, the MC generators are reweighted on the true level to match with the data. For this, the MC/data ratio observed for the ξ and β^{JJ} distributions in Figs. 9.1 and 9.4 can be fitted with a polynomial function. The procedure is repeated iteratively to find the best combination of polynomials of ξ and β^{JJ} .

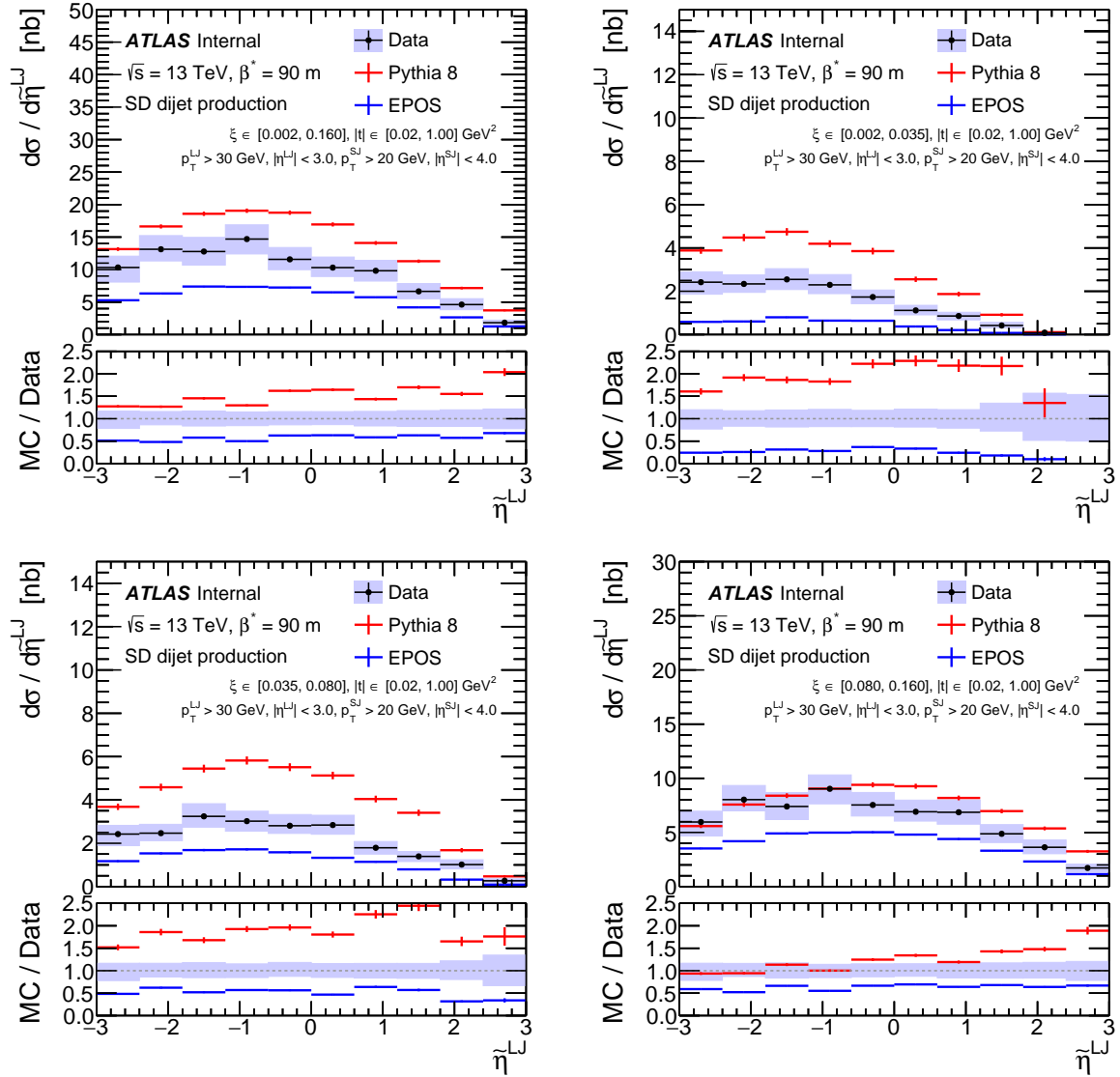


Figure 9.3: The differential cross section for leading jet transverse momentum η^{LJ} for SD dijet production, shown for full range and three subranges of ξ . Data is compared to two MC models, Pythia 8 (red) and EPOS (blue).

The satisfactory results for Pythia 8 are obtained after applying the weights:

- $f_{p1}(\xi) = 0.806 + 19.1\xi - 278\xi^2 + 992\xi^3$,
- $f_{p2}(\log_{10} \beta^{JJ}) = 2.509 - 1.631 \log_{10} \beta^{JJ} + 0.503 \log_{10}^2 \beta^{JJ} - 0.055 \log_{10}^3 \beta^{JJ}$.

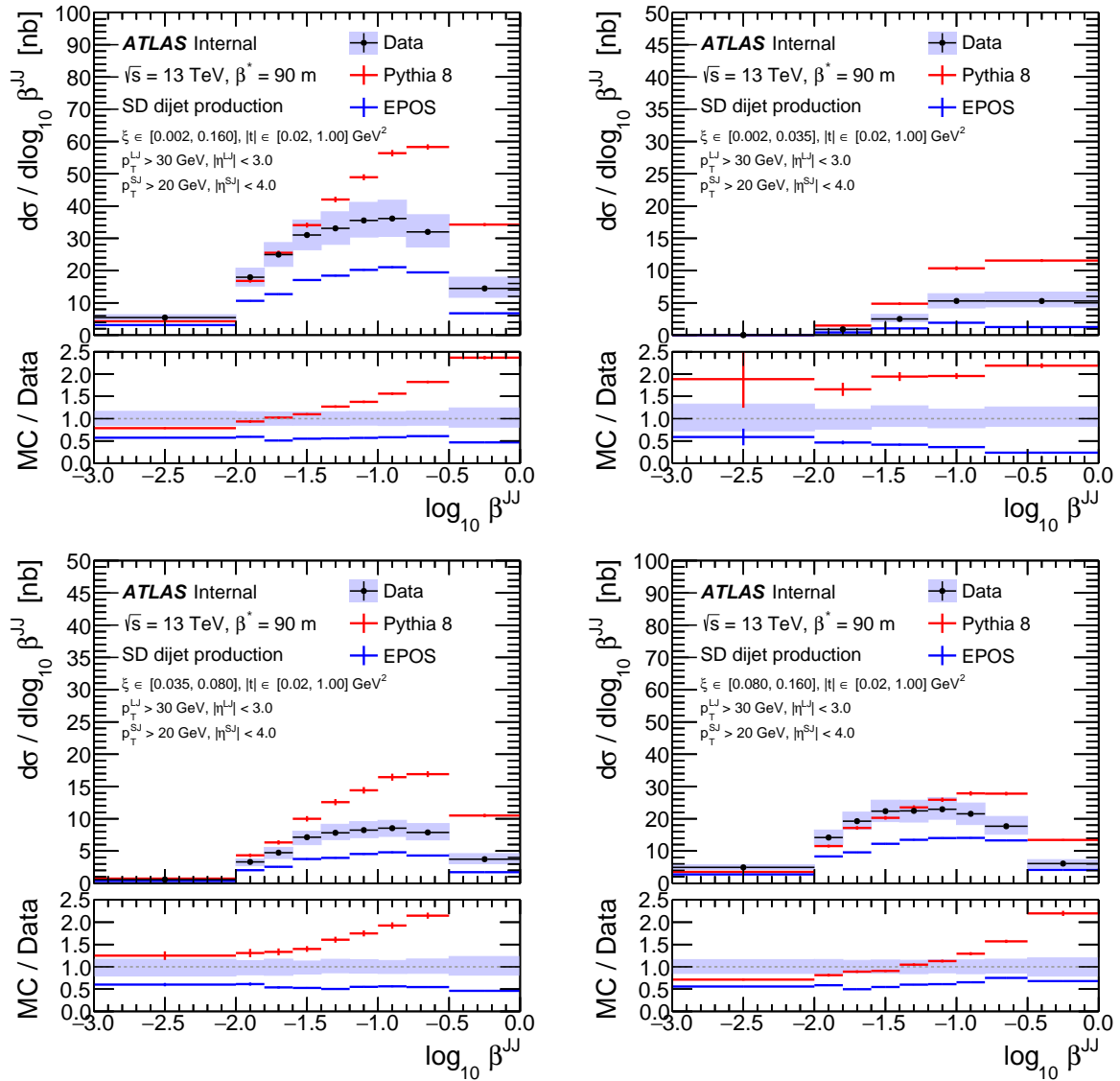


Figure 9.4: The differential cross section for fraction of the Pomeron momentum carried by jets β^{JJ} for SD dijet production, shown for full range and three subranges of ξ . Data is compared to two MC models, Pythia 8 (red) and EPOS (blue).

The polynomials for the EPOS sample are the following:

- $f_{E1}(\xi) = 0.093 + 24.3\xi - 226\xi^2 + 741\xi^3$,
- $f_{E2}(\log_{10} \beta^{JJ}) = 0.318 + 0.548 \log_{10} \beta^{JJ} - 0.434 \log_{10}^2 \beta^{JJ} + 0.099 \log_{10}^3 \beta^{JJ}$.

Source	σ_{JJ}^{SD} [nb]	σ_{JJ}^{CD} [pb]	$\sigma_{JJ}^{\text{incl}}$ [nb]	R_{SD}	B [GeV $^{-2}$]
Nominal value	57.2	329	2407	0.0238	4.168
Statistical	± 0.8	± 59	± 38	± 0.0004	± 0.041
Jet Trigger (up)	+1.5	+11	+154	+0.0003	+0.001
Jet Trigger (low)	-1.2	-9	-33	-0.0009	-0.001
Jet Calibration (up)	+8.5	+45	+682	+0.0061	+0.049
Jet Calibration (low)	-7.7	-55	-767	-0.0025	-0.027
Jet Efficiencies (up)	+1.1	+6	+5	+0.0005	+0.003
Jet Efficiencies (low)	-2.2	-14	-19	-0.0008	-0.001
ALFA (up)	+1.7	+32	-	+0.0006	+0.035
ALFA (low)	-1.5	-32	-	-0.0006	-0.039
Unfolding (up)	+3.0	+24	+5	+0.0001	+0.110
Unfolding (low)	-2.0	-26	-18	-0.0004	-0.052
Other (up)	+2.0	+14	+77	+0.0013	+0.038
Other (low)	-2.0	-14	-201	-0.0001	-0.042
Fit range (up)	-	-	-	-	+0.144
Fit range (low)	-	-	-	-	-0.214
Total systematic (up)	+9.6	+61	+703	+0.0063	+0.195
Total systematic (low)	-8.7	-71	-793	-0.0028	-0.229

Table 9.1: The nominal values and statistical and systematic contributions to the uncertainties for the integrated cross sections σ_{JJ}^{SD} , σ_{JJ}^{CD} and $\sigma_{JJ}^{\text{incl}}$, as well as for the ratio of SD to inclusive dijet production R_{SD} and the slope parameter B . ALFA does not affect the $\sigma_{JJ}^{\text{incl}}$ measurement. The systematic uncertainty of the fit range applies only to B . The values of total systematic uncertainties are calculated by adding different uncertainty contributions in quadrature.

The results of reweighting are shown in Fig. 9.5. The MC/data ratio improves significantly. On the basis of the reweighted samples, the contribution of the SD component for the measured distributions can be evaluated. The results are presented in Fig. 9.6 and Fig. 9.7, for Pythia 8 and EPOS generator, respectively. The MC samples are separated into SD/SD', DD, CD and ND components.

According to both generators, the SD/SD' events dominate the distributions. For Pythia 8, the SD process comprises about 90% of the observed events. The ratio is higher for the smallest ξ or t , with about 98% for the first bin of ξ , and decreases for higher values. There is a small contribution from ND events, but the CD and DD events are negligible. For EPOS, the SD' contribution is more uniform, approximating 82% of the inelastic interactions. It also predicts a significant number of CD events, about 15%. ND contribution is less than 2% and DD contribution is negligible. The high purity of the data sample is possible due to the proton tagging and ξ^{P} vs $\tilde{\xi}_{\text{CAL}}^{\text{X}}$ cut, which reduces the accidental background significantly.

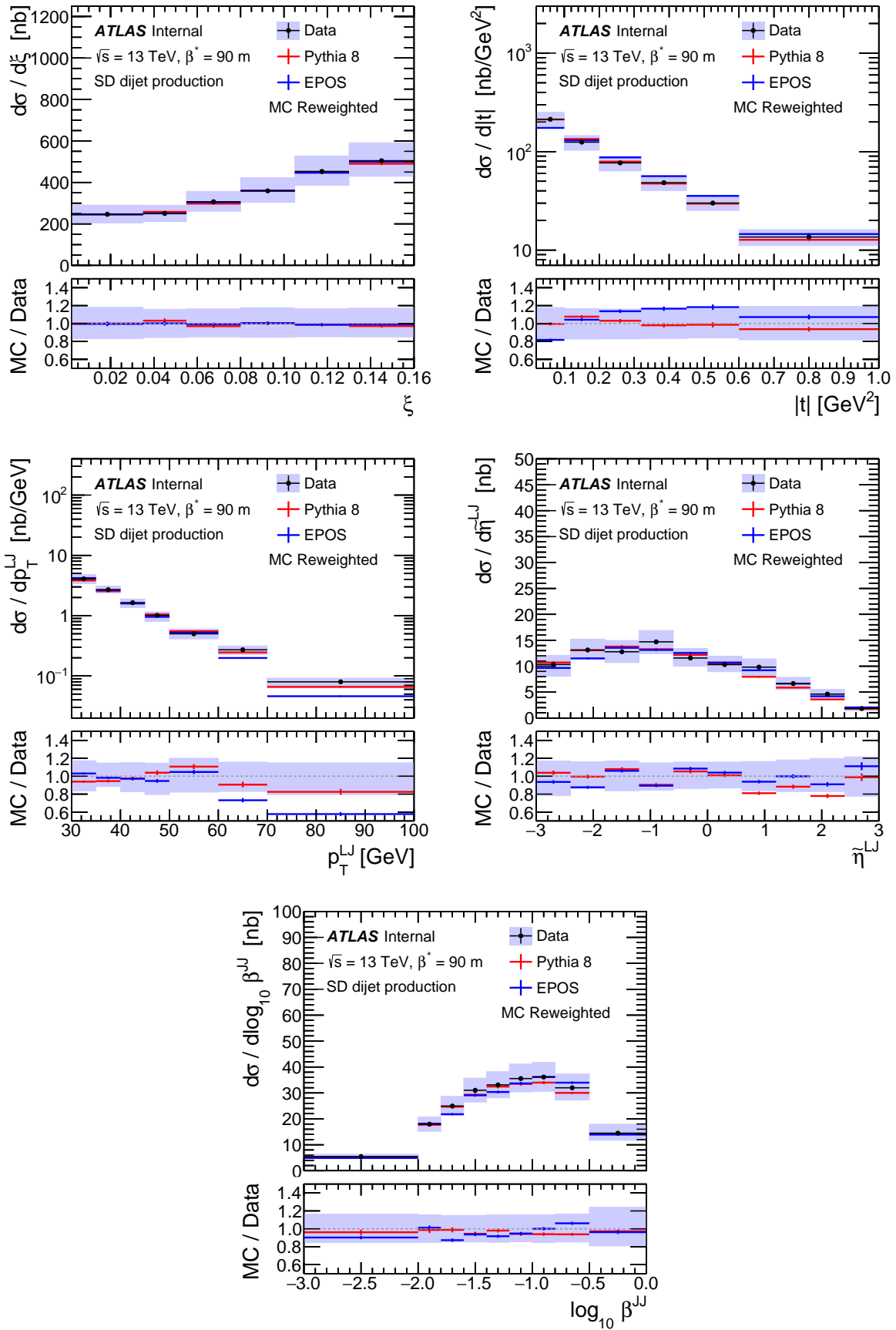


Figure 9.5: The differential cross sections for SD process after MC reweighting. All plots are presented for the full range of $\xi \in [0.002, 0.160]$.

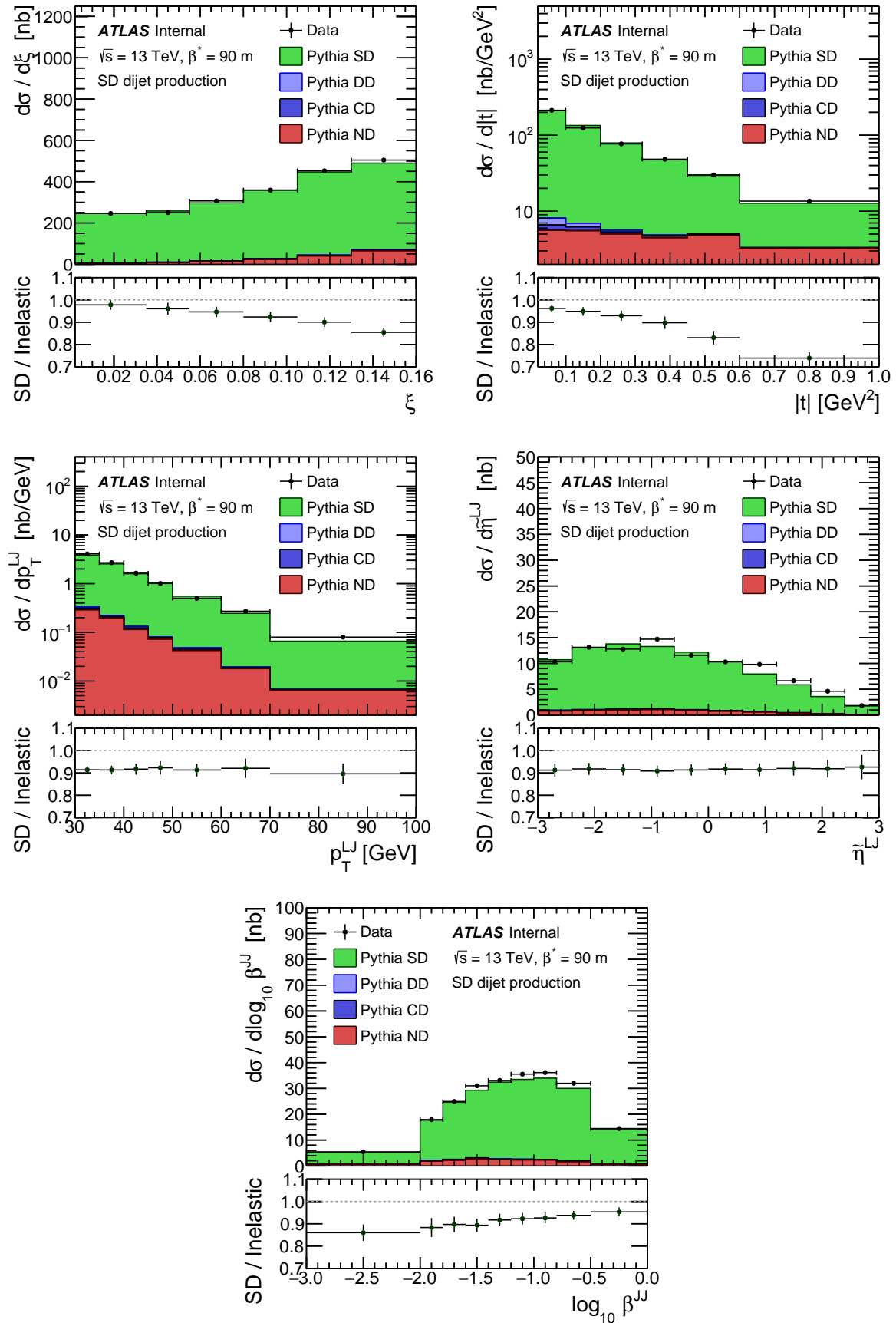


Figure 9.6: The comparison between data and Pythia 8 distributions after reweighting. The MC is separated into SD, DD, CD and ND components. The bottom pads show the SD contribution. All plots are presented for the full range of $\xi \in [0.002, 0.160]$.

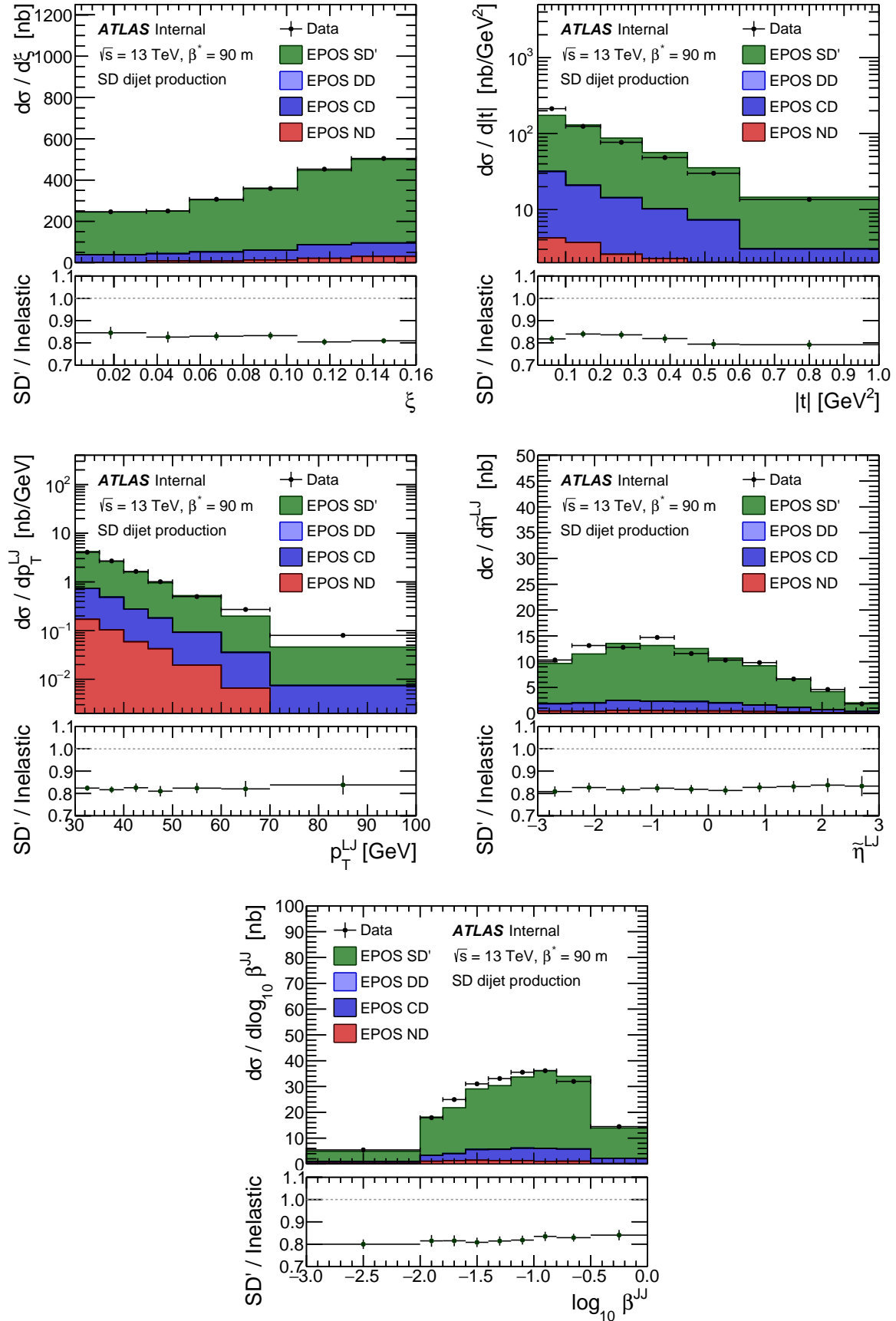


Figure 9.7: The comparison between data and EPOS distributions after reweighting. The MC is separated into SD', DD, CD and ND components. The bottom pads show the SD' contribution. All plots are presented for the full range of $\xi \in [0.002, 0.160]$.

9.1.4 The ratio of the SD to inclusive dijet production

Trigger L1_MBTS_1 has almost 100% efficiency for the SD dijet events. Nevertheless, the data collected with this trigger cannot be used as the base for SD analysis, due to the enormous prescaling of about 19200. However, it can be used to estimate the cross section for inclusive dijet production, which is produced in all inelastic events, especially in ND events.

The differential cross section for inclusive dijet production is evaluated in the function of leading jet transverse momentum p_T^{LJ} , similarly to the SD analysis. The unfolding process can be neglected, as is proved in Fig. 9.8. It compares the distributions of p_T^{LJ} between the reconstruction level (red) and the true level (blue), and the ratio is almost one. The plots are based on the Pythia 8 sample, ignoring the scattered protons. Total uncertainty analysis is performed, excluding the ALFA component, and the results are presented in Fig. 9.9. Similarly to SD analysis, the dominant source of uncertainty comes from jet calibration, which is at the level of 25-40%.

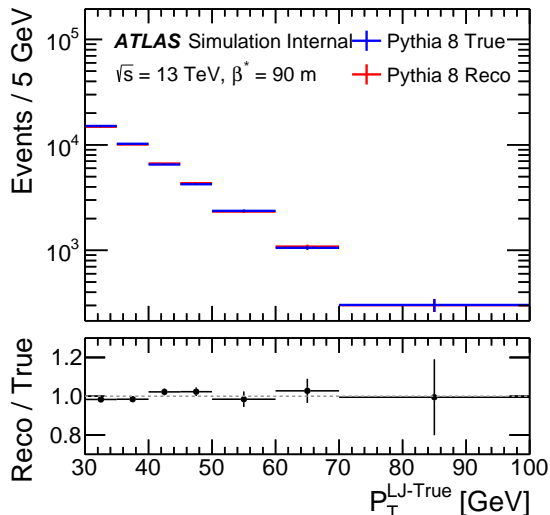


Figure 9.8: The ratio between reconstruction (red) and true (blue) levels for dijet production. Based on the Pythia 8 sample, ignoring forward proton measurement.

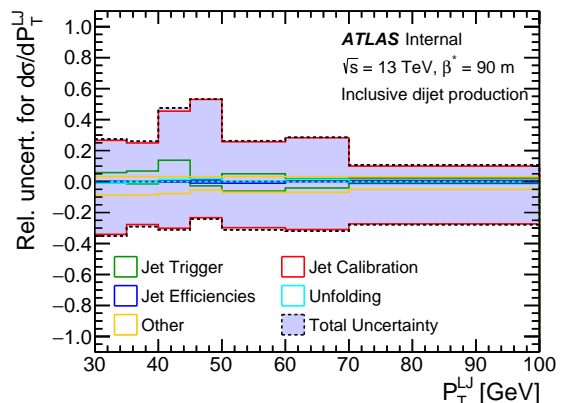


Figure 9.9: The systematic uncertainties for inclusive dijet production. Jet calibration is the dominant source of uncertainty.

The differential cross section for inclusive and diffractive dijet production is compared in Fig. 9.10. The ratio of SD to inclusive dijet production R_{SD} is added below. It seems to be increasing as a function of p_T^{LJ} , starting from 1% to 8%. The total cross sections for inclusive dijet production in the jet fiducial region are evaluated to:

$$\sigma_{JJ}^{\text{incl}} = 2407 \pm 38 \text{ (stat)} \begin{matrix} +703 \\ -793 \end{matrix} \text{ (syst)} \text{ nb.} \quad (9.10)$$

Therefore, the absolute value of the ratio R_{SD} in the full kinematic region is:

$$R_{SD} = 0.0238 \pm 0.0004 \text{ (stat)} \begin{matrix} +0.0063 \\ -0.0028 \end{matrix} \text{ (syst)}. \quad (9.11)$$

The uncertainty for R_{SD} includes correlations between uncertainties for $\sigma_{\text{JJ}}^{\text{SD}}$ and $\sigma_{\text{JJ}}^{\text{incl}}$, e.g., calibration corrections. The SD cross section corresponds to approximately 2.4% of dijet production in this region. The ratio is on a level similar to the one measured for the TOTEM kinematic region [52]:

$$R_{\text{SD}}^{\text{TOTEM}} = 0.0209 \pm 0.0008 \text{ (stat)} \begin{matrix} +0.0021 \\ -0.0026 \end{matrix} \text{ (syst)}. \quad (9.12)$$

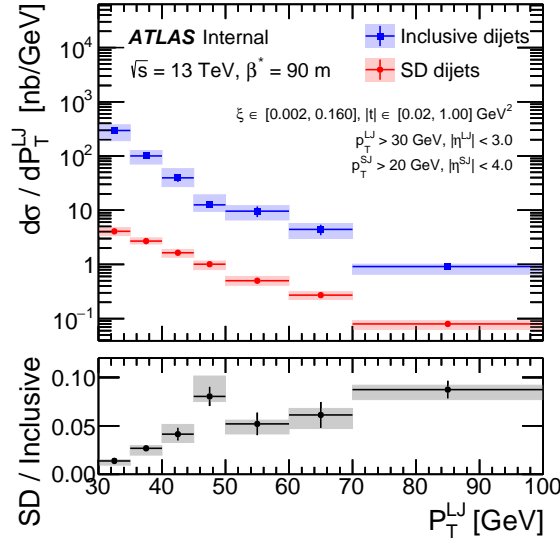


Figure 9.10: The differential cross section for inclusive (blue) and SD (red) dijet production. The ratio of the SD to inclusive dijet production is plotted below. The error bars and boxes correspond to the statistical and systematic uncertainties respectively.

9.2 Dijets production in central diffraction

This is the first time that CD dijet production has been measured at the LHC. The statistics is limited compared to the SD analysis. Fig. 9.11 shows the differential cross sections for the production of CD dijets as a function of $-\log_{10} \xi^{\text{PP}}$ and p_T^{LJ} . The bin edges are set to:

- relative energy loss $\log_{10} \xi^{\text{PP}}$: $-4.0, -3.3, -2.9, -2.6, -2.3, -2.0, -1.6$;
- transverse momentum of leading jet p_T^{LJ} : $30.0, 40.0, 60.0, 100.0$ [GeV].

The limit for $\log_{10} \xi^{\text{PP}} < -1.6$ arises from the upper limit of ξ in the fiducial region: $\log_{10} 0.160^2 \approx -1.6$.

The value of the total cross section for CD dijet production in the full kinematic region calculated from the data equals:

$$\sigma_{\text{JJ}}^{\text{CD}} = 329 \pm 59 \text{ (stat)} \begin{matrix} +61 \\ -71 \end{matrix} \text{ (syst)} \text{ pb}. \quad (9.13)$$

This means that CD dijet production is about 170 times rarer than SD dijet production in a given kinematic region. The statistical uncertainty is comparable to the systematic uncertainty. The systematic contributions to the uncertainties are provided in Table 9.1. The values of total systematic uncertainties are calculated by adding different uncertainty contributions in quadrature. The large systematic uncertainty is due to jet calibration, the second one comes from ALFA kinematic reconstruction.

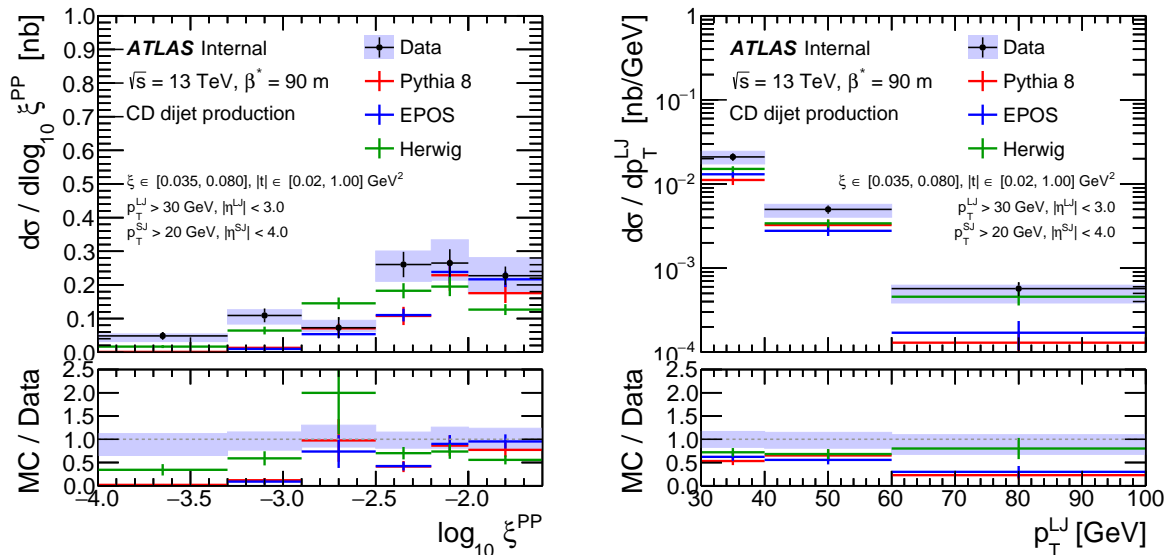


Figure 9.11: The differential cross section for CD dijet production for ξ^{PP} and p_{T}^{LJ} . Data is compared to three MC models: Pythia 8 (red), EPOS (blue), and Herwig (green).

Both Pythia 8 and EPOS provide similar predictions for two-forward-proton events, but with different contributions from SD/SD' and CD components - Fig. 9.12. Pythia 8 predicts that about 25% of two-forward-proton events are due to SD diffraction (with topology shown in Fig. 6.20a). EPOS provides an almost clean CD sample. Both generators fail to describe the smallest ξ^{PP} , i.e. $\log_{10} \xi^{\text{PP}} < -2.9$. Herwig CD component describes the data better than Pythia 8 or EPOS, even for the smallest ξ^{PP} . Unfortunately, the other components (SD, DD and ND) were not available. Low statistics in the data and MC make the analysis prone to fluctuations.

For MC, only statistical uncertainties are evaluated. The generators predict the following total cross sections:

$$\sigma_{\text{JJ}}^{\text{CD-Pythia8}} = 182 \pm 50 \text{ (stat) pb}, \quad (9.14)$$

$$\sigma_{\text{JJ}}^{\text{CD-EPOS}} = 192 \pm 36 \text{ (stat) pb}, \quad (9.15)$$

$$\sigma_{\text{JJ}}^{\text{CD-Herwig}} = 240 \pm 33 \text{ (stat) pb}. \quad (9.16)$$

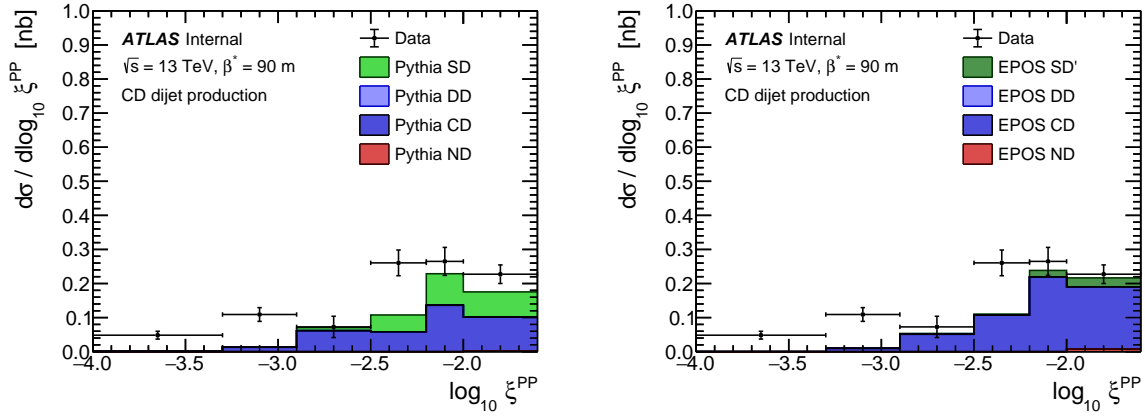


Figure 9.12: The differential cross section for dijet production with two forward protons in the function of ξ^{PP} . Data is compared with Pythia 8 and EPOS predictions. MC is separated into SD/SD', DD, CD and ND components.

9.3 Exclusive dijets production search

In exclusive dijet production, which is a special case of Double Pomeron Exchange, the central state consists of only two jets without any Pomeron remnants. Clean events are highly desired by theoretical physicists, but the cross section for such a process is very small. Quantitative measurement requires high precision and dedicated procedures. Unfortunately, the resources for this analysis were insufficient. Therefore, here are only qualitative results from the exclusive dijet production search. Unfolding and normalisation are not performed.

Data were compared with two MC samples. The first is the inclusive Herwig sample, used for CD analysis. The second is an exclusive sample prepared with the Superchic MC generator [110]. The sample consists of 5000 events, with $p_{\text{T}}^{\text{LJ}} > 10$ GeV and a two-forward-protons filter. The exponentially decreasing cross section makes the nominal data sample unusable. According to Superchic, the total number of exclusive events with $p_{\text{T}}^{\text{LJ}} > 30$ GeV for a given integrated luminosity is expected to be around three. It would be impossible to distinguish them from the inclusive background. Furthermore, Superchic predicts most events with both $\xi^{\text{P}} < 0.2$. It can be seen in Fig. 9.13 on the left. This region is dominated by accidentals in the data. Inclusive MC predicts events with a larger ξ^{P} , visible in Fig. 9.13 on the right.

The simulation shows that the threshold for p_{T} of jets has to be decreased for the exclusive search for dijet production. In this analysis, the limit is set to $p_{\text{T}} > 10$ GeV for both jets. It is much less than the recommended value of 20 GeV [75] and the search would be biased - jet calibration and jet reconstruction are not fully efficient at this scale. Furthermore, no suitable trigger was used to collect data for such a small jet p_{T} . The highest number of candidates for exclusive dijets was observed for the trigger exploited by the Central Exclusive Production (CEP) analysis [28], with the logic of the trigger named “HLT_mb_sptrk_vetombts2in_L1_ALFA_CEP”. It is a high-level trigger that comprises signals from MBTS, ID, and ALFA. It requires two protons observed at two ALFA stations on the opposite sides, a lack of signal in all but at most one of the inner

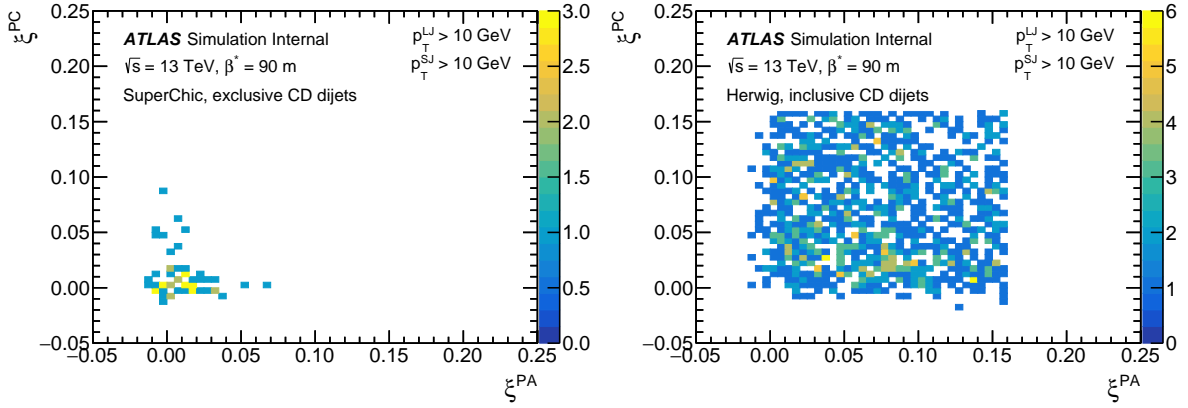


Figure 9.13: The correlation between ξ^{PA} and ξ^{PC} for exclusive dijet production (Superchic) and inclusive dijet production (Herwig). Both plots shows events with leading and secondary jet $p_T > 10$ GeV.

MBTS tiles, and the presence of space points in ID that can form an online track. The conditions are perfect for exclusive pion measurement, in which no particles should be present in the rapidity region between the forward and central systems. Exclusive dijet production has a similar topology, but due to additional QCD radiation, the veto on MBTS could exclude many potential candidates.

By definition, the value of β^{JJ} for exclusive production should be around 1.0, but is usually lower due to QCD radiation. Furthermore, the jet calibration is optimised for p_T and the mass of the dijet system calculated as the square of four momenta is significantly underestimated. Therefore, it is more efficient to look at the ratio $\tilde{\xi}_{JJ}^X/\xi^P$, than to use the definition from Eq. (1.30). The plots in Fig. 9.14 show the correlations between sides A and C, obtained for four samples: inclusive jet data sample with $p_T^{LJ} > 30$ GeV, CEP data sample with $p_T^{LJ} > 10$ GeV, and exclusive (Herwig) and inclusive (Superchic) MC samples. The selections are similar to the CD analysis, but include the smallest $\xi < 0.02$ region. In order to exclude elastic background, only anti-elastic configurations are analysed.

Inclusive events focus on the smallest $\tilde{\xi}_{JJ}^X/\xi^P$ region, when exclusive events have higher ratios. Comparison can be done in one-dimensional distributions of \tilde{r}^{JJ} variable:

$$\tilde{r}^{JJ} = \sqrt{\left(\frac{\tilde{\xi}_{JJ}^{XA}}{\xi^{PA}}\right)^2 + \left(\frac{\tilde{\xi}_{JJ}^{XC}}{\xi^{PC}}\right)^2}, \quad (9.17)$$

which shows the distance from point (0, 0). The plots of \tilde{r}^{JJ} for the analysed samples are presented in Fig. 9.15. Exclusive simulation provides maximum for $\tilde{r}^{JJ} \sim 0.6$ (bottom right). A similar distribution is obtained with the CEP data sample (top right). There is a possibility that the veto for inner MBTS tiles could introduce such a bias. However, the correlation is observed between central and forward detectors which should limit this potential bias from MBTS. Therefore, it can be a hint that some of the observed events are candidates for exclusive dijet production. The nominal data sample and the inclusive MC sample have maximum values for $\tilde{r}^{JJ} \sim 0.2$ and decrease for larger \tilde{r}^{JJ} (left plots).

The plots present possible candidates for exclusive dijet production and show the

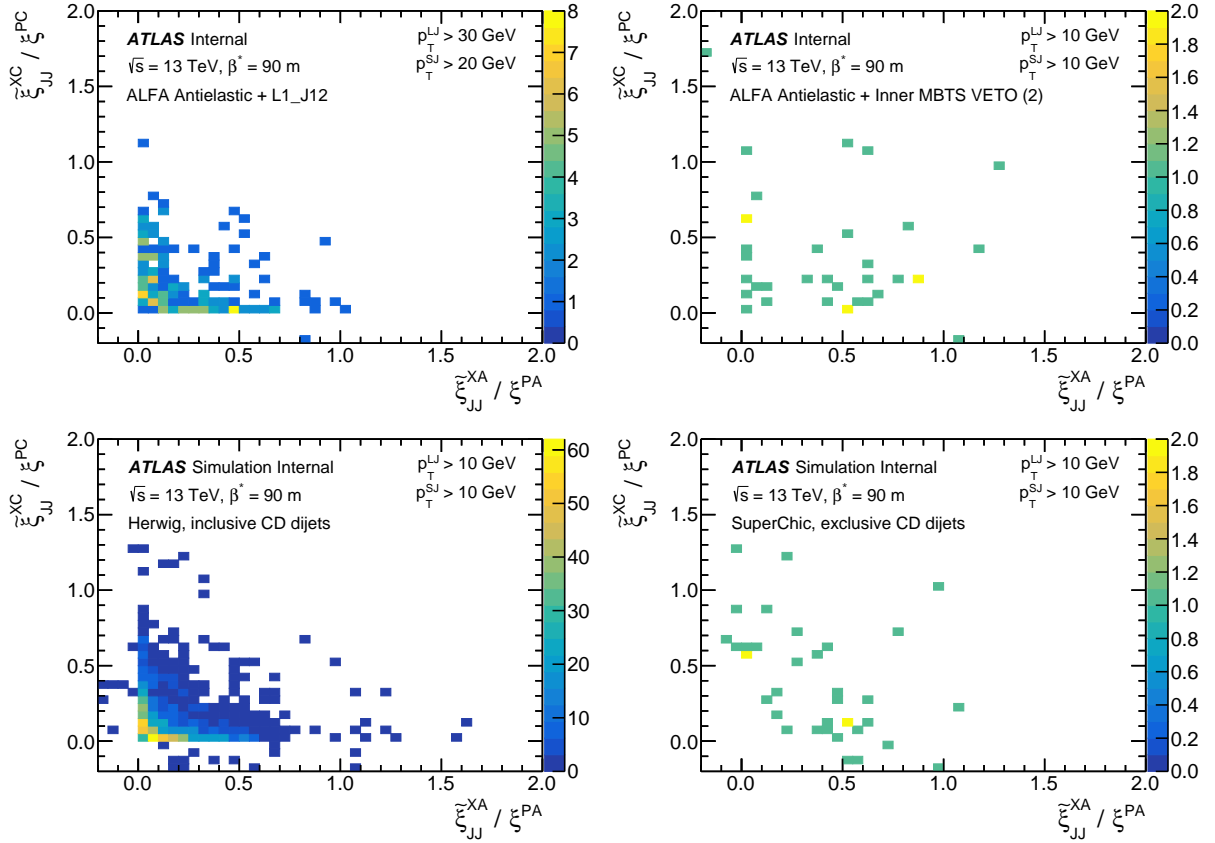


Figure 9.14: The correlation of ratios $\tilde{\xi}_{JJ}^X / \xi^P$ between side A and C for four samples: inclusive jet data with $p_T^{LJ} > 30$ GeV (top left), CEP data with $p_T^{LJ} > 10$ GeV (top right), inclusive dijet production from Herwig (bottom left) and exclusive dijet production from Superchic (bottom right). Both bottom plots shows events with $p_T^{LJ} > 10$ GeV.

potential of the ALFA detector for such measurement. It was shown that variable \tilde{r}^{JJ} can be a good approach to distinguish events. Additional studies that exploit, e.g. ID tracks multiplicity, can help to distinguish exclusive events even further. Unfortunately, the lack of resources prevents the analysis from developing further. The trigger that requires two protons in anti-elastic configurations and optional activity in the ATLAS central detector can be exploited to study this kind of process.

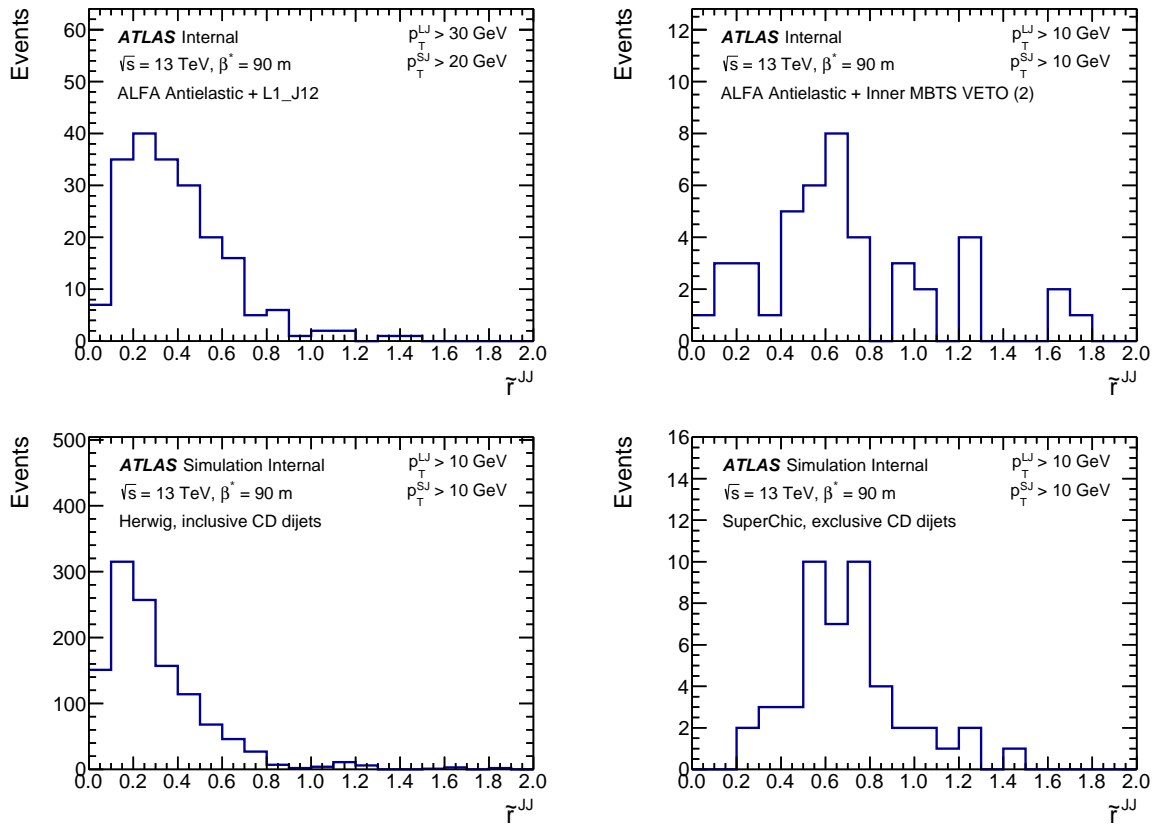


Figure 9.15: The distributions of \tilde{r}^{JJ} variable for four samples: inclusive jet data with $p_T^{LJ} > 30$ GeV (top left), CEP data with $p_T^{LJ} > 10$ GeV (top right), inclusive dijet production from Herwig (bottom left) and exclusive dijet production from Superchic (bottom right). Both bottom plots shows events with $p_T^{LJ} > 10$ GeV.

Summary

This dissertation presents the measurement of diffractive dijet production in proton-proton collisions with ALFA detectors in the ATLAS experiment. It focuses on two kinds of processes: single and central diffraction. Data were collected during the ALFA diffractive campaign in October 2015 with dedicated beam optics at ATLAS. They correspond to a 725 nb^{-1} integrated luminosity with the centre of mass energy $\sqrt{s} = 13 \text{ TeV}$. Results are compared with MC simulations using the following generators: Pythia 8 and EPOS (for SD and CD analyses), and Herwig (for CD analysis).

Detector effects are investigated with data-driven and simulation-based methods. Appropriate corrections are applied. One of them is the ALFA alignment, developed as the ATLAS qualification task. These corrections were used in other diffractive analyses that exploited the same dataset. Another is dedicated jet calibration, as the standard procedure could not be applied. Other important corrections include jet trigger efficiency, accidental background subtraction, and unfolding.

The fiducial region is derived from ALFA geometrical acceptance and jet trigger efficiency. It follows the range $\xi \in [0.002, 0.160]$ and $|t| \in [0.02, 1.00] \text{ GeV}^2$. Two jets are required: the leading one has to have transverse momentum $p_{\text{T}}^{\text{LJ}} > 30 \text{ GeV}$ and pseudo-rapidity $|\eta^{\text{LJ}}| < 3.0$, the secondary one has to have $p_{\text{T}}^{\text{SJ}} > 20 \text{ GeV}$ and $|\eta^{\text{SJ}}| < 4.0$.

The cross section for SD dijet production is analysed differently in terms of ξ , $|t|$, p_{T}^{LJ} , $|\eta^{\text{LJ}}|$ and β^{JJ} . The last one corresponds to the fraction of the Pomeron momentum carried by jets. Both MC generators do not describe the data, especially for the lowest range ξ . Pythia 8 overestimates the data and EPOS underestimates them. The total cross section measured for SD dijet production in the full kinematic region is:

$$\sigma_{\text{JJ}}^{\text{SD}} = 57.2 \pm 0.8 \text{ (stat)} \begin{matrix} +9.6 \\ -8.7 \end{matrix} \text{ (syst) nb.}$$

Compared to the estimate of the total inclusive dijet production, the diffractive production comprises about 2.4% of events.

The statistic for double proton events is limited compared to single proton analysis. The cross section for CD dijet production is estimated for two variables only: ξ^{PP} and p_{T}^{LJ} . All generators do not describe the data, the best description is provided by the Herwig sample. The value of the total cross section for CD dijet production in the full kinematic region equals:

$$\sigma_{\text{JJ}}^{\text{CD}} = 329 \pm 59 \text{ (stat)} \begin{matrix} +61 \\ -71 \end{matrix} \text{ (syst) pb.}$$

This means that CD dijet production is about 170 times rarer than SD dijet production in a given kinematic region.

The dissertation is complemented by the search for exclusive dijet production, where the central state consists of only two jets without any Pomeron remnants. The very low cross section makes the nominal sample impractical for use. Therefore, a sample based on the MBTS inner tiles veto is exploited, and the p_T cut is lowered to 10 GeV. It is not a perfect solution, because the MBTS veto can exclude many exclusive events due to additional QCD radiations from jets. However, the analysis shows a bunch of possible candidates for exclusive dijet production and the potential of the ALFA detector for such measurement. Additional studies that exploit, e.g. ID tracks multiplicity, can help to distinguish exclusive events even further.

Bibliography

- [1] A. Bettini, *Introduction to elementary particle physics; 2st ed.*, Cambridge University Press, 2014, ISBN 978-1-107-27948-3.
- [2] L3 Collaboration, O. Adriani *et al.*, *Determination of the number of light neutrino species*, [Phys. Lett. B](#), vol. 292, pp. 463–471, 1992.
- [3] S. Mele, *The Measurement of the Number of Light Neutrino Species at LEP*, [Adv. Ser. Direct. High Energy Phys.](#), vol. 23, pp. 89–106, 2015.
- [4] Planck Collaboration, N. Aghanim *et al.*, *Planck 2018 results. VI. Cosmological parameters*, [Astron. Astrophys.](#), vol. 641, p. A6, 2020.
- [5] P. W. Higgs, *Broken Symmetries and the Masses of Gauge Bosons*, [Phys. Rev. Lett.](#), vol. 13, pp. 508–509, 1964.
- [6] F. Englert and R. Brout, *Broken Symmetry and the Mass of Gauge Vector Mesons*, [Phys. Rev. Lett.](#), vol. 13, pp. 321–323, 1964.
- [7] ATLAS Collaboration, G. Aad *et al.*, *Observation of a new particle in the search for the Standard Model Higgs boson with the ATLAS detector at the LHC*, [Phys. Lett. B](#), vol. 716, pp. 1–29, 2012.
- [8] CMS Collaboration, S. Chatrchyan *et al.*, *Observation of a New Boson at a Mass of 125 GeV with the CMS Experiment at the LHC*, [Phys. Lett. B](#), vol. 716, pp. 30–61, 2012.
- [9] Particle Data Group, R. L. Workman and Others, *Review of Particle Physics*, [PTEP](#), vol. 2022, p. 083C01, 2022.
- [10] M. E. Peskin and D. V. Schroeder, *An Introduction to quantum field theory*, Addison-Wesley, 1995, ISBN 978-0-201-50397-5.
- [11] Y. Sumino, *QCD potential as a 'Coulomb plus linear' potential*, [Phys. Lett. B](#), vol. 571, pp. 173–183, 2003.
- [12] LHCb Collaboration, R. Aaij *et al.*, *Observation of $J/\psi p$ Resonances Consistent with Pentaquark States in $\Lambda_b^0 \rightarrow J/\psi K^- p$ Decays*, [Phys. Rev. Lett.](#), vol. 115, p. 072001, 2015.

- [13] B. Andersson, G. Gustafson, G. Ingelman, and T. Sjostrand, *Parton Fragmentation and String Dynamics*, [Phys. Rept.](#), vol. 97, pp. 31–145, 1983.
- [14] Particle Data Group, M. Tanabashi *et al.*, *Review of Particle Physics*, [Phys. Rev. D](#), vol. 98, no. 3, p. 030001, 2018.
- [15] G. P. Salam, *Towards Jetography*, [Eur. Phys. J. C](#), vol. 67, pp. 637–686, 2010.
- [16] CMS Collaboration, A. M. Sirunyan *et al.*, *Particle-flow reconstruction and global event description with the CMS detector*, [JINST](#), vol. 12, no. 10, p. P10003, 2017.
- [17] M. Cacciari, G. P. Salam, and G. Soyez, *The anti- k_t jet clustering algorithm*, [JHEP](#), vol. 04, p. 063, 2008.
- [18] V. Barone and E. Predazzi, *High-Energy Particle Diffraction*, Springer, 2002, ISBN 978-3-540-42107-8.
- [19] ATLAS Collaboration, G. Aad *et al.*, *Rapidity gap cross sections measured with the ATLAS detector in pp collisions at $\sqrt{s} = 7$ TeV*, [Eur. Phys. J. C](#), vol. 72, p. 1926, 2012.
- [20] Particle Data Group, C. Amsler *et al.*, *Review of Particle Physics*, [Phys. Lett. B](#), vol. 667, no. 1, 2008.
- [21] J. D. Bjorken, *Rapidity gaps and jets as a new-physics signature in very-high-energy hadron-hadron collisions*, [Phys. Rev. D](#), vol. 47, pp. 101–113, 1993.
- [22] B. Cox, J. R. Forshaw, and L. Lonnblad, *Hard color singlet exchange at the Tevatron*, [JHEP](#), vol. 10, p. 023, 1999.
- [23] L. M. Huertas Guativa, *Measurement of dijet production with a leading proton in proton-proton collisions at $\sqrt{s} = 8$ TeV with the CMS and TOTEM detectors at the LHC*, [PhD thesis](#), Rio de Janeiro State U., 2017.
- [24] S. Donnachie, H. G. Dosch, O. Nachtmann, and P. Landshoff, *Pomeron physics and QCD*, Cambridge University Press, 2004, ISBN 978-0-511-06050-2.
- [25] S. D. Campos and V. A. Okorokov, *Optical theorem, crossing property, and derivative dispersion relations: implications on the asymptotic behaviour of and*, [Chin. Phys. C](#), vol. 46, no. 8, p. 083105, 2022.
- [26] STAR Collaboration, J. Adam *et al.*, *Results on total and elastic cross sections in proton-proton collisions at $\sqrt{s} = 200$ GeV*, [Phys. Lett. B](#), vol. 808, p. 135663, 2020.
- [27] A. Donnachie and P. V. Landshoff, *Total cross-sections*, [Phys. Lett. B](#), vol. 296, pp. 227–232, 1992.
- [28] R. Sikora, *Measurement of the diffractive central exclusive production in the STAR experiment at RHIC and the ATLAS experiment at LHC*, [PhD thesis](#), AGH Kraków U., 2020.

- [29] P. D. B. Collins, *An Introduction to Regge Theory and High-Energy Physics*, Cambridge University Press, 2009, ISBN 978-0-521-11035-8.
- [30] G. Ingelman and P. E. Schlein, *Jet Structure in High Mass Diffractive Scattering*, *Phys. Lett. B*, vol. 152, pp. 256–260, 1985.
- [31] ZEUS Collaboration, S. Chekanov *et al.*, *Deep inelastic scattering with leading protons or large rapidity gaps at HERA*, *Nucl. Phys. B*, vol. 816, pp. 1–61, 2009.
- [32] T. Sjöstrand, S. Mrenna, and P. Z. Skands, *A Brief Introduction to PYTHIA 8.1*, *Comput. Phys. Commun.*, vol. 178, pp. 852–867, 2008.
- [33] T. Sjöstrand, S. Ask, J. R. Christiansen, R. Corke, N. Desai, P. Ilten, S. Mrenna, S. Prestel, C. O. Rasmussen, and P. Z. Skands, *An introduction to PYTHIA 8.2*, *Comput. Phys. Commun.*, vol. 191, pp. 159–177, 2015.
- [34] T. Sjöstrand, *Status and developments of event generators*, 4th Large Hadron Collider Physics Conference, 13–18 June 2016, Lund, Sweden, [PoS\(LHCP2016\)007](#).
- [35] ATLAS Collaboration, G. Aad *et al.*, *The Pythia 8 A3 tune description of ATLAS minimum bias and inelastic measurements incorporating the Donnachie-Landshoff diffractive model*, [Tech. Report ATL-PHYS-PUB-2016-017](#), CERN, 2016.
- [36] ATLAS Collaboration, G. Aad *et al.*, *ATLAS Pythia 8 tunes to 7 TeV data*, [Tech. Report ATL-PHYS-PUB-2014-021](#), CERN, 2014.
- [37] K. Werner, *The hadronic interaction model EPOS*, 14th International Symposium on Very High Energy Cosmic Ray Interactions, 15–22 August 2006, Weihai, China, *Nucl. Phys. B Proc. Suppl.* 175-176 (2008), pp. 81-87.
- [38] T. Pierog and K. Werner, *Muon Production in Extended Air Shower Simulations*, *Phys. Rev. Lett.*, vol. 101, p. 171101, 2008.
- [39] T. Pierog and K. Werner, *EPOS Model and Ultra High Energy Cosmic Rays*, 15th International Symposium on Very High Energy Cosmic Ray Interactions, 1–6 September 2008, Paris, France, *Nucl. Phys. B Proc. Suppl.* 196 (2009) 102-105.
- [40] H. J. Drescher, M. Hladik, S. Ostapchenko, T. Pierog, and K. Werner, *Parton based Gribov-Regge theory*, *Phys. Rept.*, vol. 350, pp. 93–289, 2001.
- [41] I. Łakomic, *The measurement of $\varphi(1020)$ meson production in proton-proton collisions at $\sqrt{s} = 14$ TeV with the ATLAS detector at the LHC*, [PhD thesis](#), AGH Kraków U., 2023.
- [42] L. T. Fulek, *Charged particle production in diffractive proton-proton scattering at the RHIC and LHC energies*, [PhD thesis](#), AGH Kraków U., 2020.
- [43] M. Bahr *et al.*, *Herwig++ Physics and Manual*, *Eur. Phys. J. C*, vol. 58, pp. 639–707, 2008.

- [44] J. Bellm *et al.*, *Herwig 7.1 Release Note*, [Tech. Report CERN-PH-TH-2017-109](#), CERN and others, 2017.
- [45] D. Amati, A. Stanghellini, and S. Fubini, *Theory of high-energy scattering and multiple production*, [Nuovo Cim.](#), vol. 26, pp. 896–954, 1962.
- [46] S. Gieseke, F. Loshaj, and P. Kirchgaesser, *Soft and diffractive scattering with the cluster model in Herwig*, [Eur. Phys. J. C](#), vol. 77, no. 3, p. 156, 2017.
- [47] ATLAS Collaboration, G. Aad *et al.*, *Dijet production in $\sqrt{s} = 7$ TeV pp collisions with large rapidity gaps at the ATLAS experiment*, [Phys. Lett. B](#), vol. 754, pp. 214–234, 2016.
- [48] H1 Collaboration, C. Adloff *et al.*, *Diffractive dijet production at HERA*, [Eur. Phys. J. C](#), vol. 6, pp. 421–436, 1999.
- [49] CDF Collaboration, D. Acosta *et al.*, *Diffractive Dijet Production at $\sqrt{s} = 630$ GeV and 1800 GeV at the Fermilab Tevatron*, [Phys. Rev. Lett.](#), vol. 88, p. 151802, 2002.
- [50] CDF Collaboration, T. Aaltonen *et al.*, *Diffractive Dijet Production in $\bar{p}p$ Collisions at $\sqrt{s} = 1.96$ TeV*, [Phys. Rev. D](#), vol. 86, p. 032009, 2012.
- [51] D0 Collaboration, V. M. Abazov *et al.*, *High Mass Exclusive Diffractive Dijet Production in $p\bar{p}$ Collisions at $\sqrt{s} = 1.96$ TeV*, [Phys. Lett. B](#), vol. 705, pp. 193–199, 2011.
- [52] CMS and TOTEM Collaboration, A. M. Sirunyan *et al.*, *Measurement of single-diffractive dijet production in proton-proton collisions at $\sqrt{s} = 8$ TeV with the CMS and TOTEM experiments*, [Eur. Phys. J. C](#), vol. 80, no. 12, p. 1164, 2020.
- [53] P. A. Malinowska, *Determination of Monte Carlo predictions for the diffractive production of dijets using the Rivet package*, [Bachelor of Engineering’s thesis](#), AGH Kraków U., 2023.
- [54] A. Buckley, J. Butterworth, D. Grellscheid, H. Hoeth, L. Lonnblad, J. Monk, H. Schulz, and F. Siegert, *Rivet user manual*, [Comput. Phys. Commun.](#), vol. 184, pp. 2803–2819, 2013.
- [55] R. De Maria, *LHC Interaction region upgrade*, [PhD thesis](#), Ecole Polytechnique, 2008.
- [56] L. Evans and P. Bryant, *LHC Machine*, [J. Instrum.](#), vol. 3, no. 08, p. S08001, 2008.
- [57] E. Lopienska, *The CERN accelerator complex, layout in 2022. Complexe des accélérateurs du CERN en janvier 2022*, Figure, CERN, 2022, <https://cds.cern.ch/record/2800984>.
- [58] ATLAS Collaboration, G. Aad *et al.*, *The ATLAS Experiment at the CERN Large Hadron Collider*, [JINST](#), vol. 3, p. S08003, 2008.

- [59] U. Egede, *The search for a Standard Model Higgs at the LHC and electron identification using transition radiation in the ATLAS tracker*, PhD thesis, Lund U., 1998.
- [60] ATLAS Collaboration, E. Stanecka, *ATLAS Inner Tracker Performance at the Beginning of the LHC Run 2*, 22nd Cracow Epiphany Conference on the Physics in LHC Run 2, 7–9 January 2016, Cracow, Poland, *Acta Phys. Polon. B* **47** (2016) 1739-1744.
- [61] ATLAS Collaboration, K. Potamianos, *The upgraded Pixel detector and the commissioning of the Inner Detector tracking of the ATLAS experiment for Run-2 at the Large Hadron Collider*, 2015 European Physical Society Conference on High Energy Physics, 22–29 July 2015, Vienna, Austria, *PoS(EPS-HEP2015)*261.
- [62] M. Limper, *Track and Vertex Reconstruction in the ATLAS Inner Detector*, PhD thesis, NIKHEF, 2009.
- [63] H. S. Bansil, *Diffraction Dijet Production in $\sqrt{s} = 7$ TeV pp collisions at the ATLAS Experiment*, PhD thesis, Birmingham U., 2013.
- [64] M. Brice, *ATLAS barrel detector*, Photo, CERN, 2003, <https://cds.cern.ch/record/619028>.
- [65] C. Marcelloni, *Moving one of the ATLAS end-cap calorimeters. Vue de la caverne ATLAS (côté A) pendant que le calorimètre bouchon est déplacé.*, Photo, CERN, 2007, <https://cds.cern.ch/record/1017394>.
- [66] L. Pontecorvo, *The ATLAS muon spectrometer*, 4th Symposium on LHC Physics and Detectors, 1–3 May 2003, Batavia, USA, *Eur. Phys. J. C* **34** (2004) pp. 117-128.
- [67] R. Nicolaidou, L. Chevalier, S. Hassani, J. F. Laporte, E. Le Menedeu, and A. Ouraou, *Muon identification procedure for the ATLAS detector at the LHC using Muonboy reconstruction package and tests of its performance using cosmic rays and single beam data*, 17th International Conference on Computing in High Energy and Nuclear Physics, 21–27 March 2009, Prague, Czech Republic, *J. Phys. Conf. Ser.* **219** (2010) 032052.
- [68] D. A. Bukin, V. P. Druzhinin, V. B. Golubev, and S. I. Serednyakov, *Scintillation counter with WLS fiber readout*, *Nucl. Instrum. Meth. A*, vol. 384, pp. 360–363, 1997.
- [69] LUCID Collaboration, F. Lasagni Manghi, *LUCID: The ATLAS Luminosity Detector*, 39th International Conference on High Energy Physics, 4–11 July 2018, Seoul, Korea, *PoS(ICHEP2018)*280.
- [70] ATLAS Collaboration, M. Aaboud *et al.*, *Evidence for light-by-light scattering in heavy-ion collisions with the ATLAS detector at the LHC*, *Nature Phys.*, vol. 13, no. 9, pp. 852–858, 2017.

- [71] ATLAS Collaboration, G. Aad *et al.*, *Observation and Measurement of Forward Proton Scattering in Association with Lepton Pairs Produced via the Photon Fusion Mechanism at ATLAS*, *Phys. Rev. Lett.*, vol. 125, no. 26, p. 261801, 2020.
- [72] M. Cacciari and G. P. Salam, *Dispelling the N^3 myth for the k_t jet-finder*, *Phys. Lett. B*, vol. 641, pp. 57–61, 2006.
- [73] M. Cacciari, G. P. Salam, and G. Soyez, *FastJet User Manual*, *Eur. Phys. J. C*, vol. 72, p. 1896, 2012.
- [74] ATLAS Collaboration, M. Aaboud *et al.*, *Jet reconstruction and performance using particle flow with the ATLAS Detector*, *Eur. Phys. J. C*, vol. 77, no. 7, p. 466, 2017.
- [75] ATLAS Collaboration, M. Aaboud *et al.*, *Determination of jet calibration and energy resolution in proton-proton collisions at $\sqrt{s} = 8$ TeV using the ATLAS detector*, *Eur. Phys. J. C*, vol. 80, no. 12, p. 1104, 2020.
- [76] ATLAS Collaboration, G. Aad *et al.*, *Topological cell clustering in the ATLAS calorimeters and its performance in LHC Run 1*, *Eur. Phys. J. C*, vol. 77, p. 490, 2017.
- [77] ATLAS Collaboration, *ATLAS Run Query*, Webpage, CERN, 2012, <https://atlas-runquery.cern.ch/>.
- [78] ATLAS Collaboration, M. Aaboud *et al.*, *Measurement of the total cross section from elastic scattering in pp collisions at $\sqrt{s} = 8$ TeV with the ATLAS detector*, *Phys. Lett. B*, vol. 761, pp. 158–178, 2016.
- [79] ATLAS Collaboration, G. Aad *et al.*, *The ATLAS Simulation Infrastructure*, *Eur. Phys. J. C*, vol. 70, no. 3, pp. 823–874, 2010.
- [80] ATLAS Collaboration, G. Duckeck *et al.*, *ATLAS Computing: technical design report*, *Tech. Report CERN-LHCC-2005-022*, CERN, 2005.
- [81] GEANT4 Collaboration, S. Agostinelli *et al.*, *GEANT4—a simulation toolkit*, *Nucl. Instrum. Meth. A*, vol. 506, pp. 250–303, 2003.
- [82] D. Costanzo, A. Dell’Acqua, M. Gallas, A. Rimoldi, J. Boudreau, V. Tsulaia, and A. Simone, *The Geant4-based simulation software of the ATLAS detector*, 2006 IEEE Nuclear Science Symposium and Medical Imaging Conference, 29 October – 4 November, 2006, San Diego, California, [NSS/MIC 2006](#).
- [83] A. P. Lind, *A Study of Diffractive Scattering with the ATLAS and ALFA Experiment*, *Master’s thesis*, Bohr Inst., 2017.
- [84] P. Jenni, M. Nordberg, M. Nessi, and K. Jon-And, *ATLAS Forward Detectors for Measurement of Elastic Scattering and Luminosity*, *Tech. Report CERN-LHCC-2008-004*, CERN, 2008.

- [85] S. A. Khalek and et al., *The ALFA Roman Pot detectors of ATLAS*, [J. Instrum.](#), vol. 11, no. 11, p. P11013–P11013, 2016.
- [86] S. Jakobsen, *Commissioning of the Absolute Luminosity For ATLAS detector at the LHC*, [PhD thesis](#), CERN, 2013.
- [87] ATLAS Collaboration, I. Lakomic, *Study of the proton reconstruction efficiency with the ALFA detector using an overlay technique of Monte Carlo signal events with zero-bias collider data.*, 7th Large Hadron Collider Physics Conference, 20–25 May 2019, Puebla, Mexico, [PoS\(LHCP2019\)002](#).
- [88] K. W. Janas, *ALFA detector alignment and overview of data collected with $\beta^* = 19$ m*, [Master's thesis](#), AGH Kraków U., 2017, (in Polish).
- [89] S. S. Mortensen, *Kinematic reconstruction of diffractive processes with tagged protons in the ALFA detector at $\sqrt{s} = 8$ TeV*, [Master's thesis](#), Niels Bohr Institute, 2013.
- [90] ATLAS Collaboration, K. Janas, *The track-based alignment of the ALFA Roman Pot detectors of the ATLAS experiment.*, 7th Large Hadron Collider Physics Conference, 20–25 May 2019, Puebla, Mexico, [PoS\(LHCP2019\)060](#).
- [91] ATLAS Collaboration, G. Aad *et al.*, *Measurement of differential cross sections for single diffractive dissociation in $\sqrt{s} = 8$ TeV pp collisions using the ATLAS ALFA spectrometer*, [JHEP](#), vol. 02, p. 042, 2020.
- [92] ATLAS Collaboration, S. Prince, *The updated ATLAS Jet Trigger for the LHC Run II*, Meeting of the APS Division of Particles and Fields, 4–8 August 2015, Ann Arbor, Michigan, USA, [DPF 2015](#).
- [93] R. Achenbach *et al.*, *The ATLAS level-1 calorimeter trigger*, [JINST](#), vol. 3, p. P03001, 2008.
- [94] ATLAS Collaboration, G. Aad *et al.*, *Selection of jets produced in 13 TeV proton-proton collisions with the ATLAS detector*, [Tech. Report ATLAS-CONF-2015-029](#), CERN, 2015.
- [95] ATLAS Collaboration, M. Aaboud *et al.*, *Search for squarks and gluinos in events with hadronically decaying tau leptons, jets and missing transverse momentum in proton–proton collisions at $\sqrt{s} = 13$ TeV recorded with the ATLAS detector*, [Eur. Phys. J. C](#), vol. 76, no. 12, p. 683, 2016.
- [96] ATLAS Collaboration, G. Aad *et al.*, *Tagging and suppression of pileup jets with the ATLAS detector*, [Tech. Report ATLAS-CONF-2014-018](#), CERN, 2014.
- [97] S. A. Farrell, *Overlap Removal, ATLAS Joint Flavour Tagging and $H \rightarrow bb$ Workshop 2017*, Presentation, CERN, 2016, <https://indico.cern.ch/event/631313/contributions/2683959/>.

- [98] ATLAS Collaboration, G. Aad *et al.*, *Jet energy measurement with the ATLAS detector in proton-proton collisions at $\sqrt{s} = 7$ TeV*, *Eur. Phys. J. C*, vol. 73, no. 3, p. 2304, 2013.
- [99] ATLAS Collaboration, M. Aaboud *et al.*, *Determination of jet calibration and energy resolution in proton-proton collisions at $\sqrt{s} = 8$ TeV using the ATLAS detector*, *Eur. Phys. J. C*, vol. 80, no. 12, p. 1104, 2020.
- [100] ATLAS Collaboration, G. Aad *et al.*, *Properties of Jets and Inputs to Jet Reconstruction and Calibration with the ATLAS Detector Using Proton-Proton Collisions at $\sqrt{s} = 13$ TeV*, *Tech. Report ATL-PHYS-PUB-2015-036*, CERN, 2015.
- [101] ATLAS Collaboration, S. Schramm, *ATLAS Jet Reconstruction, Calibration, and Tagging of Lorentz-boosted Objects*, *Tech. Report ATL-PHYS-PROC-2017-236*, CERN, 2017.
- [102] ATLAS Collaboration, G. Aad *et al.*, *Data-Quality Requirements and Event Cleaning for Jets and Missing Transverse Energy Reconstruction with the ATLAS Detector in Proton-Proton Collisions at a Center-of-Mass Energy of $\sqrt{s} = 7$ TeV*, *Tech. Report ATLAS-CONF-2010-038*, CERN, 2010.
- [103] ATLAS Collaboration, G. Aad *et al.*, *Measurement of differential cross sections for single diffractive dissociation in $\sqrt{s} = 8$ TeV pp collisions using the ATLAS ALFA spectrometer*, *JHEP*, vol. 02, p. 042, 2020.
- [104] S. Schmitt, *Data Unfolding Methods in High Energy Physics*, 12th Conference on Quark Confinement and the Hadron Spectrum, 29 August – 3rd September 2016, Thessaloniki, Greece, *EPJ Web Conf.* 137 (2017) 11008.
- [105] G. D’Agostini, *A multidimensional unfolding method based on Bayes’ theorem*, *Nucl. Instrum. Methods Phys. Res. A*, vol. 362, no. 2, pp. 487–498, 1995.
- [106] G. D’Agostini, *Improved iterative Bayesian unfolding*, *Proceedings, Alliance Workshop on Unfolding and Data Correction*, 2010.
- [107] T. Adye, *Unfolding algorithms and tests using RooUnfold*, PHYSTAT 2011 Workshop on Statistical Issues Related to Discovery Claims in Search Experiments and Unfolding, 17–20 January 2011, CERN, Geneva, Switzerland, *PHYSTAT 2011*, 313–318.
- [108] R. Brun, F. Rademakers, *et al.*, *ROOT - An Object Oriented Data Analysis Framework, Release v6.18/02*, Software, CERN, 2019, <https://root.cern/>.
- [109] P. Fornasini, *The Uncertainty in Physical Measurements: An Introduction to Data Analysis in the Physics Laboratory*, Springer, 2008, ISBN 978-0-387-78650-6.
- [110] L. A. Harland-Lang, V. A. Khoze, and M. G. Ryskin, *Exclusive physics at the LHC with SuperChic 2*, *Eur. Phys. J. C*, vol. 76, no. 1, p. 9, 2016.

Acronyms

A	ATLAS side A, with positive Z
AFP	ATLAS Forward Proton
AL	ALFA armlet: Side A - Lower RPs
ALFA	Absolute Luminosity For ATLAS
ALICE	A Large Ion Collider Experiment
ATLAS	A Toroidal LHC ApparatuS
AU	ALFA armlet: Side A - Upper RPs
C	ATLAS side C, with negative Z
CD	Central diffraction
CDF	Collider Detector at Fermilab
CEP	Central Exclusive Production
CERN	European Organization for Nuclear Research, fr. <i>Conseil Européen pour la Recherche Nucléaire</i>
CL	ALFA armlet: Side A - Lower RPs
CM	Central mass frame
CMS	Compact Muon Solenoid
CU	ALFA armlet: Side A - Upper RPs
D0	D0 experiment at Fermilab
DD	Double diffraction
DPDF	Diffraction Parton Distribution Functions
DPE	Double Pomeron Exchange
EL	Elastic scattering

EM	Electromagnetic
EMCAL	Electromagnetic Calorimeter
FCAL	Forward Calorimeter
HCAL	Hadronic Calorimeter
HEC	Hadronic Calorimeter End Caps
HERA	Hadron-Electron Ring Accelerator
HLT	High Level Trigger
IBL	Insertable B-Layer
ID	Inner Detector
IP	Interaction Point
JCT	Jet Cleaning Tool
JER	Jet Energy Resolution
JES	Jet Energy Scale
JVT	Jet Vertex Tagger
L1	Level one trigger
LAr	Liquid argon
LCW	Local cell weighting
LEP	Large Electron Positron Collider
LHC	Large Hadron Collider
LHCb	Large Hadron Collider beauty
LL	ALFA anti-elastic arm, lower RPs
LRG	Large Rapidity Gap
LU	ALFA second elastic arm
LUCID	Langton Ultimate Cosmic-ray Intensity Detector
LVDT	Linear Variable Displacement Transducer
MAPMT	Multianode Photomultiplier
MBTS	Minimum Bias Trigger Scintillators

MC	Monte Carlo
MD	Main Detector
MET	Missing Transverse Energy
MPI	Multiple parton-parton interactions
ND	Non-diffractive events
OD	Overlap Detector
OR	Overlap Removal
PDF	Parton Distribution Functions
pQCD	Perturbative quantum chromodynamics
PS	Proton Synchrotron
PSB	Proton Synchrotron Booster
QCD	Quantum chromodynamics
QFT	Quantum Field Theory
RoI	Region of Interest
RP	Roman Pot
SCT	Semiconductor Tracker
SD	Single diffraction
SM	Standard Model
SPS	Super Proton Synchrotron
TOTEM	TOTAL Elastic and diffractive cross section Measurement
TRT	Transition Radiation Tracker
UL	ALFA first elastic arm
UU	ALFA anti-elastic arm, upper RPs
WLS	Wave-Length Shifting optical fibres
ZDC	Zero Degree Calorimeter

Appendix A

ALFA alignment results

RP	B7L1U	B7L1L	A7L1U	A7L1L	A7R1U	A7R1L	B7R1U	B7R1L
LHC fill 4499								
Edge cut [mm]	6.105	-6.475	6.815	-7.165	6.755	-7.075	6.045	-6.425
Beam-screen cut [mm]	18.345	-18.415	20.435	-20.515	20.245	-20.355	18.165	-18.315
LHC fill 4505								
Edge cut [mm]	6.095	-6.515	6.795	-7.205	6.755	-7.085	6.105	-6.435
Beam-screen cut [mm]	18.295	-18.375	20.395	-20.485	20.205	-20.325	18.145	-18.285
LHC fill 4509								
Edge cut [mm]	6.095	-6.445	6.805	-7.145	6.695	-7.115	6.045	-6.445
Beam-screen cut [mm]	18.385	-18.405	20.465	-20.505	20.205	-20.415	18.165	-18.375
LHC fill 4510								
Edge cut [mm]	6.115	-6.485	6.815	-7.175	6.795	-7.055	6.125	-6.405
Beam-screen cut [mm]	18.345	-18.385	20.435	-20.495	20.255	-20.315	18.195	-18.285
LHC fill 4511								
Edge cut [mm]	6.145	-6.475	6.835	-7.155	6.775	-7.105	6.115	-6.445
Beam-screen cut [mm]	18.335	-18.355	20.435	-20.455	20.215	-20.355	18.155	-18.285

Table A.1: The vertical cuts for ALFA RPs in the beam coordinate system.

Station	B7L1	A7L1	A7R1	B7R1
LHC fill 4499				
Distance [mm]	12.594	13.741	13.665	12.557
Stat. uncertainty [mm]	± 0.001	± 0.001	± 0.001	± 0.001
Syst. uncertainty [mm]	± 0.083	± 0.015	± 0.015	± 0.017
LHC fill 4505				
Distance [mm]	12.589	13.738	13.683	12.548
Stat. uncertainty [mm]	± 0.002	± 0.002	± 0.002	± 0.002
Syst. uncertainty [mm]	± 0.083	± 0.015	± 0.016	± 0.018
LHC fill 4509				
Distance [mm]	12.590	13.741	13.685	12.549
Stat. uncertainty [mm]	± 0.001	± 0.001	± 0.002	± 0.002
Syst. uncertainty [mm]	± 0.082	± 0.015	± 0.015	± 0.016
LHC fill 4510				
Distance [mm]	12.596	13.748	13.670	12.548
Stat. uncertainty [mm]	± 0.002	± 0.002	± 0.002	± 0.002
Syst. uncertainty [mm]	± 0.083	± 0.015	± 0.016	± 0.017
LHC fill 4511				
Distance [mm]	12.589	13.744	13.667	12.560
Stat. uncertainty [mm]	± 0.002	± 0.002	± 0.002	± 0.002
Syst. uncertainty [mm]	± 0.083	± 0.015	± 0.015	± 0.017

Table A.2: Distances with uncertainties between ALFA MDs edges.

RP	B7L1U	B7L1L	A7L1U	A7L1L	A7R1U	A7R1L	B7R1U	B7R1L
LHC fill 4499								
Horizontal offset [μm]	599.66	-156.96	707.00	488.60	189.10	230.04	222.64	331.75
Stat. uncertainty [μm]	± 0.05	± 0.04	± 0.04	± 0.03	± 0.03	± 0.03	± 0.04	± 0.04
Syst. uncertainty [μm]	± 0.61	± 0.42	± 1.73	± 0.45	± 0.99	± 1.09	± 0.35	± 2.30
Time dependency [μm]	± 3.51	± 3.51	± 3.51	± 3.51	± 2.52	± 2.52	± 2.52	± 2.52
LHC fill 4505								
Horizontal offset [μm]	610.76	-145.89	721.36	501.86	190.69	231.10	225.89	335.43
Stat. uncertainty [μm]	± 0.06	± 0.07	± 0.05	± 0.05	± 0.05	± 0.04	± 0.07	± 0.06
Syst. uncertainty [μm]	± 0.26	± 0.42	± 1.34	± 1.27	± 1.13	± 1.08	± 0.71	± 2.01
Time dependency [μm]	± 1.39	± 1.39	± 1.39	± 1.39	± 1.31	± 1.31	± 1.31	± 1.31
LHC fill 4509								
Horizontal offset [μm]	620.08	-136.58	726.53	507.69	172.63	214.58	207.40	317.47
Stat. uncertainty [μm]	± 0.04	± 0.04	± 0.03	± 0.03	± 0.03	± 0.03	± 0.04	± 0.04
Syst. uncertainty [μm]	± 0.75	± 0.66	± 0.69	± 0.84	± 0.51	± 0.41	± 0.75	± 1.95
Time dependency [μm]	± 6.34	± 6.34	± 6.34	± 6.34	± 2.84	± 2.84	± 2.84	± 2.84
LHC fill 4510								
Horizontal offset [μm]	603.51	-153.45	712.64	493.49	165.85	207.59	202.36	312.16
Stat. uncertainty [μm]	± 0.06	± 0.06	± 0.03	± 0.04	± 0.04	± 0.04	± 0.06	± 0.05
Syst. uncertainty [μm]	± 0.35	± 0.38	± 1.65	± 0.99	± 0.55	± 0.29	± 0.74	± 2.20
Time dependency [μm]	± 1.26	± 1.26	± 1.26	± 1.26	± 1.81	± 1.81	± 1.81	± 1.81
LHC fill 4511								
Horizontal offset [μm]	591.31	-165.52	699.01	480.28	154.64	195.73	193.00	302.25
Stat. uncertainty [μm]	± 0.07	± 0.07	± 0.05	± 0.05	± 0.05	± 0.05	± 0.07	± 0.07
Syst. uncertainty [μm]	± 0.71	± 0.66	± 1.33	± 0.55	± 0.27	± 0.36	± 0.53	± 2.28
Time dependency [μm]	± 1.99	± 1.99	± 1.99	± 1.99	± 0.88	± 0.88	± 0.88	± 0.88

Table A.3: Horizontal offsets of the ALFA RPs with their uncertainties.

RP	B7L1	A7L1	A7R1	B7R1
LHC fill 4499				
Vertical offset [μm]	167.2	151.1	111.4	175.5
Stat. uncertainty [μm]	± 2.0	± 2.2	± 1.8	± 2.3
Syst. uncertainty [μm]	± 21.4	± 25.3	± 24.2	± 18.0
Time dependency [μm]	± 18.0	± 18.0	± 18.0	± 18.0
LHC fill 4505				
Vertical offset [μm]	193.5	172.8	126.1	187.0
Stat. uncertainty [μm]	± 2.8	± 3.1	± 3.7	± 3.2
Syst. uncertainty [μm]	± 30.5	± 23.0	± 16.2	± 17.0
Time dependency [μm]	± 16.0	± 16.0	± 22.5	± 22.5
LHC fill 4509				
Vertical offset [μm]	138.9	111.9	118.4	175.5
Stat. uncertainty [μm]	± 1.4	± 1.3	± 1.1	± 1.3
Syst. uncertainty [μm]	± 32.0	± 22.4	± 11.7	± 13.4
Time dependency [μm]	± 11.5	± 11.5	± 7.5	± 7.5
LHC fill 4510				
Vertical offset [μm]	169.7	144.1	87.6	179.6
Stat. uncertainty [μm]	± 2.6	± 2.5	± 2.5	± 2.7
Syst. uncertainty [μm]	± 18.7	± 14.2	± 13.8	± 24.5
Time dependency [μm]	± 14.5	± 14.5	± 9.0	± 9.0
LHC fill 4511				
Vertical offset [μm]	147.1	126.3	114.7	173.4
Stat. uncertainty [μm]	± 3.4	± 3.3	± 3.5	± 3.5
Syst. uncertainty [μm]	± 29.0	± 17.1	± 15.4	± 20.5
Time dependency [μm]	± 19.5	± 19.5	± 16.5	± 16.5

Table A.4: Vertical offsets of the ALFA stations with their uncertainties.

RP	B7L1U	B7L1L	A7L1U	A7L1L	A7R1U	A7R1L	B7R1U	B7R1L
LHC fill 4499								
Rotation angle [mrad]	4.37	1.30	2.81	1.86	-1.02	-0.51	0.58	-0.41
Stat. uncertainty [mrad]	±0.03	±0.03	±0.02	±0.02	±0.02	±0.02	±0.03	±0.03
Syst. uncertainty [mrad]	±0.26	±0.16	±0.33	±0.14	±0.35	±0.27	±0.46	±0.35
Time dependency [mrad]	±0.11	±0.11	±0.11	±0.11	±0.13	±0.13	±0.13	±0.13
LHC fill 4505								
Rotation angle [mrad]	4.33	1.17	2.71	1.76	-1.09	-0.50	0.58	-0.34
Stat. uncertainty [mrad]	±0.04	±0.04	±0.02	±0.03	±0.03	±0.03	±0.04	±0.04
Syst. uncertainty [mrad]	±0.22	±0.18	±0.31	±0.11	±0.32	±0.29	±0.37	±0.33
Time dependency [mrad]	±0.09	±0.09	±0.09	±0.09	±0.12	±0.12	±0.12	±0.12
LHC fill 4509								
Rotation angle [mrad]	4.65	1.27	2.88	1.85	-1.05	-0.52	0.55	-0.38
Stat. uncertainty [mrad]	±0.03	±0.03	±0.02	±0.02	±0.02	±0.02	±0.03	±0.03
Syst. uncertainty [mrad]	±0.35	±0.13	±0.28	±0.25	±0.28	±0.24	±0.39	±0.43
Time dependency [mrad]	±0.12	±0.12	±0.12	±0.12	±0.13	±0.13	±0.13	±0.13
LHC fill 4510								
Rotation angle [mrad]	4.47	1.37	2.91	1.92	-0.99	-0.52	0.58	-0.46
Stat. uncertainty [mrad]	±0.03	±0.03	±0.02	±0.02	±0.02	±0.02	±0.04	±0.03
Syst. uncertainty [mrad]	±0.27	±0.16	±0.38	±0.15	±0.34	±0.32	±0.48	±0.38
Time dependency [mrad]	±0.15	±0.15	±0.15	±0.15	±0.10	±0.10	±0.10	±0.10
LHC fill 4511								
Rotation angle [mrad]	4.37	1.24	2.80	1.83	-1.01	-0.49	0.57	-0.36
Stat. uncertainty [mrad]	±0.04	±0.04	±0.03	±0.03	±0.03	±0.03	±0.04	±0.04
Syst. uncertainty [mrad]	±0.25	±0.14	±0.33	±0.14	±0.31	±0.25	±0.48	±0.31
Time dependency [mrad]	±0.09	±0.09	±0.09	±0.09	±0.10	±0.10	±0.10	±0.10

Table A.5: Rotation angles θ_Z of the ALFA RPs with their uncertainties.